UNIVERSIDADE FEDERAL DO RIO GRANDE DO SUL
INSTITUTO DE GEOCIÊNCIAS
PROGRAMA DE PÓS-GRADUAÇÃO EM GEOCIÊNCIAS

EVOLUÇÃO GEOLÓGICA INTEGRADA DO OFIOLITO CERRO DO OURO E DO ARCO SÃO GABRIEL, ESCUDO SUL-RIOGRANDENSE, BRASIL

TIARA CERVA ALVES

ORIENTADOR – Prof. Dr. Léo Afraneo Hartmann

Porto Alegre, 2021

UNIVERSIDADE FEDERAL DO RIO GRANDE DO SUL
INSTITUTO DE GEOCIÊNCIAS
PROGRAMA DE PÓS-GRADUAÇÃO EM GEOCIÊNCIAS

EVOLUÇÃO GEOLÓGICA INTEGRADA DO OFIOLITO CERRO DO OURO E DO ARCO JUVENIL SÃO GABRIEL, ESCUDO SUL-RIOGRANDENSE, BRASIL

TIARA CERVA ALVES

ORIENTADOR – Prof. Dr. Léo Afraneo Hartmann

BANCA EXAMINADORA:

Prof. Dr. Viter Magalhães Pinto – Centro de Engenharias, Universidade Federal de Pelotas

Prof. Dr. Felipe Guadagnin – Departamento de Geologia, Universidade Federal do Pampa

Prof. Dr. Everton Marques Bongiolo – Instituto de Geociências, Universidade Federal do Rio Grande do Sul

> Tese de doutorado apresentada como requisito parcial para a obtenção do Título de Doutor em Ciências.

Porto Alegre, 2021

AGRADECIMENTOS

RESUMO

Rochas do arco São Gabriel e de fragmentos ofiolíticos estão preservadas no Cinturão Dom Feliciano e registram características similares aos regimes modernos de placas tectônicas. A análise de processos magmáticos, metamórficos e metassomáticos é necessária para entender a evolução geológica integrada de fragmentos ofiolíticos e do arco intraoceânico, sendo o objetivo desta tese. Os estudos foram desenvolvidos nas regiões do Cambaizinho, Palma e Palma Leste, no Terreno São Gabriel. Geocronologia por LA-ICP-MS U-Pb em zircão, granada e rutilo foram combinados com isótopos de boro em dravita, isótopos de Lu-Hf e química de elementos traço em zircão. As condições metamórficas foram determinadas através de modelagem termodinâmica. Amostras da infraestrutura do arco forneceram idades magmáticas de 724,6 ± 3,2 Ma (metatonalito Suíte Vila Nova), 731,6 ± 0,5 Ma (metagabro São Luís), 698,9 ± 4,2 Ma e 673,9 ± 6,8 Ma (monzogranito Suíte Sanga do Jobim). Valores positivos de $\varepsilon Hf(t)$ indicam composições de zircões derivadas de manto depletado (metatonalito = +10,1 e +7,4; metagabro = +11,1 e +7,1; monzogranito = +9,2 e +2,5). A superestrutura do arco foi investigada através da análises de metassedimentos. As idades variam de 817 Ma a 702,5 Ma, com concentração em 769,1 ± 4.6 Ma e 731,6 ± 2.2 Ma. A idade máxima de deposição de 739.04 ± 4.47 Ma foi calculada com base em amostras de xistos. A proveniência em rochas do arco é sugerida com base nas idades obtidas, nos valores de $\varepsilon Hf(t)$ (+0,4 a +11,9), na assinatura de elementos terras raras de zircões detríticos, e nos valores de $\delta^{11}B$ em dravitas (+0,51 a +3,39). A assembleia granada + estaurolita + biotita + muscovita + clorita + plagioclásio + ilmenita + quartzo foi formada na fácies anfibolito inferior, em temperaturas e pressões entre 536-555 ºC e 4,5-5,1 kbar. Idades metamórficas foram obtidas por U-Pb em granada (721 ± 14 Ma, metassedimento) e rutilo (706 ± 11 Ma, metagabro). A idade do metassomatismo de fundo oceânico da seção de manto do ofiolito foi obtida por datação U-Pb em rutilo de rocha ultramáfica (787,6 ± 2,6 Ma) e por U-Pb em zircão de cloritito metassomático (889,2 ± 2,3 Ma), com $\varepsilon Hf(t)$ do zircão entre +17,5 e +9,9. Os processos geotectônicos incluíram a construção inicial do Terreno São Gabriel em ~817-725 Ma, metamorfismo em ~721-706 Ma e metassomatismo da crosta oceânica em ~887 Ma e ~787 Ma. A presente interpretação de evolução geológica é um avanço no entendimento dos processos de geração de crosta oceânica e arco intraoceânico e colisão na Orogênese Brasiliana.

Palavras-chave: ofiolito, arco São Gabriel, geocronologia U-Pb em zircão, rutilo e granada, modelagem termodinâmica.

ABSTRACT

Neoproterozoic rocks from the São Gabriel arc are preserved in the Dom Feliciano Belt and evolved similarly to modern plate tectonic regimes. The integrated analysis of magmatic, metamorphic and metasomatic processes is necessary to understand the geological evolution of ophiolitic fragments and intra-oceanic arcs and is the objective of this thesis. The studies were developed in the Cambaizinho, Palma and Palma Leste regions, São Gabriel Terrane. LA-ICP-MS U-Pb geochronology in zircon, garnet and rutile were combined with boron isotopes in dravite, Lu-Hf isotopes and trace element chemistry in zircon. The metamorphic conditions were determined through petrography, mineral chemistry and thermodynamic modeling. Samples from the infrastructure of the arc provided zircon U-Pb magmatic ages of 724.6 ± 3.2 Ma (Vila Nova Suite metatonalite), 731.6 ± 0.5 Ma (São Luís metagabbro), 698.9 ± 4.2 Ma and 673.9 ± 6.8 Ma (Sanga do Jobim Suite monzogranite). Positive values of εHf (t) indicate zircon compositions derived from depleted mantle (metatonalite = +10.1 and +7.4; metagabbro = +11.1 and +7.1; monzogranite = +9.2 and +2.5). Investigated metasedimentary rocks represent the superstructure of the arc; the ages range from 817 to 702.5 Ma, with a concentration of 769.1 ± 4.6 Ma and 731.6 ± 2.2 Ma. The maximum depositional age of 739.04 ± 4.47 Ma was calculated using schist samples. The provenance in rocks from the arc is based on the ages, values of εHf(t) (+0 .4 to +11.9), signature of rare earth elements of detrital zircon, and values of $\delta^{11}B$ in dravites (+0.51 to +3.39). The garnet + staurolite + biotite + muscovite + chlorite + plagioclase + ilmenite + quartz assemblage was formed under lower amphibolite facies, estimated at temperatures and pressures between 536-555 ºC and 4.5-5.1 kbar. Metamorphic ages are from U-Pb in garnet (721 ± 14 Ma, metasediment) and rutile (706 ± 11 Ma, metagabbro). The age for metasomatism of the seafloor in the ophiolite mantle section is from U-Pb dating in rutile from an ultramafic rock (787.6 ± 2.6 Ma) and from U-Pb on metasomatic chloritite zircon (889.2 ± 2.3 Ma), with zircon εHf(t) between +17.5 and +9.9. The geotectonic processes included the initial construction of the São Gabriel Terrane at ~817-725 Ma, metamorphism at ~721-706 Ma, and oceanic crust metasomatism at ~887 and ~787 Ma. The present geological evolutionary interpretation is an advance in the understanding of the processes of oceanic crust and intra-oceanic arc generation in the Brasiliano Orogenesis.

Key-words: ophiolite, São Gabriel arc, zircon, rutile and garnet U-Pb geochronology, thermodynamic model.

LISTA DE ABREVIAÇÕES

ÓRGÃOS, INSTITUIÇÕES E PROGRAMAS

CNPq: Conselho Nacional de Desenvolvimento Científico e Tecnológico

CPGq-UFRGS: Centro de Estudos em Petrologia e Geoquímica da Universidade Federal do Rio Grande do Sul

DEGEO-UFOP: Departamento de Geologia da Universidade Federal de Ouro Preto

FAPERGS: Fundação de Amparo à Pesquisa do Estado do Rio Grande do Sul

IGEO-UFRGS: Instituto de Geociências da Universidade Federal do Rio Grande do Sul

IGL-UFOP: Laboratório de Geologia Isotópica da Universidade Federal de Ouro Preto

LMic-UFOP: Laboratório de Microscopia e Microanálise da Universidade Federal de Ouro Preto

PPGGEO-UFRGS: Programa de Pós-Graduação em Geociências da Universidade Federal do Rio Grande do Sul

SUMÁRIO

ESTRUTURA DA TESE

A tese está estruturada na forma de um capítulo de introdução e um capítulo contendo os artigos científicos internacionais. A introdução inclui uma sinopse sobre os assuntos abordados para o desenvolvimento da tese e uma análise integradora. O desenvolvimento da tese é apresentado na forma de três artigos científicos publicados em periódicos internacionais. Assim, este volume de tese está dividido da seguinte forma:

Capítulo 1 – (1) Introdução sobre o tema pesquisado, (2) problema científico, (3) objetivos da pesquisa, (4) análise integradora dos principais resultados e interpretações, (5) conclusões obtidas durante o desenvolvimento da tese de doutorado e (6) referências.

Capítulo 2 - Apresentação dos artigos científicos publicados em periódicos internacionais, com as classificações do Qualis-CAPES/PPGGEO, conforme listados abaixo.

Artigo 1 (Qualis A1) - *Integrated ophiolite and arc evolution, southern Brasiliano Orogen*

Autores: Cerva-Alves, T., Hartmann, L.A., Remus, M.V.D., Lana, C.

Artigo publicado na *Precambrian Research*, v. 341, 105648.

Artigo 2 (Qualis A1) - *Metamorphic evolution of the juvenile Serrinha forearc basin in the southern Brasiliano Orogen*

Autores: Cerva-Alves, T., Hartmann, L.A., Queiroga, G.N., Lana, C., Castro, M.P., Maciel, L.A.C., Remus, M.V.D.

Artigo publicado na *Precambrian Research*, v. 365, 106394.

Artigo 3 (Qualis A3) - *Rutile and zircon age and geochemistry in the evolution of the juvenile São Gabriel Terrane early in the Brasiliano Orogeny*

Autores: Cerva-Alves, T., Hartmann, L.A., Lana, C., Queiroga, G.N., Maciel, L.A.C., Leandro, C.G., Savian, J.F.

Artigo publicado no *Journal of South American Earth Sciences*, v. 112, 103505.

CAPÍTULO 1 – INTRODUÇÃO

1. Aspectos gerais

Orógenos acrescionários estão vinculados a processos convergentes relacionados ao ciclo de Wilson (Cawood *et al.*, 2009; Collins *et al.*, 2011). O registro da justaposição diacrônica de unidades geológicas contendo ofiolitos, plútons com afinidade de arco intraoceânico e rochas vulcanossedimentares é indicativo do acréscimo desses arcos ao continente (Tapster *et al.*, 2014). Esses processos geológicos foram responsáveis pela geração da crosta oceânica e cinturões orogênicos acrescionários ao longo do Neoproterozóico. A fase de colisão se inicia após o término da subducção oceânica (Wilson, 1965; Burke, 2011), quando ocorre um período de transição tectônica da subducção oceânica para a colisão continental, até culminar na colisão entre continentes (Beaumont *et al.*, 1996; Zheng *et al.*, 2015). A dinâmica na transição tectônica da subducção oceânica, incluindo a formação de bacias de *foreland*, para a colisão continental pode envolver a reversão e ruptura de placas oceânicas (Wortel & Spakman, 2000), subducção e exumação de materiais (Zheng, 2012). O entendimento dos processos relacionados às fases acrescionária é crucial para definir a evolução geológica em diversas escalas.

No Orógeno Brasiliano do Atlântico Sul (Caxito *et al.* 2021; correspondente à Província Mantiqueira de Almeida *et al.*, 1981), o Cinturão Dom Feliciano se estende por mais de 1.100 km, na direção NE-SW (Fig. 1a) (Hueck *et al.*, 2018; Caxito *et al.*, 2021). No setor centro-oeste do Cinturão, o estágio acrescionário da orogênese está preservado no Terreno São Gabriel, que fornece um raro exemplo de litosfera oceânica toniano-criogeniana. Estudos no Terreno de São Gabriel identificaram assembleias plutônicas e vulcanoclásticas com assinatura juvenil (Babinski *et al.*, 1996; Arena *et al.*, 2017; Siviero *et al.*, 2021) e rochas máfico-ultramáficas com assinatura química de MORB (Arena *et al.*, 2016, 2017; Hartmann *et al.*, 2019). Apesar de muitos esforços aplicados ao estudo das rochas do arco intraoceânico (e.g., Philipp *et al.*, 2018; Massuda *et al.*, 2020; Werle *et al.*, 2020; Hueck *et al.*, 2020; Hartmann *et al.*, 2021) e rochas do ofiolito (e.g., Arena *et al.*, 2016, 2017, 2018; Hartmann *et al.*, 2019), uma visão integrada da evolução do conjunto arco de ilhas e ofiolitos permanece ausente. A datação da crosta oceânica e do manto é um desafio devido à ausência de minerais datáveis nas rochas máfico-ultramáficas. Compreender os

processos magmáticos, metamórficos e metassomáticos envolvidos na rota de uma dorsal oceânica intermediária do Oceano Adamastor à subducção e colisão com o Cráton do Rio de La Plata continua sendo um desafio fundamental na geotectônica do Neoproterozóico, e são abordados nesta tese.

2. Problema científico

O problema científico solucionado nesta tese está inserido no conhecimento da evolução de ofiolitos e orogêneses, com foco na fração juvenil da orogênese Brasiliana. Ofiolitos são fragmentos de antigas crostas oceânicas e do manto superior, cuja evolução ocorreu em diferentes ambientes geotectônicos, influenciando de forma significativa a preservação destas rochas. O estudo de ofiolitos fornece evidências importantes sobre a dinâmica dos processos magmáticos, tectônicos e hidrotermais associados à expansão do assoalho oceânico anteriores a 180 Ma, uma vez que nenhuma litosfera oceânica mais velha do que essa idade é preservada nos oceanos modernos.

A orogênese é definida como uma interação de placas tectônicas, com o desenvolvimento de um ciclo de Wilson; a colagem orogênica é uma sequência concatenada de orogenias; a fusão é a soma desses processos, levando à formação de uma grande massa continental ou um supercontinente (Helwig, 1974; Sengör, 1990; Brito-Neves *et al.*, 2014). Um produto da interação convergente de placas litosféricas é a subducção (Stern, 2011). Arcos vulcânicos se desenvolvem acima da zona de subducção (Flores & Gazel, 2020), e podem se apresentar na forma de arco de ilhas (arco magmático intraoceânico do tipo Japão e Indonésia), ou como arco magmático do tipo continental ativo (do tipo andino), culminando em cadeia de montanhas intracontinental (Alpes) (Heilbron *et al.*, 2004). Nas décadas de 1990 e 2000, diversos estudos relacionados aos padrões de montagem do supercontinente Rodínia foram publicados, indicando uma idade final de fusão de 1 Ga (Moores, 1993, 2002; Rogers, 1996; Unrug, 1996, 1997; Li *et al.*, 2008). Processos geológicos evolutivos significativos ocorreram posteriormente, no Neoproterozoico. Estes processos envolveram o desmembramento do Rodínia, com fragmentação e afastamento de blocos em torno do Laurentia, com consequente formação de crosta oceânica, e posterior colisão para formação do supercontinente Gondwana (Hoffman, 1991; Li *et al.*, 2008). Mundialmente, ofiolitos neoproterozóicos fornecem informações

sobre a quebra do continente Rodínia e a amalgamação do continente Gondwana. Um consenso comum sobre os modelos de amalgamação do Gondwana é que o processo envolveu subducção generalizada, seguida por colisões de vários blocos continentais, resultando nos cinturões orogênicos Pan-Africano/Moçambique e Brasiliano (Cordani *et al.*, 2003; Collins & Pisarevsky, 2005; Meert & Lieberman, 2008; Gray *et al.*, 2008; Murphy *et al.*, 2013; Oriolo *et al.*, 2017; Luchi *et al.*, 2018).

O Orógeno Brasiliano do Atlântico Sul (Caxito *et al.* 2021) representa uma unidade neoproterozóica-cambriana relacionada ao encerramento de paleo-oceanos e à amalgamação do paleocontinente Gondwana Oeste (Chemale Jr., 2000; Suita *et al.*, 2004). Nos registros geológicos neoproterozóicos da América do Sul, verifica-se a ocorrência de ofiolitos obductados em arcos de ilhas oceânicos e arcos continentais (e.g., Peixoto *et al.*, 2017; Amaral *et al.*, 2020; Caxito *et al.*, 2021). Ofiolitos também são descritos em cinturões de dobras e falhas registrados nos cinturões Dom Feliciano (722 Ma; Arena *et al.*, 2018), Araguaia-Paraguai (708 Ma; Souza *et al.*, 2019), Araçuaí-Ribeira (660 Ma; Queiroga *et al.*, 2007), Brasília (760 Ma; Brown *et al.*, 2020) e na Província Borborema – Riacho do Pontal (630 Ma; Caxito *et al.*, 2014). No Rio Grande do Sul, diversos fragmentos ofiolíticos foram reconhecidos no Terreno juvenil São Gabriel, Cinturão Dom Feliciano, e na presente tese são referenciados como Ofiolito Cerro do Ouro (Goñi, 1962). Estes fragmentos incluem os ofiolitos Bossoroca, Cambaizinho, Cerro Mantiqueiras, Ibaré, Palma, Palme Leste e Passo do Ivo (Arena *et al.*, 2016, 2017, 2020; Hartmann *et al.*, 2019). Ainda no Cinturão Dom Feliciano, foram descritos o ofiolito Capané, no Complexo Porongos (Arena *et al.*, 2018) que é um cinturão de dobras e falhas (Pertille *et al.*, 2017); e o ofiolito Arroio Grande, no Terreno Jaguarão (Ramos *et al.*, 2018, 2020).

No Terreno São Gabriel localiza-se o problema estudado nesta tese. Neste terreno há registros de tectonismo convergente associado com intenso magmatismo juvenil relacionado ao arco São Gabriel. São incluídas: (1) unidades plutônicas do Complexo Cambaí, incluindo as Suítes Vila Nova, Lagoa da Meia Lua e Sanga do Jobim, que correspondem à infraestrutura do arco, (2) rochas vulcânicas basálticas a riolíticas deformadas e rochas metassedimentares do Grupo Vacacaí (Babisnski *et al.,* 1996; Chemale Jr., 2000) que compõem a superestrutura do arco, (3) complexos ofiolíticos (Goñi, 1962; Arena *et al.*, 2017, 2018, 2020; Hartmann *et al.*, 2019) e (4) granitos pós-colisionais (Chemale *et al.*, 2000; Werle *et al.*, 2020) e (5) intrusões de carbonatitos (Cerva-Alves *et al.*, 2017).

A infraestrutura do arco inclui a associação DTTG (diorito, tonalito, trondhjemito, granodiorito) da Suíte Vila Nova (ortognaisse Vila Nova; Hartmann *et al.*, 2011) e granitóides sincolisionais pertencentes às Suítes Lagoa da Meia Lua e Sanga do Jobim (Kraemer, 1995; Fernandes *et al.*, 1995; Leite *et al.*, 1998; Saalmann *et al.*, 2006, 2011; Hartmann *et al.*, 2011). Idades entre 794 ± 6 Ma e 701 ± 9,7 Ma foram obtidas pelo método U-Pb em zircão da Suíte Vila Nova (Leite *et al.*, 1998; Hartmann *et al.*, 2011; Saalmann *et al.*, 2011; Vedana *et al.*, 2018), e entre 704 ± 3 Ma e 675 ± 3,8 Ma para Suítes Sanga do Jobim e Lagoa da Meia Lua (Hartmann *et al.*, 2011; Vedana *et al.*, 2018). Outras idades também foram relacionadas à atividade magmática (plutônica) no arco, por exemplo 695 Ma, tonalito BR290 (Hartmann *et al.*, 2011) e 701 ± 9,7 Ma, trondhjemito Vila Nova (Saalmann *et al.*, 2011). Uma idade U-Pb de 879 ± 14 Ma foi obtida em zircões do diorito do Passinho (Leite *et al.*, 1998) e é interpretada como um arco toniano chamado arco Passinho (Hartmann *et al.*, 2000). As diversas datações publicadas permitiram definir o período com magmatismo ativo no arco São Gabriel, no entanto, estudos mais aprofundados no zircão são necessários para determinar o ambiente de formação dos zircões, e se houve alguma influência de contaminantes de crosta continental.

A porção supracrustal do arco é representada por sucessões metavulcanossedimentares e mármore do Grupo Vacacaí (Chemale Jr., 2000; parte do Grupo Palma - Strieder *et al.*, 2000; Goulart *et al.*, 2013; Saalmann *et al.*, 2011), incluindo os Complexos Cambaizinho e Passo Feio (Bitencourt, 1983; Remus, 1990; Hartmann *et al.*, 1990; Lopes *et al.*, 2015), e as Formações Pontas do Salso (Remus *et al.*, 1999; Saalmann *et al.*, 2005c; Vedana *et al.*, 2018), Bela Vista e Campestre (Chemale *et al.*, 1995). A datação de zircões das Formações Bela Vista e Campestre forneceram idades entre 767,2 ± 2,9 Ma e 757 ± 17 Ma para as rochas vulcânicas (Remus *et al.*, 1999; Gubert *et al.*, 2016; Arena *et al.*, 2017). Um intervalo de idade entre 920 Ma e 840 Ma, com pico máximo modal em 842 ± 5 Ma, obtido em zircões de rochas metavulcanoclásticas da Formação Campestre (Hartmann *et al.*, 2021), pode ser o elo perdido entre os arcos Passinho e São Gabriel, bem como um indicativo de construção contínua do arco.

Além da avaliação de dados obtidos a partir de rochas plutônicas e vulcânicas, uma forma de estudar a evolução geológica de orógenos é através da análise de rochas metassedimentares que se formaram em bacias do arco. Informações sobre as idades de zircões detríticos foram obtidas por vários autores e possibilitam um bom

entendimento da evolução das bacias sedimentares. Vedana *et al.* (2018) obtiveram idades entre 897 Ma e 684 Ma para a Formação Pontas do Salso. Idades determinadas para a Formação Ibaré variam entre 960 Ma e 720 Ma (Philipp *et al.*, 2021), onde foram reconhecidos cinco picos principais em 880 Ma, 840 Ma, 780 Ma, 750 Ma e 720 Ma. Na Formação Campestre, Philipp *et al.* (2021) obtiveram idades variando entre 810 Ma e 750 Ma, com pico em 870 Ma, 830 Ma e 790 Ma. No Complexo Cambaizinho, o estudo de Lena *et al.* (2014) indicou idades entre 840 Ma e 680 Ma, com pico entre 750 Ma e 700 Ma. A avaliação integrada das idades permite sugerir que o arco Passinho evoluiu de forma contínua até chegar à fase madura, correspondente ao arco São Gabriel, e sendo área-fonte dos sedimentos durante a sua evolução. No entanto, estudos isotópicos nos zircões detríticos e em outros minerais determinantes para proveniência, tais como turmalinas, são necessários para confirmar a origem juvenil dos metassedimentos. No Complexo Porongos, por exemplo, foram identificados zircões tonianos (809 Ma, 801 Ma e 773 Ma) com assinatura de reservatório crustal (Pertille *et al.*, 2017). Os valores de εHf = -21 a -10 e TDM = 2,1 a 1,7 Ga, apresentados por Pertille *et al.* (2017), levaram à interpretação de que ocorreu um evento magmático no Toniano devido à reciclagem de material Paleoproterozóico. Tem-se, portanto, o registro de dois eventos magmáticos distintos (reciclagem de material crustal e magmatismo com assinatura juvenil) ocorridos no mesmo período. Desta forma, existem duas possíveis áreas-fonte para as paleo-bacias do Grupo Vacacaí, sendo necessária a obtenção de dados adicionais (além de datação) que permitam distinguir entre as duas possíveis áreas-fonte.

No período de acresção do arco São Gabriel foram reconhecidas duas fases deformacionais (Remus, 1990; Hartmann *et al.*, 2000; Saalmann *et al.*, 2005b), que foram responsáveis pelo metamorfismo no fácies anfibolito inferior (médio em alguns setores do terreno) e xisto verde (Remus, 1990). A idade metamórfica de 696 ± 5 Ma foi determinada por Hartmann *et al.* (2011) em zircão de metatonalito amostrado na região de Buriti, e foi relacionada à zona de deformação. Devido aos baixos valores de Th/U (0,02) obtidos nos zircões analisados, estes foram considerados metamórficos (Hartmann *et al.*, 2011). Hueck *et al.* (2020), por sua vez, estabeleceram três idades metamórficas relacionadas à foliação regional na região de Ibaré, limite sudoeste do Terreno São Gabriel. As idades 757,7 ± 11,4 Ma, 747,1 ± 9,2 Ma e 743,5 ± 10,2 Ma foram obtidas pelo método K-Ar em mica branca. Porém, estas idades são coincidentes com o período de atividade vulcânica no arco São Gabriel, e não

englobam os processos metamórficos ocorridos posteriormente no terreno. Neste caso, a obtenção de dados robustos relacionados diretamente à idade do metamorfismo se faz necessária.

As fácies metamórficas a que diferentes rochas do Terreno São Gabriel foram submetidas foram determinadas por diversos autores. Os eventos M1 e M2 foram descritos em metapelitos do Complexo Passo Feio por Bitencourt (1983), sendo o evento M1 de fácies anfibolito inferior (zona da estaurolita), e o evento M2 retrogresssivo de fácies xisto verde (com estaurolita e granada sendo substituídos por clorita). Hartmann *et al.* (1990) determinaram o grau metamórfico para o Complexo Passo Feio, com base em química mineral de anfibólios obtidos em amostras de anfibolitos. Para esses autores, o evento M1 atingiu fácies anfibolito, que está registrado na porção norte e sul do Complexo Passo Feio; o evento M2 atingiu fácies xisto verde a anfibolito na borda norte, e fácies anfibolito na porção sul do complexo. A fácies prenhita-pumpellyíta foi determinada por Bicalho *et al.* (2019) para os basaltos e lavas almofadadas presentes na porção sudoeste do complexo. A fácies xisto verde foi determinada para diques, enquanto a fácies anfibolito inferior foi obtida em anfibolitos (Bicalho *et al.*, 2019). Para a região do Cambaizinho, noroeste do Terreno São Gabriel, Remus (1990) avaliou sequências pelíticas e máfica-ultramáficas de rochas do Complexo Cambaizinho, Grupo Vacacaí. Segundo este autor, a paragênese mineral relacionada ao evento M1 é compatível com fácies anfibolito, enquanto a assembleia descrita para o evento M2 é relacionada à fácies xisto verde. Saalmann *et al.* (2006), por sua vez, avaliaram as regiões do Cambaizinho e Bossoroca, onde identificaram 4 eventos deformacionais com metamorfismo associado, sendo os três primeiros relacionados à fase acrescionária. O evento M1 foi identificado através do reconhecimento de quartzo segregado e mobilizado em rochas metapelíticas nos Complexos Cambaizinho e Passo Feio, sendo formado sob condições de fácies xisto verde. O evento M2 atingiu fácies anfibolito; o evento M3 atingiu fácies xisto verde, e está relacionado às intrusões sintectônicas (Suítes Sanga do Jobim e Lagoa da Meia Lua) (Saalmann *et al.*, 2006).

A obtenção das condições de P-T dos eventos metamórficos, por modelagem termodinâmica, é restrita a rochas metapelíticas do Complexo Passo Feio, Grupo Vacacaí, na região de Caçapava do Sul. Tennholm (2019) determinou as condições do metamorfismo analisando duas amostras. As condições calculadas na primeira amostra foram de 2,7-4,8 kbar e 515-555 ºC, obtidas para o início da cristalização da

granada, com pico metamórfico em 4,7-7,6 kbar e 535-590 ºC; a segunda amostra forneceu condições de 2,36 kbar e 485 ºC para o início da cristalização, com pico metamórfico em 5,3-7 kbar e 500-550ºC. Costa *et al.* (2021), por sua vez, obtiveram as condições do início do crescimento das granadas em 3-4,3 kbar e 530-550 ºC, com pico metamórfico (M1) em 5-5,5 kbar e 560-570 ºC. Faz-se necessária, portanto, a determinação das condições do metamorfismo em outras unidades litológicas no Terreno São Gabriel.

A abertura do oceano proto-Adamastor (Hartmann *et al.*, 2019), a leste do Cráton Rio de La Plata, entre 930 Ma e 900 Ma (Arena *et al.*, 2017, 2018; Hartmann *et al.*, 2019), corresponde ao período de formação de litosfera oceânica gerada pelo início da quebra do Rodínia (Hartmann *et al.*, 2019). Fragmentos da crosta oceânica + manto gerados pela abertura do oceano proto-Adamastor foram obductados na superestrutura e infraestrutura do arco São Gabriel. Estes corpos ofiolíticos são falhados, dobrados e rompidos, com ausência da estratigrafia ofiolítica completa do tipo Penrose. Os grãos de zircão obtidos em albititos do ofiolito Cerro Mantiqueiras forneceram idade de cristalização de 923 ± 3 Ma e idade metassomática de 786 ± 13 Ma (Arena *et al.*, 2016), e 733 ± 10 Ma em zircões de metabasaltos (Leite *et al.*, 1998). No ofiolito Ibaré, zircões de albititos apresentaram idades de cristalização de 892 ± 2,8 Ma, enquanto zircões de turmalinito e cloritito forneceram idade de cristalização de 726 ± 22 Ma (Arena *et al.*, 2016, 2017). Os cristais de zircão do cloritito do ofiolito Palma fornecem idade de cristalização de 722 ± 3 Ma (Arena *et al.*, 2017); e no ofiolito Bossoroca, os zircões da amostra de turmalinito indicam idade de 920,4 ± 9,8 Ma (Hartmann *et al.*, 2019). As idades apresentadas foram obtidas a partir de zircões presentes em rochas metassomáticas da crosta oceânica. Alternativas de minerais para a datação de crosta oceânica em litologias com ausência de zircões se fazem necessárias, como por exemplo, rutilo. Além disto, é necessário o adensamento nas obtenções das idades dos ofiolitos descritos no Terreno São Gabriel devido à variação de idades observadas nos estudos pretéritos desenvolvidos nestes fragmentos.

As pesquisas desenvolvidas ao longo dos anos nos ofiolitos do Rio Grande do Sul (histórico em Hartmann *et al.*, 2021b; e também em Hartmann & Chemale Jr., 2003; Tickyj *et al.*, 2004; Saalmann *et al.*, 2011; Arena *et al.*, 2016, 2017, 2018, 2020; Ramos *et al.*, 2018, 2020; Hartmann *et al.*, 2019, 2021a, Massuda *et al.*, 2020; Werle *et al.*, 2020) e no arco de ilhas intraoceânico São Gabriel (e.g., Remus, 1990; Babinski *et al.*, 1996; Leite *et al.*, 1998; Remus *et al.*, 1999, 2000; Hartmann *et al.*, 2000, 2011;

Saalmann *et al.*, 2005a, b, c, 2006, 2011; Lena *et al.*, 2014; Philipp *et al.*, 2018, 2021; Vedana *et al.*, 2018) abordaram diversos aspectos e forneceram um número significativo de dados. Estudos relacionados aos processos de obdução de ofiolitos estão sendo difundidos em todo o mundo, e incluem a aplicação de diferentes ferramentas para a determinação dos eventos metamórficos e metassomáticos. Uma análise integrada e inovadora, abordando as relações entre a obducção dos fragmentos ofiolíticos no arco de ilhas São Gabriel, se faz necessária para o entendimento dos processos que envolveram a evolução geológica durante o Neoproterozóico do Escudo Sul-riograndense e sua importância no contexto do supercontinente Gondwana.

Persistem, portanto, vários problemas científicos a serem solucionados na evolução dos ofiolitos e das rochas encaixantes do Terreno São Gabriel. Estudos mais detalhados para a definição do ambiente de formação dos zircões das rochas do arco São Gabriel são necessários, bem como a definição das áreas-fonte para as paleo-bacias do Grupo Vacacaí. A determinação das condições de pressão-temperatura e idade (P-T-t) do metamorfismo se faz necessária para diferentes unidades do Terreno São Gabriel. Na ausência de rochas metassomáticas portadoras de zircão, minerais alternativos para datação do metassomatismo ocorrido na crosta oceânica e incluem o rutilo. Esta Tese de Doutorado soluciona esses problemas e apresenta uma análise integrada, com dados robustos, para definição da evolução das associações de rochas do Terreno São Gabriel durante a fase acrescionária do arco São Gabriel.

3. Objetivos

O objetivo desta Tese de Doutorado é a delimitação evolutiva de ofiolitos do Terreno São Gabriel no contexto de suas encaixantes plutônicas e vulcanoclásticas. As interpretações incluem o arco São Gabriel e o ofiolito Cerro do Ouro, e seu significado na construção do supercontinente Gondwana Ocidental. Para alcançar esta análise integrada, três áreas-alvo foram selecionadas para o desenvolvimento desta pesquisa, e estão localizadas nas regiões dos ofiolitos Cambaizinho, Palma e Palma Leste. A evolução conjunta do ofiolito e suas encaixantes inclui o conhecimento de:

- Idade e fonte das rochas do arco São Gabriel, nas regiões do Cambaizinho e da Palma;

- Condições e idade do metamorfismo ocorrido na região do Cambaizinho (determinação P-T-t);

- Identificação das principais fontes de zircão detrítico na Formação Serrinha e o estabelecimento da idade máxima de deposição;

- Identificação das principais fontes de turmalina de granada-estaurolita xisto na Formação Serrinha, para determinação dos ambientes de formação da rocha;

- Idade dos eventos metassomáticos ocorridos nos ofiolitos Cambaizinho e Palma Leste.

4. Análise integradora

Os principais eventos relacionados à evolução tectônica dos continentes incluem a geração de crosta oceânica, a subducção de arcos de ilhas intraoceânicos e a acresção à crosta continental. Devido aos distúrbios tectônicos causados pela fase colisional da Orogenia Brasiliana, o entendimento dos eventos geológicos ocorridos na era Neoproterozóica é um desafio. As unidades presentes no Terreno São Gabriel, incluindo mélanges de ofiolitos tonianos e o arco de ilhas intraoceânico (rochas da infraestrutura e da superestrutura do arco São Gabriel), fornecem uma oportunidade para o estudo da evolução do Gondwana durante a etapa acrescionária relacionada aos primeiros estágios da Orogenia Brasiliana. Os estudos desenvolvidos nesta tese são apresentados na forma de três artigos científicos, e abordam diferentes aspectos da evolução geológica ocorrida no período acrescionário. Assim, neste capítulo é feita uma análise integradora dos artigos científicos publicados. As rochas estudadas e a metodologia utilizada na presente tese, em cada artigo, encontram-se na Tabela 1.

Tabela 1. Síntese das rochas estudadas no Terreno São Gabriel. ETR = elementos terras raras; MT = modelagem termodinâmica; Artigo 1 = *Integrated ophiolite and arc evolution, southern Brasiliano Orogen*; Artigo 2 = *Metamorphic evolution of the juvenile Serrinha forearc basin in the southern Brasiliano Orogen*; Artigo 3 = *Rutile and zircon age and geochemistry in the evolution of the juvenile São Gabriel Terrane early in the Brasiliano Orogeny*.

Rocha	Unidade no terreno	Região	Mineral	Isótopos, química mineral	Artigo
Metatonalito	Arco São Gabriel, infraestrutura	Cambaizinho	zircão	U-Pb, Lu-Hf, ETR	1
Monzogranito (metamorfisado)	Arco São Gabriel, infraestrutura	Cambaizinho	zircão	U-Pb, Lu-Hf, ETR	1
Metagabro	Arco São Gabriel, infraestrutura	Cambaizinho	rutilo	U-Pb	3
Metagabro	Arco São Gabriel, infraestrutura	Palma	zircão	U-Pb, Lu-Hf, ETR	3
Para-anfibolito, granada xisto e granada-estaurolita xisto	Metassedimento, superestrutura	Cambaizinho	zircão	U-Pb, Lu-Hf, ETR	1, 2
Granada-estaurolita xisto	Metassedimento, superestrutura	Cambaizinho	granada turmalina	U-Pb, MT) B	2
Clorita-tremolita xisto	Ofiolito	Cambaizinho	rutilo	U-Pb	1
Cloritito	Ofiolito	Palma-Leste	zircão	U-Pb, Lu-Hf, ETR	3

No artigo *Integrated ophiolite and arc evolution, southern Brasiliano Orogen* (*Precambrian Research*) é apresentada uma análise sobre a evolução geológica integrada dos ofiolitos e do arco São Gabriel. Dados de geocronologia obtidos por LA-ICP-MS U-Pb em zircão de rochas metaígneas (infraestrutura) e metassedimentares (superestrutura), e em rutilo de clorita-tremolita xisto (ofiolito) forneceram informações sobre as idades dos eventos magmáticos e metassomáticos. Isótopos de Lu-Hf e análises químicas de elementos terras raras (ETR) do zircão indicam os ambientes de cristalização do zircão.

No artigo *Metamorphic evolution of the juvenile Serrinha forearc basin in the southern Brasiliano Orogen* (*Precambrian Research*) é apresentado um estudo com foco na determinação da idade e das condições do pico metamórfico ocorrido em uma amostra representativa dos metassedimentos presentes na superestrutura do arco, bem como na determinação do ambiente deposicional da paleo-bacia. Foram

desenvolvidos, ainda, cálculos termodinâmicos para determinação das condições de pressão e temperatura do pico metamórfico. Neste estudo, a metodologia adotada incluiu a obtenção de idade U-Pb em granada por LA-ICP-MS. Foram obtidos dados de análises químicas de rocha total e de química mineral em granada, muscovita, feldspato, biotita, estaurolita, turmalina e clorita. Estes dados possibilitaram o desenvolvimento de modelagem termodinâmica e a obtenção das pressões e temperaturas do metamorfismo através de cálculos de pseudosseções e de isopletas da granada. Adicionalmente, foram obtidos dados de isótopos de boro em turmalina (dravita) que possibilitara a interpretação do ambiente deposicional.

No artigo *Rutile and zircon age and geochemistry in the evolution of the juvenile São Gabriel Terrane early in the Brasiliano Orogeny* (*Journal of South American Earth Sciences*) foi feita uma abordagem da evolução integrada do ofiolito Cerro do Ouro (conjunto dos ofiolitos do Terreno São Gabriel) e do arco São Gabriel, sob o ponto de vista de eventos metamórficos, magmáticos e metassomáticos. A metodologia adotada inclui a delimitação dos corpos ofiolíticos utilizando o levantamento aerogamaespectrométrico fornecido pela CPRM e ajustes efetuados a partir de verificações de campo. Adicionalmente foram utilizados dados de geocronologia obtidos por LA-ICP-MS U-Pb em zircão de cloritito (ofiolito) e metagabro (infraestrutura); e em rutilo de metagabro (infraestrutura).

É feita, a seguir, uma avaliação integrada dos resultados obtidos nos três artigos. A infraestrutura do arco São Gabriel é representada neste trabalho pelo Complexo Cambaí, sendo estudadas rochas da Suíte Vila Nova. Na região do Cambaizinho, o metatonalito forneceu idade U-Pb em zircão de 724,6 ± 3,2 Ma. A datação de intrusões sintectônicas do monzogranito da Suíte Sanga do Jobim resultou em dois pulsos principais: 698,9 ± 4,2 Ma e 673,9 ± 6,8 Ma. Os valores εHf(t) em zircão são positivos para ambas as rochas e variam entre +10,1 e +7,4 no metatonalito e +9,2 a +2,5 no monzogranito. Na região da Palma, a datação U-Pb em zircão do metagabro São Luís rendeu uma idade de 731,6 ± 0,5 Ma para a atividade magmática, com valores de εHf(t) variando entre +7,1 e +11,1. As idades e as assinaturas de εHf(t) do metatonalito (Cambaizinho) e do metagabro (Palma) sugerem a mesma fonte no manto depletado. As idades obtidas no monzogranito (Suíte Sanga do Jobim, Cambaizinho) indicam que se trata de intrusões tardias quando comparadas às idades das rochas da Suíte Vila Nova. A assinatura de εHf(t) da Suíte Sanga do Jobim, com intervalo menor quando comparada aos valores obtidos na Suíte Vila Nova, permite

sugerir fonte no manto depletado, porém com o início da influência de contaminação crustal. Uma interpretação possível para estes dados é a de que durante a cristalização das rochas da Suíte Vila Nova, o arco São Gabriel se encontrava em um ambiente intraoceânico. Durante a cristalização da Suíte Sanga do Jobim, no entanto, o arco já havia cavalgado por sobre o Cráton Rio de La Plata, impactando na assinatura do εHf(t), com aspecto de mistura.

Análises em zircão detrítico (n = 286) de 4 rochas metassedimentares sustentam a investigação do arco na porção correspondente à superestrutura. Foram estudadas: uma amostra de para-anfibolito (amostra 29), uma amostra de granada-estaurolita xisto (amostra 113) e duas amostras de granada xisto (amostras 30B e 48). Na amostra de para-anfibolito, verificou-se uma distribuição de idades $^{206}Pb/^{238}U$ variando entre 2601,48 Ma e 522,94 Ma, com pico em 690 Ma. Nas amostras de estaurolita-xisto e granada xisto, as idades $^{206}Pb/^{238}U$ obtidas variam entre 817 Ma e 702,5 Ma, com dois picos registrados em 769,1 ± 4,6 Ma e 731,6 ± 2,2 Ma, e com um único grão datado em 2088,60 Ma. Foram obtidos valores de εHf(t) variando entre -7,6 e +11,4 em zircões do para-anfibolito, e entre +0,4 e +11,9 em zircões dos xistos. A turmalina foi classificada como dravita com base em química mineral. Os isótopos de $\delta^{11}B$ (+0,51 a +3,39) de dravita indicam componentes da crosta oceânica presentes nos metassedimentos.

As rochas metassedimentares estudadas na região do Cambaizinho foram anteriormente consideradas como integrantes do ofiolito Cambaizinho (Remus, 1990). Lena *et al.* (2014) fizeram uma abordagem considerando estas rochas como metassedimentos tonianos-ediacaranos, porém, mantendo-as como componentes do ofiolito Cambaizinho. Na presente tese, estas rochas estão incluídas na Formação Serrinha, sendo interpretadas como pertencentes a uma bacia defronte ao arco (*forearc*) do arco São Gabriel. No artigo 1, todas as amostras estudadas de rochas metassedimentares foram consideradas como pertencentes à mesma paleo-bacia, e foram incorporadas na Formação Serrinha. No entanto, com o andamento dos trabalhos e obtenção de novos dados (artigo 2), chegou-se à conclusão de que as rochas do para-anfibolito (amostra 29) receberam sedimentação externa à paleo-bacia, com transporte detrítico a longa distância, de ambientes extra arco. Os valores de εHf(t) e a assinatura de ETR obtidas nos zircões dos metassedimentos apontam as rochas do arco como sendo a principal fonte de sedimentos, com alguma contribuição de rochas ofiolíticas. Para a amostra de para-anfibolito também ocorre

contribuição de sedimentos a partir de rochas continentais, conforme indicado pelos valores de εHf(t) negativos.

Estudos desenvolvidos em uma amostra de metassedimento representativa da Formação Serrinha (granada-estaurolita xisto, amostra 113) permitiram a determinação das condições metamórficas a que essas rochas foram submetidas, estabelecendo o pico metamórfico entre 4,5-5,1 kbar e 536-555 °C. A datação LA-ICP-MS U-Pb de granada com baixo U (<1 ppm) forneceu uma idade de intercepto inferior de 721 ± 14 Ma, correspondente à idade de crescimento da granada.

Com base nos resultados obtidos relacionados à idade do metamorfismo (artigo 2), foi feita uma reavaliação quanto à idade máxima de deposição (MDA) da Formação Serrinha. Para a estimativa da MDA apresentada no artigo 1, foram consideradas as 4 amostras de metassedimentos e a metodologia de análise de *cluster* de zircões mais jovens, com incerteza de 2σ. Quando é considerada a idade obtida em um único zircão da amostra 113 de granada-estaurolita xisto, uma idade de 710,2 Ma (incerteza de 2σ) pode ser sugerida para a MDA. Porém, essas idades são mais jovens do que a idade obtida para o metamorfismo na amostra 113. Assim, optou-se por reavaliar os dados relacionados aos zircões detríticos. Foi aplicado um algoritmo denominado *Maximum Likehood Age* (Vermeesch, 2021) para recalcular o MDA da Formação Serrinha, resultando em uma idade de 739,04 ± 4,47 Ma.

Adicionalmente, outra metodologia foi utilizada para a obtenção da idade do metamorfismo ocorrida na infraestrutura do arco. A datação por LA-ICP-MS U-Pb em rutilo do metagabro forneceu uma idade metamórfica de 706 ± 11 Ma.

Um único evento metamórfico de fácies anfibolito inferior foi evidenciado, com pico vinculado ao crescimento da granada de metassedimentos e fase final representada pela cristalização de rutilo em metagabro. O evento metamórfico está relacionado a pulsos de calor ocorridos durante subsidência e colisão, e ao aumento do grau geotérmico pela intrusão de rochas graníticas, que é a própria formação de estrutura do arco. O evento metamórfico definido nesta tese ocorreu de forma continuada entre 721 ± 14 Ma e 706 ± 11 Ma, com diferentes pulsos, correspondendo à colisão entre o arco intraoceânico e o continente.

Com relação ao metassomatismo, está sendo relatada nesta tese a primeira datação de rutilo de rocha ultramáfica no Escudo Brasileiro, com idade de 787,6 ± 2,6 Ma para o xisto magnesiano (clorita-tremolita xisto) do ofiolito Cambaizinho. É aberta

uma nova possibilidade para obtenção de dados relacionados ao metassomatismo de rochas com ausência de zircão, tradicionalmente utilizado em geocronologia. A datação do rutilo corresponde à idade metamórfica da seção mantélica do ofiolito. A datação de zircão de cloritito amostrado no ofiolito Palma Leste forneceu uma idade de 889,2 ± 2,3 Ma para o metassomatismo da crosta oceânica. Os valores εHf(t) positivos (+9,9 a +17,5) indicam fonte do zircão no manto depletado.

5. Conclusões

Esta tese delimitou a evolução geológica de ofiolitos no contexto da infraestrutura e superestrutura do arco São Gabriel, contribuindo para o avanço do conhecimento sobre a evolução de uma parte do Gondwana. Assim, a evolução do Terreno São Gabriel, durante a fase acrescionária, incluiu eventos magmáticos, metamórficos e metassomáticos. O arco São Gabriel teve sua atividade plutônica registrada em 724,6 ± 3,2 Ma e 731,6 ± 0,5 Ma, com intrusões sintectônicas em 698,9 ± 4,2 Ma e 673,9 ± 6,8 Ma. A fase final de colisão e empurrão do arco São Gabriel sobre o Cráton Rio de La Plata é indicada pelo metamorfismo da infraestrutura, registrado entre 721 ± 14 Ma e 706 ± 11 Ma, com pico metamórfico na idade mais velha. O metassomatismo na dorsal meso-oceânica registrada em ofiolitos ocorreu em 889 ± 2,3 Ma e 787,6 ± 2,6 Ma. As idades obtidas para as rochas do arco São Gabriel são correlacionáveis com outros arcos intraoceânicos tonianos do Cinturão Brasília (arco de Goiás, 862-630 Ma) e do Cinturão Ribeira (arco Serra da Prata – 856-838 Ma; arco Rio Negro – 790-620 Ma). As condições aqui estabelecidas para a geração e formação da crosta oceânica durante a subducção e colisão para formar arcos tonianos ao longo do Orógeno Brasiliano constituem uma contribuição para o conhecimento da construção de Gondwana Ocidental.

6. Referências

Almeida, F.F.M., Hasui, Y., Brito-Neves, B.B., Fuck, R.A. 1981. Brazilian structural provinces: an introduction. *Earth Science Reviews*, 17, 1-29.

Amaral, L., Caxito, F.A., Pedrosa-Soares, A.C., Queiroga, G., Babinski, M., Trindade, R., Lana, C., Chemale, F. 2020. The Ribeirão da Folha ophiolite-bearing accretionary wedge (Araçuaí orogen, SE Brazil): New data for Cryogenian plagiogranite and Metasedimentary rocks. *Precambrian Research*, 336, 105522.

Arena, K.R., Hartmann, L.A., Lana, C. 2016. Evolution of Neoproterozoic ophiolites from the southern Brasiliano Orogen revealed by zircon U-Pb-Hf isotopes and geochemistry. *Precambrian Research*, 285, 299-314.

Arena, K.R., Hartmann, L.A., Lana, C. 2017. Tonian emplacement of ophiolites in the southern Brasiliano Orogen delimited by U-Pb-Hf isotopes of zircon from metasomatites. *Gondwana Research*, 49, 296-332.

Arena, K.R., Hartmann, L.A., Lana, C. 2018. U–Pb–Hf isotopes and trace elements of metasomatic zircon delimit the evolution of Neoproterozoic Capané Ophiolite in the southern Brasiliano Orogen. *International Geology Review*, 60 (7), 911-928.

Arena, K.R., Hartmann, L.A., Lana, C., Queiroga, G.N., Castro, M.P. 2020. Geochemistry and $\delta^{11}B$ evolution of tourmaline from tourmalinite as a record of oceanic crust in the Tonian Ibaré ophiolite, southern Brasiliano Orogen. *Annals of the Brazilian Academy of Sciences*, 92 (1), e20180193.

Babinski, M., Chemale Jr., F., Hartmann, L.A., Van Schmus, W.R., Silva, L.Z. 1996. Juvenile accretion at 750-700 Ma in southern Brazil. *Geology*, 24 (5), 439-442.

Beaumont, C., Kamp, P.J.J., Hamilton, J., Fullsack, P. 1996. The continental collision zone, South Island, New Zealand: comparison of geodynamical models and observations. *Journal of Geophysical Research*, 101 (B2), 3333-3359.

Bicalho, V., Remus, M.V.D., Rizzardo, R., Dani, N. 2019. Geochemistry, metamorphic evolution and tectonic significance of metabasites from Caçapava do Sul, southern Brazil. *Brazilian Journal of Geology*, 49 (2). Doi: 10.1590/2317-4889201920180039

Bitencourt, M.F.A.S. 1983. Geologia, Petrologia e Estrutura dos Metamorfitos da Região de Caçapava do Sul, RS. Porto Alegre, 161p. MSc Thesis, Programa de Pós-graduação em Geociências, Instituto de Geociências, Universidade Federal do Rio Grande do Sul.

Brito-Neves, B.B., Fuck, R.A., Pimentel, M.M. 2014. The Brasiliano collage in South America: a review. *Brazilian Journal of Geology*, 44, 493-518.

Brown T., M., Fuck A., R., Dantas L., E. 2020. Isotopic age constraints and geochemical results of disseminated ophiolitic assemblage from Neoproterozoic mélange, central Brazil. *Precambrian Research*, 339, 105581.

Burke, K. 2011. Plate tectonics, the Wilson cycle, and mantle plumes: Geodynamics from the top. *Annual Review of Earth and Planetary Sciences*, 37, 1-29. Doi: 10.1146/annurev-earth-040809-152521.

Cawood, P.A., Kröner, A., Collins, W.J., Kusky, T.M., Mooney, W.D., Windley, B.F. 2009. Accretionary orogens through Earth history. *Geological Society, London, Special Publications*, 318, 1-6.

Caxito, F.A., Heilbron, M., Valeriano, C.M., Bruno, H., Pedrosa-Soares, A., Alkmim, F.F., Chemale, F., Hartmann, L.A., Dantas, E., Basei, M.A.S. 2021. Integration of elemental and isotope data supports a Neoproterozoic Adamastor Ocean realm. *Geochemical Perspectives Letters*, 17, 6-10.

Caxito, F.A., Uhlein, A., Stevenson, R., Uhlein, G.J. 2014. Neoproterozoic oceanic crust remnants in northeast Brazil. *Geology*, 42(5), 387-390.

Chemale Jr. F. 2000. Evolução Geológica do Escudo Sul-rio-grandense. *In*: Holz, M., De Ros, L.F. (Eds.). Geologia do Rio Grande do Sul. Centro de investigação do Gondwana, Universidade Federal do Rio Grande do Sul, Porto Alegre, Brasil, p. 13-55.

Chemale, Jr. F, Hartmann, L.A., Silva, L.C. 1995. Stratigraphy and tectonism of the Brasiliano Cycle in southern Brazil. *Communications of the Geological Survey of Namibia*, 10, 151-166.

Collins, W.J., Belousova, E.A., Kemp, A.I.S., Murphy, J.B. 2011. Two contrasting Phanerozoic orogenic systems revealed by hafnium isotope data. *Nature Geoscience*, 4, 333-337.

Collins A.S., Pisarevski S.A. 2005. Amalgamating eastern Gondwana: The evolution of the Circum-Indian orogens. *Earth-Science Reviews*, 71, 229-270.

Cordani, U.G., D'Agrella-Filho, M.S., Brito Neves, B.B., Trindade, R.I.F. 2003. Tearing up Rodinia: the neoproterozoic palaeogeography of South American cratonic fragments. *Terra Nova*, 15, 350-359.

Costa, E.O., Bitencourt, M.F., Tennholm, T., Konopásek, J., Moita, T.F. 2011. P-T-D evolution of the southeast Passo Feio Complex and the meaning of the Caçapava Lineament, Dom Feliciano Belt, southernmost Brazil. *Journal of South American Earth Sciences*, 112, 103465.

Fernandes, L.A.D., Menegat, R., Costa, A.F.U., Porcher, C.C., Tommasi, A., Kraemer, G., Ramgrab, G.E., Camozzato, E. 1995. Evolução tectônica do Cinturão Dom Feliciano no Escudo Sul-Rio-Grandense: parte I – uma contribuição a partir do registro geológico. Revista Brasileira de Geociências, 25(4), 351-374.

Flores, K.E., Gazel, E. 2020. A 100 m.y. record of volcanic arc evolution in Nicaragua. *Island Arc*, 29, e12346.

Goñi, J.C. 1962. Origine des roches ultrabasiques et serpentineuses du précambrien de Rio Grande do Sul (Brésil). Mode de gisement et minéralisations. Esc. Geol. UFRGS, 12, 7-91.

Goulart, R.V., Remus, M.V.D., Reis, R.S. 2013. Composição isotópica de Sr, C e O e geoquímica de ETRs das rochas carbonáticas do Bloco São Gabriel, Rio Grande do Sul. Pesquisas em Geociências, 40, 75-97.

Gray, D.R., Foster, D.A., Meert, J.G., Goscombe, B.D., Armstrong, R., Trouw, R.A.J., Passchier, C.W. 2008. A Damara orogen perspective on the assembly of southewestern Gondwana. *In*: Pankhurst, R.J., Trouw, R.A.J., Brito-Neves, B.B., De Wit, M.J. (Eds) *West Gondwana Pre-Cenozoic Correlations Across the South Atlantic Region*. Geological Society, London, Special Publications, 294, p. 257-278.

Gubert, M.L., Philipp, R.P., Basei, M.A.S. 2016. The Bossoroca Complex, São Gabriel Terrane, Dom Feliciano Belt, southernmost Brazil: U-Pb geochronology and tectonic implications for the Neoproterozoic São Gabriel Arc. *Journal of south American Earth Sciences*, 70, 1-17.

Hartmann, L.A, Chemale Jr., F. 2003. Mid amphibolite facies metamorphism of harzburgites in the Neoproterozoic Cerro Mantiqueiras Ophiolite, southernmost Brazil. Anais da Academia Brasileira de Ciências, 75, 109-128.

Hartmann, L.A., Leite, J.A.D., Silva, L.C., Remus, M.V.D., McNaughton, N.J., Groves, D.I., Fletcher, I.R., Santos, J.O.S., Vasconcellos, M.A.Z. 2000. Advances in SHRIMP geochronology and their impact on understanding the tectonic and metalogenic evolution of southern Brazil. *Australian Journal of Earth Sciences*, 47, 829-844.

Hartmann, L.A., Massuda, A.J., Cerva-Alves, T., Lana, C., Leandro, C.G., Savian, J.F. 2021. Aeromagnetometry and aerogammaspectrometry integrated with U-Pb zircon geochronology of northern Bossoroca ophiolite, Brasiliano Orogen. *Annals of the Brazilian Academy of Sciences*, 93(1), e20190791.

Hartmann, L.A., Philipp, R.P., Santos, J.O.S., McNaughton, N.J. 2011. Time frame of the 753-680 Ma juvenile accretion during the São Gabriel Orogeny, southern Brazilian Shield. *Gondwana Research*, 19, 84-99.

Hartmann, L.A., Tindle, A., Bitencourt, M.F. 1990. O metamorfismo de fácies anfibolito no Complexo Metamórfico Passo Feio, RS, com base em química dos minerais. Pesquisas em Geociências, 17(1-2), 62-71.

Hartmann, L.A., Werle, M., Michelin, C.R.L. Lana, C., Queiroga, G.N., Castro, M.P., Arena, K.R. 2019. Proto-Adamastor ocean crust (920 Ma) described in Brasiliano

Orogen from coetaneous zircon and tourmaline. *Geoscience Frontier*, 10(4), 1623-1633.

Heilbron, M., Pedrosa-Soares, A.C., Neto, M.C.C., Silva, L.C., Trouw, R.A.J., Janasi, V.A. 2004. Província Mantiqueira. *In*: Mantesso-Neto, V., Bartorelli, A., Carneiro, C.D.R., Brito-Neves, B.B. (eds.) Geologia do Continente Sul-Americano: Evolução da Obra de Fernando Flávio de Almeida, p. 203-234.

Helwig, J. 1974. Eugeosynclinal basement and a collage concept of orogenic belts. *In*: Dott Junior R.H., Shaver R.H. (Eds.). *Modern and Ancient Geosynclinal Sedimentation*. Society of Economic Paleontologists and Mineralogists, Special Publication, 19, p. 339-376.

Hoffman, P.F. 1991. Did the breakout of Laurentia turn Gondwanaland inside-out? *Science*, 252, 1409-1412.

Hueck, M., Oyhantçabal, P., Philipp, R.P., Basei, M.A.S., Siegesmund, S. 2018. The Dom Feliciano belt in southern Brazil and Uruguay. *In*: Siegesmund, S., Basei, M.A.S., Oyhantcabal, P., Oriolo, S. (Eds.). *Geology of Southwest Gondwana*. Regional Geology Reviews. Springer Nature, p. 243-265.

Hueck, M., Wemmer, K., Basei, M.A.S., Philipp, R.P., Oriolo, S., Heidelbach, F., Oyhantçabal, P., Siegesmund, S. 2020. Dating recurrent shear zone activity and the transition from ductile to brittle deformation: white mica geochronology applied to the Neoproterozoic Dom Feliciano Belt in south Brazil. *Journal of Structural Geology*, 141, 104199.

Kraemer, G. 1995. Evolução magmática e tectônica da suíte ortometamórfica Imbicuí, região de Lavras do Sul, RS. Porto Alegre, p.99. MSc Thesis, Programa de Pós-Graduação em Geociências, Instituto de Geociências, Universidade Federal do Rio Grande do Sul.

Leite, J.A.D., Hartmann, L.A., McNaughton, N.J., Chemale Jr., F. 1998. SHRIMP U/Pb zircon geochronology of Neoproterozoic juvenile and crustal-reworked terranes in southernmost Brazil. *International Geology Reviewer*, 40, 688-705.

Lena, L.O.F., Pimentel, M.M., Philipp, R.P., Armstrong, R., Sato, K. 2014. The evolution of the Neoproterozoic São Gabriel juvenile terrane, southern Brazil based on high spatial resolution U-Pb ages and δ18O data from detrital zircons. *Precambrian Research*, 247, 126-138.

Li, Z.X., Bogdanova, S.V., Colins, A.S., Davidson, A., De Waele, B., Ernst, R.E., Fitzsimons, I.C.W., Fuck, R.A., Gladkochub, D.P., Jacobs, J.,Karlstrom, K.E., Lu, S., Natapov, L.M., Pease, V., Pisarevsky, S.A., Thrane, K., Vernikovsky, V. 2008.

Assembly, configuration, and break-up history of Rodinia: A synthesis. *Precambrian Research*, 160, 179-210.

Lopes, C.G., Pimentel, M.M., Philipp, R.P., Gruber, L., Armstrong, R., Junges, S. 2015. Provenance of the Passo Feio complex, Dom Feliciano belt: implications for the age of supracrustal rocks of the São Gabriel arc, southern Brazil. *Journal of South American Earth Sciences*, 58, 9-17.

Luchi, M.G.L., Dopico, C.I.M., Wemmer, K., Siegesmund, S. 2018. Untangling the Neoproterozoic-Early Paleozoic Tectonic Evolution of the Eastern Sierras Pampeanas Hidden in the Isotopical Record. *In*: Siegesmund, S., Basei, M.A.S., Oyhantçabal, P.,Oriolo, S. (eds). *Geology of Southwest Gondwana*. Regional Geology Reviews, Springer Nature, 433 - 466.

Massuda, A.J., Hartmann, L.A., Queiroga, G.N., Castro, M.P., Leandro, C.G., Savian, J.F. 2020. Mineralogical evolution of the northern Bossoroca ophiolite, São Gabriel Terrane. Brazilian *Journal of Geology*, 50(4), e20190120.

Meert, J.G., Lieberman, B.S. 2008. The Neoproterozoic assembly of Gondwana and its relationship to the Ediacaran-Cambrian radiation. *Gondwana Research*, 14, 5-21.

Moores, E.M. 1993. Neoproterozoic oceanic crustal thinning,emergence of continents, and origin of the Phanerozoic ecosystem; a model. *Geology*, 21, 5-8.

Moores, E.M. 2002. Pre-1Ga (pre-Rodinian) ophiolites: Their tectonic and environmental implications. *Geological Society of American Bulletin*, 114, 80-95.

Murphy, J.B., Pisarevsky, S., Nance, R.D. 2013. Potential geodynamic relationships between the development of peripheral orogens along the northern margin of Gondwana and the amalgamation of West Gondwana. *Mineralogy and Petrology*, 107, 635-650.

Oriolo, S., Oyhantçabal, P., Wemmer, K., Siegesmund, S. 2017. Contemporaneous assembly of Western Gondwana and final Rodinia break-up: Implications for the supercontinent cycle. *Geoscience Frontiers*, 8, 1431-1445.

Peixoto, C.A., Heilbron, M., Ragatky, D., Armstrong, R., Dantas, E., Valeriano, C.M., Simonetti, A. 2017. Tectonic evolution of the juvenile Tonian Serra da Prata magmatic arc in the Ribeira Belt, SE Brazil: implications for early West Gondwana amalgamation. *Precambrian Research*, 302, 221-254.

Pertille, J., Hartmann, L.A., Santos, J.O.S., McNaughton, N.J., Armstrong, R. 2017. Reconstructing the Cryogenian–Ediacaran evolution of the Porongos fold and thrust belt, Southern Brasiliano Orogen, based on Zircon U–Pb–Hf–O isotopes. *International Geology Review*, 59(12), 1532-1560.

Philipp, R.P., Pimentel, M.M., Basei, M.A.S. 2018. The tectonic evolution of the São Gabriel terrane, Dom Feliciano belt, southern Brazil: the closure of the Charrua Ocean. *In*: Siegesmund, S., Basei, M.A.S., Oyhantcabal, P., Oriolo, S. (Ed). *Geology of Southwest Gondwana*. Regional Geology Reviews. Springer Nature, 243-265.

Philipp, R.P., Pimentel, M.M., Basei, M.A.S., Salvi, M., De Lena, L.O.F., Vedana, L.A., Gubert, M.L., Lopes, C.G., Laux, J.H., Camozzato, E. 2021. U-Pb detrital zircon dating Applied to metavolcano-sedimentary complexes of the São Gabriel Terrane: New constraints of the evolution of the Dom Feliciano Belt. *Journal of South American Earth Sciences*, 110, 103409.

Queiroga, G.N., Pedrosa-Soares, A.C., Noce, C.M., Alkmim, F.F., Pimentel, M.M., Dantas, E., Martins, M., Castañeda, C., Suita, M.T.F., Prichard, H. 2007. Age of the Ribeirão da Folha ophiolite, Araçuaí Orogen: The U-Pb zircon (LA-ICPMS) dating of a plagiogranite. *Geonomos*, 15(1), 61-65.

Ramos, R.C., Koester, E., Vieira, D.T. 2020. Sm-Nd systematics of metaultramafic-mafic rocks from the Arroio Grande Ophiolite (Brazil): Insights on the evolution of the South Adamastor paleo-ocean. *Geoscience Frontiers*, 11(6), 2287-2296.

Ramos, R.C., Koester, E., Vieira, D.T., Porcher, C.C., Gezatt, J.N., Silveira, R.L. 2018. Insights on the evolution of the Arroio Grande Ophiolite (Dom Feliciano Belt, Brazil) from Rb-Sr and SHRIMP U-Pb isotopic geochemistry. *Journal of South American Earth Sciences*, 86, 38-53.

Remus, M.V.D. 1990. Geologia e geoquímica do Complexo Cambaizinho, São Gabriel, RS. Porto Alegre, p.267. MSc. Thesis, Programa de Pós-Graduação em Geociências, Instituto de Geociências, Universidade Federal do Rio Grande do Sul.

Remus, M.V.D., Hartmann, L.A., McNaughton, N.J., Groves, D.I., Fletcher, I.R. 2000. The link between hydrothermal epigenetic copper mineralization and the Caçapava granite of the Brasiliano Cycle in southern Brazil. *Journal of South American Earth Science*, 13, 191-216.

Remus, M.V.D., McNaughton, N.J., Hartmann, L.A., Koppe, J.C., Fletcher, I.R., Groves, D.I., Pinto, V.M. 1999. Gold in the Neoproterozoic juvenile Bossoroca volcanic arc of southernmost Brazil: isotopic constraints on timing and sources. *Journal of South American Earth Sciences*, 12, 349-366.

Rogers, J.J.W., 1996. A History of continents in the past three billion years. The Journal of Geology 104, 91-107.

Saalmann K., Gerdes A., Lahaye Y., Hartmann L.A., Remus M.V.D., Laufer A. 2011. Multiple accretion at the eastern margin of the Rio de la Plata craton: the prolonged

Brasiliano Orogeny in southernmost Brazil. *International Journal of Earth Sciences*, 100(2-3), 355-378.

Saalmann, K., Hartmann, L.A., Remus, M.V.D. 2005a. Tectonic Evolution of Two Contrasting Schist Belts in Southernmost Brazil: A Plate Tectonic Model for the Brasiliano Orogeny. *International Geology Review*, 47, 1234-1259.

Saalmann, K., Hartmann, L.A., Remus, M.V.D., Koester, E., Conceição, R.V. 2005b. Sm-Nd isotope geochemistry of metamorphic volcano-sedimentary successions in the São Gabriel Block, southernmost Brazil: evidence for the existence of juvenile Neoproterozoic oceanic crust to the east of the Rio de la Plata Craton. *Precambrian Research*, 136, 159-175.

Saalmann, K., Remus, M.V.D., Hartmann, L.A. 2005c. Geochemistry and crustal evolution of volcano-sedimentary successions and orthogneisses in the São Gabriel block, southernmost Brazil – relics of neoproterozoic magmatic arcs. *Gondwana Research*, 8(2), 143-161.

Saalmann, K., Remus, M.V.D., Hartmann, L.A. 2006. Tectonic evolution of the Neoproterozoic São Gabriel block, southern Brazil: constraints on Brasiliano Orogenic evolution of the Rio de La Plata cratonic margin. *Journal of South American Earth Sciences*, 21, 204-227.

Sengör, A.M. 1990. Plate tectonics and orogenic research after 25 years. *Earth-Science Reviews*, 27,1-201.

Siviero, R.S., Bruguier, O., Fernandes, L.A.D., Koester, E., Porcher, C.C., Kraemer, G. 2021. Age and geochemistry of Cambaí Complex, São Gabriel terrane, Brazil: arc-related TTG-like rocks. *Journal of South American Earth Sciences*, 108, 103165.

Souza, C.S.M., Hauser, N., Dantas, E.L., Reimold, W.U., Schmitt, R.T., Chaves, J.G.S., Osorio, L.F.B. 2019. Does the metavolcanic-sedimentary Rio do Coco Group, Araguaia Belt, Brazil, represent a continuity of the Quatipuru ophiolitic complex? - constraints from U-Pb and Sm-Nd isotope data. *Journal of South American Earth Sciences*, 94, 102233.

Stern, C.R. 2011. Subduction erosion: rates, mechanisms, and its role in arc magmatism and the evolution of the continental crust and mantle. *Gondwana Research*, 20, 284-308.

Strieder, A.J., Roldão, D.G., Hartmann, L.A. 2000. The Palma volcano-sedimentary supersuite, Precambrian Sul-Riograndense Shield, Brazil. International *Geology Review*, 42(11), 984-999.

Suita, M.T.S., Pedrosa-Soares, A.C., Leite, C.A.S., Nilson, A.A., Prichard, H.M. 2004 Complexos ofiolíticos do Brasil e a metalogenia comparada das faixas Araçuaí e Brasília. In: Pereira, E.S., Castroviejo, R., Ortiz, F. (Eds). *Complejos ofiolíticos em Ibero América guías de prospección para metales preciosos*. ProyectoXIII.1 – CYTED, Ciência y tecnologia para el desarrollo.

Tapster, S., Roberts, N.M.W., Petterson, M.G., Saunders, A.D., Naden, J. 2014. From continent to intra-oceanic arc: Zircon xenocrystals record the crustal evolution of the Solomon island arc. *Geology*, 42(12), 1087-1090.

Tennholm, T. 2019. Metamorphic evolution of the Passo Feio Complex (central part of the Dom Feliciano Belt, southern Brazil). Norway, p. 110. Department of Geosciences, Faculty of Science and Technology, The Arctic University of Norway.

Tickyj, H., Hartmann, L.A., Vasconcellos, M.A.Z., Philipp, R.P., Remus, M.V.D. 2004. Electron microprobe dating of monazite substantiates ages of major geological events in the southern Brazilian shield. *Journal of South American Earth Sciences*, 16, 699-713.

Unrug, R. 1996. The Assembly of Gondwanaland. *Episodes*, 19(1/2), 11-20.

Unrug, R. 1997. Rodinia to Gondwana. The Geodynamic Map of Gondwana Supercontinent Assembly. *GSA Today*, 7(1), 1-6.

Vedana, L.A., Philipp, R.P., Basei, M.A.S. 2018. Tonian to early Cryogenian synorogenic basin of the São Gabriel terrane, Dom Feliciano Belt, southernmost Brazil. *International Geology Review*, 60(1), 109-133.

Vermeesch, P. 2021. Maximum depositional age estimation revisited. *Geoscience Frontier*, 12, 843-850.

Werle, M., Hartmann, L.A., Queiroga, G.N., Lana, C., Pertille, J., Michelin, C.R.L., Remus, M.V.D., Roberts, M.P., Castro, M.P., Leandro, C.G., Savian, J.F. 2020. Oceanic crust and mantle evidence for the evolution of Tonian-Cryogenian ophiolites, southern Brasiliano Orogen. *Precambrian Research*, 351, 105979.

Wilson, J.T. 1965. A new class of faults and their bearing on continental drift. *Nature*, 207, 343-347.

Wortel, M.J.R., Spakman, W. 2000. Subduction and slab detachment in the Mediterranean-Carpathian region. *Science*, 80(290), 1910-1917.

Zheng, Y.F. 2012. Metamorphic chemical geodynamics in continental subduction zones. *Chemical Geology*, 328, 5-48.

Zheng, Y.F., Chen, Y.X., Dai, L.Q., Zhao, Z.F. 2015. Developing plate tectonics theory from oceanic subduction zones to collisional orogens. *Science China: Earth Sciences*. Doi: 10.1007/s11430-015-5097-3

CAPÍTULO 2 – ARTIGOS PUBLICADOS

Artigo 1 – Tiara CERVA-ALVES, Léo Afraneo HARTMANN, Marcus Vinícius Dorneles REMUS, Cristiano LANA. 2020. *Integrated ophiolite and arc evolution, southern Brasiliano Orogen. Precambrian Research*, v. 341, 105648. https://doi.org/10.1016/j.precamres.2020.105648

Integrated ophiolite and arc evolution, southern Brasiliano Orogen

T. Cerva-Alves [a] ✉, L.A. Hartmann [a] ✉, M.V.D. Remus [a] ✉, C. Lana [b] ✉

[a] Instituto de Geociências, Universidade Federal do Rio Grande do Sul, Avenida Bento Gonçalves, 9500, 91501-970 Porto Alegre, Rio Grande do Sul, Brazil

[b] Departamento de Geologia, Escola de Minas, Universidade Federal de Ouro Preto, Morro do Cruzeiro, 35400-000 Ouro Preto, Minas Gerais, Brazil

ABSTRACT

Integrated study of Tonian ophiolite mélanges and intra-oceanic arc of the São Gabriel juvenile terrane exposes a key geotectonic unit in the evolutionary history of Gondwana during Brasiliano Orogen. LA-ICP-MS U-Pb geochronology in rutile and zircon were combined with Lu-Hf and rare earth elements in zircon. We report the first rutile dating of ultramafic rock in the Brazilian Shield of 787.6 ± 2.6 Ma for the Cambaizinho ophiolite magnesian schist. Dating of rutile corresponds to the metamorphic age of the mantle section of the ophiolite. São Gabriel arc infrastructure is represented by the Cambaí Complex, including the Vila Nova Suite metatonalite with zircon U-Pb age of 724.6 ± 3.2 Ma and late Sanga do Jobim Suite monzogranite intrusions with two main pulses at 698.9 ± 4.2 Ma and 673.9 ± 6.8 Ma. Zircon $\varepsilon Hf_{(t)}$ values are positive for both rocks and range between +10.1 and +7.4 in metatonalite and +9.2 to +2.5 in monzogranite. Detrital zircon from metasedimentary rocks support superstructure arc investigation. Ages range from 817 to 650 Ma, with strong concentration between 750 and 730 Ma. Positive $\varepsilon Hf_{(t)}$ values and Rare Earth Elements (REE) signature point to main source of metasedimentary rocks in the arc, with ophiolitic contribution. Therefore, geotectonic processes in the Brasiliano Orogen include the construction of São Gabriel terrane with Tonian oceanic crust evolving to intra-oceanic subduction until 650 Ma to final development along the margin of continental crust. Overthrusting of the São Gabriel terrane onto the Rio de La Plata Craton occurred at 650-620 Ma. Our data correlate with Tonian intra-oceanic arcs from Brasilia belt (Goiás arc ca. 862-630 Ma) and Ribeira belt (Serra da Prata arc - 856-838 Ma; Rio Negro arc - 790-620 Ma). Oceanic crust generation combined with subduction to form Tonian arcs along the Brasiliano Orogen were most significant for construction of West Gondwana.

Keywords: Zircon U-Pb-Hf isotopes; Zircon rare earth elements; Dating of metamorphosed mantle; Brasiliano Orogeny

1. Introduction

Large rearrangement of continental masses occurred during the Neoproterozoic. The results include opening and closure of Tonian oceans, subduction related to new crustal growth with collage of juvenile volcanic arc terranes, followed by amalgamation of the Gondwana paleocontinent. Some remnants of oceanic crust and mantle were

preserved as ophiolitic complexes in continental orogens (Li *et al.*, 2008; Stewart, 2009; Hodel *et al.*, 2019). Records of Neoproterozoic ophiolites are found along orogenic belts on all continents (Stewart, 2009; Arena *et al.*, 2017, 2018), including (Fig. 1a) East African and Brasiliano orogenic belts related to West Gondwana orogenic system (Pedrosa-Soares *et al.*, 1998; Stern *et al.*, 2004; Caxito *et al.*, 2014; Arena *et al.*, 2016; Blades *et al.*, 2019; Ganade Araujo *et al.*, 2016; Hartmann *et al.*, 2019; Amaral *et al.*, 2020; Brown *et al.*, 2020). Studies suggested similar stages and tectonic regimes for Brasiliano Orogen construction (Almeida and Hasui, 1984; Silva *et al.*, 2005; Brito Neves *et al.*, 2014; Basei *et al.*, 2018), with convergent oceanic plate regime and intra-oceanic arcs (e.g. São Gabriel and Goiás juvenile terranes) evolving to continent-continent collision, compared to Alpine-Himalayan belt (Silva *et al.*, 2005; Brito Neves *et al.*, 2014; Ganade Araujo *et al.*, 2014; Basei *et al.*, 2018). These models indicate different ages for each event along the continental masses, in diachronous processes.

The integrated evolution of ophiolite with host oceanic arc remains poorly described in the Brasiliano Orogen. We selected a complex terrane in southern Brazil to make this description and thus establish parameters for understanding the relationship between obducted oceanic crust + mantle and host juvenile island arc.

The southern portion of the Brasiliano Orogen is the Dom Feliciano belt, exposed in the states of Santa Catarina and Rio Grande do Sul, Brazil, and eastern Uruguay (Fig. 1b). Three Brasiliano events were recognized through zircon dating, including the ~879 Ma Passinho event, 767-675 Ma São Gabriel event and 650-600 Ma Dom Feliciano event (Saalmann *et al.*, 2011; Gubert at al., 2016; Vedana *et al.*, 2018). Tonian ophiolites obducted onto metavolcanosedimentary and magmatic rocks of intra-oceanic arcs, accreted to continental crust were recognized in the Sul-Riograndense Shield (Babinski *et al.*, 1996; Chemale Jr., 2000; Hartmann *et al.*, 2011, 2019; Arena *et al.*, 2016, 2017; Philipp *et al.*, 2018), constituting a significant step in evolution of Gondwana reconstruction. Oceanic crust generation and serpentinization events were dated by Arena *et al.* (2016, 2017) in ophiolites from São Gabriel terrane, yielding ages between 923 ± 3 Ma and 722 ± 3 Ma. The infrastructure (Cambaí Complex) and superstructure (Vacacaí Complex) of two juvenile arcs (Table 1) evolved from 923 Ma to 650 Ma (Leite *et al.*, 1998; Hartmann *et al.*, 2011, Lena *et al.*, 2014; Lopes *et al.*, 2015). Zircon analyses marked three Brasiliano events. However, the timeline of accretion and continental interaction remain poorly constrained. Besides,

there is a paradox related to ages of metasedimentary rocks of the Cambaizinho Complex. Previous studies considered the metassedimentary rocks as part of the Cambaizinho ophiolite sequence and thus the oldest unit of Cambaí Complex (Remus, 1990; Saalmann *et al.*, 2005a, 2011; Hartmann *et al.*, 2011; Philipp *et al.*, 2018). On the other hand, detrital zircon provenance shows arc source, related partly to ocean floor deposition (Lena *et al.*, 2014).

Table 1. Stratigraphy of São Gabriel terrane (São Gabriel island arc + obducted ophiolites) and associated units, with selected examples and approximate ages.

Geotectonics	Stratigraphic unit	Description	Age, Ma
Intraplate	Paraná Basin	Voluminous siltite, some lamite, conglomerate, limestone	450-60
Post-orogenic	São Sepé, Ramada, São Manoel, Santa Rita, Jaguari, Lavras, Cerro da Cria Granites	Shallow level, strong contact aureole	600-550
Foreland	Camaquã Basin	Volcanics, trachyandesite, sedimentary rocks	575
São Gabriel island-arc	Superstructure, Vacacaí Group – Campestre, Pontas do Salso, Bela Vista, Serrinha Formations Passo Feio (in part) Complex	Island-arc volcanics and sediments, turbidite, graywacke, tuff, andesite, marble	755
	Infrastructure, Cambaí Complex– Lagoa da Meia-Lua,Vila Nova and Sanga do Jobim Suites, Cerca de Pedra granodiorite, Imbicuí gneiss	Granitic rocks, syntectonic	(770), 730-700, 680
Oceanic crust + mantle	Cerro do Ouro Ophiolite: Cerro Mantiqueiras, Cambaizinho, Palma, Ibaré, Bossoroca (Arroio Lageadinho Formation), Passo do Ivo	Ultramafic, mafic, andesitic, Talc-olivine metaserpentinite, amphibolite, BIF, gabbro-harzburgite. Metasomatites – chromite-talc-magnesite fels, tourmalinite, rodingite, chloritite	920-720

To elucidate tectonic processes and delimit their duration, we integrate geological mapping, petrography, backscattered electron images and isotopic data of zircon grains from the rocks sampled in Cambaizinho Complex. Field and petrographic

evidence integrated with geochronology support the interpretation that the Cambaizinho ophiolite was metamorphosed at 787.6 ± 2.6 Ma in a mid-ocean ridge, and later obducted onto the São Gabriel intra-oceanic arc. Zircon U-Pb isotopes point to juvenile magmatic activity at 724.6 ± 3.2 Ma (Vila Nova Suite), 698.9 ± 4.2 Ma (Sanga do Jobim Suite) with a final pulse at 673.9 ± 6.8 Ma. Positive zircon εHf(t) signatures indicate that both studied intrusive rocks originated in the depleted mantle. Metasedimentary rocks yielded detrital zircon age ranging mainly from 650 to 817 Ma. Metasedimentary rocks were part of an intra-arc basin, with source derived mainly from arc rocks. Therefore, we consider that the metasedimentary rock and Cambaizinho Complex had distinct evolution in time and space. Generation and emplacement of island arc and ophiolite from oceanic to continental crust are thus more tightly constrained in the environment of Brasiliano Orogen and Gondwana amalgamation.

2. Geological setting and previous data

The Dom Feliciano belt resulted from collision among the Rio de la Plata, Congo and Kalahari cratons along shear zones, with closure of the Adamastor Ocean (Saalmann *et al.*, 2011; Hueck *et al.*, 2018). In Rio Grande do Sul state, the Sul-Riograndense Shield has four major domains (Fig. 1c), including the São Gabriel terrane, Porongos fold and thrust belt (also known as Tijucas terrane and Encruzilhada domain), Pelotas Batholith, foreland associations (Camaquã Basin), and Archaean and Paleoproterozoic basement in the Taquarembó block (Jost and Hartmann, 1984; Soliani, 1986; Fragoso-César, 1991; Remus *et al.*, 1999; Chemale Jr., 2000; Paim and Lopes, 2000; Paim *et al.*, 2014; Philipp *et al.*, 2002; Basei *et al.*, 2008, 2011; Hartmann *et al.*, 2008; Saalmann *et al.*, 2011; Pertille *et al.*, 2017).
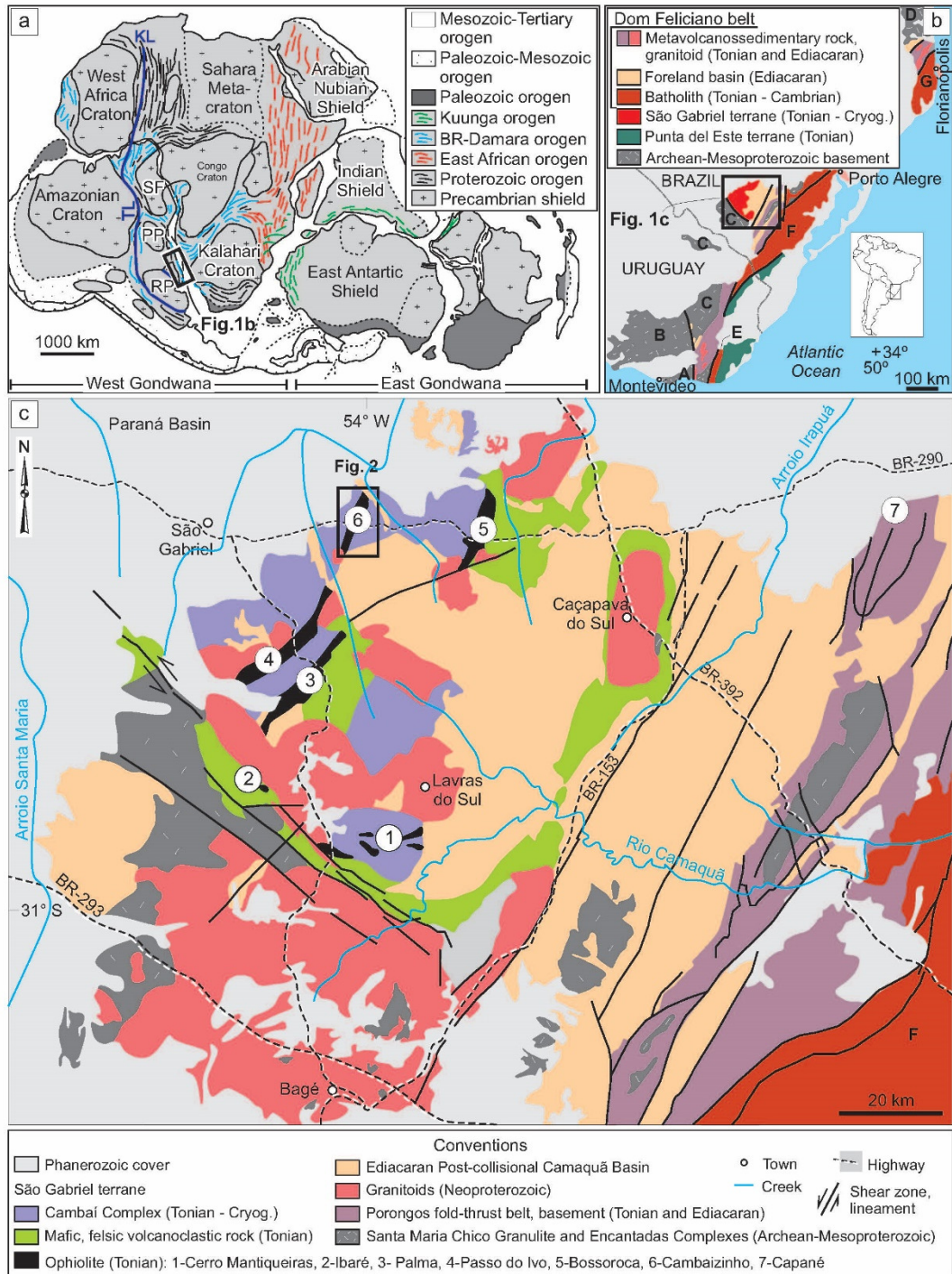
Fig. 1. (a) São Gabriel juvenile terrane in simplified Gondwana configuration at 530 Ma showing cratons and orogenic belts. Modified from Li *et al.* (2008); Gray *et al.* (2008), Luchi *et al.* (2018); El-Rahman *et al.* (2019). BR = Brasiliano Orogen; KL = Kandi Lineament; NP = Nico Peres terrane; PP = Paranapanema block; RP = Rio de La Plata Craton; SF = São Francisco Craton; TL = Transbrasiliano lineament. (b) Tectonostratigraphic terranes of Uruguayan and southern Brazilian Shields. Cryog. = Cryogenian; A = Tandilia terrane; B = Piedra Alta terrane; C = Nico Perez terrane; D = Luis Alves terrane; E = Aiguá Batholith; F = Pelotas Batholith; G = Florianópolis Batholith. Modified from Hartmann *et al.* (2019), Will *et al.* (2019). (c) Geologic map of São Gabriel terrane and fragments of Nico Perez terrane and Porongos fold-thrust belt. Modified from Arena *et al.* (2016), Hartmann *et al.* (2019).

The São Gabriel terrane records rocks formed during a subduction period of Brasiliano orogeny (Vedana *et al.*, 2017) and comprises ophiolites, two intra-oceanic arc sequences (Passinho ca. 879 Ma and São Gabriel ca.758-700 Ma) and post-tectonic granites (Chemale Jr. *et al.*, 1995; Babinski *et al.*, 1996, Saalmann *et al.*, 2005b, 2011; Hartmann *et al.*, 2000, 2011; Arena *et al.*, 2016; Pertille *et al.*, 2017). Oceanic crust and mantle obducted over and wedged into the São Gabriel arc include Cerro do Ouro Tonian ophiolite mélanges (Goñi, 1962) – Cerro Mantiqueiras, Ibaré, Palma, Passo do Ivo, Bossoroca (included in Arroio Lajeadinho Formation) and Cambaizinho ophiolites (Arena *et al.*, 2016, 2017). Ophiolite bodies in São Gabriel terrane are faulted, folded and disrupted, without preservation of complete Penrose-type ophiolite stratigraphy. Zircon grains obtained in rocks from Cerro Mantiqueiras ophiolite yielded 923 ± 3 Ma crystallization age and 786 ± 13 Ma metamorphic ages for albitite (Arena *et al.*, 2016), and 733 ± 10 Ma in metabasalt (Leite *et al.*, 1998). In Ibaré ophiolite, albitite zircon yielded crystallization ages of 892 ± 2.8 Ma, whereas tourmalinite and chloritite zircon presented a crystallization age of 726 ± 22 Ma (Arena *et al.*, 2016, 2017). Zircon crystals from chloritite provide crystallization age of 722 ± 3 Ma for Palma ophiolite (Arena *et al.*, 2017), and in Bossoroca ophiolite, zircons from tourmalinite sample indicate age of 920.4 ± 9.8 Ma (Hartmann *et al.*, 2019).

Arc infrastructure includes DTTG association (diorite, tonalite, trondhjemite, granodiorite) from Vila Nova Suite (also known as Vila Nova orthogneiss; Hartmann *et al.*, 2011) and granitoids that belong to Lagoa da Meia Lua and Sanga do Jobim Suites, all from Cambaí Complex (Kraemer, 1995; Fernandes *et al.*, 1995; Leite *et al.*, 1998; Saalmann *et al.*, 2006, 2011; Hartmann *et al.*, 2011). Zircon U-Pb ages spread between 701 ± 9.7 Ma and 794 ± 6 Ma for Vila Nova Suite (Leite *et al.*, 1998; Hartmann *et al.*, 2011; Saalmann *et al.*, 2011; Vedana *et al.*, 2018), and between 675 ± 3.8 Ma and 704 ± 3 Ma for Sanga do Jobim and Lagoa da Meia Lua Suites (Hartmann *et al.*, 2011; Vedana *et al.*, 2018). Oldest 879 ± 14 Ma zircon U-Pb age is from the Passinho diorite (Leite et a., 1998) and is interpreted as Passinho arc (Hartmann *et al.*, 2000).

The supracrustal portion arc is represented by metavolcanosedimentary successions and marble of Vacacaí Group (Chemale Jr., 2000; previously part of Palma Group - Strieder *et al.*, 2000; Goulart *et al.*, 2013; Saalmann *et al.*, 2011), including Cambaizinho and part of Passo Feio Complexes (Bitencourt, 1983; Remus, 1990; Hartmann *et al.*, 1990; Lopes *et al.*, 2015), Pontas do Salso (Remus *et al.*, 1999;

Saalmann *et al.*, 2005a; Vedana *et al.*, 2018), Bela Vista and Campestre Formations (Chemale *et al.*, 1995). Zircon dating yielded ages between 767.2 ± 2.9 and 757 ± 17 Ma for volcanic rocks from Bela Vista and Campestre Formations (Remus *et al.*, 1999; Gubert *et al.*, 2016; Arena *et al.*, 2017).

Four deformational events were identified in São Gabriel terrane (Remus, 1990; Saalmann *et al.*, 2006). S1 structure is related to first folding event. S2 deformation reached amphibolite facies metamorphic peak and F2 folds are isoclinal recumbent rootless, transposing F1 banding. S3 deformation generated subvertical foliation planes dipping steeply either to WNW or ESE along major NE-striking shear zones (Saalmann *et al.*, 2006). In this phase, overall geometry of the area was built. S3 SW-NE strike-slip shearing is observed in syntectonic plutonic rocks of the Cambaí Complex due to lower viscosity (Saalmann *et al.*, 2006). S1 and S2 were not observed in rocks from Cambaí Complex. S4 deformation is a semi-brittle thrusting event leading to local cataclastic deformation and rock fracturing.

In the Cambaizinho Complex, ophiolitic and metasedimentary bodies extend mainly for 20 km NE-SW and width of 2 km (Fig. 2), dipping either 80° - 85° NW or 60° - 85° SE. The Cambaizinho ophiolite is composed of magnesian schist (talc-chlorite and talc-tremolite schist, olivine-talc schist) and serpentinite associated with amphibolite and chemical metasedimentary rocks (Remus, 1990; Remus *et al.*, 1993). Because different processes participated in rock generation in the Cambaizinho Complex, the metasedimentary rocks studied in this article are presently designated "Serrinha Formation". Mafic-ultramafic rocks remain in Cambaizinho ophiolite.
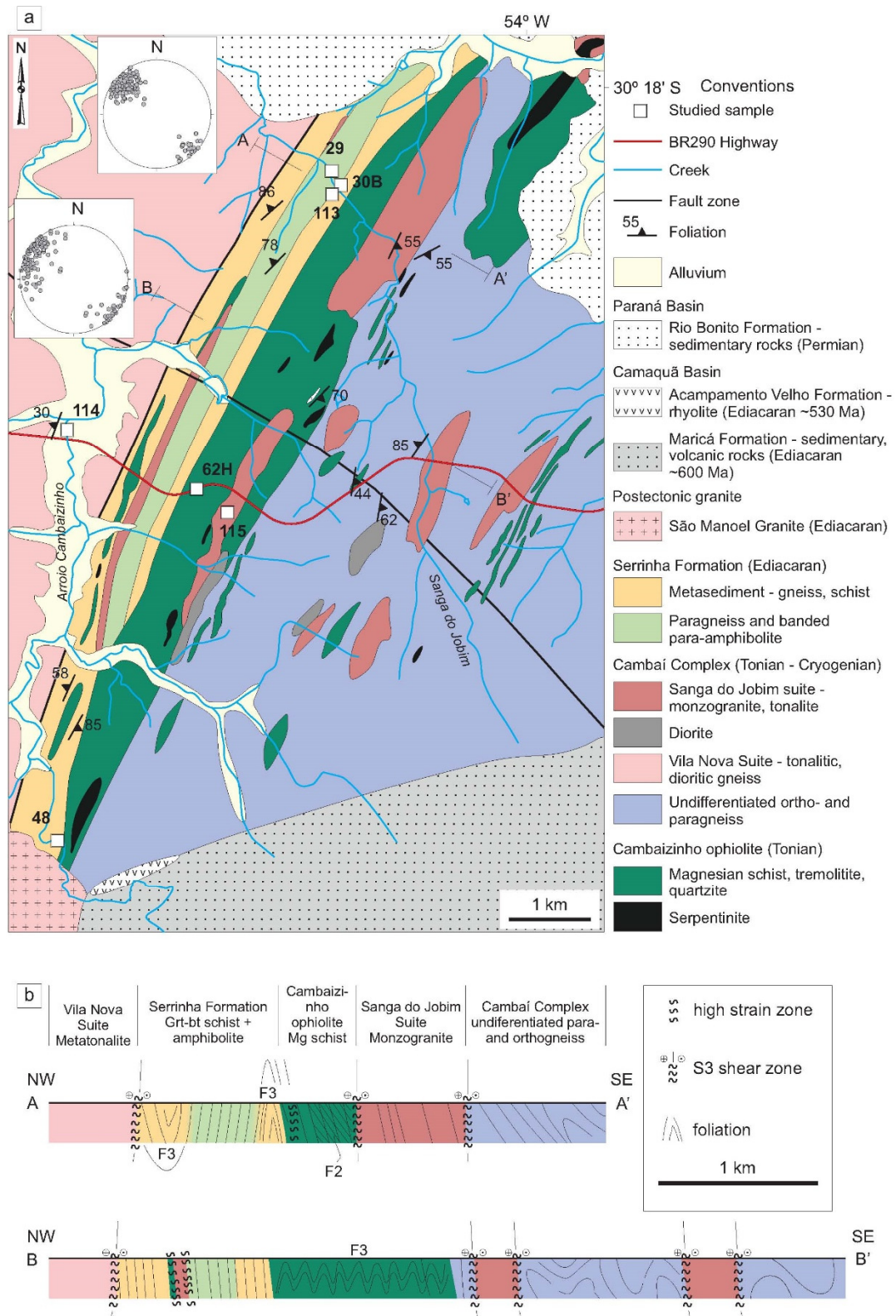
Fig. 2. (a) Geological map of the Cambaizinho Complex in northwest of São Gabriel terrane (modified from Remus, 1990) with location of sampled rocks indicated and sketch of A-A' and B-B' geological sections with additional stereoplots of main foliation (S2, S3). (b) A-A' and B-B' geological cross-sections in Cambaizinho Complex (modified from Remus, 1990; Saalmann et al., 2006).

Cambaí Complex in northwest São Gabriel terrane is made of voluminous plutonic bodies comprising metadiorites, metatonalites and metatrondhjemites of Vila

Nova Suite. Synkinematic granites intrude the Cambaizinho ophiolite and Vila Nova Suite, belonging to Sanga do Jobim Suite, Cambaí Complex. Sanga do Jobim Suite includes Capivaras diorite (Garavaglia *et al.*, 2002), Sanga do Jobim monzogranite (Remus, 1990) and Cerca de Pedra tonalite (Hartmann *et al.*, 2011). In the northwest of São Gabriel terrane, Sanga do Jobim monzogranite occurs in elliptical forms with major axis oriented NNE (Fig. 1c), with centimetric xenoliths of quartz-feldspar gneiss, banded amphibolite and magnesian schists (Remus, 1990). Field and isotopic evidence suggest two main intrusion pulses at 700 and 675 Ma (Hartmann *et al.*, 2011; Vedana *et al.*, 2018).

Metasedimentary rocks include paragneiss (biotite gneiss, garnet-biotite gneiss), schist (biotite schist, garnet-biotite-plagioclase schist either with or without staurolite), banded amphibolite, metapelite and quartzite intercalated with calcite and dolomite marble lenses. The local occurrence of staurolite in garnet-biotite schist yields the maximum of metamorphic grade (Remus, 1990). Previous field criteria led to interpretation that the metassedimentary sequence represents the oldest unit in São Gabriel terrane, being part of the mafic-ultramafic Cambaizinho ophiolite sequence (Remus, 1990; Hartmann *et al.*, 2011). However, ages younger than the ages of ophiolite indicate that detrital zircon originated from the erosion of the arc (Lena *et al.*, 2014).

The result obtained in those previous selected studies define the evolution of São Gabriel arc, both infrastructure and superstructure, constraining obduction processes (Cerro do Ouro Ophiolite) and their characterization. The use of integrated techniques (mapping, petrography, determination of U-Pb isotopic composition in rutile and U-Pb-Hf and REE in zircon) in this investigation lead to redefinition of ages and genesis for metasedimentary rocks, which are here called Serrinha Formation.

3. Methods

3.1. Sampling and petrography

Seven samples were collected for the present study (Fig. 2), some from sites previously sampled for different analyses by Remus (1990), Saalmann *et al.* (2006) and Hartmann *et al.* (2011). Coordinates of samples are presented in Table 2. Polished thin sections for petrography were prepared at Universidade Federal do Rio Grande do Sul, Instituto de Geociências laboratories (IGeo, UFRGS). Field description and

microscopic analyses were used to classify the samples: ultramafic rock (chlorite-tremolite schist), metatonalite, monzogranite, para-amphibolite, metapelite (staurolite-free and staurolite-bearing garnet-biotite-plagioclase schist). Ultramafic rocks provided rutile metamorphic age while igneous and metasedimentary rocks were selected for crystallization and detrital zircon dating. Rutile from the chlorite-tremolite schist corresponds to sample 62H from Cambaizinho ophiolite. Igneous rocks include sample 114, metatonalite from Vila Nova Suite, and sample 115, monzogranite from Sanga do Jobim Suite, both from the Cambaí Complex. Metassedimentary rocks originated in the Serrinha Formation comprise the para-amphibolite sample 29, hornblende-plagioclase granofels. Metapelites include samples 48 and 30B garnet-biotite-plagioclase schist, and 113, similar to sample 48 and 30B but staurolite-bearing.

Table 2. Summary of rock types and sample location.

Sample	Rock type	Stratigraphy	Coordinates, Datum SIRGAS2000	
62H	chlorite-tremolite schist	Cambaizinho ophiolite	30°20'45.30" 54°02'15.74" W	S;
114	metatonalite	Vila Nova Suite, Cambaí Complex	30°20'21.08" 54°03'09.09" W	S;
115	monzogranite	Sanga do Jobim Suite, Cambaí Complex	30°20'55.01" 54°02'03.17" W	S;
29	para-amphibolite	Serrinha Formation, Vacacaí Complex	30°18'34.24" 54°01'20,11" W	S;
30B	garnet-biotite-plagioclase schist	Serrinha Formation, Vacacaí Complex	30°18'40,17" 54°01'16.72" W	S;
48	garnet-biotite-plagioclase schist	Serrinha Formation, Vacacaí Complex	30°23'09.99" 54°03'12.90" W	S;
113	staurolite-garnet-biotite-plagioclase schist	Serrinha Formation, Vacacaí Complex	30°18'44.07" 54°01'20.15" W	S;

3.2. Rutile U-Pb isotopes

Rutile grains were hand-picked, mounted in epoxy resin and polished. Fractures and mineral inclusions were identified with backscattered electron (BSE) images obtained with a ZEISS EVO MA10 conventional scanning electron microscope fitted with tungsten filament, operating at voltages of 0.2–20 kV at 'Centro de Estudos em Petrologia e Geoquímica, Instituto de Geociências, Universidade Federal do Rio Grande do Sul'. ZEISS microscope is equipped with a secondary electron detector camera; the BSE is coupled with energy dispersive X-ray spectrometry detector (EDS), calibrated with natural and synthetic standards.

U-Pb isotopic compositions were determined in 35 rutile grains, with a Thermo-Fisher Element II sector field ICPMS 193 nm Photon Machines Arf Excimer laser at Departamento de Geologia, Universidade Federal de Ouro Preto, Brazil (DEGEO, UFOP). Analyses were performed during different analytical sessions with spot sizes of 50 µm, with a laser energy density of ca. 2-3 J/cm^2 and repetition rates of 5 Hz. A sample-standard bracketing method was used to correct for mass fractionation using Antônio Pereira AP rutile as a primary standard (average ID TIMS age of 499.4 ± 0.5/0.6/0.8 Ma; Santos *et al.*, 2020), and different secondary standard was analyzed – Diamantina rutile – DR2 (average ID TIMS age of 527.8 ± 1.1/1.2/1.3 Ma and 531.3 ± 1.8/1.9/2.1 Ma – variation detected by the TIMS technique only; Santos *et al.*, 2020). Calculated ^{206}Pb/^{238}U weighted mean average ages for Antonio Pereira AP primary standard are within 1.2% accuracy of the reported ages.

High Th concentrations and variable common-Pb (Pb$_{cm}$) compositions impeded the use of ^{208}Pb to correct for Pb$_{cm}$. For this reason, screening the dataset with Th/U < 2 filter should also eliminate potential sources of non-rutile bonded Th. Pb$_{cm}$ corrections were applied either using ^{204}Pb- or the ^{208}Pb-based method.

3.3. Zircon U-Pb isotopes

U-Pb laser-ablation inductively coupled plasma mass spectrometry (LA-ICPMS) analyses of zircon (n = 372 crystals, 376 analyses) from samples 114 (n = 49 analyses, one per crystal), 115 (n = 43 analyses, one per crystal), 29 (n = 67 crystals, 70 analyses), 30B (n = 140 analyses, one per crystal), 48 (n = 55 crystals, 56 analyses) and 113 (n = 140 analyses, one per crystal), were done at Isotopic Geochemistry Laboratory, Universidade Federal de Ouro Preto (IGL, UFOP). Textural and chemical zoning observed through CL images guided two analyses in different sectors of same grain. Sample preparation occurred at IGeo, UFRGS. Hand sample was crushed, zircon grains were concentrated using conventional magnetic and density separation methods, including jaw and disc crusher, Frantz separator, panning, and heavy liquids. Final selection was carried out by hand picking using a binocular microscope and tweezers. Zircons were mounted in 25 mm-diameter circular epoxy resin and polished using diamond paste to expose their interior parts.

Internal structures and inclusions in zircons were defined using cathodoluminescence (CL) images obtained before U-Pb analysis. The equipment

used included Scanning Electron Microscopy (SEM) with JEOL 6510 equipped with Centaurus cathodoluminescence detector at DGeo, UFOP.

A ThermoScientific Element 2 sector field (SF) ICP-MS coupled to a CETAC LSX-213 G2 + laser system was used for U-Pb isotope analyses of zircon. The equipment ran in standard high-sensitivity mode (STDS), using spot size of 20 µm, laser energy of 15%, laser shot frequency of 10 Hz and shutter delay of 15 s. Detailed description method is in Gerdes and Zeh (2006, 2009) and Lana *et al.* (2017). Standards used for calibration included GJ-1 zircon (Jackson *et al.*, 2004) and additional BB and Plešovice zircon standards. In sample 29, Concordia age is 601.5 ± 6.1 Ma (2σ, n = 11; MSWD 0.32) for GJ-1 standard, 558.5 ± 5.1 Ma (2σ in %, n = 12; MSWD = 0.48) for BB standard, 338.6 ± 3.4 Ma (2σ in %, n = 12; MSWD = 0.24) for Plešovice standard. In sample 30B, Concordia age was 602 ± 4.1 Ma (2σ in %, n = 22; MSWD = 0.31) for GJ-1 standard, 560.4 ± 4.2 Ma (2σ in %, n = 19; MSWD = 0.4) for BB standard and 337.6 ± 2.6 Ma (2σ in %, n = 20; MSWD = 1.03) for Plešovice standard. For sample 48, Concordia age was 601.5 ± 6.2 Ma (2σ in %, n = 10, MSWD = 0.4) for GJ-1standard and 336 ± 4.3 Ma (2σ in %, n = 9, MSWD = 0.35) for Plešovice standard. In sample 113, Concordia age was 601.5 ± 3.9 Ma (2σ in %, n = 22; MSWD = 0.28) for GJ-1 standard, 561.2 ± 3.8 Ma (2σ in %, n = 20; MSWD = 0.101) for BB standard and 338.3 ± 2.5 Ma (2σ in %, n = 20; MSWD = 0.35) for Plešovice standard. For sample 114, Concordia age was 601.5 ± 3.9 Ma (2σ in %, n = 12, MSWD = 1.5) for GJ-1 standard, 561.7 ± 5.2 Ma (2σ in %, n = 10, MSDW = 0.15) for BB standard and 339.2 ± 3.4 Ma (2σ in %, n = 12, MSWD = 0.33) for Plešovice standard. In sample 115, Concordia age was 602.5 ± 5.4 Ma (2σ in %, n = 12, MSWD = 0.34) for GJ-1 standard, 560.5 ± 4.7 Ma (2σ in %, n = 14, MSDW = 0.3) for BB standard and 335.2 ± 3.2 Ma (2σ in %, n = 12, MSWD = 0.41) for Plešovice standard.

Glitter Data Reduction Software for laser ablation microprobe was used to reduce data (Van Achterbergh *et al.*, 2001). Calculated ages and Concordia diagrams were done using IsoplotEx 4 (Ludwig, 2003). Errors are reported at the 2σ level.

3.4. Zircon Lu-Hf isotopes

Lu and Hf isotopic determinations used Thermo-Fisher Neptune with MC-ICPMS coupled to Photon Machines 193 (λ = 193 nm) ArF Excimer laser ablation system, at IGL, UFOP. Total number of analyses is 168, corresponding to 25 analyses in

metatonalite sample 114, 19 analyses in monzogranite sample 115, and 124 analyses in metasedimentary rocks, being 25 analyses in sample 29, 29 analyses in sample 30B, 23 analyses in sample 48 and 47 analyses in sample 113. The 50 µm spot laser was fired at 5 Hz repetition rate and 3 J cm^{-2} energy density during 60 s. Isotopes ^{172}Yb, ^{173}Yb and ^{175}Lu were simultaneously monitored during each analysis step to allow for correction of isobaric interferences of Lu and Yb isotopes on mass 176. Corrections for background signal and instrumental mass bias were done following the methods of Gerdes and Zeh (2006, 2009).

Yb and Lu isotopic ratios were corrected using βHf of individual integration steps (n = 60) of each analysis divided by the average offset factor of the complete analytical session. Five standard zircons were used to calibrated results: BB (Santos *et al.*, 2017), 91500 (Blichert-Toft, 2008), Mud tank (Woodhead and Hergt, 2005), GJ-1 (Morel *et al.*, 2008) and Plešovice (Sláma *et al.*, 2008). Analyses of reference material yielded ^{176}Hf/^{177}Hf values with 2σ and n = 20 of 0.281671 ± 0.000020 for BB; 0.282292 ± 0.000029 for 91500; 0.282508 ± 0.000017 for Mud tank; 0.282009 ± 0.000017 for GJ-1 and 0.282489 ± 0.000024 for Plešovice. These values agree within error with recommended values.

For initial ^{176}Hf/^{177}Hf ratios (^{176}Hf/^{177}Hf$_{(t)}$) calculations, measured ^{176}Lu/^{177}Hf and ^{176}Hf/^{177}Hf ratios were used, considering ^{176}Lu decay constant λ = 1.867 x 10^{-11}a^{-1} (Söderlund *et al.*, 2004). We used Chondritic Uniform Reservoir (CHUR) ^{176}Lu/^{177}Hf of 0.0336 for initial epsilon Hf (εHf$_{(t)}$) and ^{176}Hf/^{177}Hf of 0.282785 for T$_{DM}$ calculation (Bouvier *et al.*, 2008). We also used Depleted Mantle values of ^{176}Lu/^{177}Hf = 0.03933 and ^{176}Hf/^{177}Hf = 0.283294 (Blichert-Toft and Puchtel, 2010) and average continental crust with ^{176}Lu/^{177}Hf ratio of 0.0113 (Rudnick and Gao, 2003).

3.5. Zircon rare earth elements

To obtain the REE concentrations in dated zircon grains, we used Thermo-Fisher Element II sector field ICP-MS coupled to a Photon Machines 193 nm ArF Excimer laser at IGL, UFOP. The laser produced spotsizes of 25 µm, in 0.7 L/min He stream, during a period of 30 s at 6 Hz frequency and a laser energy density of 10-12 J cm^{-2}. A total of 140 analyses were performed, including 15 analyses in sample 29, 30 analyses in sample 30B, 25 analyses in sample 48, 25 analyses in sample 113, 23 analyses in sample 114, and 22 analyses in sample 115.

The analyzed isotopes include ^{139}La, ^{140}Ce, ^{141}Pr, ^{146}Nd, ^{147}Sm, ^{153}Eu, ^{157}Gd, ^{159}Tb, ^{163}Dy, ^{165}Ho, ^{166}Er, ^{169}Tm, ^{172}Yb, ^{175}Lu. Procedures for data reduction (Schannor *et al.*, 2019) used software Glitter using NIST 612 glass as primary standard and glass NIST 610, basaltic glasses BCR and BHVO-1 as secondary standards. Errors obtained from the averaged counts for each mass for both standards and values were compared to primary and secondary standards to determine concentrations. REE concentrations were normalized to C1 chondrite (Sun and McDonough 1989).

4. Results

4.1. Rutile U-Pb dating

Rutile-bearing sample 62H is crenulated, fine grained, green coloured, and composed of tremolite (90% vol.), chlorite (9%), rutile (1%) and accessory ilmenite (Fig. 3a-d). Tremolite is present in two generations - Amp 1 in fine crystals, aligned in the matrix and Amp 2 in large crystals cutting foliation and containing rutile inclusions (Fig. 3b-c). Kinks of chlorite flakes are a common feature (Fig. 3d).
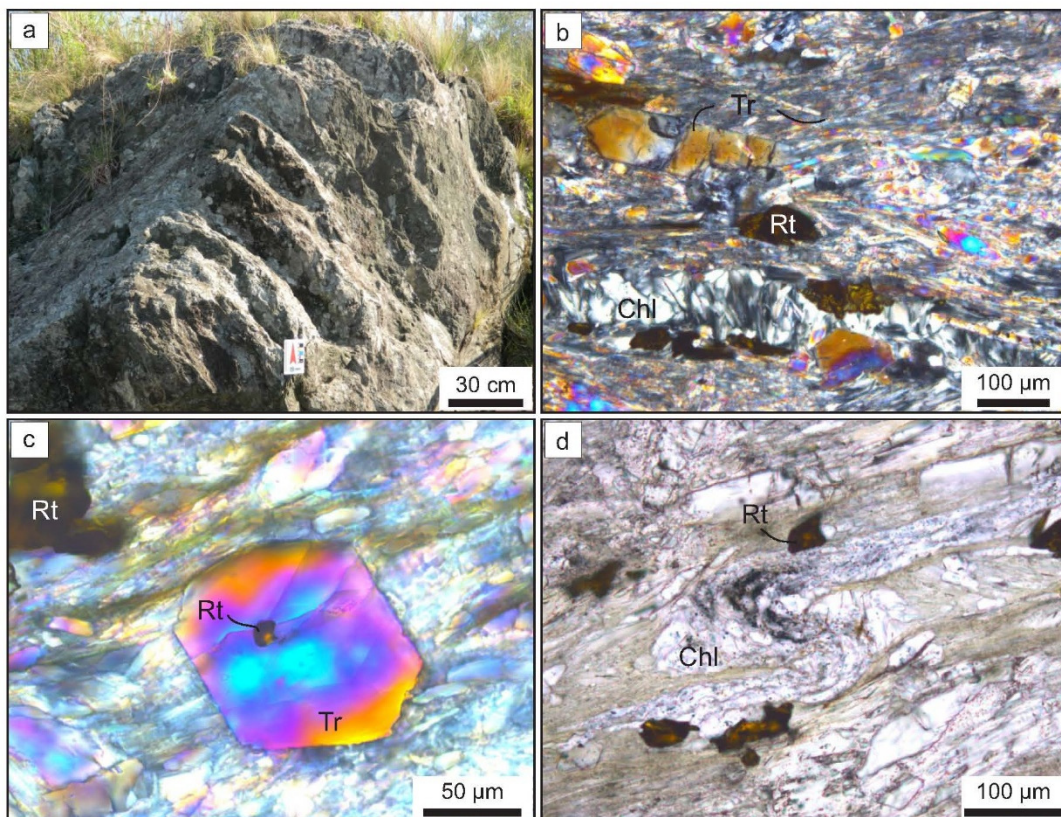
Fig. 3. Selected field image and photomicrograph of magnesian schist, Cambaizinho ophiolite (sample 62h). (a) chlorite-tremolite schist outcrop. (b) texture exhibited by deformed matrix and porphyroblastic amphibole, chlorite flakes and rutile, crossed polarizers. (c) basal tremolite section with rutile inclusion, crossed polarizers. (d)

chlorite kinking flake, planed polarizers. Mineral abbreviations follow Whitney and Evans (2010). Chl = chlorite, Tr = tremolite, Rt = rutile.

Rutile is yellow-brown to nearly black in plane-parallel polarized light and occurs as sub-euhedral crystals mainly in the matrix; crystals in strings vary in size from 5-400 µm long. BSE imaging of 35 rutile crystals (3 shown in Fig. 4) displays anhedral shapes and no internal contrast. Rutile occurs as inclusions in Amp 2, but rutile in the matrix contains inclusions of tremolite. Rutile U-Pb analyses (Supplementary Table S1) obtained in the matrix (inclusions in tremolite too small) display concordant age of 787.6 ± 2.6 Ma (Fig. 5). The measured U contents vary from 6.24 to 16.44 ppm.
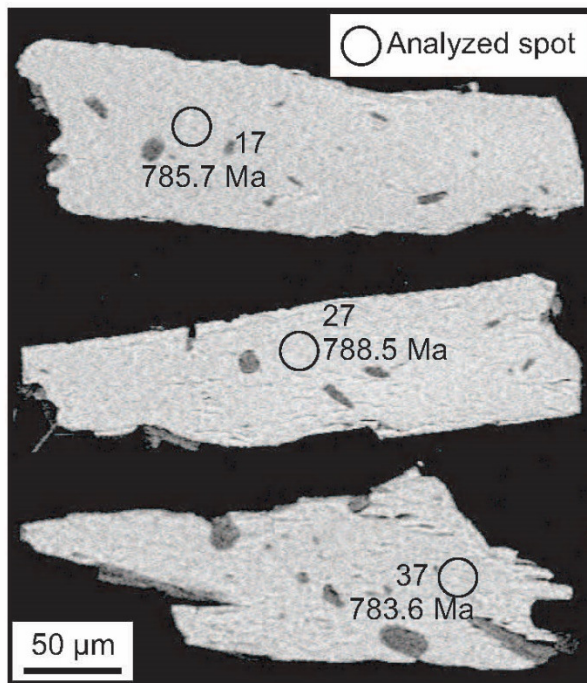
Fig. 4. Selected backscattered electron images of rutile from Cambaizinho ophiolite showing tremolite inclusions, number and Concordia ages of analyzed spots.
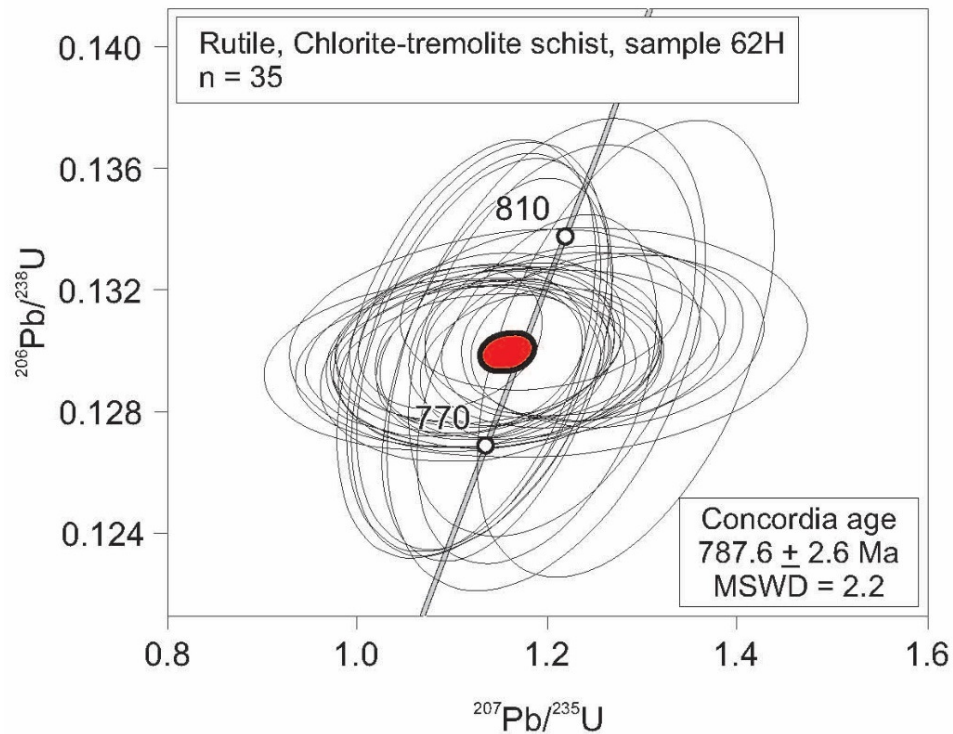
Fig. 5. U-Pb Concordia diagram for rutile from the Cambaizinho Ophiolite. Data-point error ellipses are 2σ.

4.2. Zircon U-Pb dating

Main field and microscopic features of samples collected for U-Pb dating are in Figure 6. A summary of zircon U-Pb data is listed in Supplementary Table S2. All studied zircon grains are colorless under the microscope. CL images of selected zircon with analyzed spots are shown in Figure 7. Concordant results are presented in Concordia diagrams and histograms of age data (Figs. 8 and 9).
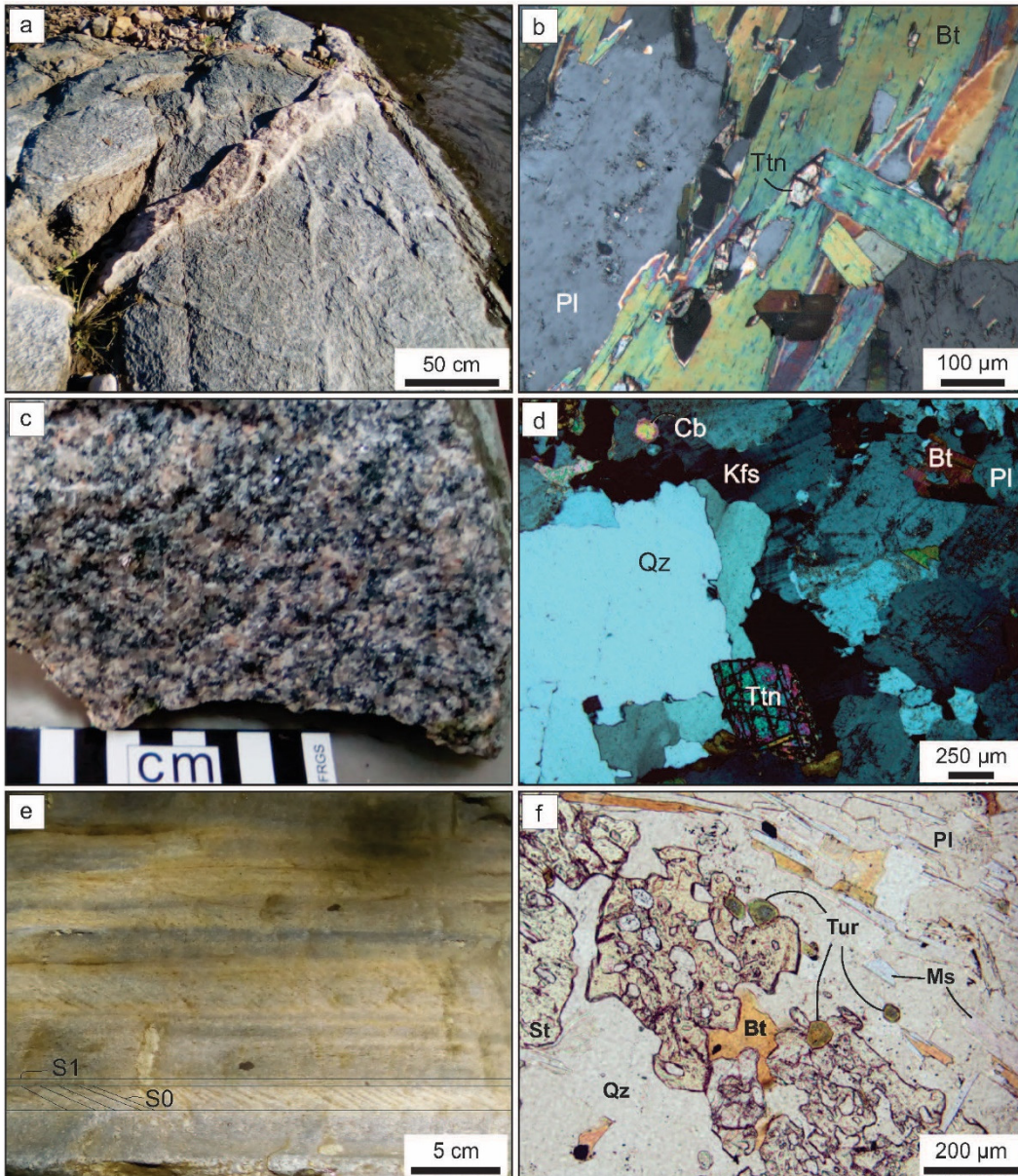
Fig. 6. Selected field photograph and photomicrography. (a-b) Metatonalite, Vila Nova Suite, Cambaí Complex (sample 114), photomicrography in crossed polarizers. (c-d) Monzogranite, Sanga do Jobim Suite, Cambaí Complex (sample 115), photomicrography crossed polarizers. (e-f) Staurolite-garnet-biotite-plagioclase schist (sample 113) from Serrinha Formation, photomicrography with plane polarizers. Mineral abbreviations follow Whitney and Evans (2010). Bt = biotite, Cb = carbonate, Kfs = K-feldspar, Ms = muscovite, Pl = plagioclase, Qz = quartz, St = staurolite, Tur = tourmaline, Ttn = titanite.

Metatonalite sample 114 is foliated, light gray, medium- to coarse-grained (Fig. 6a-b). Texture is polygonal granoblastic, with plagioclase (50% vol.), quartz (25%), biotite (24%), titanite (1%), accessories are hornblende, zircon and apatite; minor epidote and chlorite are secondary. Zircon ranges in length between 100 and 250 µm, with aspect ratio 2:1 to 3:1. In CL images, all grains show euhedrally zoned cores, with

oscilatory luminescence and eventual sector zoning. All grains have light-coloured overgrowths (Fig. 7a). In most cases, overgrowth is too small to analyze with the laser. Th/U ratios range between 0.10 and 0.75. Isotopic data of 40 grains yielded a Concordia age of 724.6 ± 3 Ma interpreted as the age of magmatic crystallization of the protolith.
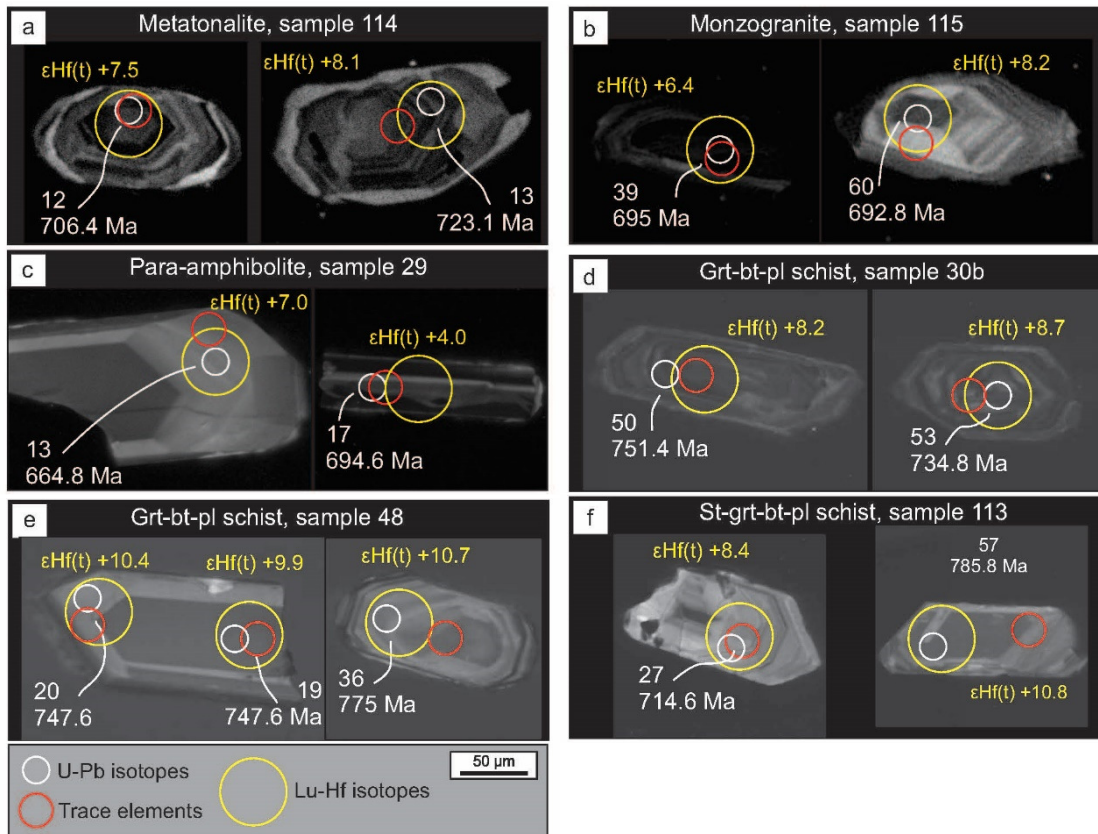
Fig. 7. Selected CL images of zircon from (a) Vila Nova Suite, (b) Sanga do Jobim Suite and (c-f) Serrinha Formation showing analyzed spots with Concordant U-Pb ages in white circle, εHf(t) in yellow circle and rare earth elements in red circle.

In general, Sanga do Jobim monzogranite sample 115 is leucocratic, medium- to coarse-grained, equigranular to porphyritic (Fig. 6c-d). Mineralogy is made up of alkali feldspar (30% vol.), quartz (25%), plagioclase (20%), biotite (20%) and hornblende (5%). Accessories include titanite, zircon, apatite and opaque minerals; minor secondary minerals are epidote, chlorite and carbonate. Zircon crystals are euhedral, prismatic to elongated, with internal oscillatory zoning and local irregular sector zoning (Fig. 7b). Crystals range in length between 100 to 550 μm, with aspect ratio 2:1 to 5:1. Th/U varies between 0.08 and 0.70. Concordant age of 673.9 ± 6.8 Ma, and an older

zircon population is 698.9 ± 4.2 Ma are interpreted as the age of magmatic crystallization of the protolith.
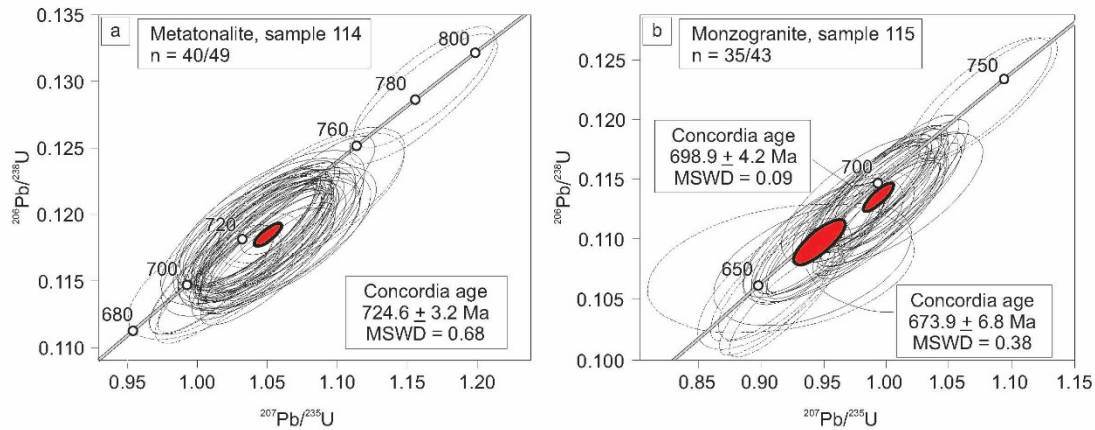
Fig. 8. U-Pb Concordia diagram for igneous zircon from (a) Vila Nova Suite metatonalite and (b) Sanga do Jobim granodiorite. Doted lines are not used in age determination, data-point error ellipses are 2σ.

Metassedimentary rocks in the four studied outcrops trend NE-SW, and layers (S$_1$) dip steeply locally with internal preserved cross-bedding (Fig. 6e-f). Sample 29 is medium-grained, green to gray striped para-amphibolite with planar structure defined by amphibole-rich and plagioclase-rich millimetric bands. The rock consists mainly of amphibole (60% vol.) and plagioclase (25%), with minor quartz + biotite + ilmenite + calcite (14%). Accessories (1%) are titanite, apatite and zircon. Pelitic schists occur with different compositions and variable assemblages. Samples 30B and 48 are mesocratic, greenish-gray, fine- to medium-grained, heterogeneous semi-pelitic schists with schistose fabric. Samples show high alignment of micaceous minerals in bands contained in granoblastic rock (quartz, plagioclase). Both consist mainly of plagioclase (45% vol.), biotite (25%), quartz (20%), garnet (5%) and muscovite (4%), with accessories (1%) tourmaline and zircon; secondary minerals are epidote, chlorite, and Fe-oxides. Sample 113 has similar macroscopic texture to samples 30B and 48 but contains additional staurolite (20% vol.); also plagioclase (20%), biotite (19%), garnet (15%), muscovite (15%), quartz (10%), with minor tourmaline (1%) and <1% of zircon, chlorite, monazite, ilmenite.

Detrital zircons obtained in the amphibolite (sample 29) are mainly euhedral, elongate prismatic, with pyramidal terminations, size from 60 to 300 μm, aspect ratio

1:1 to 5:1. Some crystals show pronounced rounding. Oscillatory growth zoning (Fig. 7c) and Th/U ratio of 0.19 to 0.87 (Supplementary Table S2) indicate igneous source (e.g. Corfu *et al.*, 2003; Hartmann and Santos, 2004). A total of 70 zircon spots were analyzed, 61 were accepted (95% concordant) and used in final density plot and age histogram (Fig. 9a, b). Ages vary between 522.94 to 2601.48 Ma, with two peak concentration groups at 680 - 700 Ma and 730 - 740 Ma.

In the garnet-biotite-plagioclase schist (sample 30B), zircon morphology is similar to sample 29, however with size varying between 70 and 300 µm and aspect ratio 2:1 to 4:1 (Fig. 7d). The Th/U ratios vary between 0.31 and 1.25, with one 0.05 exceptional value. A total of 140 zircon were analyzed, 72 accepted (95% concordant). Ages are restricted to 716.65 - 749.52 Ma, with a peak between 730-740 Ma.

The zircon population of sample 48 (garnet-biotite-plagioclase schist) is mostly rounded to subrounded, prismatic, size between 50 and 350 µm, aspect ratio 2:1 to 5:1, Th/U ratios between 0.25 and 1.07. Out of 56 analyzed spots, 43 were used (95% concordant). Ages vary between 707.2 and 775.0 Ma, with peak between 720 - 740 Ma and an older 2088.1 Ma age.

Zircon grains from the staurolite-garnet-biotite-plagioclase schist are euhedral to rounded, with internal zoning, size varying between 50 and 250 µm, aspect ratio 1:1 to 3:1 and Th/U ratio from 0.22 to 1.54. A total of 140 grains were analyzed, 110 analytical results used (95% concordant). We defined ages from 702.51 to 817.87 Ma, with two peaks concentrated at 720-740 Ma and 750-770 Ma.
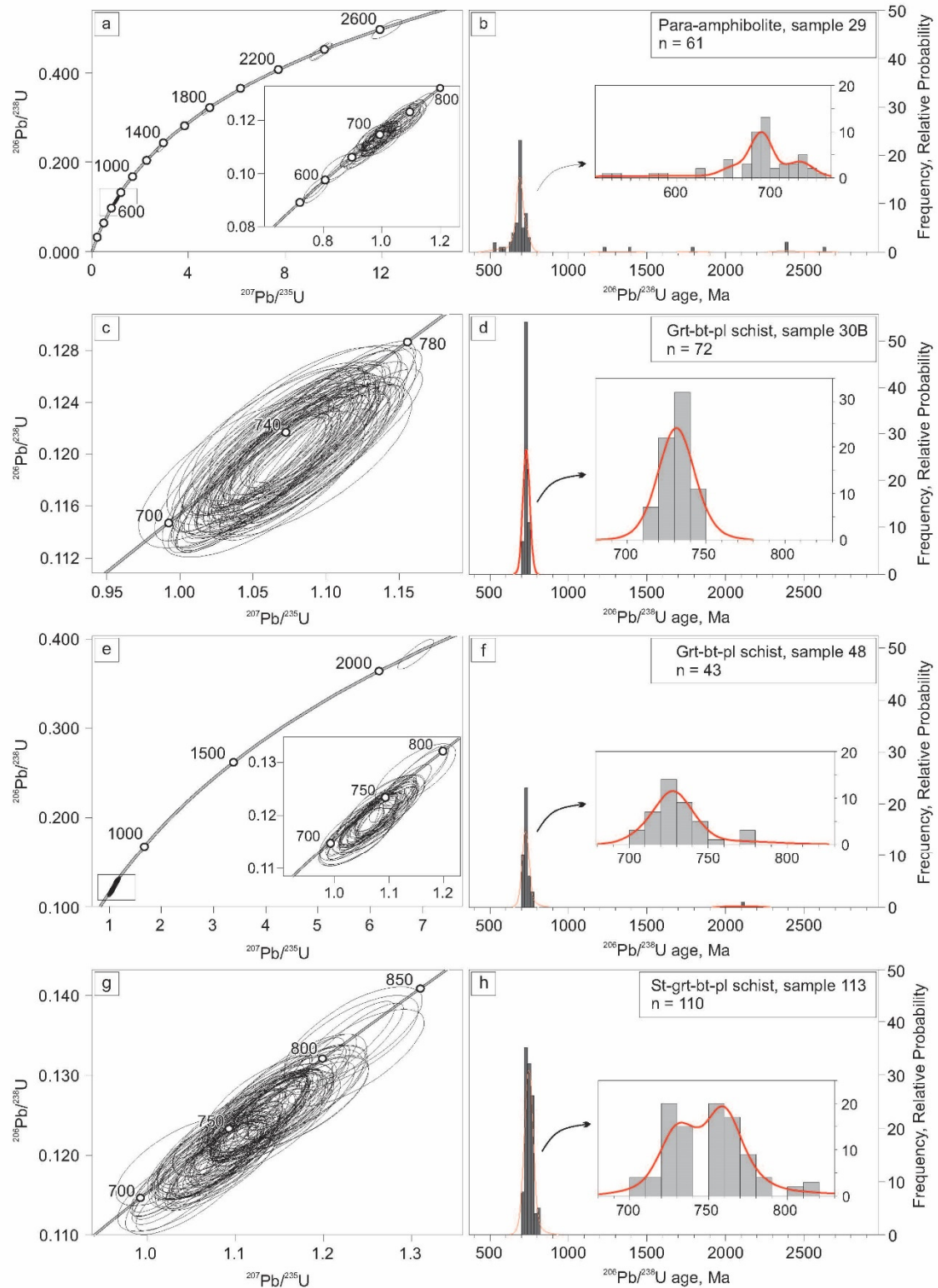
Fig. 9. Concordia plots and histograms of U-Pb ages plotted for detrital zircons from Serrinha Formation metasedimentary rock samples. Data-point error ellipses are 2σ.

4.3 Zircon Lu-Hf isotopes

Lu-Hf isotopic analyses in selected, concordant U-Pb dated zircons are shown in Supplementary Table S3. All analyzed zircon grains from Cambaí Complex are mantle-derived, with $\varepsilon Hf_{(t)}$ = +7.4 to +10.1 in metatonalite (n = 25), and $\varepsilon Hf_{(t)}$ = +2.5 to +9.2 in monzogranite (n = 19) (Fig. 10). Zircon from metatonalite has T_{DM} = 1.06 to 1.16 Ga, and in the monzogranite T_{DM} = 1.07 to 1.37 Ga.

Detrital zircons from amphibolite (sample 29) yielded $\varepsilon Hf(t)$ = -7.6 to +11.4, with T_{DM} = 0.95 to 2.93 Ga. Negative $\varepsilon Hf(t)$ are observed in Archean and Proterozoic (1211.92 Ma, 1778.03 Ma, 2377.38 Ma) and Ediacaran (583.08 Ma) zircons. In the garnet-biotite-plagioclase schist (30B), zircons yielded $\varepsilon Hf(t)$ from +3.1 to +9.4, with T_{DM} from 1.05 to 1.42 Ga. Sample 48 (garnet-biotite-plagioclase schist) has zircon grains with $\varepsilon Hf(t)$ = 0.8 – 10.8 and T_{DM} = 0.98 – 1.52 Ga. Zircons analyzed in sample 113 (staurolite-garnet-biotite-plagioclase schist) provide $\varepsilon Hf(t)$ from 0.4 to 11.9 and T_{DM} from 0.95 to 1.5 Ga.
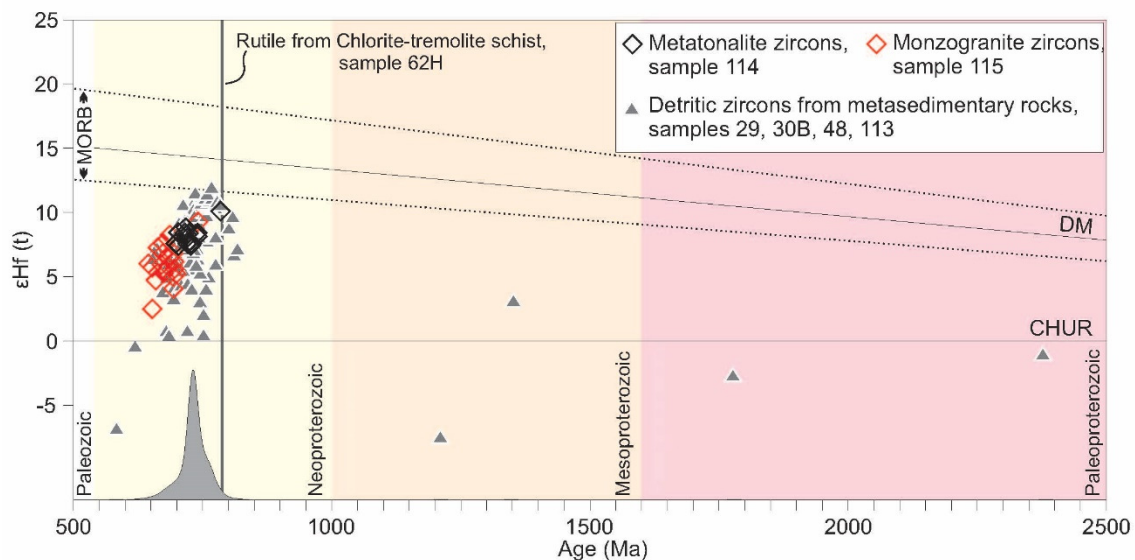
Fig. 10. Epsilon Hafnium values plotted against the U-Pb ages for selected individual zircon grains from metatonalite and monzogranite from Cambaí Complex and metassedimentary rocks from Serrinha Formation. The crustal evolution limits were projected to the depleted mantle curve using Lu/Hf ratio of average crust (0.015, Griffin *et al.*, 2004). The fields defined for the depleted mantle array and MORB is from Dhuime *et al.* (2011) and Griffin *et al.* (2004). Included in the diagram are probability density plots (shown as solid grey fields) for the concordant detrital zircon data and rutile U-Pb LA-ICP-MS concordant age (shown as solid gray field) for Cambaizinho ophiolite. CHUR = chondritic uniform reservoir, DM = depleted mantle.

4.4. Zircon rare earth elements

Zircon REE are in Supplementary Table S4 and Figure 11. ΣREEs average is 586.63 ppm in metatonalite zircon, with average La_N/Sm_N = 0.069, La_N/Yb_N = 0.002, and Gd_N/Yb_N = 0.033 (CI chondrite normalized values). Monzogranite total ΣREE content is about six times higher, with average value of 3565.56 ppm, with average La_N/Sm_N = 0.046, La_N/Yb_N = 0.005, and Gd_N/Yb_N = 0.127 (CI chondrite normalized values). In zircons from metasedimentary rocks, ΣREEs values are variable between 204.62 and 3346.31 ppm, highest at 7318.88 ppm. There is considerable overlap of content of LREE and MREE abundances for zircon from metatonalite and monzogranite. However, monzogranite is more enriched in HREE (Fig. 11).

Based on REE patterns, we identified two zircon groups. One group has strong and the other has weak positive Ce anomaly. Zircon from metatonalite shows high positive Ce anomaly, and significant negative Eu anomalies (Eu/Eu* = 0.42 - 0.66, average 0.50). Monzogranite zircon has both large and small positive Ce anomalies and negative Eu anomalies (Eu/Eu* = 0.2 - 0.68, average 0.41). Detrital zircon has either large or small positive Ce anomalies, and weak negative Eu anomalies.
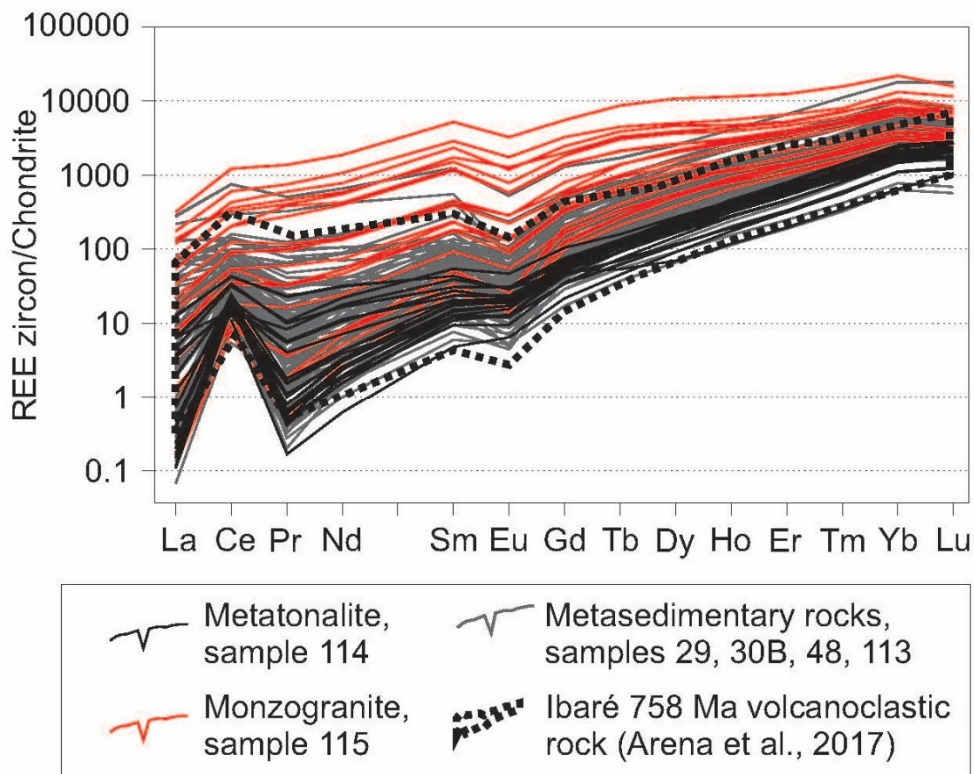
Fig. 11. Chondrite-normalized REE for detrital zircons and published volcanic zircon (Sun and McDonough 1989).

5. Discussion

Rutile crystals from Cambaizinho ophiolite ultramafic rock provide the Concordia age of 787.6 ± 2.6 Ma. This is the first rutile dating from an ophiolitic ultramafic rock in Brasiliano Orogen, solving the lack of other datable minerals. Rutile is a common mineral present in high-pressure metamorphosed metasedimentary and mafic rocks, but is absent in peridotites (Zack and Kooijman, 2017). For moderate to low metamorphic grade, rutile is reported as the dominant Ti-phase exceptionally in rocks with abundant Mg and Al and absence of Ca and Fe (Zack and Kooijman, 2017). A difficulty in interpretation of U-Pb rutile ages is the variation observed in the Pb closing temperatures between 400-500 ºC (Mezger *et al.*, 1989), but the mineral can actually remain stable up to 630 ºC, and resistant to later isotopic resetting (Cherniak, 2000) , an unresolved issue. In the present study, rutile yielded geochronological information about high temperature crystallization, not reset by younger events.

The Cambaizinho ophiolite age is compatible with Cerro Mantiqueiras ophiolite metamorphic age (786 ± 13 Ma; Arena *et al.*, 2016). In modern oceanic extensional zones, granulite facies metamorphic fabric was registered (Stakes *et al.*, 1991; Deans and Yoshinobu, 2019), which leads us to interpret the Cambaizinho ophiolite metamorphism as a mid-ocean ridge event, coeval with serpentinization of mantle peridotite reported in Cerro Mantiqueiras (Arena *et al.*, 2017). Consequently, both ophiolite mélanges were submitted to similar conditions at the same time, allowing correlation.

Laser U-Pb zircon dating of igneous and detrital samples is essential for Cambaizinho ophiolite framing in the São Gabriel arc. Distribution of U-Pb ages from this research is compared with ages of Brasiliano units in southern Brazil (Fig. 12). The $\varepsilon Hf_{(t)}$ data from selected igneous and detritic zircons is here integrated with available literature data for São Gabriel terrane and Porongos fold and thrust belt (Figs. 10 and 13). The 724.6 ± 3.2 Ma crystallization age of Vila Nova metatonalite agrees with Cambaí Complex evolution (Fig. 12). Mantle-derived juvenile magmas are characterized by positive $\varepsilon Hf_{(t)}$ and recycled magmas originated by the melting of older crust yield negative $\varepsilon Hf_{(t)}$ (Vervoort and Kemp, 2016). Positive εHf values from +10.1 to +7.4 (+8.1 average) observed in metatonalite Cambaí Complex concurs with juvenile mantle-derived signature for zircon. A metamorphic event around 720 Ma was observed in Cambaí Complex rocks (Hartmann *et al.*, 2011). However, zircon aspect, CL images and Th/U values (> 0.1) indicate magmatic origin for the studied zircon.
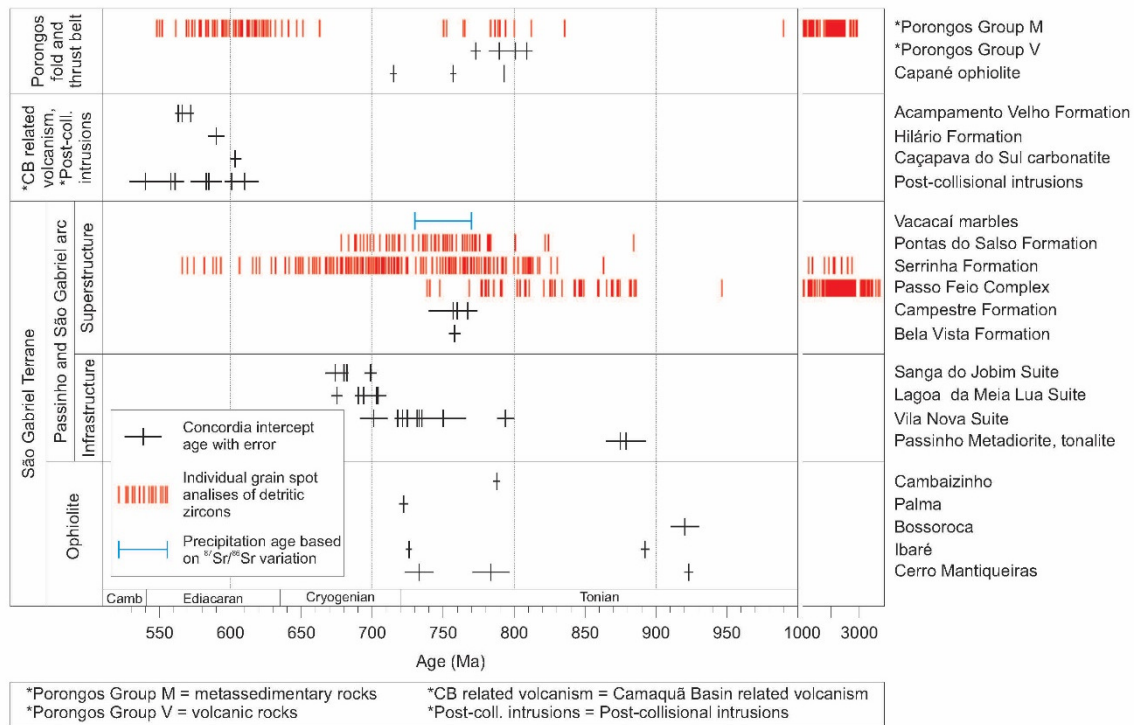
Fig. 12. Time-space plot of selected recently published U-Pb geochronological data from São Gabriel terrane, Porongos fold and thrust belt and magmatism related to Camaquã Basin, including ages obtained in this work. Data includes U-Pb zircon ages from Cerro do Ouro ophiolites: albitite and metabasalt from Cerro Mantiqueiras ophiolite (Leite *et al.*, 1998; Arena *et al.*, 2016); albitite, tourmalinite and chloritite from Ibaré ophiolite (Arena *et al.*, 2016, 2017); tourmalinite from Bossoroca ophiolite (Hartmann *et al.*, 2019); Palma ophiolite (Arena *et al.*, 2017) and U-Pb rutile dating from Cambaizinho ophiolite (this work). Infrastructure Cambaí Complex: Passinho diorite (Leite *et al.*, 1998) and tonalite (Philipp *et al.*, 2014); Vila Nova suite orthogneiss, metatrondhjemite, metatonalite (Leite *et al.*, 1998; Hartmann *et al.*, 2011; Saalmann *et al.*, 2011; Vedana *et al.*, 2018); Lagoa da Meia Lua suite trondhjemite, tonalite ang granite (Hartmann *et al.*, 2011; Vedana *et al.*, 2018); Sanga do Jobim suite granodiorite, tonalite (Hartmann *et al.*, 2011); Superstructure Vacacaí Group: Bela Vista Formation Ibaré volcanoclastic rock (Arena *et al.*, 2017); Campestre Formation metavolcanic rock (Remus *et al.*, 1999; Gubert *et al.*, 2016); Passo Feio Complex metavolcanosedimentary rocks (Remus *et al.*, 2000; Lopes *et al.*, 2015); Serrinha Formation metasedimentary rocks (Hartmann *et al.*, 2011; Lena *et al.*, 2014); Pontas do Salso Formation metarkose and phyllite (Vedana *et al.*, 2017); Cambaí and Passo Feio marbles (Goulart *et al.*, 2013); post-collisional intrusion Caçapava, Lavras, Santa Rita, São Sepé granites (Leite *et al.*, 1998; Remus *et al.*, 1999, 2000; Arena *et al.*, 2017), Caçapava carbonatite (Cerva-Alves *et al.*, 2017) and magmatism related to Camaquã Basin Hilário Formation (Janikian *et al.*, 2008), Acampamento Velho Formation andesite and basalt (Gubert *et al.*, 2016; Vedana *et al.*, 2017). Porongos fold and thrust belt includes a rodingite blackwall from the Capané ophiolite (Arena *et al.*, 2018), Porongos group metavolcanic (Saalmann *et al.*, 2011; Pertille *et al.*, 2017) and metassedimentary rocks (Pertille *et al.*, 2015a, b, 2017).

In Sanga do Jobim monzogranite, two magmatic pulses were identified at 698.9 ± 4.2 Ma and 673.9 ± 6.8 Ma. The monzogranite is intrusive into both Vila Nova metatonalite and Cambaizinho ophiolite. Overgrowth in metatonalite zircon is interpreted as evidence of contact metamorphism. The first monzogranite pulse age in Cambaizinho region overlaps with ca. 700 Ma metamorphic event recognized in São Gabriel terrane (Leite *et al.*, 1998; Remus *et al.*, 1999; Hartmann *et al.*, 2000; Saalmann *et al.*, 2005a, b, 2006). The $\varepsilon Hf_{(t)}$ obtained in Sanga do Jobim monzogranite vary from +2.5 to +9.2, with an average of +6.0. The lower $\varepsilon Hf_{(t)}$ in monzogranite compared with metatonalite suggests some contamination by oldest crustal components.

The present detrital zircon record of Serrinha Formation contains mainly Neoproterozoic ages (817 - 652 Ma), peak between 730 - 740 Ma, and negligible Meso- to Paleoproterozoic and Ediacaran contribution. These data indicate a post-652 Ma depositional age for these sediments. According to published and present crystallization ages obtained in zircons from volcanic and plutonic rocks from São Gabriel arc (Fig. 12), volcanism was active from 757 ± 17 Ma to 767.2 ± 2.9 Ma (Remus *et al.*, 1999; Gubert *et al.*, 2016; Arena *et al.*, 2017) and plutonic rocks from Vila Nova Suite crystallized from 735 ± 7 Ma to 701 ± 9.7 Ma (Leite *et al.*, 1998; Hartmann *et al.*, 2011; Saalmann *et al.*, 2011; Vedana *et al.*, 2018) with an oldest age of 794 ± 6 Ma (Vedana *et al.*, 2018). The ages obtained in zircons from metassediments indicate a mixed source for these sediments with ages known both from volcanic and plutonic rocks. Zircon ages <640 Ma were considered by Lena *et al.* (2014) as potential Pb loss; a lower intercept age of 579 ± 6 Ma is related to a shear-zone metamorphism event (Hartmann *et al.*, 2011). Initial studies in the Cambaizinho region positioned metasedimentary rocks and mafic-ultramafic sequence in the same unit named Cambaizinho Complex (Remus, 1990). However, isotopic studies showed absence of temporal relationships between the generation of mafic-ultramafic rocks and sedimentation (Lena *et al.*, 2014). In zircon from Serrinha Formation, $\varepsilon Hf_{(t)}$ varies between +0.4 and +11.9. Detrital zircon from metasedimentary rocks has similar $\varepsilon Hf_{(t)}$ and REE signature to zircon from volcanosedimentary rocks, Bela Vista Formation and ophiolite tourmalinites and chloritites (Fig. 13), indicating two different sources for these sediments. Absence of metamorphic overgrowth in zircon from detrital grains of Serrinha Formation hinders the determination of metamorphic ages.

A 65 Ma-gap in magmatic activity in São Gabriel terrane occurred between 675-610 Ma (Fig. 12), with occurrence of post-collisional intrusions, volcanism and reactivation of deep faults with mantle access and carbonatite intrusions (Leite *et al.*, 1998; Remus *et al.*, 1999, 2000; Gastal *et al.*, 2006; Janikian *et al.*, 2008; Gubert *et al.*, 2016; Arena *et al.*, 2017; Cerva-Alves *et al.*, 2017; Vedana *et al.*, 2017). Acampamento Velho Formation ignimbrites were described in the Cambaizinho region (Remus, 1990). Published studies about zircon from post-collisional intrusions (e.g. Cerro da Cria and Santa Rita Granites) and foreland Camaquã Basin are characterized by negative εHf$_{(t)}$, indicating continent-derived contribution (Fig. 13). Ages and εHf$_{(t)}$ integrated analyses led us to interpreted that the São Gabriel terrane was already accreted to the Rio de La Plata Craton at ca. 610 Ma. Negative εHf values from post-600 Ma detrital zircon grains are another indication of metamorphism caused by interaction with continental fluids.
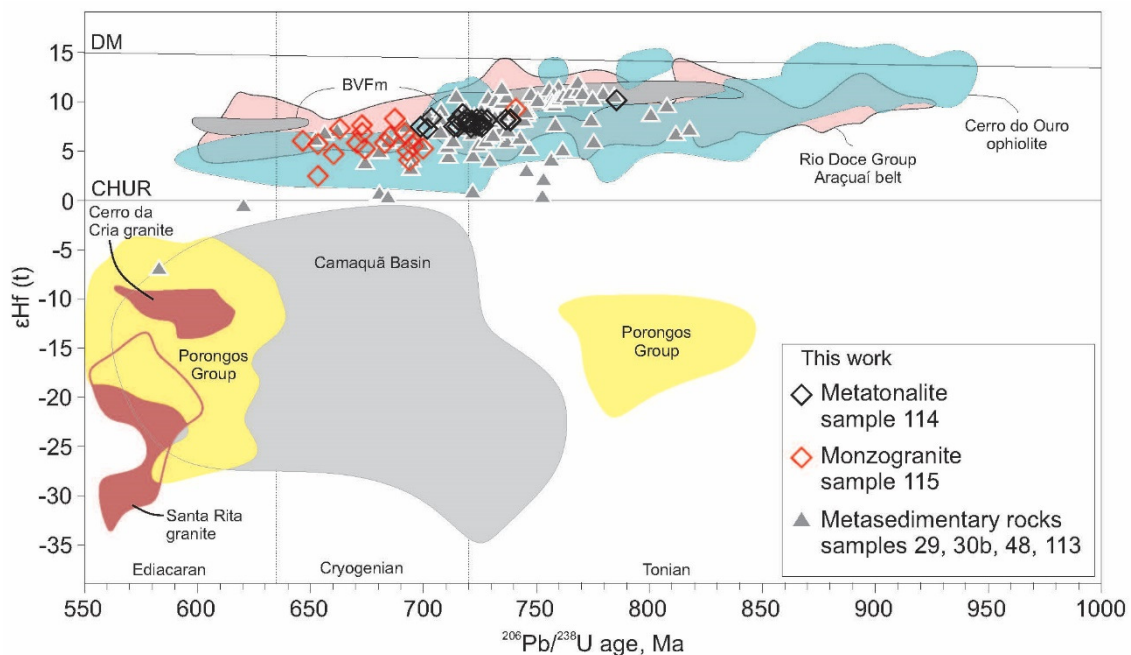
Fig. 13. Diagram of εHf (t) vs U-Pb ages of zircon grains from this study, three samples with symbols. Colored fields encircle published data from Sul-Riograndense Shield. Cerro do Ouro ophiolite include Cerro Mantiqueiras and Ibaré albitite (Arena *et al.*, 2016); Ibaré tourmalinite (Arena *et al.*, 2017); Bossoroca tourmalinite (Hartmann *et al.*, 2019); Ibaré and Palma Chloritite (Arena *et al.*, 2017); Capané rodingite blackwall (Arena *et al.*, 2018); BVFm - Bela Vista Formation, Ibaré Complex, volcanoclastic rock (Arena *et al.*, 2017); Cerro da Cria Granite (Werle, 2019); Santa Rita Granite (Arena *et al.*, 2017); Camaquã Basin, Guaritas and Santa Bárbara Formations (Oliveira *et al.*, 2014); Porongos Group (Pertille *et al.*, 2015a, b, 2017). Sul-Riograndense Shield data compared with Rio Doce Group, Araçuaí belt (Schannor *et al.*, 2019).

The São Gabriel terrane was formed during a Wilson Cycle about 200 Ma long, with ophiolite register indicating ocean crust generation from ca. 923 - 723 Ma (Arena *et al.*, 2016, 2017). In our reconstruction, the Tonian-Cryogenian juvenile São Gabriel arc displays a crustal-derived isotopic influence in the final stage (ca. 700 Ma), represented by the Sanga do Jobim monzogranite. Oceanic crust generation is registered up to 722 Ma. The oldest Passinho arc is not recognized in the Cambaizinho region. Based on the data here presented, and integrated with previous published studies, our geodynamic model shows evolution of Cambaizinho ophiolite and São Gabriel arc within the Brasiliano Orogeny (Fig. 14).

Tonian-Cryogenian juvenile magmatic arcs are registered in Mantiqueira and Tocantins provinces of the Brasiliano Orogen, including Goiás arc (ca. 862 - 630 Ma) in Brasília belt, Serra da Prata (856-838 Ma) and Rio Negro (ca. 790-620 Ma) arcs in the Ribeira belt (Peixoto *et al.*, 2017). Ophiolites in the São Gabriel terrane and mafic-ultramafic rocks in the Goiás arc seem comparable (Goñi, 1962; Pimentel and Fuck, 1992; Laux *et al.*, 2004, 2005; Arena *et al.*, 2016, 2017; Hartmann *et al.*, 2019). Recent isotopic dating and positive $\varepsilon Hf_{(t)}$ from zircon of Araçuaí belt metassedimentary rocks (Schannor *et al.*, 2019) indicate intra-oceanic activity coeval with São Gabriel terrane. Within Gondwana, juvenile terranes with documented Tonian ophiolites were described in the Arabian-Nubian Shield (Stern *et al.*, 2004; Bahariya, 2018), suggesting similar processes in the construction of the supercontinent.

a 760 - 725 Ma

São Gabriel arc

Proto-Adamastor Ocean

b 650 - 610 Ma

Kalahari

Rio de La Plata Cráton

Adamastor Ocean

c 920 - 780 Ma

São Gabriel arc oldest registered age ~794 Ma

metamorphism in mid-ocean ridge ~787 Ma

oldest oceanic crust registered at ~923 Ma

oceanic crust

mantle

subducting slab

d 780 - 720 Ma

São Gabriel arc volcanism ~767-757 Ma

São Gabriel arc plutonism ~794-701

limestone precipitation ~770-730 Ma

younger oceanic crust registered at ~722 Ma

ophiolite obduction

oceanic crust

mantle

Fig. 14. (a-b) Reconstruction models during the Neoproterozoic Brasiliano orogeny for São Gabriel terrane evolution (Modified from Saalmaan *et al.*, 2011; Arena *et al.*, 2017; Hartmann *et al.*, 2019). (c-f) Envisaged tectonic model for the São Gabriel terrane based on obtained and published data. K, RLP = Kalahari or Rio de La Plata Cratons undeterminated.

6. Conclusions

The interpretation of data led us to reach several conclusions regarding evolution of the Cambaizinho ophiolite and adjacent units of the juvenile São Gabriel terrane, mostly Cambaizinho ophiolite, and pertinence to Gondwana.

1 – The novel geochronological data constraining evolution of the Cambaizinho ophiolite and São Gabriel arc at 787-674 Ma provide new insights into the evolution of the Brasiliano Orogen in SW Gondwana and invite comparisons with equivalent units in the Arabian-Nubian Shield and NE Africa;

2 – Ocean crust generation in São Gabriel terrane occurred from 923 ± 3.1 to 722 ± 3 Ma, with mid-ocean ridge metamorphism at ca. 787 Ma, dated in rutile from the Cambaizinho ophiolite;

3 – No evidence of Passinho arc (ca. 879 Ma) was found adjacent to the Cambaizinho ophiolite or associated rocks;

4 – Field evidence and the presence of zircon rim overgrowth in metatonalite and absence in monzogranite zircon is interpreted as intrusion of monzogranite at ca. 700 Ma, causing zircon overgrowth;

5 – Field evidence, dating and isotopic data lead us to consider the Sanga do Jobim monzogranite as representatitive of latest orogenic São Gabriel arc magmatism;

6 – Detrital zircon ages support a post-652 Ma depositional age for the Cambaizinho basin, with a minor contribution of old crustal material;

7 – Our data integrated with published zircon U-Pb and εHf(t) values available for the São Gabriel terrane indicate juvenile activity between 900 and 674 Ma interpreted as intra-oceanic arc. The continental crust-derived influence started at 700 Ma, with environment evolving to an active continental margin.

Appendix A. Supplementary data

Supplementary data to this article can be found online at

https://doi.org/10.1016/j.precamres.2020.105648.

Supplementary Table S1. rutile LA-ICPMS U-Pb geochronology data.
#Parte 1

Sample	U (µg g-1)	Th/U	Ages					
			207Pb/206Pb	2s (%)	207Pb/235U	2s (%)	206Pb/238U	2s (%)
Cambaizinho ophiolite, magnesian schist, sample 62H								
7	7.38	0.000	819.95	179.84	776.01	47.83	784.46	29.55
9	10.05	0.000	904.11	178.76	795.44	49.00	780.75	26.90
10	8.96	0.004	906.79	211.76	802.96	58.71	789.83	30.12
13	9.44	0.000	771.10	199.80	765.45	52.36	787.23	31.02
15	10.21	0.004	1037.92	201.18	837.93	58.50	788.24	35.16
17	9.37	0.001	768.82	210.48	765.85	55.23	788.59	31.60
19	6.24	0.000	748.56	211.90	760.53	55.16	788.35	32.19
20	9.03	0.003	788.19	204.05	769.87	53.87	787.29	30.13
27	7.44	0.000	903.52	236.05	800.14	65.47	787.23	36.35
29	7.90	0.000	733.01	210.01	756.22	54.30	787.82	13.33
31	10.52	0.003	748.56	325.08	758.31	85.72	785.29	13.34
32	8.37	0.001	771.10	229.64	766.73	60.48	789.00	11.91
34	12.94	0.002	850.78	220.73	786.59	59.87	787.88	13.57
37	8.30	0.000	773.69	246.10	763.50	64.80	783.64	13.58
38	6.86	0.008	900.83	382.16	801.13	108.26	789.53	17.70
40	7.63	0.003	941.79	216.36	813.91	60.91	791.77	13.09
47	7.93	0.000	1020.05	201.30	834.03	58.19	789.71	13.21
50	8.97	0.000	870.69	210.63	797.61	57.78	795.66	12.25
51	10.31	0.000	908.28	162.83	802.78	44.84	789.06	11.44
52	13.28	0.000	710.93	153.66	752.45	39.17	790.30	10.97
53	11.09	0.001	782.41	166.16	767.49	43.51	786.06	12.27
55	12.69	0.000	835.28	159.41	783.13	42.65	788.71	12.03
57	7.42	0.002	925.71	200.98	808.16	56.05	789.95	13.56
58	8.59	0.000	992.43	197.04	826.93	56.36	790.53	12.97
59	11.68	0.002	732.02	247.38	755.08	64.20	786.59	11.92
60	8.50	0.001	808.28	181.19	774.41	48.04	786.41	12.51
69	8.50	0.002	899.94	181.63	797.68	49.87	785.23	11.80
70	16.44	0.002	800.34	236.87	770.85	62.98	784.35	11.69
71	8.76	0.000	770.12	286.90	763.66	75.92	785.11	12.51
73	10.22	0.001	757.74	217.21	760.73	56.68	785.41	11.92
74	9.20	0.000	863.06	296.08	789.62	81.53	787.59	13.21
76	9.14	0.001	770.77	223.20	764.08	58.59	785.47	12.98
77	7.68	0.001	766.87	225.05	765.23	59.12	788.41	12.98
78	8.56	0.002	784.98	219.90	771.02	58.20	790.00	13.45

| 79 | 12.40 | 0.004 | 805.42 | 264.02 | 773.93 | 70.71 | 786.76 | 14.04 |

#Parte2

Sample	Isotopic ratios						
	207Pb/206Pb	2s (%)	207Pb/235U	2s (%)	206Pb/238U	2s (%)	Rho
Cambaizinho ophiolite, magnesian schist, sample 62H							
7	0.0664	8.6106	1.1474	8.6115	0.1294	3.9914	0.4635
9	0.0692	8.6730	1.1889	8.6740	0.1288	3.6505	0.4209
10	0.0693	10.2786	1.2051	10.2794	0.1303	4.0418	0.3932
13	0.0649	9.4915	1.1252	9.4924	0.1299	4.1753	0.4399
15	0.0739	9.9634	1.2824	9.9643	0.1301	4.7256	0.4743
17	0.0648	9.9954	1.1260	9.9962	0.1301	4.2470	0.4249
19	0.0642	10.0296	1.1149	10.0304	0.1301	4.3278	0.4315
20	0.0654	9.7203	1.1345	9.7212	0.1299	4.0557	0.4172
27	0.0692	11.4517	1.1990	11.4524	0.1299	4.8910	0.4271
29	0.0637	9.9153	1.1059	9.9161	0.1300	1.7959	0.1811
31	0.0642	15.3870	1.1103	15.3876	0.1295	1.8021	0.1171
32	0.0649	10.9091	1.1279	10.9099	0.1302	1.6027	0.1469
34	0.0674	10.6200	1.1699	10.6208	0.1300	1.8276	0.1721
37	0.0650	11.6959	1.1211	11.6966	0.1293	1.8381	0.1571
38	0.0691	18.5319	1.2012	18.5324	0.1303	2.3785	0.1283
40	0.0705	10.5592	1.2290	10.5600	0.1307	1.7548	0.1662
47	0.0732	9.9426	1.2737	9.9435	0.1303	1.7755	0.1786
50	0.0681	10.1660	1.1936	10.1669	0.1314	1.6356	0.1609
51	0.0693	7.9054	1.2048	7.9064	0.1302	1.5391	0.1947
52	0.0631	7.2289	1.0981	7.2301	0.1304	1.4732	0.2038
53	0.0653	7.9080	1.1294	7.9091	0.1297	1.6568	0.2095
55	0.0669	7.6509	1.1625	7.6520	0.1301	1.6192	0.2116
57	0.0699	9.7840	1.2165	9.7849	0.1304	1.8225	0.1863
58	0.0722	9.6913	1.2578	9.6921	0.1305	1.7419	0.1797
59	0.0637	11.6779	1.1036	11.6786	0.1298	1.6079	0.1377
60	0.0661	8.6588	1.1440	8.6598	0.1297	1.6879	0.1949
69	0.0690	8.8065	1.1937	8.8074	0.1295	1.5949	0.1811
70	0.0658	11.3053	1.1365	11.3060	0.1294	1.5808	0.1398
71	0.0649	13.6273	1.1214	13.6279	0.1295	1.6909	0.1241
73	0.0645	10.2962	1.1153	10.2970	0.1296	1.6105	0.1564
74	0.0678	14.2731	1.1764	14.2737	0.1300	1.7806	0.1247
76	0.0649	10.6026	1.1223	10.6033	0.1296	1.7538	0.1654
77	0.0648	10.6840	1.1247	10.6848	0.1301	1.7469	0.1635
78	0.0653	10.4699	1.1369	10.4707	0.1304	1.8065	0.1725
79	0.0660	12.6118	1.1430	12.6125	0.1298	1.8940	0.1502

Supplementary Table S2. Zircon LA-ICPMS U-Pb geochronology data.

#Parte 1

Sample	U (µg g-1)	Th/U	Ages 207Pb/206Pb	2s	206Pb/238U	2s	207Pb/235U	2s
Vila Nova Suite, metatonalite, sample 114								
7	85.66	0.35	725.99	43.41	723.17	19.85	723.86	18.53
8	87.35	0.52	723.25	45.66	723.75	19.99	723.62	18.93
9	103.46	0.39	742.34	45.02	721.50	19.95	726.59	18.92
10	87.43	0.49	731.96	79.32	719.37	22.88	722.43	26.33
11	81.98	0.46	745.70	43.68	719.20	20.10	725.66	18.84
12	100.48	0.42	751.58	44.91	698.61	19.64	711.30	18.82
13	128.45	0.51	749.87	42.74	717.64	19.75	725.50	18.51
14	75.42	0.43	747.44	79.27	725.24	22.76	730.69	26.41
15	100.89	0.51	751.51	43.35	717.35	19.87	725.69	18.69
16	51.22	0.10	730.69	44.59	702.19	19.45	709.01	18.53
17	54.81	0.32	733.14	79.99	703.46	22.54	710.58	26.23
18	109.50	0.47	740.59	44.66	723.75	20.49	727.87	19.19
19	113.05	0.44	759.76	43.40	716.78	19.89	727.27	18.75
27	127.66	0.56	731.68	79.33	726.51	23.36	727.77	26.60
28	139.37	0.54	742.97	79.13	723.75	22.67	728.45	26.29
30	118.30	0.64	723.15	46.08	725.64	20.09	725.03	19.05
31	96.32	0.49	761.34	43.73	717.59	20.33	728.28	19.09
32	138.45	0.75	766.93	77.93	717.24	23.09	729.39	26.47
33	70.36	0.41	785.57	44.27	711.65	19.81	729.70	18.98
36	61.56	0.47	774.13	45.28	709.34	19.98	725.10	19.19
37	75.94	0.46	775.86	44.04	714.99	20.23	729.88	19.15
38	54.75	0.60	776.28	44.61	785.42	21.26	783.05	19.67
39	95.35	0.56	745.01	45.38	701.44	19.03	711.89	18.46
40	92.06	0.49	772.24	78.39	722.08	23.78	734.41	26.98
48	127.74	0.49	751.97	44.00	721.16	20.09	728.70	18.91
49	148.45	0.49	761.95	78.18	738.69	24.02	744.48	27.03
50	105.86	0.48	756.10	43.88	738.63	20.96	742.98	19.41
51	135.25	0.58	739.69	43.86	728.06	20.66	730.92	19.16
52	71.98	0.55	763.16	78.84	718.28	23.39	729.26	26.77
53	95.35	0.47	717.21	50.20	725.30	20.59	723.32	19.94
56	83.98	0.51	748.08	79.24	721.04	23.58	727.65	26.82
59	116.71	0.63	767.22	78.28	736.45	24.03	744.11	27.09
60	104.10	0.46	739.82	44.41	724.95	20.20	728.60	18.96
68	90.02	0.53	729.87	44.64	719.60	20.67	722.10	19.25
70	121.85	0.66	762.98	44.25	722.25	20.58	732.25	19.32
73	109.95	0.53	729.78	45.92	728.12	21.23	728.52	19.76
74	142.19	0.67	726.02	43.39	726.05	21.00	726.04	19.24
77	119.24	0.60	734.55	79.55	728.98	24.05	730.35	27.04
78	113.54	0.53	746.50	44.27	718.85	20.80	725.60	19.38

Sample	U (μg g-1)	Th/U	Ages 207Pb/206Pb	2s	206Pb/238U	2s	207Pb/235U	2s
80	60.97	0.33	747.74	79.62	716.03	24.10	723.75	27.16
88	77.29	0.48	773.07	78.71	719.26	23.89	732.46	27.10
89	59.97	0.68	788.51	44.27	780.29	22.88	782.43	20.70
90	69.73	0.47	792.17	44.19	708.13	20.71	728.62	19.60
92	68.43	0.29	757.65	46.11	719.95	21.08	729.18	19.88
93	89.03	0.55	759.75	50.52	715.63	21.46	726.39	20.80
94	98.16	0.51	761.01	44.40	718.22	21.02	728.68	19.62
95	72.43	0.44	737.66	44.40	723.80	21.35	727.19	19.68
96	69.65	0.49	752.23	45.75	720.46	21.32	728.23	19.95
100	59.03	0.42	774.34	45.32	713.67	21.27	728.48	20.00
Sanga do Jobim suite, monzogranite, sample 115								
7	92.84	0.46	714.10	43.05	740.43	24.51	743.73	22.57
12	27.34	0.46	747.09	43.55	740.89	24.38	740.66	23.15
18	817.64	0.13	698.75	47.54	700.39	22.68	703.65	20.30
19	423.65	0.41	719.01	43.78	695.36	22.93	707.70	20.75
27	434.18	0.23	719.28	46.72	694.04	23.06	699.96	20.71
28	377.52	0.10	753.68	50.57	697.70	23.72	702.83	21.51
29	73.77	0.37	733.01	48.52	693.87	23.05	703.17	21.41
30	66.65	0.24	704.85	48.71	692.55	22.48	695.46	20.89
31	80.45	0.40	720.75	43.54	687.11	22.76	702.36	21.27
36	389.92	0.17	751.45	47.86	684.77	22.74	700.71	20.68
39	351.54	0.18	752.17	43.33	693.64	22.70	695.25	20.41
47	587.70	0.21	706.03	47.40	699.30	23.53	701.56	21.04
48	170.52	0.30	700.45	44.10	705.07	23.13	707.76	20.84
49	184.32	0.57	739.98	55.58	692.55	22.71	695.63	20.51
50	41.59	0.38	707.20	82.08	687.40	23.19	701.81	22.48
53	208.83	0.16	708.80	44.56	696.21	22.70	697.46	20.56
54	21.17	0.32	716.31	45.00	689.86	23.53	694.27	24.17
55	60.87	0.19	705.58	44.64	696.61	23.16	709.35	21.68
59	182.51	0.28	679.27	52.26	682.99	23.21	699.24	21.42
60	513.29	0.20	748.23	54.63	692.55	22.83	692.83	20.41
70	352.40	0.30	701.47	45.43	691.69	22.83	708.86	20.73
71	152.40	0.57	708.57	66.15	698.56	23.15	700.86	20.87
72	93.65	0.33	658.16	197.21	692.55	25.91	708.43	28.32
73	255.50	0.28	672.40	64.15	693.52	23.00	697.08	20.84
74	207.91	0.20	749.87	49.31	692.04	25.71	694.00	27.87
75	715.06	0.11	751.84	46.63	681.56	23.46	701.23	21.57
76	375.47	0.15	694.80	83.90	701.70	23.95	710.43	21.63
77	213.52	0.35	670.47	83.23	673.70	22.89	679.50	21.05
78	90.50	0.38	693.73	43.71	670.26	22.09	678.52	20.56
88	288.39	0.32	763.62	43.02	673.82	25.99	681.56	28.19
89	56.53	0.25	708.23	45.23	672.78	21.96	674.28	20.96
90	39.45	0.42	759.09	80.17	671.69	22.72	671.86	23.11
91	70.84	0.36	695.31	59.26	672.15	25.17	677.38	27.91

Sample	U (µg g-1)	Th/U	Ages 207Pb/206Pb	2s	206Pb/238U	2s	207Pb/235U	2s
92	27.52	0.41	699.43	54.31	667.85	22.33	674.16	22.31
93	42.46	0.25	708.56	45.58	673.36	22.31	679.39	21.59
94	32.43	0.27	701.13	48.83	672.84	22.55	677.25	21.83
95	5.94	0.35	700.36	81.29	662.79	23.63	673.52	35.94
96	780.03	0.13	691.94	55.25	645.75	21.71	662.69	20.02
97	4.79	0.36	683.05	63.11	660.03	24.81	659.61	49.98
111	477.63	0.08	764.80	45.80	653.13	25.35	657.03	27.63
118	81.75	0.70	709.58	129.51	646.27	21.59	658.62	20.48
119	28.99	0.35	666.50	59.61	653.59	22.03	660.24	22.63
120	32.03	0.46	738.14	45.74	652.72	22.03	655.82	22.00
Serrinha Formation, para-amphibolite, sample 29								
7	115.64	0.50	737.03	79.06	682.29	24.95	695.17	27.35
8	67.68	0.29	732.18	47.06	680.20	22.20	692.39	20.74
9	109.09	0.39	555.62	46.09	530.73	17.36	535.45	16.81
10	236.04	0.51	616.84	83.78	628.46	23.31	625.94	25.99
11	43.00	0.44	745.92	47.46	678.63	22.32	694.43	20.96
12	185.81	0.19	696.57	43.69	674.04	21.65	679.25	19.76
13	40.79	0.27	680.99	46.71	661.58	21.45	666.00	19.97
14	69.88	0.55	725.07	46.75	698.94	22.65	705.17	20.87
15	83.98	0.51	695.54	81.54	656.68	24.23	665.51	26.93
16	64.82	0.26	2398.42	33.86	2377.38	67.43	2388.73	36.67
17	260.58	0.62	692.53	80.59	694.82	25.21	694.28	27.39
18	263.26	0.37	686.96	43.11	694.24	22.27	692.53	19.96
19	193.77	0.44	687.52	80.85	693.14	25.12	691.82	27.33
20	329.16	0.32	726.85	79.58	698.01	25.10	704.88	27.46
27	246.78	0.54	579.58	45.50	522.94	17.44	533.63	16.96
28	80.07	0.22	2383.18	34.00	2387.11	68.14	2384.99	36.88
29	252.21	0.59	700.45	43.42	707.04	22.92	705.47	20.44
30	74.95	0.38	757.26	45.32	687.11	22.58	703.76	20.88
31	27.97	0.38	788.51	48.76	724.90	23.78	740.63	22.17
32	52.00	0.24	761.38	47.46	734.99	24.01	741.54	21.92
33	125.65	0.52	686.14	43.82	673.86	21.99	676.70	19.95
34	58.31	0.43	711.94	45.80	668.74	21.77	678.72	20.22
37	15.05	0.73	2636.40	38.87	2601.48	75.12	2621.16	40.24
39	125.10	0.58	779.74	46.11	729.80	24.05	742.19	21.90
40	62.28	0.45	753.89	45.29	711.27	23.18	721.61	21.15
47	76.69	0.54	649.78	45.76	656.74	21.59	655.17	19.78
48	286.39	0.47	729.24	42.78	699.52	22.72	706.62	20.43
49	236.85	0.69	719.35	79.59	698.59	25.61	703.53	27.69
50	56.35	0.35	718.28	46.86	703.34	23.12	706.91	21.14
51	102.91	0.68	769.17	78.18	735.16	26.71	743.62	28.54
52	60.21	0.35	724.66	47.17	662.22	22.02	676.58	20.67
53	69.12	0.49	732.35	44.55	738.84	24.19	737.24	21.45
54	103.71	0.29	730.52	47.57	680.20	22.66	691.99	21.10

Sample	U (µg g-1)	Th/U	Ages 207Pb/206Pb	2s	206Pb/238U	2s	207Pb/235U	2s
55	195.74	0.33	703.41	45.37	697.32	23.46	698.76	21.11
56	355.77	0.42	811.33	42.94	721.72	23.94	743.93	21.64
57	148.76	0.38	693.46	80.91	684.38	25.36	686.50	27.51
59	193.21	0.46	712.61	43.09	690.30	22.63	695.56	20.36
60	50.71	0.27	714.25	45.73	652.02	21.60	666.15	20.18
67	88.36	0.27	749.27	79.54	740.80	26.90	742.91	28.72
68	180.78	0.35	757.51	78.40	690.07	25.85	706.12	27.95
69	66.72	0.89	736.34	80.57	717.39	26.26	722.00	28.41
70	136.35	0.54	712.49	43.77	685.37	22.65	691.74	20.48
71	143.31	0.70	618.55	45.62	572.81	19.30	618.55	45.62
72	99.82	0.60	753.48	43.95	735.33	24.32	739.83	21.60
75	58.24	0.36	647.92	47.02	655.81	22.17	654.04	20.31
76	193.24	0.56	735.28	44.13	680.26	22.92	693.17	20.87
79	74.89	0.57	1780.59	37.52	1778.03	53.97	1779.21	34.37
80	67.64	0.87	745.26	45.50	745.46	25.21	745.41	22.28
87	79.70	0.26	731.48	44.73	684.50	22.89	695.56	20.88
88	89.89	0.33	698.25	45.00	688.85	23.11	691.06	20.84
89	156.34	0.39	752.48	78.65	714.85	26.69	724.01	28.45
90	33.90	0.21	1398.12	59.31	1352.58	45.20	1370.34	36.90
91	58.38	0.46	776.60	44.60	757.99	25.39	762.72	22.40
92	114.60	0.35	730.02	44.61	684.56	23.00	695.26	20.93
93	80.91	0.42	708.91	45.21	692.74	23.32	696.56	21.05
94	95.48	0.49	765.90	78.71	731.41	27.04	739.96	28.79
95	141.73	0.56	744.64	44.24	692.68	23.32	705.04	21.15
96	80.52	0.87	1232.08	40.48	1211.92	39.23	1219.19	29.52
97	132.71	0.48	577.31	46.11	583.08	19.74	581.91	18.43
99	133.89	0.31	644.94	45.85	620.08	21.29	625.45	19.71
100	160.28	0.46	715.20	45.45	699.00	23.59	702.85	21.27

Serrinha Formation, garnet-biotite-plagioclase schist, sample 30B

Sample	U (µg g-1)	Th/U	Ages 207Pb/206Pb	2s	206Pb/238U	2s	207Pb/235U	2s
7	323.34	0.63	764.26	50.05	724.15	26.32	734.02	23.85
8	177.29	0.64	780.36	77.99	716.65	26.89	732.27	28.70
12	60.62	0.05	725.69	52.75	722.48	25.64	723.26	23.52
15	193.38	0.52	745.26	44.18	737.11	25.00	739.13	22.02
16	196.95	0.48	732.75	44.28	725.99	24.61	727.65	21.76
17	1236.33	1.09	813.54	43.59	730.03	24.80	750.88	22.26
19	203.66	0.52	767.90	45.14	716.77	24.36	729.27	21.97
20	412.64	1.25	820.23	43.81	737.51	25.06	758.33	22.46
28	266.89	0.72	767.16	45.06	722.25	23.68	733.28	21.47
29	219.10	0.51	769.90	44.23	731.75	24.45	741.21	21.83
31	183.44	0.43	754.80	45.07	736.70	25.07	741.20	22.23
32	245.57	0.56	740.56	79.25	744.18	27.72	743.28	29.05
33	277.97	0.58	775.42	77.87	727.44	27.26	739.30	28.85
34	218.24	0.63	801.29	43.27	732.33	24.79	749.55	22.12
35	258.40	0.76	763.62	44.32	744.58	26.01	749.35	22.77

Sample	U (μg g-1)	Th/U	Ages 207Pb/206Pb	2s	206Pb/238U	2s	207Pb/235U	2s
36	139.68	0.56	763.94	44.96	718.96	24.38	729.98	21.92
37	206.90	0.65	791.72	44.82	742.22	24.41	754.67	21.96
38	123.82	0.62	742.62	45.58	726.23	24.47	730.25	21.89
39	116.03	0.45	728.02	50.00	735.67	26.28	733.78	23.52
47	236.36	0.62	743.95	79.44	737.16	27.33	738.85	28.89
48	225.29	0.74	770.45	44.13	729.22	24.80	739.42	22.07
49	201.99	0.52	770.70	45.71	736.13	24.83	744.74	22.26
50	210.88	0.64	808.59	43.70	734.80	24.90	753.29	22.28
53	155.01	0.60	751.49	46.47	730.26	24.63	735.50	22.15
54	205.09	0.57	759.87	44.77	740.96	25.01	745.68	22.16
55	343.56	0.77	797.12	43.44	732.45	25.02	748.58	22.28
56	268.70	0.82	735.67	43.79	733.94	24.90	734.37	21.86
57	78.25	0.48	759.05	47.72	719.19	24.26	728.94	22.17
58	154.73	0.85	727.02	44.70	732.85	24.91	731.41	21.93
60	135.61	0.46	796.19	44.69	724.04	24.59	741.90	22.19
69	246.42	0.60	743.28	43.58	738.77	25.00	739.89	21.91
70	136.78	0.61	732.84	45.87	726.80	24.73	728.28	22.04
72	134.72	0.96	755.48	46.32	731.87	24.97	737.71	22.37
74	159.37	0.73	753.83	45.52	719.94	24.66	728.23	22.11
75	54.63	0.44	784.98	50.80	727.55	24.23	741.78	22.71
77	283.44	0.61	786.05	44.82	730.49	25.52	744.30	22.73
78	197.39	0.63	743.65	45.07	734.80	24.79	736.99	21.99
79	219.32	0.76	788.11	45.75	731.98	23.88	745.96	21.77
80	190.87	0.98	760.08	80.12	745.61	26.87	749.24	28.91
87	24.15	0.31	798.11	58.66	735.09	24.78	750.85	24.32
89	161.81	0.62	812.39	46.76	722.77	23.67	745.00	21.96
91	234.80	0.64	766.74	45.99	718.96	25.33	730.67	22.71
92	168.09	0.54	782.09	45.74	734.23	25.59	746.15	22.85
95	193.06	0.66	772.72	44.71	731.70	24.56	741.87	21.99
96	135.09	0.51	788.19	44.92	730.43	24.80	744.79	22.27
98	180.30	0.66	769.44	46.65	746.13	24.54	751.99	22.14
100	161.11	0.44	772.15	47.56	732.50	25.84	742.35	23.21
108	170.23	0.48	805.42	47.60	727.67	25.73	747.01	23.38
109	167.96	0.45	793.32	45.41	745.61	25.89	757.65	23.01
114	174.08	0.59	767.20	44.22	735.78	25.01	743.60	22.17
117	226.65	0.67	805.54	77.10	728.99	27.36	748.06	29.04
118	236.60	0.64	767.85	44.20	739.52	25.11	746.59	22.21
119	215.76	0.60	766.55	43.59	727.20	24.58	736.92	21.84
120	180.77	0.53	762.12	44.51	722.08	24.49	731.91	21.91
127	96.63	0.54	773.07	47.46	726.17	24.83	737.75	22.56
128	188.34	0.68	751.30	45.99	737.85	24.42	741.19	21.91
130	182.57	0.53	736.90	46.32	736.07	25.08	736.28	22.30
131	193.92	0.63	765.25	45.58	726.46	24.24	736.02	21.87
132	68.54	0.51	774.34	48.55	749.52	25.30	755.78	22.91

Sample	U (µg g-1)	Th/U	Ages 207Pb/206Pb	2s	206Pb/238U	2s	207Pb/235U	2s
139	137.86	0.67	749.64	46.24	737.80	25.17	740.74	22.41
148	230.81	0.54	769.17	47.92	727.90	25.65	738.09	23.13
150	101.69	0.84	785.01	45.66	727.26	24.70	741.57	22.30
153	220.19	0.68	774.66	44.66	734.17	25.25	744.24	22.44
154	140.01	0.57	811.44	44.89	731.52	24.79	751.50	22.40
157	421.34	1.24	779.51	45.17	746.82	26.12	755.05	23.04
158	254.96	0.70	738.54	80.84	734.06	28.18	735.16	29.56
159	191.58	0.62	770.12	44.14	740.73	25.11	748.08	22.21
169	172.74	0.57	730.68	80.49	722.42	27.08	724.44	28.80
173	91.78	0.44	757.88	46.79	717.40	24.41	727.29	22.15
178	173.81	0.72	773.61	46.63	740.04	24.53	748.43	22.19
188	94.35	0.53	807.01	48.82	728.53	24.34	748.08	22.64
195	165.37	0.53	759.57	79.39	728.82	27.26	736.41	28.98

Serrinha Formation, garnet-biotite-plagioclase schist, sample 48

Sample	U (µg g-1)	Th/U	207Pb/206Pb	2s	206Pb/238U	2s	207Pb/235U	2s
7	73.05	0.57	774.61	78.27	707.94	25.98	724.13	28.17
9	227.57	1.07	777.02	77.43	721.86	26.65	735.44	28.44
10	40.67	0.44	790.13	53.80	737.06	24.95	750.34	23.60
11	153.37	0.48	771.92	78.77	742.91	26.35	750.18	28.49
12	61.00	0.51	772.15	48.12	725.59	24.82	737.08	22.63
13	101.58	0.30	770.51	44.01	731.56	24.12	741.22	21.58
14	49.67	0.32	775.59	79.71	707.25	26.40	723.84	28.67
15	268.69	0.37	773.06	77.99	729.90	26.41	740.59	28.37
16	69.39	0.44	780.08	78.73	775.01	27.26	776.32	29.08
17	87.40	0.33	742.95	44.25	714.44	23.46	721.36	21.10
18	123.29	0.46	757.86	44.90	726.39	24.06	734.14	21.61
19	46.79	0.46	795.73	45.34	734.94	24.31	750.14	22.01
20	45.01	0.25	809.54	46.21	733.05	23.86	752.19	21.93
27	102.85	0.26	762.97	44.34	710.59	23.48	723.31	21.26
28	54.67	0.31	754.14	45.25	728.75	24.22	735.01	21.72
30	191.63	0.56	759.99	78.64	713.00	26.58	724.44	28.45
31	96.82	0.42	745.92	44.82	715.65	23.46	723.01	21.18
32	177.11	0.57	761.07	43.26	724.56	24.01	733.54	21.39
33	73.44	0.45	808.57	46.93	731.56	24.60	750.80	22.52
35	216.25	0.66	785.97	43.10	727.37	23.99	741.89	21.49
36	30.70	0.61	790.76	48.05	770.62	25.90	775.81	23.20
37	91.53	0.68	761.99	44.37	710.53	23.59	723.03	21.34
39	101.34	0.49	774.98	44.00	722.09	24.13	735.10	21.66
40	48.71	0.60	768.82	47.42	708.92	23.13	723.46	21.49
49	113.51	0.65	776.82	47.94	740.96	25.21	749.94	22.81
51	49.55	0.48	772.31	49.08	724.44	24.04	736.24	22.26
52	125.67	0.92	763.25	43.73	724.90	24.24	734.34	21.61
53	62.96	0.47	790.45	46.78	737.87	24.07	751.03	22.01
54	198.91	0.73	768.56	43.70	742.45	24.75	748.99	21.88

Sample	U (µg g-1)	Th/U	Ages					
			207Pb/206Pb	2s	206Pb/238U	2s	207Pb/235U	2s
58	67.30	0.37	783.32	48.84	717.32	24.50	733.51	22.63
59	165.65	0.53	769.37	43.57	722.37	24.25	733.93	21.65
67	103.02	0.35	792.36	44.16	738.10	24.76	751.69	22.11
68	67.54	0.55	779.99	50.75	735.69	25.34	746.74	23.34
69	178.99	0.80	779.37	43.46	729.67	24.57	741.99	21.87
70	33.85	0.41	777.57	48.45	739.41	25.33	748.96	22.98
71	97.08	0.66	782.75	46.12	719.85	24.32	735.32	22.12
72	85.47	0.37	761.51	48.35	728.63	24.88	736.75	22.62
74	108.90	0.50	777.22	78.51	722.37	27.07	735.88	28.87
75	436.06	0.44	786.41	43.11	773.53	26.46	776.85	22.85
77	209.94	0.56	2101.17	35.91	2088.60	64.14	2094.94	37.15
78	199.99	0.60	769.53	43.60	743.88	25.20	750.31	22.17
79	169.23	0.74	787.39	43.73	754.58	25.62	762.91	22.50
80	72.14	0.40	775.04	78.99	740.33	27.72	749.01	29.31
Serrinha Formation, staurolite-garnet-biotite-plagioclase schist, sample 113								
7	95.52	0.55	787.96	77.61	760.02	25.68	767.14	28.07
9	755.38	1.00	834.10	41.37	808.13	25.78	815.08	22.25
10	157.59	0.47	799.96	76.66	757.72	25.69	768.50	28.00
11	188.80	0.64	781.71	43.36	761.97	22.97	767.01	20.67
12	81.06	0.57	822.73	76.26	812.06	26.81	814.92	28.77
13	239.80	0.58	806.87	42.51	753.18	22.64	766.85	20.52
14	124.50	0.99	774.82	77.90	731.93	24.76	742.58	27.46
15	220.02	1.03	812.49	43.04	733.95	21.68	753.63	20.09
18	18.59	0.29	846.76	54.40	768.80	23.74	789.06	23.24
19	55.43	0.32	801.93	44.53	719.00	21.95	739.46	20.48
20	51.53	0.50	784.34	46.31	732.92	21.68	745.72	20.40
27	40.25	0.47	786.63	49.11	702.51	21.75	722.89	20.98
28	113.46	0.64	791.85	44.33	758.98	23.82	767.37	21.43
29	289.82	1.14	773.43	77.61	771.38	25.64	771.90	27.94
30	65.78	0.37	784.48	55.71	761.68	23.66	767.50	23.01
31	45.62	0.31	738.26	47.71	713.92	22.44	719.82	20.89
32	141.13	0.48	802.12	77.27	761.51	25.16	771.91	27.85
34	171.64	0.55	793.99	76.60	764.95	25.87	772.40	28.04
35	18.72	0.31	811.44	54.37	735.91	22.24	754.87	22.17
37	219.70	0.53	775.01	77.53	729.45	24.77	740.74	27.40
38	172.66	0.47	825.14	75.79	774.42	26.14	787.60	28.31
39	99.01	0.48	788.83	44.26	758.01	23.43	765.86	21.15
49	114.94	0.78	766.21	78.33	729.28	25.08	738.41	27.64
50	125.86	0.68	813.54	44.52	750.77	22.98	766.73	21.08
51	53.71	0.45	798.75	45.25	764.73	23.75	773.46	21.53
53	77.18	0.49	782.01	45.11	728.07	21.69	741.44	20.24
54	193.13	0.66	738.18	43.96	737.12	22.48	737.39	20.30
55	134.20	0.71	802.73	76.88	758.41	25.58	769.73	28.01
56	407.23	0.66	750.54	42.77	711.20	21.87	720.74	19.93

Sample	U (µg g-1)	Th/U	Ages 207Pb/206Pb	2s	206Pb/238U	2s	207Pb/235U	2s
57	53.69	0.32	808.59	46.87	779.68	24.96	787.21	22.52
58	31.23	0.36	794.28	47.30	728.65	22.73	744.96	21.30
67	157.63	0.55	773.28	77.98	733.95	25.27	743.73	27.74
68	63.37	0.42	779.59	52.37	726.16	22.51	739.37	21.83
69	418.66	0.57	786.90	76.95	725.30	25.92	740.54	28.03
70	150.76	0.98	804.06	44.17	780.31	24.13	786.49	21.57
71	185.93	0.93	808.39	76.61	760.08	25.99	772.45	28.22
72	455.02	0.82	753.17	42.70	775.33	23.83	769.64	20.90
73	407.34	1.13	812.54	42.46	810.81	24.62	811.27	21.53
74	47.24	0.43	818.70	45.31	755.77	23.21	771.86	21.35
76	58.97	0.41	848.26	76.10	768.74	26.89	789.41	28.98
77	59.16	0.49	804.15	45.73	739.31	22.23	755.61	20.76
79	169.20	0.83	780.15	78.00	729.40	24.88	741.98	27.59
88	98.23	0.48	795.16	48.66	737.58	23.00	752.01	21.64
90	123.48	0.62	768.37	78.22	747.55	25.63	752.78	27.96
91	61.43	0.44	763.94	79.55	737.41	25.36	744.02	28.01
93	88.33	0.91	790.76	44.20	727.95	22.62	743.54	20.77
94	62.22	0.81	763.19	48.50	707.49	21.96	720.98	20.86
96	73.46	0.45	800.74	77.70	725.47	25.10	744.15	27.83
97	106.99	0.65	791.18	43.40	741.50	23.18	753.98	20.96
98	60.38	0.43	804.67	44.75	754.50	23.81	767.28	21.58
99	40.50	0.48	768.93	80.81	705.47	24.56	720.83	27.77
107	154.75	0.62	772.07	78.04	746.74	26.04	753.11	28.19
108	45.40	0.58	791.08	47.40	726.05	22.16	742.16	20.94
109	27.52	0.30	821.14	79.30	747.03	25.84	765.84	28.75
110	134.36	0.64	755.21	43.96	731.99	23.11	737.74	20.83
111	83.86	0.49	797.78	44.69	724.32	22.67	742.51	20.93
112	53.57	0.45	813.15	53.43	731.93	24.01	752.25	23.13
113	186.29	0.75	828.07	43.39	747.83	23.52	768.25	21.37
114	58.05	0.73	792.36	44.80	723.28	22.86	740.35	21.04
116	65.24	0.46	791.11	46.70	727.90	22.70	743.58	21.17
117	134.18	0.51	773.04	43.41	748.70	23.47	754.83	21.01
118	25.91	0.53	814.71	63.96	729.92	24.01	751.10	24.87
119	241.82	0.22	788.78	43.08	755.08	23.83	763.64	21.26
120	59.06	0.50	818.79	45.42	745.36	23.91	763.97	21.87
127	256.15	0.71	770.69	42.20	748.35	23.70	753.97	20.99
128	49.92	0.43	787.95	78.34	723.34	25.93	739.30	28.29
129	86.18	0.46	833.79	43.47	770.92	24.45	787.25	21.90
131	253.43	0.88	813.34	42.35	738.62	23.85	757.42	21.41
132	306.99	0.43	804.39	76.09	722.06	25.94	742.44	28.03
133	177.55	0.63	824.13	42.49	772.87	24.67	786.18	21.84
134	37.04	0.44	793.52	79.18	762.89	27.43	770.73	29.37
136	62.07	0.47	775.04	63.62	728.01	23.79	739.65	24.39
137	91.94	0.65	824.38	76.54	758.01	26.62	775.03	28.70

Sample	U (µg g-1)	Th/U	Ages 207Pb/206Pb	2s	206Pb/238U	2s	207Pb/235U	2s
139	86.64	0.46	792.92	77.36	759.33	26.93	767.90	28.74
140	76.69	0.76	754.61	47.40	738.51	23.94	742.51	21.81
147	117.77	0.59	769.46	43.70	744.61	23.84	750.84	21.29
150	152.28	0.52	792.90	43.52	759.10	24.00	767.72	21.44
151	158.98	1.54	809.07	76.57	817.87	27.82	815.51	29.25
152	105.70	0.44	802.88	44.50	764.32	23.52	774.22	21.30
154	99.50	0.63	767.98	78.24	731.36	26.31	740.43	28.32
155	424.19	1.21	807.70	41.45	720.16	23.93	741.80	21.43
156	39.36	0.49	802.25	47.06	760.48	24.80	771.17	22.50
157	38.35	0.53	847.29	77.24	768.68	27.62	789.11	29.59
158	150.72	0.65	762.99	43.05	765.64	24.67	764.97	21.60
160	93.24	0.75	772.97	78.35	734.70	26.09	744.22	28.26
167	151.57	0.40	861.62	74.39	800.72	28.42	817.01	29.61
168	162.81	0.85	787.08	43.03	784.43	25.06	785.12	21.88
169	51.17	0.63	785.30	45.00	746.28	24.40	756.11	21.92
170	177.34	0.72	749.79	44.65	752.66	24.33	751.94	21.58
171	97.44	0.39	801.55	76.94	783.12	28.08	787.92	29.38
172	171.09	0.79	820.87	76.00	775.85	27.59	787.56	29.11
173	65.30	0.82	779.58	49.01	759.90	24.96	764.91	22.75
174	123.73	0.65	794.26	43.57	757.20	24.48	766.64	21.77
175	109.73	0.76	791.36	43.60	740.18	23.96	753.02	21.51
176	80.82	0.60	786.63	44.33	759.10	24.58	766.11	21.89
177	152.35	1.05	794.64	45.18	756.69	24.61	766.35	22.09
178	104.02	0.49	804.47	43.82	763.23	24.45	773.81	21.82
187	204.08	0.37	701.21	80.88	725.36	25.72	719.48	27.86
188	302.72	0.56	787.91	42.37	762.26	25.14	768.81	21.98
189	309.14	0.96	755.02	42.73	771.61	25.11	767.36	21.77
190	60.89	0.48	796.51	44.68	756.80	24.93	766.92	22.24
191	63.67	0.48	802.43	46.47	786.38	25.35	790.57	22.64
192	81.19	0.69	813.93	77.05	755.82	26.73	770.67	28.76
193	73.19	0.49	824.36	76.90	775.90	27.59	788.52	29.31
194	36.91	0.46	788.25	78.69	766.56	27.83	772.12	29.45
195	435.61	0.79	761.14	42.46	748.01	24.39	751.30	21.43
196	74.79	0.83	788.14	78.33	705.70	26.52	725.73	28.61
197	73.91	0.64	781.95	45.31	759.85	24.47	765.48	21.92
198	111.49	0.75	753.81	44.60	728.24	24.70	734.54	21.98
199	258.74	0.33	727.00	43.02	717.96	23.60	720.16	20.94

#Parte 2

Sample	Isotopic ratios 207Pb/206Pb	2s	207Pb/235U	2s (%)	206Pb/238U	2s (%)	Rho	% conc d
Vila Nova Suite, metatonalite, sample 114								
7	0.06353	2.04702	1.03988	3.54484	0.11872	2.89406	0.82	99.93
8	0.06345	2.15237	1.03941	3.62173	0.11882	2.91278	0.80	100.05
9	0.06402	2.12865	1.04538	3.60951	0.11843	2.91503	0.81	99.33
10	0.06371	3.74421	1.03702	5.02514	0.11806	3.35155	0.67	99.61
11	0.06412	2.06631	1.04351	3.59862	0.11803	2.94626	0.82	99.14
12	0.06430	2.12677	1.01481	3.64381	0.11446	2.95875	0.81	98.24
13	0.06425	2.02335	1.04319	3.53651	0.11776	2.90052	0.82	98.95
14	0.06418	3.75124	1.05366	5.00174	0.11908	3.30841	0.66	99.28
15	0.06430	2.05288	1.04356	3.56836	0.11771	2.91872	0.82	98.88
16	0.06367	2.10460	1.01027	3.59609	0.11508	2.91591	0.81	99.07
17	0.06374	3.77670	1.01337	5.06301	0.11530	3.37204	0.67	99.03
18	0.06397	2.11117	1.04796	3.65628	0.11882	2.98519	0.82	99.46
19	0.06455	2.05792	1.04675	3.57554	0.11761	2.92395	0.82	98.59
27	0.06370	3.74471	1.04776	5.05075	0.11930	3.38929	0.67	99.86
28	0.06404	3.74189	1.04914	4.98993	0.11882	3.30116	0.66	99.38
30	0.06344	2.17229	1.04225	3.63876	0.11915	2.91921	0.80	100.11
31	0.06460	2.07430	1.04878	3.63544	0.11775	2.98558	0.82	98.56
32	0.06477	3.69966	1.05103	5.01889	0.11769	3.39142	0.68	98.36
33	0.06535	2.10806	1.05166	3.61145	0.11672	2.93234	0.81	97.56
36	0.06499	2.15197	1.04238	3.66511	0.11632	2.96682	0.81	97.86
37	0.06505	2.09362	1.05201	3.64242	0.11730	2.98060	0.82	97.99
38	0.06506	2.12112	1.16232	3.56657	0.12957	2.86727	0.80	100.34
39	0.06410	2.14693	1.01599	3.57262	0.11495	2.85557	0.80	98.56
40	0.06494	3.72462	1.06120	5.09058	0.11853	3.47005	0.68	98.35
48	0.06431	2.08373	1.04963	3.60049	0.11837	2.93626	0.82	98.99
49	0.06462	3.70841	1.08174	5.05199	0.12141	3.43078	0.68	99.25
50	0.06444	2.07945	1.07866	3.64563	0.12140	2.99441	0.82	99.45
51	0.06394	2.07309	1.05411	3.64004	0.11957	2.99202	0.82	99.64
52	0.06466	3.74071	1.05076	5.07546	0.11787	3.43036	0.68	98.52
53	0.06327	2.36398	1.03881	3.81469	0.11909	2.99391	0.78	100.30
56	0.06420	3.75011	1.04752	5.09286	0.11835	3.44585	0.68	99.12
59	0.06478	3.71624	1.08097	5.06523	0.12102	3.44182	0.68	99.00
60	0.06395	2.09906	1.04942	3.61036	0.11903	2.93746	0.81	99.53
68	0.06365	2.10662	1.03635	3.68849	0.11810	3.02773	0.82	99.68
70	0.06465	2.09924	1.05681	3.66512	0.11856	3.00438	0.82	98.66
73	0.06364	2.16692	1.04928	3.76182	0.11957	3.07502	0.82	99.97
74	0.06353	2.04628	1.04427	3.67229	0.11922	3.04934	0.83	100.03
77	0.06379	3.75682	1.05296	5.12037	0.11972	3.47915	0.68	99.84
78	0.06415	2.09487	1.04338	3.69927	0.11797	3.04895	0.82	99.10
80	0.06419	3.76815	1.03966	5.17407	0.11748	3.54570	0.69	98.96
88	0.06496	3.74055	1.05723	5.12215	0.11804	3.49924	0.68	98.23
89	0.06544	2.10880	1.16100	3.75310	0.12867	3.10463	0.83	99.76

Sample	Isotopic ratios 207Pb/206Pb	2s	207Pb/235U	2s (%)	206Pb/238U	2s (%)	Rho	% conc d
90	0.06555	2.10641	1.04947	3.73106	0.11611	3.07958	0.83	97.22
92	0.06449	2.18583	1.05059	3.78189	0.11816	3.08623	0.82	98.76
93	0.06455	2.39564	1.04497	3.96461	0.11741	3.15897	0.80	98.55
94	0.06459	2.10559	1.04960	3.73464	0.11786	3.08448	0.83	98.59
95	0.06388	2.09768	1.04659	3.75112	0.11883	3.10977	0.83	99.56
96	0.06432	2.16690	1.04869	3.79765	0.11825	3.11877	0.82	98.96
100	0.06500	2.15385	1.04919	3.80721	0.11707	3.13940	0.82	98.00
Sanga do Jobim suite, monzogranite, sample 115								
7	0.06317	2.02636	1.08020	4.20906	0.12172	3.46075	0.82	99.84
12	0.06417	2.06066	1.07392	4.32852	0.12180	3.44016	0.79	100.31
18	0.06272	2.23214	0.99969	3.93683	0.11477	3.37527	0.86	99.80
19	0.06332	2.06245	1.00768	4.00685	0.11390	3.43636	0.86	98.52
27	0.06333	2.20064	0.99243	4.02949	0.11367	3.46166	0.86	99.42
28	0.06437	2.39570	0.99808	4.17062	0.11430	3.54278	0.85	99.54
29	0.06374	2.29056	0.99874	4.15021	0.11364	3.46087	0.83	98.94
30	0.06290	2.28935	0.98361	4.08290	0.11342	3.38067	0.83	99.85
31	0.06337	2.05173	0.99715	4.12746	0.11248	3.44961	0.84	98.09
36	0.06430	2.26629	0.99390	4.01982	0.11207	3.45649	0.86	97.99
39	0.06432	2.05224	0.98320	3.98956	0.11360	3.40988	0.85	100.04
47	0.06293	2.22818	0.99557	4.08562	0.11458	3.50724	0.86	99.95
48	0.06277	2.07105	1.00780	4.02318	0.11558	3.41997	0.85	99.89
49	0.06395	2.62705	0.98395	4.00864	0.11342	3.41561	0.85	99.82
50	0.06297	3.85884	0.99607	4.36180	0.11253	3.51278	0.81	98.21
53	0.06302	2.09562	0.98752	4.01120	0.11405	3.39659	0.85	100.09
54	0.06324	2.11891	0.98130	4.72155	0.11295	3.55206	0.75	99.63
55	0.06292	2.09829	1.01094	4.17713	0.11412	3.46380	0.83	98.47
59	0.06215	2.44570	0.99103	4.16938	0.11177	3.53669	0.85	97.94
60	0.06420	2.58567	0.97849	3.99947	0.11342	3.43382	0.86	100.23
70	0.06280	2.13376	1.00997	3.99778	0.11327	3.43745	0.86	97.84
71	0.06301	3.11062	0.99419	4.05606	0.11445	3.45363	0.85	99.94
72	0.06154	9.19727	1.00912	5.44346	0.11342	3.89661	0.72	98.03
73	0.06195	2.99874	0.98679	4.06530	0.11358	3.45425	0.85	99.76
74	0.06425	2.33463	0.98077	5.43515	0.11333	3.86850	0.71	99.98
75	0.06431	2.20805	0.99493	4.18994	0.11152	3.58198	0.85	97.46
76	0.06260	3.93662	1.01309	4.16282	0.11500	3.55787	0.85	99.04
77	0.06189	3.88953	0.95268	4.18013	0.11016	3.53427	0.85	99.41
78	0.06257	2.05052	0.95080	4.08843	0.10957	3.42789	0.84	99.04
88	0.06467	2.04113	0.95664	5.56578	0.11018	4.01088	0.72	99.13
89	0.06300	2.12698	0.94267	4.18469	0.11001	3.39562	0.81	100.04
90	0.06453	3.80101	0.93804	4.62184	0.10982	3.51696	0.76	100.24
91	0.06262	2.78083	0.94861	5.53660	0.10990	3.89319	0.70	99.49
92	0.06274	2.55021	0.94244	4.45219	0.10916	3.47691	0.78	99.32
93	0.06301	2.14355	0.95247	4.28735	0.11010	3.44642	0.80	99.37

Sample	Isotopic ratios 207Pb/206Pb	2s	207Pb/235U	2s (%)	206Pb/238U	2s (%)	Rho	% conc d
94	0.06279	2.29336	0.94837	4.34285	0.11002	3.48513	0.80	99.61
95	0.06277	3.81779	0.94122	7.12967	0.10829	3.70506	0.52	98.66
96	0.06252	2.59117	0.92062	4.04765	0.10536	3.48910	0.86	97.70
97	0.06226	2.95535	0.91480	9.99181	0.10781	3.90467	0.39	100.32
111	0.06471	2.17371	0.90995	5.60016	0.10663	4.02907	0.72	99.66
118	0.06304	6.09137	0.91294	4.15716	0.10545	3.46734	0.83	98.38
119	0.06178	2.78407	0.91600	4.58133	0.10671	3.50065	0.76	99.25
120	0.06389	2.16117	0.90768	4.47657	0.10656	3.50552	0.78	99.78
Serrinha Formation, para-amphibolite, sample 29								
7	0.06386	3.73525	0.98305	5.36586	0.11164	3.85232	0.72	98.11
8	0.06371	2.22156	0.97763	4.09349	0.11128	3.43821	0.84	98.21
9	0.05869	2.11280	0.69442	4.00981	0.08581	3.40803	0.85	99.09
10	0.06037	3.88066	0.85235	5.49608	0.10240	3.89197	0.71	100.37
11	0.06413	2.24544	0.98161	4.12849	0.11101	3.46445	0.84	97.69
12	0.06266	2.05032	0.95221	3.95474	0.11022	3.38174	0.86	99.20
13	0.06220	2.18650	0.92690	4.05100	0.10808	3.41025	0.84	99.30
14	0.06350	2.20448	1.00268	4.06707	0.11452	3.41779	0.84	99.08
15	0.06263	3.82645	0.92597	5.44871	0.10724	3.87902	0.71	98.64
16	0.15469	1.99109	9.51225	3.92077	0.44599	3.37757	0.86	99.45
17	0.06254	3.77985	0.98132	5.37818	0.11381	3.82590	0.71	100.04
18	0.06237	2.02031	0.97790	3.93984	0.11371	3.38241	0.86	100.21
19	0.06239	3.78874	0.97652	5.38026	0.11352	3.82003	0.71	100.16
20	0.06355	3.75325	1.00212	5.33531	0.11436	3.79192	0.71	98.99
27	0.05934	2.09421	0.69138	4.05492	0.08450	3.47227	0.86	97.97
28	0.15331	1.99601	9.47363	3.94376	0.44817	3.40135	0.86	100.02
29	0.06277	2.03919	1.00326	3.98305	0.11592	3.42146	0.86	100.19
30	0.06448	2.14817	0.99989	4.07509	0.11248	3.46291	0.85	97.60
31	0.06544	2.32274	1.07386	4.17327	0.11902	3.46714	0.83	97.84
32	0.06460	2.25128	1.07571	4.12328	0.12077	3.45445	0.84	99.08
33	0.06235	2.05293	0.94730	4.00235	0.11019	3.43574	0.86	99.55
34	0.06311	2.15497	0.95118	4.04806	0.10931	3.42679	0.85	98.50
37	0.17822	2.34022	12.21628	4.20413	0.49714	3.49258	0.83	99.18
39	0.06517	2.19374	1.07704	4.11728	0.11987	3.48418	0.85	98.29
40	0.06437	2.14560	1.03537	4.05478	0.11665	3.44058	0.85	98.53
47	0.06130	2.13138	0.90646	4.06167	0.10725	3.45751	0.85	100.21
48	0.06363	2.01845	1.00553	3.97689	0.11462	3.42660	0.86	98.96
49	0.06333	3.74943	0.99946	5.38586	0.11446	3.86643	0.72	99.26
50	0.06330	2.20721	1.00612	4.11167	0.11528	3.46902	0.84	99.46
51	0.06484	3.71280	1.07997	5.34283	0.12080	3.84200	0.72	98.83
52	0.06349	2.22418	0.94707	4.14572	0.10819	3.49857	0.84	97.84
53	0.06372	2.10295	1.06693	4.05230	0.12144	3.46392	0.85	100.18
54	0.06366	2.24524	0.97686	4.16578	0.11128	3.50894	0.84	98.26
55	0.06286	2.13183	0.99008	4.13900	0.11424	3.54777	0.86	99.76

Sample	Isotopic ratios 207Pb/206Pb	2s	207Pb/235U	2s (%)	206Pb/238U	2s (%)	Rho	% conc d
56	0.06616	2.05304	1.08060	4.06218	0.11846	3.50519	0.86	96.98
57	0.06256	3.79534	0.96620	5.44435	0.11200	3.90337	0.72	99.66
59	0.06313	2.02756	0.98382	4.00679	0.11303	3.45591	0.86	99.21
60	0.06318	2.15263	0.92717	4.09342	0.10644	3.48170	0.85	97.85
67	0.06423	3.76542	1.07852	5.37863	0.12178	3.84073	0.71	99.68
68	0.06448	3.71622	1.00455	5.42223	0.11299	3.94846	0.73	97.69
69	0.06384	3.80621	1.03615	5.42531	0.11771	3.86610	0.71	99.33
70	0.06313	2.05943	0.97636	4.04558	0.11218	3.48216	0.86	99.04
71	0.06042	2.11360	0.77410	4.10650	0.09293	3.52080	0.86	98.37
72	0.06436	2.08204	1.07223	4.07074	0.12083	3.49801	0.86	99.36
75	0.06125	2.18893	0.90433	4.17424	0.10709	3.55428	0.85	100.24
76	0.06381	2.08428	0.97915	4.11554	0.11129	3.54872	0.86	98.10
79	0.10887	2.05750	4.76758	4.02770	0.31761	3.46252	0.86	99.87
80	0.06411	2.15255	1.08365	4.17596	0.12259	3.57843	0.86	99.97
87	0.06369	2.11129	0.98382	4.10808	0.11202	3.52403	0.86	98.37
88	0.06271	2.11252	0.97504	4.11900	0.11278	3.53601	0.86	99.65
89	0.06433	3.72510	1.04018	5.42369	0.11727	3.94209	0.73	98.70
90	0.08872	3.09387	2.85579	4.82012	0.23345	3.69615	0.77	98.65
91	0.06507	2.12079	1.11946	4.13346	0.12477	3.54792	0.86	99.34
92	0.06365	2.10526	0.98323	4.11883	0.11203	3.54014	0.86	98.43
93	0.06302	2.12631	0.98576	4.13726	0.11345	3.54904	0.86	99.42
94	0.06474	3.73586	1.07248	5.40639	0.12015	3.90799	0.72	98.81
95	0.06409	2.09281	1.00243	4.12074	0.11344	3.54974	0.86	98.21
96	0.08144	2.06287	2.32252	4.10119	0.20683	3.54462	0.86	99.35
97	0.05928	2.12170	0.77374	4.12768	0.09467	3.54064	0.86	100.17
99	0.06116	2.13368	0.85146	4.18460	0.10097	3.59976	0.86	99.11
100	0.06321	2.13963	0.99811	4.15335	0.11453	3.55981	0.86	99.42

Serrinha Formation, garnet-biotite-plagioclase schist, sample 30B

Sample	Isotopic ratios 207Pb/206Pb	2s	207Pb/235U	2s (%)	206Pb/238U	2s (%)	Rho	% conc d
7	0.06469	2.37516	1.06040	4.51125	0.11889	3.83536	0.85	98.65
8	0.06519	3.71027	1.05685	5.42490	0.11759	3.95770	0.73	97.86
12	0.06352	2.48741	1.03868	4.49601	0.11860	3.74526	0.83	99.88
15	0.06411	2.09016	1.07079	4.14905	0.12114	3.58411	0.86	99.72
16	0.06373	2.09074	1.04751	4.14431	0.11921	3.57828	0.86	99.76
17	0.06623	2.08468	1.09490	4.14938	0.11991	3.58768	0.86	97.21
19	0.06480	2.14330	1.05079	4.17780	0.11761	3.58613	0.86	98.28
20	0.06644	2.09760	1.11033	4.15861	0.12121	3.59083	0.86	97.24
28	0.06478	2.13938	1.05891	4.06909	0.11856	3.46129	0.85	98.49
29	0.06486	2.10063	1.07505	4.10714	0.12021	3.52930	0.86	98.71
31	0.06440	2.13544	1.07502	4.18165	0.12107	3.59528	0.86	99.38
32	0.06397	3.74616	1.07927	5.43406	0.12237	3.93641	0.72	100.11
33	0.06503	3.70179	1.07115	5.41809	0.11946	3.95631	0.73	98.39
34	0.06584	2.06561	1.09215	4.12936	0.12031	3.57559	0.87	97.69
35	0.06467	2.10298	1.09174	4.24990	0.12244	3.69311	0.87	99.35

Sample	Isotopic ratios 207Pb/206Pb	2s	207Pb/235U	2s (%)	206Pb/238U	2s (%)	Rho	% conc d
36	0.06468	2.13358	1.05221	4.16592	0.11799	3.57809	0.86	98.48
37	0.06554	2.13610	1.10272	4.07987	0.12203	3.47598	0.85	98.34
38	0.06403	2.15524	1.05276	4.15904	0.11925	3.55705	0.86	99.44
39	0.06359	2.35886	1.05991	4.45019	0.12089	3.77358	0.85	100.25
47	0.06407	3.75745	1.07022	5.42716	0.12115	3.91607	0.72	99.76
48	0.06488	2.09618	1.07139	4.15865	0.11977	3.59171	0.86	98.61
49	0.06489	2.17130	1.08226	4.17317	0.12097	3.56381	0.85	98.83
50	0.06607	2.08869	1.09988	4.14426	0.12074	3.57942	0.86	97.54
53	0.06430	2.20069	1.06340	4.18744	0.11995	3.56253	0.85	99.28
54	0.06456	2.12312	1.08419	4.15115	0.12181	3.56712	0.86	99.36
55	0.06571	2.07203	1.09016	4.16120	0.12033	3.60864	0.87	97.84
56	0.06382	2.06832	1.06111	4.13788	0.12059	3.58387	0.87	99.93
57	0.06453	2.26251	1.05012	4.21806	0.11803	3.55993	0.84	98.65
58	0.06356	2.10824	1.05512	4.16286	0.12040	3.58953	0.86	100.19
60	0.06568	2.13155	1.07645	4.17104	0.11887	3.58526	0.86	97.58
69	0.06405	2.06089	1.07235	4.12696	0.12143	3.57555	0.87	99.84
70	0.06373	2.16562	1.04879	4.19520	0.11935	3.59302	0.86	99.79
72	0.06442	2.19470	1.06790	4.21941	0.12023	3.60370	0.85	99.20
74	0.06437	2.15639	1.04868	4.20885	0.11816	3.61447	0.86	98.85
75	0.06533	2.41849	1.07621	4.26806	0.11948	3.51670	0.82	98.07
77	0.06536	2.13423	1.08136	4.26197	0.11999	3.68910	0.87	98.14
78	0.06406	2.13141	1.06644	4.15294	0.12074	3.56427	0.86	99.69
79	0.06543	2.17950	1.08476	4.07737	0.12025	3.44597	0.85	98.12
80	0.06456	3.79921	1.09151	5.38055	0.12262	3.81002	0.71	99.51
87	0.06574	2.79890	1.09484	4.52960	0.12079	3.56137	0.79	97.89
89	0.06619	2.23599	1.08280	4.11710	0.11865	3.45700	0.84	97.01
91	0.06477	2.18317	1.05360	4.31119	0.11799	3.71755	0.86	98.39
92	0.06524	2.17658	1.08517	4.27713	0.12064	3.68190	0.86	98.39
95	0.06495	2.12471	1.07640	4.13346	0.12020	3.54557	0.86	98.62
96	0.06543	2.13969	1.08237	4.17535	0.11998	3.58542	0.86	98.06
98	0.06485	2.21547	1.09718	4.12333	0.12271	3.47758	0.84	99.21
100	0.06493	2.25971	1.07736	4.35795	0.12034	3.72631	0.86	98.66
108	0.06597	2.27376	1.08693	4.37162	0.11950	3.73378	0.85	97.40
109	0.06559	2.16496	1.10890	4.26216	0.12262	3.67137	0.86	98.40
114	0.06478	2.09941	1.07993	4.15961	0.12091	3.59093	0.86	98.94
117	0.06597	3.68313	1.08909	5.40991	0.11973	3.96254	0.73	97.44
118	0.06480	2.09877	1.08607	4.15691	0.12156	3.58818	0.86	99.04
119	0.06476	2.06918	1.06628	4.12521	0.11942	3.56874	0.87	98.67
120	0.06462	2.11150	1.05611	4.15621	0.11853	3.57989	0.86	98.65
127	0.06496	2.25518	1.06798	4.25576	0.11924	3.60911	0.85	98.42
128	0.06429	2.17774	1.07501	4.12034	0.12127	3.49781	0.85	99.54
130	0.06386	2.18846	1.06498	4.21239	0.12096	3.59928	0.85	99.96
131	0.06472	2.16316	1.06446	4.13351	0.11929	3.52231	0.85	98.69

Sample	Isotopic ratios 207Pb/206Pb	2s	207Pb/235U	2s (%)	206Pb/238U	2s (%)	Rho	% conc d
132	0.06500	2.30769	1.10502	4.25091	0.12330	3.56998	0.84	99.16
139	0.06424	2.18893	1.07408	4.21664	0.12126	3.60397	0.85	99.59
148	0.06484	2.27571	1.06868	4.36096	0.11954	3.72010	0.85	98.61
150	0.06533	2.17396	1.07577	4.19288	0.11943	3.58527	0.86	98.06
153	0.06501	2.12275	1.08125	4.20722	0.12063	3.63244	0.86	98.64
154	0.06616	2.14631	1.09618	4.17388	0.12017	3.57975	0.86	97.33
157	0.06516	2.14856	1.10352	4.27657	0.12283	3.69767	0.86	98.90
158	0.06391	3.82013	1.06272	5.57055	0.12061	4.05433	0.73	99.84
159	0.06487	2.09650	1.08912	4.15042	0.12177	3.58199	0.86	99.01
169	0.06367	3.79864	1.04105	5.48363	0.11859	3.95481	0.72	99.71
173	0.06449	2.21806	1.04678	4.21936	0.11772	3.58932	0.85	98.63
178	0.06498	2.21618	1.08985	4.14542	0.12165	3.50329	0.85	98.87
188	0.06602	2.33263	1.08912	4.22977	0.11965	3.52843	0.83	97.38
195	0.06455	3.76459	1.06525	5.45544	0.11970	3.94838	0.72	98.96
Serrinha Formation, garnet-biotite-plagioclase schist, sample 48								
7	0.06501	3.72043	1.04043	5.35827	0.11608	3.85609	0.72	97.83
9	0.06508	3.68196	1.06327	5.35141	0.11849	3.88339	0.73	98.23
10	0.06549	2.56365	1.09378	4.39114	0.12113	3.56508	0.81	98.30
11	0.06493	3.74259	1.09345	5.28935	0.12215	3.73768	0.71	99.10
12	0.06493	2.28616	1.06662	4.26399	0.11914	3.59931	0.84	98.51
13	0.06488	2.09038	1.07506	4.05253	0.12017	3.47179	0.86	98.77
14	0.06504	3.78923	1.03984	5.45330	0.11596	3.92177	0.72	97.78
15	0.06496	3.70595	1.07377	5.31383	0.11988	3.80823	0.72	98.63
16	0.06518	3.74561	1.14805	5.27535	0.12775	3.71479	0.70	99.91
17	0.06404	2.09244	1.03488	4.03774	0.11720	3.45326	0.86	99.11
18	0.06449	2.12856	1.06065	4.08425	0.11928	3.48573	0.85	99.02
19	0.06567	2.16258	1.09337	4.10026	0.12076	3.48359	0.85	98.05
20	0.06610	2.20877	1.09760	4.07702	0.12043	3.42687	0.84	97.53
27	0.06465	2.10363	1.03878	4.06047	0.11653	3.47305	0.86	98.31
28	0.06438	2.14352	1.06241	4.10274	0.11968	3.49825	0.85	99.22
30	0.06456	3.72901	1.04104	5.40964	0.11695	3.91901	0.72	98.49
31	0.06413	2.12069	1.03818	4.04720	0.11741	3.44710	0.85	99.05
32	0.06459	2.05168	1.05942	4.04626	0.11896	3.48752	0.86	98.85
33	0.06607	2.24268	1.09473	4.19076	0.12017	3.54018	0.84	97.51
35	0.06536	2.05217	1.07643	4.03333	0.11945	3.47223	0.86	98.12
36	0.06551	2.28973	1.14696	4.22306	0.12698	3.54844	0.84	99.41
37	0.06462	2.10461	1.03821	4.07587	0.11652	3.49046	0.86	98.34
39	0.06502	2.09166	1.06260	4.09075	0.11853	3.51556	0.86	98.30
40	0.06483	2.25204	1.03909	4.10344	0.11625	3.43024	0.84	98.06
49	0.06508	2.27952	1.09295	4.24817	0.12181	3.58479	0.84	98.88
51	0.06494	2.33190	1.06491	4.19910	0.11894	3.49209	0.83	98.47
52	0.06466	2.07492	1.06105	4.08459	0.11902	3.51831	0.86	98.79
53	0.06550	2.22944	1.09521	4.09605	0.12127	3.43617	0.84	98.32

Sample	Isotopic ratios 207Pb/206Pb	2s	207Pb/235U	2s (%)	206Pb/238U	2s (%)	Rho	% concd
54	0.06482	2.07515	1.09099	4.08008	0.12207	3.51295	0.86	99.20
58	0.06528	2.32490	1.05937	4.27845	0.11770	3.59166	0.84	97.86
59	0.06485	2.06931	1.06022	4.09302	0.11858	3.53140	0.86	98.50
67	0.06556	2.10494	1.09657	4.11301	0.12131	3.53357	0.86	98.27
68	0.06518	2.41442	1.08637	4.35754	0.12089	3.62750	0.83	98.59
69	0.06516	2.06713	1.07664	4.10392	0.11984	3.54530	0.86	98.41
70	0.06510	2.30415	1.09093	4.28176	0.12154	3.60892	0.84	98.80
71	0.06526	2.19517	1.06304	4.17666	0.11814	3.55326	0.85	97.97
72	0.06461	2.29314	1.06595	4.26295	0.11966	3.59363	0.84	98.97
74	0.06509	3.73318	1.06418	5.42858	0.11858	3.94117	0.73	98.24
75	0.06537	2.05317	1.14918	4.15562	0.12749	3.61299	0.87	99.65
77	0.13024	2.04530	6.87114	4.11385	0.38264	3.56939	0.87	99.83
78	0.06485	2.07064	1.09372	4.12738	0.12232	3.57039	0.87	99.22
79	0.06540	2.08265	1.11986	4.14245	0.12418	3.58084	0.86	98.98
80	0.06502	3.75461	1.09105	5.44550	0.12170	3.94415	0.72	98.91

Serrinha Formation, staurolite-garnet-biotite-plagioclase schist, sample 113

Sample	Isotopic ratios 207Pb/206Pb	2s	207Pb/235U	2s (%)	206Pb/238U	2s (%)	Rho	% concd
7	0.06542	3.69688	1.12872	5.14759	0.12513	3.58201	0.70	99.02
9	0.06688	1.98533	1.23163	3.93166	0.13356	3.39359	0.86	99.09
10	0.06580	3.65878	1.13156	5.12836	0.12473	3.59352	0.70	98.54
11	0.06523	2.06356	1.12844	3.80494	0.12547	3.19676	0.84	99.29
12	0.06652	3.65297	1.23128	5.06831	0.13425	3.51334	0.69	99.59
13	0.06602	2.03089	1.12810	3.77854	0.12394	3.18635	0.84	98.16
14	0.06501	3.70285	1.07785	5.15005	0.12024	3.57938	0.70	98.51
15	0.06619	2.05823	1.10058	3.74252	0.12059	3.12572	0.84	97.34
18	0.06729	2.61554	1.17517	4.19192	0.12666	3.27583	0.78	97.38
19	0.06586	2.12572	1.07147	3.86483	0.11799	3.22772	0.84	97.18
20	0.06531	2.20487	1.08427	3.82836	0.12041	3.12968	0.82	98.23
27	0.06538	2.33876	1.03793	4.01945	0.11514	3.26897	0.81	97.13
28	0.06554	2.11289	1.12919	3.94154	0.12495	3.32737	0.84	98.85
29	0.06497	3.68826	1.13872	5.10260	0.12711	3.52609	0.69	99.88
30	0.06531	2.65239	1.12947	4.22861	0.12542	3.29332	0.78	99.19
31	0.06390	2.25432	1.03178	4.01356	0.11711	3.32065	0.83	99.13
32	0.06587	3.68915	1.13874	5.08749	0.12539	3.50325	0.69	98.60
34	0.06561	3.65233	1.13977	5.11848	0.12599	3.58599	0.70	98.98
35	0.06616	2.59976	1.10314	4.12223	0.12093	3.19907	0.78	97.44
37	0.06502	3.68548	1.07408	5.14656	0.11981	3.59226	0.70	98.42
38	0.06660	3.63179	1.17205	5.10091	0.12764	3.58181	0.70	98.27
39	0.06545	2.10849	1.12603	3.89681	0.12478	3.27711	0.84	98.92
49	0.06475	3.71803	1.06933	5.20157	0.11978	3.63766	0.70	98.71
50	0.06623	2.12927	1.12786	3.88004	0.12352	3.24360	0.84	97.86
51	0.06576	2.15937	1.14200	3.93898	0.12595	3.29434	0.84	98.82
53	0.06524	2.14676	1.07550	3.81352	0.11957	3.15187	0.83	98.15
54	0.06390	2.07714	1.06724	3.83908	0.12114	3.22863	0.84	99.91

Sample	Isotopic ratios 207Pb/206Pb	2s	207Pb/235U	2s (%)	206Pb/238U	2s (%)	Rho	% concd
55	0.06589	3.67093	1.13415	5.12458	0.12485	3.57571	0.70	98.48
56	0.06427	2.02490	1.03362	3.82783	0.11664	3.24840	0.85	98.63
57	0.06607	2.24005	1.17121	4.07060	0.12857	3.39882	0.83	98.99
58	0.06562	2.25541	1.08271	3.99697	0.11967	3.29983	0.83	97.76
67	0.06497	3.70555	1.08020	5.19620	0.12059	3.64272	0.70	98.63
68	0.06516	2.49139	1.07129	4.11756	0.11924	3.27831	0.80	98.16
69	0.06539	3.66469	1.07367	5.26400	0.11909	3.77885	0.72	97.89
70	0.06593	2.10954	1.16968	3.90327	0.12868	3.28411	0.84	99.16
71	0.06606	3.66101	1.13987	5.15189	0.12514	3.62476	0.70	98.34
72	0.06435	2.02240	1.13397	3.83856	0.12781	3.26258	0.85	100.68
73	0.06619	2.03072	1.22327	3.81649	0.13403	3.23137	0.85	99.89
74	0.06639	2.16900	1.13862	3.91162	0.12439	3.25518	0.83	97.86
76	0.06734	3.65982	1.17592	5.21120	0.12665	3.70976	0.71	97.33
77	0.06593	2.18413	1.10468	3.86072	0.12152	3.18351	0.82	97.79
79	0.06518	3.71064	1.07662	5.17513	0.11980	3.60737	0.70	98.25
88	0.06565	2.32047	1.09723	4.03493	0.12122	3.30092	0.82	98.03
90	0.06482	3.71421	1.09882	5.19404	0.12295	3.63079	0.70	99.25
91	0.06468	3.77445	1.08078	5.24323	0.12119	3.63937	0.69	99.06
93	0.06551	2.10655	1.07981	3.90357	0.11955	3.28638	0.84	97.85
94	0.06466	2.30120	1.03411	4.00485	0.11600	3.27769	0.82	98.08
96	0.06582	3.70893	1.08105	5.20923	0.11912	3.65786	0.70	97.44
97	0.06552	2.06858	1.10130	3.90266	0.12190	3.30935	0.85	98.29
98	0.06595	2.13722	1.12901	3.96885	0.12417	3.34425	0.84	98.28
99	0.06483	3.83761	1.03380	5.31382	0.11565	3.67552	0.69	97.82
107	0.06493	3.70769	1.09950	5.23337	0.12281	3.69339	0.71	99.10
108	0.06552	2.25885	1.07698	3.94005	0.11922	3.22825	0.82	97.78
109	0.06647	3.79763	1.12600	5.27607	0.12286	3.66264	0.69	97.49
110	0.06441	2.08282	1.06795	3.93610	0.12025	3.33987	0.85	99.17
111	0.06573	2.13210	1.07771	3.93745	0.11892	3.31023	0.84	97.50
112	0.06621	2.55539	1.09772	4.30939	0.12024	3.46999	0.81	97.25
113	0.06669	2.08001	1.13103	3.92777	0.12300	3.33181	0.85	97.29
114	0.06556	2.13545	1.07329	3.96651	0.11873	3.34262	0.84	97.64
116	0.06552	2.22570	1.07990	3.97912	0.11954	3.29843	0.83	97.84
117	0.06496	2.06281	1.10306	3.90892	0.12315	3.32031	0.85	99.13
118	0.06626	3.05987	1.09534	4.63380	0.11989	3.47984	0.75	97.13
119	0.06545	2.05250	1.12139	3.92453	0.12427	3.34502	0.85	98.83
120	0.06639	2.17413	1.12207	4.03342	0.12257	3.39730	0.84	97.51
127	0.06489	2.00437	1.10129	3.90784	0.12309	3.35465	0.86	99.20
128	0.06542	3.73161	1.07113	5.31852	0.11874	3.78970	0.71	97.79
129	0.06687	2.08577	1.17129	3.95878	0.12703	3.36475	0.85	97.87
131	0.06622	2.02556	1.10844	3.97326	0.12140	3.41817	0.86	97.47
132	0.06594	3.63425	1.07756	5.25576	0.11852	3.79675	0.72	97.20
133	0.06656	2.03570	1.16900	3.95180	0.12737	3.38713	0.86	98.25

Sample	Isotopic ratios 207Pb/206Pb	2s	207Pb/235U	2s (%)	206Pb/238U	2s (%)	Rho	% conc d
134	0.06560	3.77492	1.13625	5.36501	0.12563	3.81225	0.71	98.93
136	0.06502	3.02436	1.07185	4.59301	0.11956	3.45673	0.75	98.38
137	0.06657	3.66724	1.14531	5.22509	0.12478	3.72195	0.71	97.75
139	0.06558	3.68815	1.13031	5.26584	0.12501	3.75854	0.71	98.83
140	0.06439	2.24585	1.07770	4.10101	0.12138	3.43139	0.84	99.41
147	0.06485	2.07519	1.09482	3.97495	0.12244	3.39025	0.85	99.12
150	0.06558	2.07480	1.12994	3.94256	0.12497	3.35247	0.85	98.82
151	0.06609	3.65982	1.23257	5.14872	0.13527	3.62147	0.70	100.23
152	0.06589	2.12475	1.14362	3.89492	0.12588	3.26433	0.84	98.67
154	0.06480	3.71491	1.07345	5.31820	0.12014	3.80562	0.72	98.72
155	0.06604	1.98074	1.07625	4.03269	0.11819	3.51272	0.87	97.03
156	0.06587	2.24685	1.13717	4.12379	0.12521	3.45794	0.84	98.56
157	0.06731	3.71433	1.17528	5.32133	0.12664	3.81056	0.72	97.36
158	0.06465	2.04224	1.12416	3.98112	0.12611	3.41739	0.86	100.03
160	0.06496	3.72333	1.08121	5.28978	0.12072	3.75748	0.71	98.67
167	0.06777	3.58534	1.23586	5.20508	0.13226	3.77335	0.72	97.95
168	0.06540	2.04919	1.16675	3.96334	0.12940	3.39247	0.86	99.86
169	0.06534	2.14264	1.10572	4.07171	0.12273	3.46236	0.85	98.65
170	0.06425	2.11364	1.09708	4.02451	0.12385	3.42480	0.85	100.04
171	0.06585	3.67299	1.17273	5.28983	0.12917	3.80677	0.72	99.34
172	0.06646	3.63921	1.17196	5.24225	0.12790	3.77323	0.72	98.46
173	0.06516	2.33139	1.12405	4.19049	0.12511	3.48207	0.83	99.29
174	0.06562	2.07744	1.12767	4.00696	0.12464	3.42636	0.86	98.72
175	0.06553	2.07776	1.09932	4.00776	0.12167	3.42710	0.86	98.24
176	0.06538	2.11110	1.12656	4.02981	0.12497	3.43258	0.85	99.03
177	0.06563	2.15458	1.12707	4.06518	0.12455	3.44724	0.85	98.69
178	0.06594	2.09281	1.14275	3.98980	0.12569	3.39686	0.85	98.58
187	0.06279	3.79882	1.03111	5.33683	0.11910	3.74843	0.70	100.76
188	0.06542	2.01813	1.13222	4.03786	0.12552	3.49735	0.87	99.09
189	0.06441	2.02467	1.12918	4.00307	0.12715	3.45330	0.86	100.50
190	0.06569	2.13122	1.12825	4.09084	0.12457	3.49183	0.85	98.63
191	0.06588	2.21883	1.17841	4.08085	0.12974	3.42492	0.84	99.41
192	0.06624	3.68562	1.13612	5.25647	0.12440	3.74789	0.71	98.02
193	0.06657	3.68459	1.17400	5.27363	0.12791	3.77293	0.72	98.35
194	0.06543	3.74869	1.13919	5.37403	0.12627	3.85065	0.72	99.23
195	0.06459	2.01404	1.09577	3.99842	0.12303	3.45413	0.86	99.51
196	0.06543	3.73128	1.04365	5.44648	0.11569	3.96758	0.73	97.19
197	0.06524	2.15605	1.12523	4.03835	0.12510	3.41463	0.85	99.21
198	0.06437	2.11279	1.06146	4.16272	0.11960	3.58669	0.86	99.09
199	0.06356	2.02930	1.03246	4.02284	0.11781	3.47349	0.86	99.64

Supplementary Table S3. Analytical results zircon Lu-Hf isotopes.

#Parte1

Spot	$^{176}Yb/^{177}Hf^a$	±2σ	$^{176}Lu/^{177}Hf^a$	±2σ	$^{178}Hf/^{177}Hf$	$^{180}Hf/^{177}Hf$	SigHf (V)[b]
Vila Nova Suite, metatonalite, sample 114, n=25							
7	0.0156	13	0.00067	4	1.467186	1.886842	14
8	0.0208	24	0.00092	9	1.467237	1.886934	13
10	0.0219	19	0.00094	6	1.467199	1.886787	15
11	0.0119	10	0.00058	4	1.467193	1.886976	11
12	0.0211	22	0.00090	8	1.467225	1.886830	17
13	0.0132	17	0.00058	6	1.467220	1.886914	15
15	0.0206	17	0.00090	6	1.467226	1.886842	14
17	0.0090	8	0.00041	3	1.467207	1.886838	15
27	0.0247	24	0.00109	9	1.467214	1.886938	13
30	0.0176	14	0.00077	5	1.467222	1.886856	13
37	0.0163	20	0.00070	8	1.467149	1.886814	15
38	0.0199	17	0.00091	6	1.467213	1.886884	11
39	0.0223	21	0.00096	7	1.467231	1.886788	14
49	0.0222	23	0.00094	8	1.467224	1.886817	13
50	0.0171	16	0.00073	6	1.467165	1.886874	13
51	0.0241	19	0.00104	6	1.467214	1.886932	14
56	0.0175	15	0.00075	5	1.467222	1.886855	13
59	0.0249	35	0.00107	13	1.467182	1.886749	14
60	0.0139	13	0.00062	5	1.467203	1.886804	15
74	0.0184	15	0.00082	5	1.467208	1.886820	14
80	0.0139	11	0.00061	4	1.467233	1.886809	15
93	0.0277	24	0.00123	8	1.467217	1.886808	13
95	0.0134	11	0.00061	4	1.467234	1.886838	14
96	0.0187	20	0.00083	8	1.467255	1.886926	14
100	0.0129	10	0.00058	3	1.467233	1.886824	16
Sanga do Jobim Suite, monzogranite, sample 115, n=20							
12	0.0594	48	0.00202	12	1.467276	1.886943	14
18	0.0691	56	0.00215	13	1.467260	1.886836	13
19	0.0447	36	0.00153	9	1.467243	1.886883	13
39	0.0414	33	0.00137	8	1.467177	1.886707	15
47	0.0413	33	0.00147	9	1.467219	1.887004	12
49	0.0289	23	0.00106	6	1.467166	1.886844	12
53	0.0792	63	0.00230	14	1.467167	1.886803	19
59	0.0307	25	0.00114	7	1.467179	1.886776	12
60	0.0317	26	0.00118	7	1.467220	1.886860	13
72	0.0491	40	0.00166	10	1.467244	1.886904	11
75	0.0525	47	0.00174	12	1.467195	1.886806	12
77	0.0849	84	0.00254	22	1.467251	1.886633	15
78	0.0629	53	0.00215	15	1.467219	1.886844	13

Spot	$^{176}Yb/^{177}Hf^a$	±2σ	$^{176}Lu/^{177}Hf^a$	±2σ	$^{178}Hf/^{177}Hf$	$^{180}Hf/^{177}Hf$	SigHf (V)[b]
88	0.0543	61	0.00187	18	1.467242	1.886812	14
93	0.0961	81	0.00347	22	1.467242	1.886709	11
94	0.0565	50	0.00194	13	1.467206	1.886908	13
96	0.0332	31	0.00121	9	1.467270	1.886821	11
118	0.0319	26	0.00115	7	1.467248	1.886866	13
119	0.0571	48	0.00199	13	1.467214	1.886840	12
Serrinha Formation, para-amphibolite, sample 29, n = 25							
13	0.0282	26	0.00109	8	1.467199	1.886989	10
14	0.0154	13	0.00062	4	1.467221	1.886794	11
16	0.0083	7	0.00033	2	1.467159	1.886733	15
17	0.0931	82	0.00326	22	1.467275	1.886843	8
18	0.0237	19	0.00089	5	1.467254	1.886742	11
29	0.0268	23	0.00099	8	1.467307	1.886710	15
32	0.0274	22	0.00124	8	1.467307	1.886852	7
33	0.0558	48	0.00195	14	1.467213	1.886918	8
54	0.0207	20	0.00078	7	1.467236	1.886759	8
57	0.0257	21	0.00095	6	1.467203	1.886774	5
60	0.0357	31	0.00142	10	1.467235	1.886870	12
75	0.0315	25	0.00120	7	1.467214	1.886707	15
76	0.0760	70	0.00269	20	1.467312	1.886982	5
79	0.0126	10	0.00049	3	1.467218	1.886965	11
80	0.0162	27	0.00068	10	1.467323	1.886685	10
88	0.0342	32	0.00123	9	1.467288	1.886689	11
90	0.0234	21	0.00083	6	1.467234	1.886785	16
91	0.0243	22	0.00094	6	1.467244	1.886739	12
92	0.0400	34	0.00143	10	1.467226	1.886922	12
94	0.0280	25	0.00112	7	1.467253	1.886829	12
95	0.0194	16	0.00076	5	1.467292	1.886819	11
96	0.0140	17	0.00054	6	1.467231	1.886804	5
97	0.0358	29	0.00135	8	1.467269	1.886851	13
99	0.0148	13	0.00052	4	1.467391	1.886605	6
100	0.0446	39	0.00166	12	1.467301	1.886900	9
Serrinha Formation, Garnet-biotite-plagioclase schist, sample 30b, n = 29							
8	0.0277	23	0.00112	7	1.467213	1.886852	12
15	0.0290	24	0.00107	7	1.467221	1.886878	14
16	0.0281	23	0.00119	7	1.467167	1.886882	16
19	0.0222	18	0.00084	5	1.467157	1.886799	12
20	0.0459	37	0.00179	11	1.467203	1.886851	14
29	0.0408	33	0.00166	10	1.467162	1.886884	15
32	0.0329	27	0.00141	9	1.467231	1.886868	14
33	0.0246	20	0.00102	6	1.467220	1.886961	15
37	0.0372	30	0.00155	9	1.467249	1.886773	13
38	0.0287	23	0.00121	7	1.467287	1.886898	11
50	0.0342	27	0.00135	8	1.467241	1.886881	11

Spot	$^{176}Yb/^{177}Hf^a$	±2σ	$^{176}Lu/^{177}Hf^a$	±2σ	$^{178}Hf/^{177}Hf$	$^{180}Hf/^{177}Hf$	SigHf (V)[b]
53	0.0308	25	0.00131	8	1.467246	1.886850	12
54	0.0361	30	0.00142	9	1.467191	1.886850	15
57	0.0199	16	0.00083	5	1.467213	1.886791	11
69	0.0324	57	0.00132	22	1.467230	1.886857	15
70	0.0674	54	0.00275	16	1.467195	1.886876	11
72	0.0778	63	0.00315	19	1.467164	1.886943	10
78	0.0342	30	0.00136	9	1.467210	1.886907	14
79	0.0325	29	0.00124	8	1.467195	1.886910	15
80	0.1243	100	0.00474	28	1.467166	1.886932	10
98	0.0331	26	0.00136	8	1.467226	1.886762	12
109	0.0354	28	0.00145	9	1.467196	1.886888	13
139	0.0393	32	0.00155	9	1.467197	1.886856	12
153	0.0335	27	0.00125	8	1.467231	1.886782	14
154	0.0313	25	0.00125	8	1.467273	1.886763	13
158	0.0328	27	0.00135	8	1.467175	1.886775	14
159	0.0327	26	0.00138	9	1.467191	1.886808	11
173	0.0177	15	0.00075	5	1.467271	1.886921	16
188	0.0808	69	0.00329	21	1.467231	1.886917	13

Serrinha Formation, Garnet-biotite-plagioclase schist, sample 48, n = 23

Spot	$^{176}Yb/^{177}Hf^a$	±2σ	$^{176}Lu/^{177}Hf^a$	±2σ	$^{178}Hf/^{177}Hf$	$^{180}Hf/^{177}Hf$	SigHf (V)[b]
7	0.0400	38	0.00146	11	1.467211	1.886830	14
9	0.0320	28	0.00115	8	1.467257	1.886923	12
10	0.0184	20	0.00075	7	1.467170	1.886817	14
11	0.0861	73	0.00308	21	1.467201	1.886857	10
12	0.0185	16	0.00075	6	1.467251	1.886931	12
13	0.0174	15	0.00077	5	1.467215	1.886839	13
14	0.0430	51	0.00175	17	1.467241	1.886952	12
15	0.0650	53	0.00255	15	1.467264	1.886826	11
16	0.0466	45	0.00196	16	1.467219	1.886845	12
17	0.0272	27	0.00113	9	1.467253	1.886858	14
19	0.0438	59	0.00163	19	1.467266	1.886798	14
20	0.0320	27	0.00122	8	1.467216	1.886791	16
27	0.0504	41	0.00179	11	1.467235	1.886894	13
28	0.0164	14	0.00071	5	1.467223	1.886905	13
30	0.0336	27	0.00121	8	1.467243	1.886739	11
31	0.0412	34	0.00174	11	1.467238	1.886800	12
32	0.0382	35	0.00143	10	1.467238	1.886854	13
33	0.0179	18	0.00074	6	1.467234	1.886883	16
35	0.0381	57	0.00139	16	1.467236	1.886857	12
36	0.0229	19	0.00091	7	1.467262	1.886656	10
37	0.0309	33	0.00113	9	1.467216	1.886792	12
39	0.0340	28	0.00152	10	1.467294	1.886891	11
74	0.0463	41	0.00193	12	1.467254	1.886864	13

Serrinha Formation, Staurolite-garnet-biotite-plagioclase schist, sample 113, n = 47

Spot	$^{176}Yb/^{177}Hf^a$	±2σ	$^{176}Lu/^{177}Hf^a$	±2σ	$^{178}Hf/^{177}Hf$	$^{180}Hf/^{177}Hf$	SigHf (V)[b]
7	0.0321	26	0.00126	8	1.467288	1.886799	17

Spot	$^{176}Yb/^{177}Hf^a$	±2σ	$^{176}Lu/^{177}Hf^a$	±2σ	$^{178}Hf/^{177}Hf$	$^{180}Hf/^{177}Hf$	SigHf (V)[b]
9	0.0608	49	0.00215	13	1.467215	1.886612	14
10	0.0252	20	0.00099	6	1.467284	1.886493	10
11	0.0348	28	0.00145	9	1.467296	1.886780	12
12	0.0418	33	0.00170	10	1.467220	1.886768	13
13	0.0248	25	0.00108	10	1.467341	1.886481	10
14	0.0707	61	0.00263	19	1.467298	1.886822	14
15	0.0376	31	0.00148	10	1.467251	1.886599	10
18	0.0143	13	0.00054	4	1.467145	1.886807	15
20	0.0296	27	0.00115	9	1.467243	1.886833	10
27	0.0376	35	0.00148	12	1.467241	1.886925	10
28	0.0260	24	0.00104	7	1.467213	1.886736	11
32	0.0621	59	0.00249	20	1.467259	1.886249	9
34	0.0299	25	0.00130	8	1.467192	1.886901	12
35	0.0204	17	0.00086	5	1.467212	1.886754	10
37	0.0810	68	0.00323	21	1.467274	1.886622	12
38	0.0344	28	0.00148	9	1.467198	1.886779	10
39	0.0335	28	0.00142	9	1.467235	1.886730	9
50	0.0236	20	0.00096	6	1.467239	1.886838	11
51	0.0223	25	0.00092	7	1.467192	1.886922	13
54	0.0242	20	0.00104	6	1.467223	1.886834	12
55	0.0323	26	0.00123	8	1.467248	1.886989	12
56	0.0859	88	0.00311	31	1.467259	1.886801	9
57	0.0375	31	0.00141	10	1.467210	1.886791	12
72	0.0842	86	0.00335	26	1.467300	1.886684	9
79	0.0342	29	0.00123	8	1.467283	1.886758	12
90	0.0129	11	0.00055	4	1.467167	1.886860	11
91	0.0198	17	0.00074	5	1.467243	1.886814	11
93	0.0626	52	0.00230	14	1.467216	1.886807	10
94	0.0503	43	0.00176	13	1.467224	1.886845	10
97	0.0167	14	0.00074	5	1.467252	1.886702	10
107	0.0170	15	0.00076	5	1.467308	1.886599	10
111	0.0366	44	0.00138	14	1.467225	1.886863	11
132	0.0968	106	0.00326	29	1.467217	1.886926	11
147	0.0656	57	0.00261	19	1.467233	1.886850	13
151	0.0681	81	0.00268	26	1.467339	1.886810	7
157	0.0188	31	0.00072	10	1.467215	1.886846	12
160	0.0514	49	0.00200	15	1.467198	1.886859	13
167	0.0765	76	0.00294	22	1.467201	1.886784	17
168	0.0325	28	0.00137	9	1.467227	1.886937	9
170	0.0410	36	0.00147	10	1.467239	1.886862	10
174	0.0300	30	0.00116	9	1.467239	1.886840	13
177	0.0211	17	0.00086	5	1.467283	1.886694	9
192	0.0222	18	0.00086	5	1.467310	1.886712	11
197	0.0303	25	0.00126	8	1.467247	1.886918	12

Spot	$^{176}Yb/^{177}Hf^a$	±2σ	$^{176}Lu/^{177}Hf^a$	±2σ	$^{178}Hf/^{177}Hf$	$^{180}Hf/^{177}Hf$	SigHf (V)[b]
198	0.0247	20	0.00107	7	1.467243	1.886854	8
199	0.0471	60	0.00167	19	1.467237	1.886832	10

#Parte2

Spot	$^{176}Hf/^{177}Hf$	±2σ[c]	$^{176}Hf/^{177}Hf_{(t)}$[d]	$\varepsilon_{Hf(t)}$[d]	±2σ[c]	TDM_2 (Ga)[e]	206Pb/238U (Ma)	Age
Vila Nova Suite, metatonalite, sample 114, n=25								
7	0.282557	24	0.282548	7.8	0.7	1.14	723.17	
8	0.282573	29	0.282561	8.2	0.7	1.11	723.75	
10	0.282568	17	0.282555	8.0	0.7	1.13	719.37	
11	0.282574	19	0.282566	8.3	0.7	1.11	719.20	
12	0.282569	14	0.282557	7.5	0.7	1.13	698.61	
13	0.282568	19	0.282560	8.1	0.7	1.12	717.64	
15	0.282593	12	0.282581	8.8	0.7	1.08	717.35	
17	0.282584	24	0.282578	8.4	0.7	1.09	703.46	
27	0.282559	21	0.282544	7.7	0.7	1.15	726.51	
30	0.282569	20	0.282559	8.2	0.7	1.12	725.64	
37	0.282556	17	0.282546	7.5	0.7	1.15	714.99	
38	0.282587	15	0.282574	10.1	0.7	1.06	785.42	
39	0.282564	17	0.282551	7.4	0.7	1.14	701.44	
49	0.282567	14	0.282554	8.4	0.7	1.12	738.69	
50	0.282563	13	0.282553	8.3	0.7	1.12	738.63	
51	0.282571	13	0.282557	8.2	0.7	1.12	728.06	
56	0.282552	24	0.282542	7.5	0.7	1.15	721.04	
59	0.282567	22	0.282552	8.2	0.8	1.12	736.45	
60	0.282551	21	0.282542	7.6	0.7	1.15	724.95	
74	0.282550	16	0.282539	7.5	0.7	1.16	726.05	
80	0.282571	14	0.282563	8.3	0.7	1.11	721.16	
93	0.282586	18	0.282570	8.4	0.7	1.10	715.63	
95	0.282571	16	0.282562	8.3	0.7	1.11	723.80	
96	0.282563	12	0.282552	7.9	0.7	1.13	720.46	
100	0.282557	17	0.282549	7.6	0.7	1.14	713.67	
Sanga do Jobim Suite, monzogranite, sample 115, n=20								
12	0.282530	16	0.282503	5.6	0.8	1.24	695.36	
18	0.282539	16	0.282511	5.4	0.9	1.23	673.70	
19	0.282542	15	0.282522	6.2	0.8	1.20	694.04	
39	0.282552	18	0.282534	6.4	0.8	1.18	684.77	
47	0.282548	18	0.282529	5.9	0.8	1.20	670.26	
49	0.282593	20	0.282578	9.2	0.7	1.07	740.89	
53	0.282521	20	0.282491	5.2	0.9	1.26	699.30	
59	0.282568	14	0.282554	6.8	0.7	1.15	672.78	

Spot	$^{176}Hf/^{177}Hf$	$\pm2\sigma^c$	$^{176}Hf/^{177}Hf_{(t)}{}^d$	$\varepsilon_{Hf(t)}{}^d$	$\pm2\sigma^c$	TDM$_2$ (Ga)^e	206Pb/238U (Ma)	Age
60	0.282600	11	0.282585	8.3	0.7	1.08	687.40	
72	0.282524	11	0.282503	4.8	0.8	1.26	660.03	
75	0.282541	20	0.282519	5.8	0.8	1.21	682.99	
77	0.282475	26	0.282444	2.5	1.1	1.37	653.13	
78	0.282518	26	0.282490	5.0	0.9	1.27	692.55	
88	0.282566	26	0.282542	6.8	0.9	1.17	691.69	
93	0.282508	16	0.282463	4.1	1.1	1.32	693.52	
94	0.282570	17	0.282547	6.0	0.9	1.18	646.27	
96	0.282591	30	0.282575	7.6	0.8	1.11	672.84	
118	0.282587	20	0.282572	7.3	0.7	1.12	662.79	
119	0.282557	13	0.282533	5.7	0.8	1.20	652.72	
Serrinha Formation, para-amphibolite, sample 29, n = 25								
13	0.282581	22	0.282568	7.1	0.8	1.13	661.58	
14	0.282515	17	0.282507	5.8	0.7	1.23	698.94	
16	0.281244	19	0.281229	-1.1	0.7	2.93	2377.38	
17	0.282504	30	0.282462	4.1	1.1	1.32	694.82	
18	0.282451	19	0.282439	3.3	0.7	1.37	694.24	
29	0.282550	20	0.282536	7.0	0.7	1.17	707.04	
32	0.282661	27	0.282644	11.4	0.7	0.95	734.99	
33	0.282491	23	0.282467	3.8	0.9	1.32	673.86	
54	0.282387	30	0.282377	0.8	0.7	1.49	680.20	
57	0.282376	34	0.282364	0.4	0.7	1.52	684.38	
60	0.282569	20	0.282552	6.3	0.8	1.16	652.02	
75	0.282579	18	0.282564	6.8	0.7	1.14	655.81	
76	0.282529	29	0.282495	4.9	1.0	1.26	680.26	
79	0.281590	25	0.281573	-2.8	0.7	2.55	1778.03	
80	0.282579	32	0.282569	9.0	0.8	1.09	745.46	
88	0.282544	17	0.282528	6.3	0.8	1.19	688.85	
90	0.282033	13	0.282011	3.0	0.7	1.90	1352.58	
91	0.282536	16	0.282522	7.7	0.7	1.17	757.99	
92	0.282540	18	0.282522	6.0	0.8	1.21	684.56	
94	0.282527	21	0.282512	6.7	0.7	1.21	731.41	
95	0.282569	21	0.282559	7.5	0.7	1.13	692.68	
96	0.281815	36	0.281803	-7.6	0.7	2.37	1211.92	
97	0.282235	18	0.282221	-7.0	0.8	1.84	583.08	
99	0.282386	37	0.282380	-0.5	0.7	1.51	620.08	
100	0.282541	19	0.282520	6.2	0.8	1.21	699.00	
Serrinha Formation, Garnet-biotite-plagioclase schist, sample 30b, n = 29								
8	0.282570	27	0.282555	7.9	0.7	1.13	716.65	
15	0.282597	18	0.282582	9.3	0.7	1.07	737.11	
16	0.282594	27	0.282578	8.9	0.7	1.08	725.99	
19	0.282599	14	0.282588	9.0	0.7	1.06	716.77	
20	0.282546	16	0.282521	7.1	0.8	1.19	737.51	
29	0.282604	14	0.282582	9.2	0.8	1.07	731.75	

Spot	$^{176}Hf/^{177}Hf$	$\pm2\sigma^c$	$^{176}Hf/^{177}Hf_{(t)}{}^d$	$\varepsilon_{Hf(t)}{}^d$	$\pm2\sigma^c$	TDM$_2$ (Ga)^e	206Pb/238U (Ma)	Age
32	0.282566	14	0.282546	8.2	0.7	1.13	744.18	
33	0.282569	19	0.282556	8.1	0.7	1.12	727.44	
37	0.282569	18	0.282547	8.2	0.8	1.13	742.22	
38	0.282587	18	0.282570	8.6	0.7	1.09	726.23	
50	0.282571	15	0.282553	8.2	0.7	1.12	734.80	
53	0.282588	17	0.282570	8.7	0.7	1.09	730.26	
54	0.282591	18	0.282571	9.0	0.8	1.09	740.96	
57	0.282604	19	0.282593	9.3	0.7	1.05	719.19	
69	0.282569	20	0.282551	8.2	0.9	1.13	738.77	
70	0.282534	18	0.282497	6.1	0.9	1.24	726.80	
72	0.282564	13	0.282520	7.0	0.9	1.19	731.87	
78	0.282583	20	0.282564	8.6	0.8	1.10	734.80	
79	0.282565	23	0.282548	8.0	0.7	1.14	731.98	
80	0.282467	18	0.282400	3.1	1.2	1.42	745.61	
98	0.282587	20	0.282568	9.0	0.7	1.09	746.13	
109	0.282583	21	0.282562	8.8	0.7	1.10	745.61	
139	0.282569	18	0.282548	8.1	0.8	1.13	737.80	
153	0.282557	20	0.282540	7.7	0.7	1.15	734.17	
154	0.282572	18	0.282555	8.2	0.7	1.12	731.52	
158	0.282578	18	0.282560	8.4	0.7	1.11	734.06	
159	0.282567	15	0.282547	8.2	0.7	1.13	740.73	
173	0.282606	21	0.282596	9.4	0.7	1.05	717.40	
188	0.282550	24	0.282504	6.4	1.0	1.22	728.53	
Serrinha Formation, Garnet-biotite-plagioclase schist, sample 48, n = 23								
7	0.282616	21	0.282597	9.2	0.8	1.05	707.94	
9	0.282537	28	0.282522	6.8	0.7	1.19	721.86	
10	0.282622	32	0.282612	10.4	0.7	1.01	737.06	
11	0.282537	20	0.282494	6.3	1.0	1.24	742.91	
12	0.282595	15	0.282584	9.1	0.7	1.07	725.59	
13	0.282572	28	0.282561	8.4	0.7	1.11	731.56	
14	0.282595	45	0.282571	8.2	0.9	1.10	707.25	
15	0.282585	22	0.282550	8.0	0.9	1.13	729.90	
16	0.282615	21	0.282587	10.3	0.8	1.04	775.01	
17	0.282647	52	0.282631	10.5	0.7	0.98	714.44	
19	0.282623	50	0.282600	9.9	0.9	1.03	734.94	
20	0.282634	37	0.282617	10.5	0.7	1.00	733.05	
27	0.282559	13	0.282535	7.0	0.8	1.17	710.59	
28	0.282630	17	0.282620	10.5	0.7	1.00	728.75	
30	0.282520	13	0.282504	6.0	0.7	1.23	713.00	
31	0.282603	15	0.282580	8.7	0.8	1.08	715.65	
32	0.282504	30	0.282485	5.6	0.8	1.26	724.56	
33	0.282618	17	0.282607	10.1	0.7	1.02	731.56	
35	0.282514	22	0.282495	6.0	0.9	1.24	727.37	
36	0.282616	25	0.282602	10.8	0.7	1.01	770.62	

Spot	$^{176}Hf/^{177}Hf$	$\pm2\sigma^c$	$^{176}Hf/^{177}Hf_{(t)}$[d]	$\varepsilon_{Hf(t)}$[d]	$\pm2\sigma^c$	TDM_2 (Ga)[e]	$^{206}Pb/^{238}U$ (Ma)	Age
37	0.282504	17	0.282489	5.4	0.8	1.26	710.53	
39	0.282373	27	0.282353	0.8	0.7	1.52	722.09	
74	0.282597	17	0.282571	8.6	0.8	1.10	722.37	

Serrinha Formation, Staurolite-garnet-biotite-plagioclase schist, sample 113, n = 47

Spot	$^{176}Hf/^{177}Hf$	$\pm2\sigma^c$	$^{176}Hf/^{177}Hf_{(t)}$[d]	$\varepsilon_{Hf(t)}$[d]	$\pm2\sigma^c$	TDM_2 (Ga)[e]	$^{206}Pb/^{238}U$ (Ma)	Age
7	0.282646	18	0.282628	11.4	0.7	0.97	760.02	
9	0.282578	16	0.282545	9.6	0.8	1.11	808.13	
10	0.282623	15	0.282609	10.7	0.7	1.00	757.72	
11	0.282622	15	0.282601	10.5	0.7	1.02	761.97	
12	0.282487	11	0.282461	6.7	0.8	1.27	812.06	
13	0.282384	36	0.282369	2.1	0.7	1.48	753.18	
14	0.282549	39	0.282513	6.7	0.9	1.20	731.93	
15	0.282542	46	0.282522	7.1	0.8	1.19	733.95	
18	0.282622	14	0.282614	11.1	0.7	0.99	768.80	
20	0.282587	26	0.282571	8.8	0.7	1.09	732.92	
27	0.282599	43	0.282579	8.4	0.8	1.09	702.51	
28	0.282607	31	0.282592	10.2	0.7	1.04	758.98	
32	0.282481	34	0.282445	5.0	0.9	1.32	761.51	
34	0.282627	27	0.282608	10.9	0.7	1.00	764.95	
35	0.282607	23	0.282595	9.7	0.7	1.04	735.91	
37	0.282483	35	0.282439	4.0	1.0	1.35	729.45	
38	0.282546	33	0.282524	8.1	0.7	1.16	774.42	
39	0.282600	79	0.282580	9.7	0.7	1.06	758.01	
50	0.282610	20	0.282597	10.1	0.7	1.03	750.77	
51	0.282608	25	0.282594	10.4	0.7	1.03	764.73	
54	0.282501	64	0.282487	5.9	0.7	1.25	737.12	
55	0.282595	34	0.282578	9.6	0.7	1.06	758.41	
56	0.282501	53	0.282459	4.4	1.1	1.32	711.20	
57	0.282618	31	0.282597	10.8	0.8	1.02	779.68	
72	0.282512	17	0.282463	6.0	1.1	1.28	775.33	
79	0.282573	15	0.282556	8.2	0.8	1.12	729.40	
90	0.282625	17	0.282617	10.8	0.7	0.99	747.55	
91	0.282608	18	0.282598	9.9	0.7	1.04	737.41	
93	0.282577	15	0.282546	7.8	0.9	1.14	727.95	
94	0.282569	15	0.282546	7.4	0.8	1.15	707.49	
97	0.282586	19	0.282576	9.2	0.7	1.08	741.50	
107	0.282472	16	0.282461	5.2	0.7	1.30	746.74	
111	0.282577	21	0.282558	8.2	0.8	1.12	724.32	
132	0.282499	16	0.282455	4.4	1.3	1.32	722.06	
147	0.282580	18	0.282544	8.1	0.9	1.14	744.61	
151	0.282512	19	0.282471	7.2	1.1	1.25	817.87	
157	0.282646	16	0.282636	11.9	0.8	0.95	768.68	
160	0.282595	17	0.282567	8.7	0.9	1.10	734.70	
167	0.282569	20	0.282524	8.7	1.0	1.15	800.72	
168	0.282608	16	0.282588	10.6	0.7	1.03	784.43	

Spot	$^{176}Hf/^{177}Hf$	$\pm2\sigma^c$	$^{176}Hf/^{177}Hf_{(t)}{}^d$	$\varepsilon_{Hf(t)}{}^d$	$\pm2\sigma^c$	TDM_2 (Ga)^e	206Pb/238U (Ma)	Age
170	0.282341	19	0.282320	0.4	0.8	1.57	752.66	
174	0.282604	19	0.282588	10.0	0.8	1.05	757.20	
177	0.282435	20	0.282423	4.1	0.7	1.37	756.69	
192	0.282636	20	0.282624	11.2	0.7	0.98	755.82	
197	0.282611	19	0.282593	10.2	0.7	1.03	759.85	
198	0.282594	19	0.282579	9.0	0.7	1.08	728.24	
199	0.282555	20	0.282533	7.1	0.9	1.17	717.96	

Supplementary Table S4. Analytical results zircon trace elements.

#Parte 1

Spot	206Pb/238U Age (Ma)	La	Ce	Pr	Nd	Sm147	Eu153	Gd	Tb
Vila Nova Suite, metatonalite, sample 114									
7	723.17	0.0462	10.49	0.0434	0.859	1.432	0.552	7.32	2.78
8	723.75	0.0547	10.71	0.0945	1.519	2.69	1.128	12.36	4.54
10	719.37	0.0413	10.25	0.0568	0.926	1.87	0.743	9.36	3.52
11	719.20	0.09	10.98	0.1052	1.413	2.35	0.983	11.98	4.4
13	717.64	<0.0165	12.21	0.0419	0.734	1.67	0.735	9.16	3.62
14	725.24	0.17	14.45	0.166	2.03	2.56	1.1	12.33	4.67
15	717.35	1.509	9.13	0.799	8.39	5.92	1.705	10.38	2
16	702.19	0.0353	14.9	0.0384	0.915	1.84	0.744	10.23	3.97
17	703.46	<0.0191	6.61	0.0156	0.288	0.718	0.368	4.44	1.719
19	716.78	0.026	14.45	0.0585	1.176	1.99	0.898	10.79	4.15
27	726.51	0.096	15.15	0.0556	1.198	2.17	1.009	12.39	4.86
28	723.75	1.107	19.08	0.979	10.1	8.25	2.69	20.93	5.95
30	725.64	0.109	11.19	0.1453	2.01	3.16	1.132	13.72	4.67
31	717.59	0.461	12.39	0.523	5.16	3.64	1.303	12.41	4.32
33	711.65	0.026	9.75	0.0761	1.49	2.84	1.104	12.37	4.2
32	717.24	0.901	9.85	0.513	5.08	4.25	1.245	9.11	2.62
36	709.34	3.02	25.79	2.17	14.92	6.57	1.674	13.83	4.16
37	714.99	1.515	20.95	0.926	7.87	4.64	1.704	15.11	5.03
38	785.42	0.854	10.39	0.385	3.41	3.2	1.206	11	3.49
89	780.29	0.287	8.09	0.144	1.82	1.9	0.69	7.08	2.33
88	719.26	<0.0179	12.69	0.0441	1.068	2.23	0.968	12.52	4.93
Sanga do Jobim suite, monzogranite, sample 115									
7	740.43	5.29	51.32	9.52	60.28	57.88	12.34	101.97	33.31
12	740.89	1.481	30.49	2.88	23.7	33.39	7.16	110.62	36.37
19	695.36	7.57	72.93	10.82	64.39	58.68	16.07	122.48	49.41
27	694.04	26.97	252.7	54.09	350.36	336.67	66.32	480.78	138.93
29	693.87	13.68	126.45	36.33	199.61	182.86	33.37	288.87	78.84
30	692.55	41.63	370.51	72.64	497.38	436.36	98.66	652.1	164.04
31	687.11	75.79	759.69	130.91	871.14	765.04	184.77	1133.08	327.48
36	684.77	2.06	21.37	3.02	21.34	27.46	5.18	68.47	22.08
39	693.64	3.83	32.72	5.58	34.17	35.82	5.78	72.74	24.32
47	699.30	1.711	21.42	3.19	23.96	28.77	8.03	80.27	26.9
48	705.07	33.24	217.4	43.11	275.39	225.08	44.49	371.75	110.16
50	687.40	12.96	125.94	26.01	184.3	170.27	33.35	275.64	79.02
53	696.21	17.75	190.67	37.68	256.4	258.41	72.47	409.29	121.42

Spot	206Pb/238U Age (Ma)	La	Ce	Pr	Nd	Sm147	Eu153	Gd	Tb
54	689.86	0.186	12.1	0.169	2.41	4.65	1.011	25.24	10.23
55	696.61	4.19	55.58	8.93	66.13	69.46	16.68	167.78	51.19
59	682.99	0.0268	4.5	0.0513	1.39	3.87	0.827	20.99	7.95
60	692.55	0.275	5.13	0.352	3.55	7.03	1.55	34.65	12.52
70	691.69	0.318	6.29	0.341	3.4	5.25	0.938	26.55	10.94
71	698.56	0.774	11.73	1.547	11.4	14.66	3.18	36.69	12.54
72	692.55	0.046	6.59	0.181	3.22	7.96	1.58	41.48	15.45
Serrinha Formation, para-amphibolite, sample 29									
7	682.29	0.0473	6.58	0.463	8.17	16.97	5.09	71.29	24.22
8	680.20	0.0315	6.47	0.329	5.83	10.77	3.23	41.36	13.94
9	530.73	0.096	5.19	0.194	3.06	7.86	1.122	36.58	13.77
10	628.46	4.49	27.1	1.191	8.46	8.21	2.61	32.59	10.43
11	678.63	0.0253	6.75	0.331	6.62	15.11	4.23	64.83	23.31
36	not determinated	0.0679	6.36	0.299	5.59	11.14	3.58	44.07	14.24
13	661.58	<0.0201	4.75	0.0402	0.86	2.95	0.725	17.16	6.58
14	698.94	8.47	31.26	2.28	12.65	7.13	1.77	19.97	6.55
15	656.68	0.0547	9.93	0.319	5.69	10.1	2.9	43.81	15.68
16	2377.38	<0.0162	16.8	0.0367	0.679	1.59	0.523	5.85	1.99
28	2387.11	0.0452	16.49	0.0251	0.433	0.857	0.307	3.57	1.39
17	694.82	0.614	24.97	1.063	13.83	25.77	6.42	109.02	36.78
19	693.14	0.589	13.41	0.778	8.73	10.45	1.96	40.79	14.3
20	698.01	10.51	95.67	11.79	73.3	61.98	13.26	112.6	27.53
Serrinha Formation, garnet-biotite-plagioclase schist, sample 30B									
7	724.15	87.36	288.87	33.12	174.23	95.18	11.48	124.09	24.03
8	716.65	0.976	27.46	0.411	4.41	4.04	0.769	16.41	6.55
16	725.99	1.89	27.42	1.102	7.6	5.69	1.052	19.99	6.41
17	730.03	66.98	450.01	47.23	306.81	184.52	29.81	264.34	63.19
29	731.75	3.68	36.49	1.88	13.69	9.67	1.56	23.66	7.1
31	736.70	3.21	45.21	2.19	11.85	5.6	0.93	22.65	7.88
32	744.18	9.1	57.98	4.47	26.09	17.24	2.94	36.31	10.89
33	727.44	4.38	36.9	2.01	14	8.32	0.881	16.17	5.15
34	732.33	3.82	38.99	2.91	16.86	8.67	1.25	16.99	5.72
35	744.58	2.02	47.62	0.793	6.97	9.2	2.87	39.19	14.2
36	718.96	15.06	51.43	6.17	40.2	24.3	3.19	41.88	11.25
37	742.22	3.83	53.21	2.2	10.35	5.9	1.086	18.45	7.11
38	726.23	0.126	26.21	0.229	2.84	5.02	2.01	22.95	8.56
39	735.67	5.32	54.47	2.89	18.95	15.25	2.13	33.98	10.05
47	737.16	0.061	21.45	0.115	1.55	2.91	0.79	15.33	6.1
48	729.22	1.78	23.85	0.791	4.62	3.22	0.764	11.14	3.95
49	736.13	9.28	52.39	2.99	15.16	6.78	1.36	21.17	7.06
50	734.80	1.76	29.85	0.581	4.61	5.65	1.61	22.72	8.69
53	730.26	14.97	70.35	6.9	34.82	9.42	1.33	17.52	5.43
54	740.96	0.585	32.86	0.681	5.86	6.44	1.46	25.64	9.61
55	732.45	17.08	80.97	7.14	32.43	12.86	1.7	27.02	8.01
56	733.94	1.55	47.59	0.88	7.31	9.2	2.57	38.73	14.04
57	719.19	0.271	10.19	0.281	2.77	4.17	1.55	15.23	5.21
58	732.85	1.54	26.28	1.079	9.25	8.77	2.73	31.3	11.49
60	724.04	1.25	44.11	0.52	3.08	3.19	0.724	15.01	6.15
Serrinha Formation, garnet-biotite-plagioclase schist, sample 48									
7	707.94	<0.027	4.98	0.0304	0.868	3.12	0.58	19.63	7.55
9	721.86	0.46	28.84	0.562	7.34	12.23	2.32	60.06	20.95
10	737.06	0.167	9.48	0.047	0.727	1.18	0.26	8.18	3.47

Spot	206Pb/238U Age (Ma)	La	Ce	Pr	Nd	Sm147	Eu153	Gd	Tb
11	742.91	0.713	13.03	0.591	8.15	15.01	2.2	80.58	29.96
12	725.59	4.93	17.18	1.239	7.01	3.82	0.878	13.19	4.81
13	731.56	2.01	11.94	0.521	2.94	1.46	0.411	6.24	2.39
17	714.44	5.45	17.74	1.545	8.47	4.12	0.953	11.87	4.81
31	715.65	1.538	15.67	0.521	3.83	3.19	0.672	18.59	7.77
32	724.56	2.95	22.09	1.449	9.71	8.44	1.85	32.01	11.72
36	770.62	0.052	11.57	0.139	2.81	5.63	1.338	27.23	9.85
37	710.53	5.01	29.5	1.629	10.18	7.32	1.202	27.8	9.46
39	722.09	<0.036	19.67	0.0362	0.757	1.68	0.698	8.5	3.77
40	708.92	0.04	24.32	0.0591	1.75	5.45	2.63	34.43	14.07
38	not determinated	17.02	52.78	3.87	18.79	7.32	1.31	19.83	6.4
34	not determinated	16.84	71.18	7.35	40.39	17.46	7.69	38.47	12.23
33	731.56	<0.028	8.79	0.0186	0.693	1.97	0.813	9.48	3.83
30	713.00	0.256	15.75	0.124	1.9	3.86	0.865	19.86	7.76
29	not determinated	30.07	86.19	8.82	47.27	19.33	0.706	55.61	18.28
28	728.75	1.78	22.82	1.33	10.19	9.23	4.39	25.03	8.58
27	710.59	0.142	26.89	0.127	2.36	7.86	0.857	50.46	20.54
20	733.05	0.068	5.15	0.0677	1.057	2.67	0.544	14.4	5.85
19	734.94	2.22	15.74	1.13	7.9	9.18	2.07	43.88	16.16
17	not determinated	0.048	7.82	0.0312	0.613	1.88	0.3	12.34	5.25
16	775.01	<0.033	8.89	0.0633	1.48	4.07	0.751	23.68	9.76
15	729.90	3.59	35.76	1.452	8.38	8.27	1.78	41.57	17.19
8	not determinated	0.113	20.44	0.627	9.83	12.33	3.34	38.48	11.57
74	722.37	0.208	11.25	0.163	1.95	4.2	0.997	24.45	10.65
59	722.37	0.065	10.38	0.26	2.67	5.63	1.119	31.65	12.26
Serrinha Formation, staurolite-garnet-biotite-plagioclase schist, sample 113									
7	760.02	10.05	38.58	6.3	41.7	43.85	7.58	102.76	29.83
10	757.72	52.39	179.8	30.33	197.84	83.12	4.96	121.66	28.7
11	761.97	1.207	16.16	0.402	3.15	3.98	0.671	18.25	7.99
12	812.06	0.114	14.4	0.23	4.05	8.8	2.67	42.38	16.19
13	753.18	19.79	62.9	10.16	71.48	63.59	4.71	100.51	21.67
14	731.93	0.129	33.66	0.401	8.17	18.13	4.15	93.86	34.85
15	733.95	0.495	36.91	0.837	10.57	17.36	3.77	62.34	21.13
18	768.80	0.274	3.35	0.1511	1.387	2.56	0.391	12.59	4.88
BC020	not determinated	3.11	17.94	1.36	7.78	3.13	0.949	11.71	4.37
20	732.92	31.2	76.53	9.25	48.79	14.55	2.55	29.31	8.75
27	702.51	0.168	10.13	0.167	1.569	2.79	0.583	12.67	5.35
28	758.98	7.26	27.03	1.952	10.91	4.92	1.098	14.79	5.48
BC024	not determinated	0.0849	26.14	0.626	9.89	14.9	2.83	52.14	15.48
BC025	not determinated	0.948	17.46	0.555	5.16	6.82	0.922	33.4	13.69
BC036	not determinated	0.0153	4.7	0.0716	1.533	3.97	0.995	19.43	7.36
32	761.51	0.545	30.29	0.285	3.8	10.07	2.34	57.84	24.15
34	764.95	14.62	36.58	3.24	15.5	4.94	1.364	14.06	5.38
35	735.91	2.53	12.14	1.016	7.18	6.36	1.304	17.02	5.25
37	729.45	2.26	21.62	1.628	14.05	18.16	2.2	64.44	21.52
38	774.42	0.573	26.38	0.287	3.06	5.25	2.33	23.6	8.6

Spot	206Pb/238U Age (Ma)	La	Ce	Pr	Nd	Sm147	Eu153	Gd	Tb
39	758.01	0.45	10.93	<0.199	<1.48	3.7	<0.51	14.52	7.98
BC043	not determinated	<0.0170	10.88	0.1064	2.08	4.29	0.874	18.15	6.13
50	750.77	<0.030	10.38	0.0693	1.64	2.95	0.952	13.54	4.94
51	764.73	4.09	23.58	2.66	17.57	20.87	5.05	44.36	11.24
53	728.07	0.195	21.41	0.208	2.34	3.87	1.026	23.42	10.31
54	737.12	0.037	24.72	0.122	2.36	4.24	1.81	19.07	7.22
55	758.41	0.138	19.71	0.104	2.12	4.88	1.25	20.66	7.73
56	711.20	0.143	14.19	0.675	9.57	15.96	4.84	60.28	20.16
57	779.68	<0.201	5.72	0.105	1.4	3.22	0.267	21.35	7.43

Total REE = Total rare earth elements
LREE = light rare earth elements (La, Ce, Pr, Nd)
MREE = middle rare earth elements (Sm, Eu, Gd, Tb)
HREE = heavy rare earth elements (Dy, Ho, Er, Tm, Yb, Lu)
LaN = lanthanium normalized to chondrite
SmN = samarium normalized to chondrite
YbN = Ytterbium normalized to chondrite
GdN = Gadolinium normalized to chondrite

#Parte 2

Spot	Dy	Ho	Er	Tm	Yb	Lu
Vila Nova Suite, metatonalite, sample 114						
7	36.8	15.31	75.41	20.78	247.42	44.22
8	57.73	23.2	110.88	29.49	348.36	59.8
10	43.97	17.82	88.1	24.19	288.95	50.92
11	54.96	22.65	113.05	27.77	306.34	69.87
13	48.64	20.05	98.95	27.2	329.73	56.21
14	62.91	26.39	130.55	36.07	429.64	71.51
15	18.07	6.75	33.3	8.9	112.04	26.31
16	51.56	20.94	104.16	28.05	337.48	56.56
17	23.44	9.89	50.83	14.4	189.24	31.35
19	55.03	22.99	106.01	29.22	347.58	56.78
27	62.1	26.14	127.5	33.86	406.94	67.61
28	67.77	24.9	115.53	30.4	369.84	59.45
30	57.13	23.65	116.48	29.42	326.68	71.1
31	53.74	21.91	104.24	28.7	345.79	56.54
33	53.08	20.72	97.82	26.09	313.07	51.93
32	29.49	11.03	52.36	14.58	184.01	30.61
36	47.75	18.69	88.98	23.08	279.4	45.86
37	60.5	24.24	114.86	30.13	361.42	58.61
38	41.23	16.23	76.99	20.95	260.34	43.37
89	27.92	11.4	54.87	15.3	186.74	32.19
88	63.65	26.9	127.81	34.82	425.27	69.26
Sanga do Jobim suite, monzogranite, sample 115						
7	315.13	88.61	335.57	76.77	770.11	99.68
12	382.32	123.22	488.68	105.03	1050.73	139.06
19	538.43	156.37	593.38	133.41	1316.35	164.52

Spot	Dy	Ho	Er	Tm	Yb	Lu
27	1120.46	257.33	838.5	177.43	1585.23	182.16
29	653.04	177.59	655.53	133.62	1245.17	172.58
30	1241.09	306.07	1065.32	198.39	2208.78	287.83
31	2632.03	626.88	2023.01	390.6	3511.75	391.64
36	215.3	63.36	235.76	51.11	514.87	65.27
39	234.45	69.13	271.98	64.09	669.47	85.16
47	279.18	89.42	347.33	76.9	786.61	96
48	906.1	220.09	760.1	153.18	1407.87	173.72
50	660.16	163.62	585.22	122.1	1086.47	141.98
53	991.58	246.05	839.92	177.65	1711.29	215.27
54	128.17	49.06	215.06	51.98	538.23	77.96
55	493.42	148.65	563.03	123.29	1198.93	150.13
59	96.95	36.73	159.63	38.68	413.41	59.4
60	143.37	51.46	213.81	48.65	499.95	66.47
70	140.55	52.21	228.45	56.24	599.15	79.38
71	135.1	44.37	182.1	41.64	437.81	57.92
72	184.85	66.83	286.22	65.59	665.05	90.29

Serrinha Formation, para-amphibolite, sample 29

Spot	Dy	Ho	Er	Tm	Yb	Lu
7	264.88	87.87	363.7	83.08	925.93	108.35
8	160.26	53.82	232.02	57.19	647.95	74.65
9	158.7	55.57	230.79	53.98	549.68	70.98
10	110.01	37.61	150.75	33.2	337.66	52.88
11	261.72	88.43	356.85	82.39	858.93	100.16
36	158.61	54.69	228.09	56.14	645.11	76.71
13	83.07	30.45	128.89	31.44	351.02	42.97
14	70.89	24.84	109.9	26.81	313.76	41.59
15	181.82	65.5	276.49	65.08	691.82	83.41
16	23.8	8.81	40.03	10.74	131.56	17.4
28	16.66	6.22	29.81	8.28	104.77	14.53
17	400.05	131.3	532.49	119.31	1240.29	145.01
19	157.83	56.87	240.29	57.42	618.22	73.63
20	217.63	64.91	265.87	65.97	735.29	95.7

Serrinha Formation, garnet-biotite-plagioclase schist, sample 30B

Spot	Dy	Ho	Er	Tm	Yb	Lu
7	182.43	54.62	233.23	61.67	725.84	107.45
8	81.84	31.99	148.34	37.06	413.59	61.08
16	77.37	29.73	142.29	38.52	477.52	71.86
17	628.28	228.55	1063.74	275.17	3047	450.28
29	86.31	33.26	161.51	43.76	510.58	84.09
31	109.08	46.82	243.46	58.91	659.94	136.5
32	122.99	48.37	222.39	60.88	748.78	106.93
33	63.3	24.9	124.06	34.11	408.79	58.08
34	69.17	27.59	135.79	37.93	462.92	67.16
35	172.78	64.22	295.67	76.16	874	117.73
36	117.6	42.05	194.36	50.58	607.1	87.59
37	88.12	35.73	171.56	46.38	563.81	80.8
38	104.81	40.74	192.94	51.14	623.56	86.57
39	112.58	40.52	184.02	48.47	623.61	81.99
47	83.9	33.96	162.82	44.84	559.84	80.81
48	49.12	19.66	97.02	27.46	359.93	48.41
49	91.72	36.69	178.01	49.09	608.07	89.26
50	103.43	41.68	193.59	51.86	651.09	92.94
53	67.56	26.2	129.59	35.6	444.91	66.94
54	122.74	47.54	227.22	60.26	703.27	102.7

Spot	Dy	Ho	Er	Tm	Yb	Lu
55	94.14	34.92	161.82	43.25	513.57	70.31
56	177.89	69.89	316.84	81.5	951.49	130.52
57	60.6	22.4	105.59	28.55	351.48	52.24
58	145.28	57.05	268.49	71.1	860.52	122.4
60	84.45	34.23	164.17	43.7	528.55	73.22

Serrinha Formation, garnet-biotite-plagioclase schist, sample 48

Spot	Dy	Ho	Er	Tm	Yb	Lu
7	95.36	36.07	155.31	36.46	381.21	52.14
9	237.62	83.83	342.9	76.69	746.25	101.48
10	46.43	19.26	95.68	25.26	287.69	43.13
11	351.18	129.07	548.24	120.54	1181.19	169.54
12	61.82	24.98	116.52	29.47	340.95	50.42
13	32.66	13.56	66.92	19.29	251.7	39.72
17	61.43	23.41	114.02	30.83	382.81	57.2
31	105.75	44.14	213.89	57.36	681.9	100.03
32	141.4	50.12	222.24	52.68	546.79	78.25
36	119.91	44.17	193.84	46.47	521.38	68.85
37	110.35	40.53	174.01	42.97	466.19	61.07
39	57.39	25.45	133.08	39.26	522.67	81.68
40	191.64	77.19	359.9	89.79	992.64	138.46
38	77.02	27.68	123.04	29.34	315.57	48.47
34	135.94	47.61	208.81	48.85	511.73	93.35
33	49.66	20.14	99.8	27.53	339.83	53.21
30	96.34	37.59	170.63	43.22	477.88	64.41
29	192.57	66.01	259.76	55.91	541.07	68.84
28	104.69	37.59	172.71	46.61	564.05	87.74
27	265.24	100.16	436.14	104.25	1085.66	136.91
20	77.37	30.85	147.39	37.3	440.54	64.06
19	201.23	78.41	347.38	73.09	673.61	129.57
17	73.99	32.31	163.33	44.34	545.79	82.72
16	133.84	54.11	266.56	70.01	846.7	127.93
15	225.71	90.4	438.41	113.51	1264.34	190.31
8	123.03	41.27	163.81	36.93	379.23	49.58
74	142.73	58.61	284.99	75.24	880.22	130.2
59	162.86	62.74	296.99	78.94	914.64	129.73

Serrinha Formation, staurolite-garnet-biotite-plagioclase schist, sample 113

Spot	Dy	Ho	Er	Tm	Yb	Lu
7	263.03	77.96	310.19	75.81	875.17	110.04
10	264.3	81.79	341.74	78.96	842.43	123.23
11	110.16	44.92	221.29	63.02	798.88	110.12
12	202.97	75.5	348.22	90.1	1064.97	140.51
13	153.05	40.56	171.56	45.1	533.56	76.83
14	422.99	150.98	638.43	151.03	1575.27	192.34
15	234.45	80.5	345.89	82.85	944.68	119.05
18	62.91	24.53	112.68	29.61	332.5	47.11
BC020	52.51	19.62	93	25.2	315.01	46.12
20	102.16	36.96	160.87	40.03	445.17	62.13
27	73.3	29.3	141.52	38.48	478.47	61.88
28	67.04	26.33	128.63	34.73	421.35	63.08
BC024	166.76	53.33	208.72	49.83	532.15	63.09
BC025	179.7	72.67	340.33	90.92	1043.05	134.19
BC036	89	32.94	142.69	36.65	420.06	53.82
32	321	123.97	563.47	141.48	1652.2	201.03
34	70.1	28.2	138.69	39.44	512.78	73.2
35	50.89	19.16	91.93	24.62	291	50.54

Spot	Dy	Ho	Er	Tm	Yb	Lu
37	260.43	97.48	452.27	114.8	1294.72	179.9
38	106.3	41.29	197.63	55.85	702.47	97.74
39	114.47	49.31	241.96	66.32	719.57	127.67
BC043	73.51	25.65	111.99	27.92	316.05	38.42
50	62.04	24.1	113.79	31.63	392.77	53.36
51	83.9	21.44	88.76	24.75	320.22	46.98
53	140.79	58.73	297.58	81.9	960.82	146.72
54	87.93	33.97	168.37	47.55	593.63	88.43
55	100.66	40.88	191.1	52.82	619.42	84.82
56	222.18	74.48	313.45	78.55	839.33	105.42
57	107.6	43.47	197.23	49.48	510.08	78.43

#Parte 3

Spot	Total REE	LREE	MREE	HREE	LaN/SmN	LaN/YbN	GdN/YbN	Eu/Eu*
Vila Nova Suite, metatonalite, sample 114								
7	1186.63	11.44	12.08	439.94	0.021	0.000	0.024	0.42
8	1386.30	12.38	20.72	629.46	0.013	0.000	0.029	0.50
10	1260.09	11.27	15.49	513.95	0.014	0.000	0.027	0.44
11	1346.14	12.59	19.71	594.64	0.025	0.000	0.032	0.46
13	1326.59	12.99	15.19	580.78	0.000	0.000	0.023	0.46
14	1519.79	16.82	20.66	757.07	0.043	0.000	0.024	0.49
15	962.56	19.83	20.01	205.37	0.165	0.010	0.077	0.66
16	1333.61	15.89	16.78	598.75	0.012	0.000	0.025	0.42
17	1036.77	6.91	7.25	319.15	0.000	0.000	0.019	0.48
19	1367.93	15.71	17.83	617.61	0.008	0.000	0.026	0.47
27	1487.59	16.50	20.43	724.15	0.029	0.000	0.025	0.47
28	1460.72	31.27	37.82	667.89	0.087	0.002	0.047	0.60
30	1386.24	13.45	22.68	624.46	0.022	0.000	0.035	0.45
31	1368.71	18.53	21.67	610.92	0.082	0.001	0.030	0.53
33	1306.22	11.34	20.51	562.71	0.006	0.000	0.033	0.48
32	1072.89	16.34	17.23	322.08	0.137	0.004	0.041	0.60
36	1285.24	45.90	26.23	503.76	0.297	0.008	0.041	0.52
37	1422.50	31.26	26.48	649.76	0.211	0.003	0.035	0.57
38	1278.47	15.04	18.90	459.11	0.172	0.002	0.035	0.56
89	1131.05	10.34	12.00	328.42	0.098	0.001	0.031	0.51

Spot	Total REE	LREE	MREE	HREE	LaN/SmN	LaN/YbN	GdN/YbN	Eu/Eu*
88	1501.42	13.80	20.65	747.71	0.000	0.000	0.024	0.44
Average values	1306.07	17.12	19.54	545.60	0.069	0.002	0.033	0.50
Sanga do Jobim suite, monzogranite, sample 115								
7	2758.21	126.41	205.50	1685.87	0.059	0.005	0.110	0.49
12	3276.02	58.55	187.54	2289.04	0.029	0.001	0.087	0.33
19	4000.17	155.71	246.64	2902.46	0.083	0.004	0.077	0.57
27	6561.97	684.12	1022.70	4161.11	0.052	0.012	0.251	0.50
29	4691.41	376.07	583.94	3037.53	0.048	0.008	0.192	0.44
30	8333.35	982.16	1351.16	5307.48	0.062	0.014	0.244	0.56
31	14510.92	1837.53	2410.37	9575.91	0.064	0.015	0.267	0.61
36	2001.42	47.79	123.19	1145.67	0.048	0.003	0.110	0.35
39	2302.88	76.30	138.66	1394.28	0.069	0.004	0.090	0.34
47	2568.99	50.28	143.97	1675.44	0.038	0.002	0.084	0.48
48	5646.75	569.14	751.48	3621.06	0.095	0.017	0.218	0.47
50	4354.44	349.21	558.28	2759.55	0.049	0.009	0.210	0.47
53	6242.06	502.50	861.59	4181.76	0.044	0.007	0.198	0.68
54	1806.32	14.87	41.13	1060.46	0.026	0.000	0.039	0.23
55	3814.00	134.83	305.11	2677.45	0.039	0.003	0.116	0.45
59	1527.40	5.97	33.64	804.80	0.004	0.000	0.042	0.22
60	1781.32	9.31	55.75	1023.71	0.025	0.000	0.057	0.25
70	1901.70	10.35	43.68	1155.98	0.039	0.000	0.037	0.20
71	1690.02	25.45	67.07	898.94	0.034	0.001	0.069	0.40
72	2127.89	10.04	66.47	1358.83	0.004	0.000	0.052	0.21
Average values	4094.86	301.329	459.893	2635.867	0.046	0.005	0.127	0.41
Serrinha Formation, para-amphibolite, sample 29								
7	2648.93	15.26	117.57	1833.81	0.002	0.000	0.064	0.38
8	1988.05	12.66	69.30	1225.89	0.002	0.000	0.053	0.41
9	1718.30	8.54	59.33	1119.70	0.008	0.000	0.055	0.17
10	1445.65	41.24	53.84	722.11	0.353	0.010	0.080	0.42
11	2548.32	13.73	107.48	1748.48	0.001	0.000	0.062	0.35
36	1304.70	12.32	73.03	1219.35	0.004	0.000	0.057	0.43

Spot	Total REE	LREE	MREE	HREE	LaN/SmN	LaN/YbN	GdN/YbN	Eu/Eu*
13	1362.49	5.65	27.42	667.84	0.000	0.000	0.040	0.24
14	1376.81	54.66	35.42	587.79	0.767	0.019	0.053	0.42
15	2109.29	15.99	72.49	1364.12	0.003	0.000	0.052	0.36
16	2637.19	17.52	9.95	232.34	0.000	0.000	0.037	0.46
28	2590.50	16.99	6.12	180.27	0.034	0.000	0.028	0.46
17	3481.74	40.48	177.99	2568.45	0.015	0.000	0.073	0.32
19	1988.41	23.51	67.50	1204.26	0.036	0.001	0.055	0.25
20	2550.02	191.27	215.37	1445.37	0.109	0.010	0.127	0.48
Serrinha Formation, garnet-biotite-plagioclase schist, sample 30B								
7	2927.75	583.58	254.78	1365.24	0.593	0.086	0.141	0.32
8	1551.58	33.26	27.77	773.90	0.156	0.002	0.033	0.25
16	1634.44	38.01	33.14	837.29	0.214	0.003	0.035	0.27
17	7835.94	871.03	541.86	5693.02	0.234	0.016	0.072	0.41
29	1748.99	55.74	41.99	919.51	0.246	0.005	0.038	0.30
31	2090.93	62.46	37.06	1254.71	0.370	0.003	0.028	0.22
32	2219.54	97.64	67.38	1310.34	0.341	0.009	0.040	0.35
33	1528.49	57.29	30.52	713.24	0.340	0.008	0.033	0.23
34	1628.10	62.58	32.63	800.56	0.284	0.006	0.030	0.31
35	2468.00	57.40	65.46	1600.56	0.142	0.002	0.037	0.39
36	2011.72	112.86	80.62	1099.28	0.400	0.018	0.057	0.30
37	1830.76	69.59	32.55	986.40	0.419	0.005	0.027	0.29
38	1893.93	29.41	38.54	1099.76	0.016	0.000	0.030	0.48
39	1969.90	81.63	61.41	1091.19	0.225	0.006	0.045	0.28
47	1751.64	23.18	25.13	966.17	0.014	0.000	0.023	0.29
48	1380.94	31.04	19.07	601.60	0.357	0.004	0.026	0.35
49	1905.16	79.82	36.37	1052.84	0.884	0.011	0.029	0.32
50	1944.87	36.80	38.67	1134.59	0.201	0.002	0.029	0.38
53	1661.80	127.04	33.70	770.80	1.026	0.024	0.033	0.31
54	2087.82	39.99	43.15	1263.73	0.059	0.001	0.030	0.30
55	1837.67	137.62	49.59	918.01	0.857	0.024	0.044	0.27

Spot	Total REE	LREE	MREE	HREE	LaN/SmN	LaN/YbN	GdN/YbN	Eu/Eu*
56	2583.94	57.33	64.54	1728.13	0.109	0.001	0.034	0.36
57	1379.72	13.51	26.16	620.86	0.042	0.001	0.036	0.53
58	2350.13	38.15	54.29	1524.84	0.113	0.001	0.030	0.45
60	1726.39	48.96	25.07	928.32	0.253	0.002	0.023	0.27
Serrinha Formation, garnet-biotite-plagioclase schist, sample 48								
7	1501.25	5.88	30.88	756.55	0.000	0.000	0.043	0.17
9	2443.39	37.20	95.56	1588.77	0.024	0.000	0.067	0.21
10	1278.03	10.42	13.09	517.45	0.091	0.000	0.024	0.19
11	3392.90	22.48	127.75	2499.76	0.031	0.000	0.056	0.15
12	1402.81	30.36	22.70	624.16	0.833	0.010	0.032	0.34
13	1183.32	17.41	10.50	423.85	0.889	0.006	0.021	0.36
17	1439.10	33.21	21.75	669.70	0.854	0.010	0.026	0.39
31	1970.50	21.56	30.22	1203.07	0.311	0.002	0.023	0.21
32	1906.26	36.20	54.02	1091.48	0.226	0.004	0.048	0.30
36	1823.86	14.57	44.05	994.62	0.006	0.000	0.043	0.27
37	1697.75	46.32	45.78	895.12	0.442	0.008	0.049	0.23
39	1616.73	20.46	14.65	859.53	0.000	0.000	0.013	0.46
40	2641.29	26.17	56.58	1849.62	0.005	0.000	0.029	0.45
38	748.44	92.46	34.86	621.12	1.501	0.039	0.052	0.31
34	1257.90	135.76	75.85	1046.29	0.623	0.024	0.062	0.88
33	1347.32	9.50	16.09	590.17	0.000	0.000	0.023	0.48
30	1653.45	18.03	32.35	890.07	0.043	0.000	0.034	0.24
29	1450.44	172.35	93.93	1184.16	1.004	0.040	0.085	0.06
28	1825.49	36.12	47.23	1013.39	0.124	0.002	0.037	0.83
27	2948.18	29.52	79.72	2128.36	0.012	0.000	0.038	0.10
20	1560.37	6.34	23.46	797.51	0.016	0.000	0.027	0.21
19	2336.51	26.99	71.29	1503.29	0.156	0.002	0.054	0.26
17	970.76	8.51	19.77	942.48	0.016	0.000	0.019	0.14
16	2322.86	10.43	38.26	1499.15	0.000	0.000	0.023	0.18
15	3170.57	49.18	68.81	2322.68	0.280	0.002	0.027	0.24
8	890.58	31.01	65.72	793.85	0.006	0.000	0.084	0.43
74	2348.23	13.57	40.30	1571.99	0.032	0.000	0.023	0.23

Spot	Total REE	LREE	MREE	HREE	LaN/SmN	LaN/YbN	GdN/YbN	Eu/Eu*
59	2432.31	13.38	50.66	1645.90	0.007	0.000	0.029	0.20
Serrinha Formation, staurolite-garnet-biotite-plagioclase schist, sample 113								
7	2752.87	96.63	184.02	1712.20	0.148	0.008	0.097	0.33
10	3188.97	460.36	238.44	1732.45	0.407	0.045	0.119	0.15
11	2162.17	20.92	30.89	1348.39	0.196	0.001	0.019	0.20
12	2823.17	18.79	70.04	1922.27	0.008	0.000	0.033	0.35
13	2128.65	164.33	190.48	1020.66	0.201	0.027	0.156	0.18
14	4056.32	42.36	150.99	3131.04	0.005	0.000	0.049	0.25
15	2694.78	48.81	104.60	1807.42	0.018	0.000	0.055	0.31
18	1403.72	5.16	20.42	609.34	0.069	0.001	0.031	0.17
BC020	601.81	30.19	20.16	551.46	0.641	0.007	0.031	0.42
20	1801.17	165.77	55.16	847.32	1.384	0.050	0.054	0.37
27	1558.89	12.03	21.39	822.95	0.039	0.000	0.022	0.25
28	1573.58	47.15	26.29	741.16	0.953	0.012	0.029	0.36
BC024	1195.97	36.74	85.35	1073.88	0.004	0.000	0.081	0.28
BC025	1939.82	24.12	54.83	1860.86	0.090	0.001	0.026	0.15
BC036	813.23	6.32	31.76	775.16	0.002	0.000	0.038	0.28
32	3893.98	34.92	94.40	3003.15	0.035	0.000	0.029	0.23
34	1723.05	69.94	25.74	862.41	1.911	0.020	0.023	0.47
35	1316.85	22.87	29.93	528.14	0.257	0.006	0.048	0.36
37	3274.93	39.56	106.32	2399.60	0.080	0.001	0.041	0.18
38	2045.78	30.30	39.78	1201.28	0.070	0.001	0.028	0.54
39	2114.89	11.38	26.20	1319.30	0.079	0.000	0.017	0.00
BC043	636.05	13.07	29.44	593.54	0.000	0.000	0.048	0.26
50	1462.93	12.09	22.38	677.69	0.000	0.000	0.029	0.39
51	1480.20	47.90	81.52	586.05	0.127	0.009	0.115	0.49
53	2477.39	24.15	38.63	1686.54	0.033	0.000	0.020	0.25
54	1816.58	27.24	32.34	1019.88	0.006	0.000	0.027	0.52
55	1904.70	22.07	34.52	1089.70	0.018	0.000	0.028	0.33
56	2470.42	24.58	101.24	1633.41	0.006	0.000	0.059	0.42
57	1805.47	7.23	32.27	986.29	0.000	0.000	0.035	0.07

References

Almeida, F.F.M., Hasui, Y. 1984. O Pré-Cambriano do Brasil. Editora Blücher, São Paulo. 374 p.

Amaral, L., Caxito, F.A., Pedrosa-Soareas, A.C., Queiroga, G., Babinski, M., Trindade, R., Lana, C., Chemale, F., 2020. The Ribeirão da Folha ophiolite-bearing accretionary wedge (Araçuaí orogen, SE Brazil): New data for Cryogenian plagiogranite and Metasedimentary rocks. Precambrian Research 336, 105522.

Arena, K.R., Hartmann, L.A., Lana, C. 2016. Evolution of Neoproterozoic ophiolites from the southern Brasiliano Orogen revealed by zircon U-Pb-Hf isotopes and geochemistry. Precambrian Research 285, 299-314.

Arena, K.R., Hartmann, L.A., Lana, C. 2017. Tonian emplacement of ophiolites in the southern Brasiliano Orogen delimited by U-Pb-Hf isotopes of zircon from metasomatites. Gondwana Research 49, 296-332.

Arena K.O., Hartmann, L.A., Lana, C. 2018. U-Pb-Hf isotopes and trace elements of metasomatic zircon delimit the evolution of the Capané ophiolite in the southern Brasiliano Orogen. International Geology Review 60 (7), 911-928.

Babinski, M., Chemale Jr., F., Hartmann, L.A., Van Schmus, W.R., Silva, L.Z. 1996. Juvenile accretion at 750-700 Ma in southern Brazil. Geology 24(5), 439-442.

Bahariya, G.A. 2018. Classification of the Neoproterozoic ophiolites of the Central Eastern Desert, Egypt based on field geological characteristics and mode of occurrence. Arabian Journal of Geosciences 11:313, 1-23.

Basei, M.A.S, Campos Neto, M.C., Castro, N.A., Nutman, A.P., Wemmer, K., Yamamoto, M.T., Hueck, M., Osako, L., Siga, O., Passarelli, C.R. 2011. Tectonic evolution of the Brusque Group, Dom Feliciano belt, Santa Catarina, Southern Brazil. Journal of South American Earth Sciences 32, 324-350.

Basei, M.A.S., Frimmel, H.E., Campos Neto, M.C., Ganade Araujo, C.E., Castro, N.A., Passarelli, C.R. 2018. The Tectonic History of the Southern Adamastor Ocean Based on a Correlation of the Kaoko and Dom Feliciano Belts. In: Siegesmund, S., Basei, M.A.S., Oyhantcabal, P., Oriolo, S. (eds). Geology of Southwest Gondwana. Regional Geology Reviews, Springer Nature, pp. 63-85.

Basei, M.A.S., Frimmel, H.E., Nutman, A.P., Preciozzi, F. 2008. West Gondwana amalgamation based on detrital zircon ages from Neoproterozoic Ribeira and Dom Feliciano Belts of South America and comparison with coeval sequences from SW Africa. In: Pankhurst, R.J., Trouw, R.A.J., Brito Neves, B.B., De Wit, M.J. (eds.), west Gondwana Pre-Cenozoic correlations across the south Atlantic region. Geological Society Special Publication 294, 239-256.

Bitencourt, M.F.A.S. 1983. Geologia, Petrologia e Estrutura dos Metamorfitos da Região de Caçapava do Sul, RS. MSc Thesis, UFRGS, Porto Alegre, pp. 161.

Blades, M.L., Foden, J., Collins, A.S., Alemu, T. Woldetinsae, G. 2019. The origin of the ultramafic rocks of the Tulu Dimtu Belt, western Ethiopia – do they represent remnants of the Mozambique Ocean? Geological Magazine 156 (1), 62-82.

Blichert-Toft, J. 2008. The Hf isotopic composition of zircon reference material 91500. Chemical Geology 253, 252-257.

Blichert-Toft, J., Puchtel, I.S. 2010. Depleted mantle sources through time: evidence from Lu-Hf and Sm-Nd isotope systematics of Archean komatiites. Earth and Planetary Science Letters 297, 598-606.

Bouvier, A., Vervoort, J.D., Patchett, P.J. 2008. The Lu-Hf and Sm-Nd isotopic composition of CHUR: constraints from unequilibrated chondrites and implications for the bulk composition of terrestrial planets. Earth and Planetary Science Letters 273, 48-57.

Brito Neves, B.B., Fuck, R.A., Pimentel, M.M. 2014. The Brasiliano collage in South America: a review. Brazilian Journal of Geology 44, 493-518.

Brown, M.T., Fuck, R.A., Dantas, E.L. 2020. Isotopic age constraints and geochemical results of disseminated ophiolitic assemblage from Neoproterozoic mélange, Central Brazil. Precambrian Research, 105581.

Caxito, F., Uhlein, A., Stevenson, R., Uhlein, G.J. 2014. Neoproterozoic oceanic crust remnants in northeast Brazil. Geology 42 (5), 387-390.

Cerva-Alves, T., Remus, M.V.D., Dani, N., Basei, M.A.S. 2017. Integrated field, mineralogical and geochemical characteristics of Caçapava do Sul alvikite and beforsite intrusions: A new Ediacaran carbonatite complex in southernmost Brazil. Ore Geology Reviews 88, 352-369.

Chemale Jr., F. 2000. Evolução Geológica do Escudo Sul-rio-grandense. In: Holz, M., De Ros, L.F. (Eds.), Geologia do Rio Grande do Sul. Centro de investigação do Gondwana, Universidade Federal do Rio Grande do Sul, Porto Alegre, Brasil, pp. 13-55.

Chemale Jr., F., Hartmann, L.A., Silva, L.C. 1995. Stratigraphy and tectonism of the Brasiliano Cycle in southern Brazil. Communs Geol. Surv. Namibia 10, 151-166.

Cherniak, D.J. 2000. Pb diffusion in rutile. Contributions to Mineralogy and Petrology 139, 198-207.

Corfu, F., Hanchar, J.M., Hoskin, P.W.O., Kinny, P. 2003. Atlas of zircon textures. Reviews in Mineralogy and Geochemistry 53, 469-500.

Deans, J.R.L., Yoshinobu, A.S. 2019. Geographically re-oriented magmatic and metamorphic foliations from ODP Hole 735B Atlantis Bank, Southwest Indian Ridge: Magmatic intrusion and crystal-plastic overprint in the footwall of an oceanic core complex. Journal of Structural Geology 126, 1-10.

Dhuime, B., Hawkesworth, C., Cawood, P. 2011. When continents formed. Science 331, 154-155.

El-Rahman, Y.A., Anbar, M.A., Li, X, Li, J., Ling, X., Wu, L., Masoud, A.E. 2019. The evolution of the Arabian-Nubian Shield and survival of its zircon U-Pb-Hf-O isotopic signature: A tale from the Um Had Conglomerate, central Eastern Desert, Egypt. Precambrian Research 320, 46-62.

Fernandes, L.A.D., Menegat, R., Costa, A.F.U., Porcher, C.C., Tommasi, A., Kraemer, G., Ramgrab, G.E., Camozzato, E. 1995. Evolução tectônica do Cinturão Dom Feliciano no Escudo Sul-Rio-Grandense: parte I – uma contribuição a partir do registro geológico. Revista Brasileira de Geociências 25 (4), 351-374.

Fragoso Cesar, A.R.S. 1991. Tectônica de placas no Ciclo Brasiliano: As orogenias dos Cinturões Dom Feliciano e Ribeira no Rio Grande do Sul. PhD thesis. Curso de Pós-Graduação em Geoquímica e Geotectônica, Instituto de Geociências, USP, pp. 362.

Ganade Araujo, C.E., Cordani, U.G., Agbossoumounde, Y., Caby, R., Basei, M.A.S., Weinberg, R., Sato, K. 2016. Tightening-up NE Brazil and NW Africa connections: New U–Pb/Lu–Hf zircon data of a complete plate tectonic cycle in the Dahomey Belt of the West Gondwana Orogen in Togo and Benin. Precambrian Research 276, 24-42.

Garavaglia, L., Bitencourt, M.F., Nardi, L.V.S. 2002. Cumulatic Diorites Related to Post-Collisional, Brasiliano/Pan-African Mafic Magmatism in the Vila Nova Belt, Southern Brazil. Gondwana Research 5 (2), 519-534.

Gastal, M.C., Lafon, J.M., Ferreira, F.J.F., Magro, F.U.S., Remus, M.V.D., Sommer, C.A. 2006. Reinterpretação do complexo intrusivo lavras do sul, RS, de acordo com os sistemas Vulcano-plutônicos de subsidência. Parte 1: geologia, geofísica e geocronologia ($^{207}Pb/^{206}Pb$ e $^{206}Pb/^{238}U$). Revista Brasileira de Geociências. 36 (1), 109-124.

Gerdes, A., Zeh, A. 2006. Combined U-Pb and Hf isotope LA-(MC)-ICP-MS analyses of detrital zircons: comparison with SHRIMP and new constraints for the provenance and age of an Armorican metasediment in Central Germany. Earth and Planetary Science Letters 249, 47-61.

Gerdes, A., Zeh, A. 2009. Zircon formation versus zircon alteration d new insights from combined U-Pb and Lu-Hf in-situ LA-ICP-MS analyses, and consequences for the interpretation of Archean zircon from the Central Zone of the Limpopo Belt. Chemical Geology 261, 230-243.

Gonçalves, G.O., Lana, C., Buick, I.S., Alkmin, F.F., Scholz, R., Queiroga, G. 2019. Twenty million years of post-orogenic fluid production and hydrothermal mineralization across the external Araçuaí orogen and adjacent São Francisco craton, SE Brazil. Lithos 342-343, 557-572.

Gonçalves, G.O., Lana, C., Scholz, R., Buick, I.S., Gerdes, A., Kamo, S.L., Corfu, F., Rubatto, D., Wiedenbeck, M., Nalini, H.A., Oliveira, L.C. 2018. The Diamantina monazite: a new low-Th reference material for microanalysis. Geostandards and Geoanalytical Research 42, 25–47.

Goñi, J.C. 1962. Origine des roches ultrabasiques et serpentineuses du précambrien de Rio Grande do Sul (Brésil). Mode de gisement et minéralisations. Esc. Geol. UFRGS 12, 7-91.

Goulart, R.V., Remus, M.V.D., Reis, R.S. 2013. Composição isotópica de Sr, C e O e geoquímica de ETRs das rochas carbonáticas do Bloco São Gabriel, Rio Grande do Sul. Pesquisas em Geociências 40, 75-97.

Gray, D.R., Foster, D.A., Meert, J.G., Goscombe, B.D., Armstrong, R., Trouw, R.A.J., Passchier, C.W. 2008. A Damara orogen perspective on the assembly of southwestern Gondwana. In: Pankhurst, R.J., Trouw, R.A.J., Brito-Neves, B.B., De Wit, M.J. (eds) West Gondwana Pre-Cenozoic Correlations Across the South Atlantic Region. Geological Society, London, Special Publications 294, 257-278.

Griffin, W.L., Belousova, E.A., Shee, S.R., Pearson, N.J., O'Reilly, S.Y. 2004. Archean crustal evolution in the northern Yilgarn Craton: U–Pb and Hf-isotope evidence from detrital zircons. Precambrian Research 131, 231-282.

Gubert, M.L., Philipp, R.P., Basei, M.A.S. 2016. The Bossoroca Complex, São Gabriel Terrane, Dom Feliciano Belt, southernmost Brazil: U-Pb geochronology and tectonic implications for the Neoproterozoic São Gabriel Arc. Journal of South American Earth Sciences 70, 1-17.

Hartmann, L.A., Leite, J.A.D., Silva, L.C., Remus, M.V.D., McNaughton, N.J., Groves, D.I., Fletcher, I.R., Santos, J.O.S., Vasconcellos, M.A.Z. 2000. Advances in SHRIMP geochronology and their impact on understanding the tectonic and metallogenic evolution of southern Brazil. Australian Journal of Earth Science 47 (5), 829-844.

Hartmann, L.A., Liu, D., Wang, Y., Massonne, H.J., Santos, J.O.S. 2008. Protolith age of Santa Maria Chico granulites dated on zircons from an associated amphibolite-facies granodiorite in southernmost Brazil. Anais da Academia Brasileira de Ciências 80, 543-551.

Hartmann, L.A., Philipp, R.P., Santos, J.O.S., McNaughton, N.J. 2011. Time frame of the 753–680 Ma juvenile accretion during the São Gabriel orogeny, Southern Brazilian shield. Gondwana Research 19, 84-99.

Hartmann, L.A., Santos, J.O.S. 2004. Predominance of high Th/U, magmatic zircon in Brazil Shield sandstones. Geology 32(1), 73-76.

Hartmann, L.A., Tindle, A., Bitencourt, M.F. 1990. O Metamorfismo de Fácies Anfibolito no Complexo Metamórfico Passo Feio, RS, com Base em Química dos Minerais. Pesquisas 17 (1-2), 62-71.

Hartmann, L.A., Werle, M., Michelin, C.R.L. Lana, C., Queiroga, G.N., Castro, M.P., Arena, K.R. 2019. Proto-Adamastor ocean crust (920 Ma) described in Brasiliano Orogen from coetaneous zircon and tourmaline. Geoscience Frontier 10 Issue 4, 1623-1633.

Hodel, F., Trindade, R.I.F., Macouin, M., Meira, V.T., Dantas, E.L., Paixão, M.A.P., Rospabé, M., Castro, M.P., Queiroga, G.N., Alkmim, A.R., Lana, C.C. 2019. A

Neoproterozoic hyper-extended margin associated with Rodinia's demise and Gondwana's build-up: The Araguaia Belt, central Brazil. Gondwana Research 66, 43-62.

Hueck, M., Oyhantçabal, P., Philipp, R.P., Basei, M.A.S., Siegesmund, S. 2018. The Dom Feliciano Belt in Southern Brazil and Uruguay. In: Siegesmund, S., Basei, M.A.S., Oyhantcabal, P., Oriolo, S. (eds). Geology of Southwest Gondwana. Regional Geology Reviews, Springer Nature, pp. 243-265.

Jackson, S.E., Pearson, N.J., Griffin, W.L., Belousova, E.A. 2004. The application of laser ablation inductively coupled plasma mass spectrometry to *in situ* U-Pb zircon geochronology. Chemical Geology 211, 47-69.

Janikian, L., Almeida, R.P., Trindade, R.I.F., Fragoso-Cesar, A.R.S., D'Agrella-Filho, M.S., Dantas, E.L., Tohver, R. 2008. The continental record of Ediacaran volcano-sedimentary successions in southern Brazil and their global implications. Terra Nova 20, 259-266.

Jost, H., Hartmann, L.A. 1984. Província Mantiqueira. In: Almeida, F.F.M. and Y. Hasui (ed.). O Pré-Cambriano do Brasil, pp. 345-368.

Kraemer, G. 1995. Evolução magmática e tectônica da suíte ortometamórfica Imbicuí, região de Lavras do Sul, RS. MSc Thesis, Instituto de Geociências, UFRGS, Porto Alegre, pp. 99.

Lana, C., Farina, F., Gerdes, A., Alkmim, A., Gonçalves, G.O., Jardim, A.C. 2017. Characterization of zircon reference materials via high precision U–Pb LA-MC-ICP-MS. Journal of Analytical Atomic Spectrometry 32 (10), 2011-2023.

Laux, J.H., Pimentel, M.P., Dantas, E.L., Armstrong, R., Armele, A., Nilson, A.A. 2004. Mafic magmatism associated with Goiás magmatic arc in the Anicuns region, Goiás, central Brazil: Sm-Nd isotopes and new ID-TIMS and SHRIMP U-Pb data. Journal of South American Earth Sciences 16, 599-614.

Laux., J.H., Pimentel, M.M., Dantas, E.L., Armstrong., R., Junges, S.L. 2005. Two neoproterozoic crustal accretion events in the Brasília belt, central Brazil. Journal of South American Earth Sciences 18, 183-198.

Leite, J.A.D., Hartmann, L.A., McNaughton, N.J., Chemale Jr., F. 1998. SHRIMP U/Pb Zircon geochronology of Neoproterozoic juvenile and crustal-reworked terranes in southernmost Brazil. International Geology Review 40, 688-705.

Lena, L.O.F., Pimentel, M.M., Philipp, R.P., Armstrong, R., Sato, K. 2014. The evolution of the Neoproterozoic São Gabriel juvenile terrane, southern Brazil based on high spatial resolution U-Pb ages and δ18O data from detrital zircons. Precambrian Research 247, 126-138.

Li, Z.X., Bogdanova, S.V., Collins, A.S., Davidson, A., De Waele, B., Ernst, R.E., Fitzsimons, I.C.W., Fuck, R.A., Gladkochub, D.P., Jacobs, J., Karlstrom, K.E., Lu, S., Natapov, L.M., Pease, V., Pisarevsky, S.A., Thrane, K., Vernikovsky, V. 2008.

Assembly, configuration, and break-up history of Rodinia: A synthesis. Precambrian Research 160, 179-210.

Lopes, C.G., Pimentel, M.M., Philipp, R.P., Gruber, L., Armstrong, R., Junges, S. 2015. Provenance of the Passo Feio complex, Dom Feliciano Belt: implications for the age of supracrustal rocks of the São Gabriel Arc, Southern Brazil. Journal of South American Earth Science 58, 9-17.

Luchi, M.G.L., Dopico, C.I.M., Wemmer, K., Siegesmund, S. 2018. Untangling the Neoproterozoic-Early Paleozoic Tectonic Evolution of the Eastern Sierras Pampeanas Hidden in the Isotopical Record. In: Siegesmund, S., Basei, M.A.S., Oyhantcabal, P., Oriolo, S. (eds). Geology of Southwest Gondwana. Regional Geology Reviews, Springer Nature, pp. 433-466.

Ludwig, K.R. 2003. Isoplot/Ex Version 3.00: A Geochronological Tool kit for Microsoft Excel. Berkeley Geochronology Center, Berkely, CA (Special Publication 4, 71 http://bgc.org/isoplot_etc/isoplot.html).

Mezger, K., Hanson, G.N., Bohlen, S.R. 1989. High-precision U-Pb ages of metamorphic rutile: application to the cooling history of high-grade terranes. Earth and Planetary Science Letters 96, 106-118.

Morel, M.L.A., Nebel, O., Nebel-Jacobsen, Y.J., Miller, J.S., Vroon, P.Z. 2008. Hafnium isotope characterization of the Gj-1 zircon reference material by solution and laser-ablation MC-ICPMS. Chemical Geology 255, 231-235.

Oliveira, C.H.E., Chemale Jr, F., Jelinek, A.R., Bicca, M.M., Philipp, R.P. 2014. U-Pb and Lu-Hf isotopes applied to the evolution of the late to post-orogenic transtensional basin of the Dom Feliciano belt, Brazil. Precambrian Research 246, 240-255.

Paim, P.S.G., Chemale Jr., F., Wildner, W. 2014. Development stages of the Camaquã Basin. Ciência e Natura (UFSM) 36, 183-193.

Paim., P.S.G., F., Lopes, R.C. 2000. A Bacia do Camaquã. In: Holz, M., De Ros, L.F. (Eds.), Geologia do Rio Grande do Sul: Centro de Investigação do Gondwana. Universidade Federal do Rio Grande do Sul, Porto Alegre, Brazil, pp. 231-274.

Pedrosa-Soares, A.C., Vidal, P., Leonardos, O.H., Brito-Neves, B.B. 1998. Neoproterozoic oceanic remnants in eastern Brazil: further evidence and refutation of an exclusively ensialic evolution for the Araçuaí–West Congo Orogen. Geology 26, 519-522.

Peixoto, C.A., Heilbron, M., Ragatky, D., Armstrong, R., Dantas, E., Valeriano, C.M., Simonetti, A. 2017. Tectonic evolution of the juvenile Tonian Serra da Prata magmatic arc in the Ribeira Belt, SE Brazil: Implications for early West Gondwana amalgamation. Precambrian Research 302, 221-254.

Pertille, J., Hartmann, L.A., Philipp., R.P. 2015a. Zircon U-Pb age constraints on the Paleoproterozoic sedimentary basement of the Ediacaran Porongos Group, Sul-Riograndense Shield, southern Brazil. Journal of South American Earth Sciences 63, 334-345.

Pertille, J., Hartmann, L.A., Philipp, R.P., Petry, T.S., Lana, C.C. 2015b. Origin of the Ediacaran Porongos Group, Dom Feliciano Belt, southern Brazilian Shield, with emphasis on whole rock and detrital zircon geochemistry and U-Pb, Lu-Hf isotopes. Journal of South American Earth Sciences 64, 69-93.

Pertille, J., Hartmann, L.A., Santos, J.O.S., McNaughton, N.J., Armstrong, R. 2017. Reconstructing the Cryogenian-Ediacaran evolution of the Porongos fold and thrust Belt, southern Brasiliano Orogen, based on zircon U-Pb-Hf-O isotopes. International Geology Review 59, 1532-1560.

Philipp, R.P., Hartmann, L.A., Lusa, M., Basei, M.A.S., Santos, J.O.S. 2014. Oldest age of magmatism in the Passinho Arc in the southwestern portion of Gondwana, Rio Grande do Sul, Brazil. In: 9th South American Symposium on Isotope Geology, Abstracts. São Paulo, pp.186.

Philipp, R.P., Machado, R., Nardi, L.V.S., Lafon, J.M. 2002. O magmatismo granítico Neoproterozóico do Batólito Pelotas no sul do Brasil: Novos dados e revisão de geocronologia regional. Revista Brasileira de Geociências 32, 277-29.

Philipp, R.P., Pimentel, M.M., Basei, M.A.S. 2018. The Tectonic Evolution of the São Gabriel Terrane, Dom Feliciano Belt, Southerm Brazil: The Closure of the Charrua Ocean. In: Siegesmund, S., Basei, M.A.S., Oyhantcabal, P., Oriolo, S. (eds). Geology of Southwest Gondwana. Regional Geology Reviews, Springer Nature, pp. 243-265.

Pimentel M.M., Fuck R.A. 1992. Neoproterozoic crustal accretion in central Brazil. Geology 20, 375-379.

Remus, M.V.D. 1990. Geologia e Geoquímica do Complexo Cambaizinho, São Gabriel, RS. MSc thesis. Instituto de Geociências, UFRGS, Porto Alegre, pp. 267.

Remus, M.V.D., Hartmann, L.A., Formoso, M.L.L. 1993. Os padrões de Elementos Terras Raras (ETR) e a afinidade geoquímica komatiítica dos xistos magnesianos e rochas associadas do Complexo Cambaizinho, São Gabriel-RS. Revista Brasileira de Geociências 23 (4), 370-387.

Remus, M.V.D., Hartmann, L.A., McNaughton, N.J., Groves, D.I., Fletcher, I.R. 2000. The link between hydrothermal epigenetic copper mineralization and the Caçapava Granite of the Brasiliano Cycle in southern Brazil. Journal of South American Earth Sciences 13, 191-216.

Remus, M.V.D., McNaughton, N.J., Hartmann, L.A., Koppe, J.C., Fletcher, I.R., Groves, D.I., Pinto, V.M. 1999. Gold in the Neoproterozoic juvenile Bossoroca Volcanic Arco f southernmost Brazil: isotopic constraints on timing and sources. Journal of South American Earth Sciences 12, 349-366.

Rudnick, R.L., Gao, S. 2003. Composition of the continental crust. In: Rudnick, R.L. (ed.), Treatise on Geochemistry. Elsevier-Pergamon, Oxford, pp. 1-64.

Saalmann K., Gerdes A., Lahaye Y., Hartmann L.A., Remus M.V.D., Laufer A. 2011. Multiple accretion at the eastern margin of the Rio de la Plata craton: the prolonged

Brasiliano orogeny in southernmost Brazil. International Journal of Earth Sciences 100(2-3), 355-378.

Saalmann, K., Hartmann , L.A., Remus, M.V.D., Koester, E., Conceição, R.V. 2005a. Sm-Nd isotope geochemistry of metamorphic volcano-sedimentary successions in the São Gabriel Block, southernmost Brazil: evidence for the existence of juvenile Neoproterozoic ocean crust to the east of the Rio de la Plata craton. Precambrian Research 136, 159-175.

Saalmann, K., Remus, M.V.D., Hartmann, L.A. 2005b. Geochemistry and crustal evolution of volcano-sedimentary successions and orthogneisses in the São Gabriel Block, southernmost Brazil - Relics of Neoproterozoic magmatic arcs. Gondwana Research 8 (2), 143-161.

Saalmann, K., Remus, M.V.D., Hartmann, L.A. 2006. Tectonic evolution of the Neoproterozoic São Gabriel block, southern Brazil: Constraints on Brasiliano Orogenic evolution of the Rio de La Plata cratonic margin. Journal of South American Earth Sciences 21, 204-227.

Santos, M.M., Lana, C., Scholz, R., Buick, I.S., Kamo, S., Corfu, F., Queiroga, G. 2020. LA-ICP-MS U-Pb dating of rutiles associated with hydrothermal mineralization along the southern Araçuaí Belt, SE Brazil. Journal of South American Earth Science, submitted.

Santos, M.M., Lana, C., Scholz, R., Buick, I., Schmitz, M.D., Kamo, S.L., Gerdes, A., Corfu, F., Tapster, S., Lancaster, P., Storey, C.D., Basei, M.A.S., Tohver, E., Alkmim, A., Nalini, H., Krambrock, K., Fantini, C., Wiedenbeck, M. 2017. A new appraisal of Sri Lankan BB zircon as a reference material for LA-ICP-MS U-Pb geochronology and Lu-Hf isotope tracing. Geostandards and Geoanalytical Research 41(3), 335-358.

Schannor, M., Lana, C., Fonseca, M.A. 2019. São Francisco-Congo Craton break-up delimited by U-Pb-Hf isotopes and trace-elements of zircon from metasediments of the Araçuaí Belt. Geoscience Frontiers 10, 611-628.

Silva, L.C., McNaughton, N.J., Armstrong, R., Hartmann, L.A., Fletcher, I.R. 2005. The neoproterozoic Mantiqueira Province and its African connections: a zircon-based U-Pb geochronologic subdivision for the Brasiliano/Pan-African systems of orogens. Precambrian Research 136, 203-240.

Sláma, J., Kosler, J., Condon, D.J., Crowely, J.L., Gerdes, A., Hanchar, J.M., Horstwood, M.S.A., Morris, G.A., Nasdala, L., Norberg, N., Schaltegger, U., Schoene, B., Tubrett, M.N., Whitehouse, M.J. 2008. Plesovice zircon - a new natural reference material for U-Pb and Hf isotopic microanalysis. Chemical Geology 249, 1-35.

Söderlund, U., Patchett, P.J., Vervoort, J.D., Isachsen, C.E. 2004. The [176]Lu decay constant determined by Lu-Hf and U-Pb isotope systematics of Precambrian mafic intrusions. Earth and Planetary Science Letters 219, 311-324.

Soliani Jr., E. 1986. Os dados geocronológicos do Escudo Sul-riograndense e suas implicações de ordem geotectônica. PhD thesis. Curso de Pós-Graduação em Geociências, USP. São Paulo, pp. 425.

Stakes, D., Mevel, C., Cannat, M., Chaput, T. 1991. Metamorphic stratigraphy of hole

735B. In: Von Herzen, R., Robinson, P.T., Adamson, A.C., Becker, K., Bloomer, S.H., Cannat, M., Dick, H.J.B. (eds.). Proceedings of the Ocean Drilling Program, Scientific Results, College Station 118, 153–180; https://doi.org/10.2973/odp.proc.sr.118.127.1991.

Stern, R.J., Johnson, P.R., Kröner, A., Yibas, B. 2004. Neoproterozoic ophiolites of the Arabian-Nubian shield. In: Kusky, T.M. (Ed). Precambrian Ophiolites and Related Rocks. Developments in Precambrian Geology 13, 95-128.

Stewart, J.H. 2009.Reconstruction Rodinia by fitting Neoproterozoic continental margins. U. S. Geological Survey. Open-File Report 2009-1191; http://pubs.usgs.gov/of/2009/1191/]

Strieder, A.J., Roldão, D.G., Hartmann, L.A. 2000. The Palma Volcano-Sedimentary Supersuite, Precambrian Sul-Riograndense Shield, Brazil. International Geology Review 42 (11), 984-999.

Sun, S.S., McDonough, W.F. 1989. Chemical and isotopic systematics of oceanic basalts: implications for mantle composition and processes. In: Saunders, A.D., Norry, M. (Eds.). Magmatism in Ocean Basins, Geological Society of London, Special Publication 42, 313-345.

Van Achterbergh, E., Ryan, C.G., Jackson, S.E., Griffin, W.L. 2001. Data reduction software for LA–ICP–MS. In: Sylvester, P.J. (ed.), Laser Ablation-ICP Mass Spectrometry in the Earth Sciences: Principles and Applications. Mineralogical Association of Canada, Short Course, Ottawa, Ontario 29, 239-243.

Vedana, L.A., Philipp, R.P., Basei, M.A.S. 2018. Tonian to early Cryogenian synorogenic basin of the São Gabriel Terrane, Dom Feliciano Belt, southernmost Brazil. International Geology Review 60 (1), 109-133.

Vedana, L.A., Philipp, R.P., Sommer, C.A. 2017. Post-collisional basalts of the Acampamento Velho Formation, Camaquã Basin, São Gabriel Terrane, southernmost Brazil. Brazilian Journal of Geology 47(3), 467-489.

Vervoort, J.D., Kemp, A.I.S. 2016. Clarifying the zircon Hf isotope record of crust–mantle evolution. Chemical Geology 425, 65-75.

Werle, M. 2019. Evolução mineralógica da porção sul do ofiolito Bossoroca e datação U-Pb do zircão dos granitos Cerro da Cria e Ramada, Terreno São Gabriel. Trabalho de Conclusão de Curso. Instituto de Geociências, UFRGS, Porto Alegre, pp. 100.

Whitney, D.L., Evans, B.W. 2010. Abbreviations for names of rock-forming minerals. American Mineralogist 95, 185-187.

Will, T.M., Gaucher, C., Ling, X.-X., Li, X.-H., Frimmel, H.E. 2019. Neoproterozoic magmatic and metamorphic events in the Cuchilla Dionisio Terrane, Uruguay, and possible correlations across the South Atlantic. Precambrian Research 320, 303-322.

Woodhead, J.D., Hergt, J.M. 2005. A preliminary appraisal of seven natural zircon reference materials for in situ Hf isotope determination. Geostandards and Geoanalytical Research 29, 183-195.

Zack, T., Kooijman, E. 2017. Petrology and Geochronology of Rutile. In: Kohn, M.J., Engi, M., Lanari, P. Petrochronology: Methods and applications. Reviews in Mineralogy and Geochemistry 83, 443-467.

Artigo 2 – Tiara CERVA-ALVES, Léo Afraneo HARTMANN, Gláucia Nascimento QUEIROGA, Cristiano LANA, Marcos Paulo de CASTRO, Luis Antonio Cruz MACIEL, Marcus Vinícius Dorneles REMUS. 2021. *Metamorphic evolution of the juvenile Serrinha forearc basin in the southern Brasiliano Orogen. Precambrian Research*, v. 365, 106394.

https://doi.org/10.1016/j.precamres.2021.106394

Metamorphic evolution of the juvenile Serrinha forearc basin in the southern Brasiliano Orogen

T. Cerva-Alves [a] ✉, L.A. Hartmann [a], G.N. Queiroga [b], C. Lana [b], M.P. Castro [b], L.A.C. Maciel [c], M.V.D. Remus [a]

[a] Instituto de Geociências, Universidade Federal do Rio Grande do Sul, Avenida Bento Gonçalves 9500, Brazil

[b] Departamento de Geologia, Escola de Minas, Universidade Federal de Ouro Preto, Morro do Cruzeiro 35400-000 Ouro Preto, Minas Gerais, Brazil

[c] Agência Nacional de Mineração, Rua Washington Luiz, 815 90010-460 Porto Alegre, Rio Grande do Sul, Brazil

ABSTRACT

Understanding the accretion of an oceanic island arc to a craton is a major issue in unravelling the evolution of the continents. P-T-t conditions registered in metamorphic rocks, the boron isotopic compositions of tourmaline provide essential information to delimit the accretionary processes. The Tonian-Cryogenian São Gabriel Terrane is a prominent juvenile structure in the southern Brasiliano Orogen that records key information about accretionary processes. Limited previous studies have investigated the São Gabriel Terrane, with little presently known about the metamorphic conditions. To pursue the objective, we combined multiple methods, including pseudosection modeling, U-Pb garnet geochronology and $\delta^{11}B$ isotopes of tourmaline applied to one key sample from the Serrinha Formation of the São Gabriel Terrane. The recorded peak P-T conditions occurred at 4.5-5.1 kbar and 536-555 °C. U-Pb dating of low-U (<1 ppm) garnet yielded a lower intercept age of 721 ± 14 Ma for the bulk garnet growth. Dravite isotopic $\delta^{11}B$ (+0.51 to +3.39) compositions indicate oceanic crust components present in the island arc rocks. The calculated P-T conditions correspond to the metamorphic peak from heat pulses during burial events. Collision and thrusting of the São Gabriel arc against and over the Rio de La Plata Craton occurred at 721 ± 14 Ma. The evaluation of the parameters obtained in this study indicate a Barrovian-type evolution and a Late Tonian age of metamorphism for the Serrinha Basin. The sedimentation of the Serrinha Basin occurred in a forearc basin of the São Gabriel island arc. Collision of the oceanic arc with the craton is thus better constrained. Our study contains one point in the evolution of the protracted, complex amalgamation of the supercontinent Gondwana during the Brasiliano Orogeny.

1. Introduction

Accretionary complexes are key geological features that mark the boundaries of tectonic plates (Condie, 2007; Kusky *et al.*, 2013). Many of these complexes comprise a combination of marine sediments from the downgoing slab of oceanic crust and the erosional products of volcanic island arcs formed on the overriding plate (Isozaki *et al.*,

1990; Cawood *et al.*, 2009). Studies along modern subduction zones indicate that some sedimentary packages, originally deposited on the oceanic plate, are subducted together with oceanic crust; whereas a large proportion of accreted sediments, attached to the upper plate, form volumetrically significant units in accretionary orogens (Underwood and Laughland, 2001; Safonova, 2017; Raymond *et al.*, 2019). The sediments themselves may record a full metamorphic evolution of the subducting slab.

Many old accretionary complexes are sandwiched between accreted terrains and record direct information about the timing of subduction and the full metamorphic evolution of tectonic accretion (Kimura and Ludden, 1995; Wakita and Metcalfe, 2005; Wakita, 2015). For instance, the metamorphic evolution of accretionary prisms has been described from the New England Fold Belt (Dirks *et al.*, 1993), Arabian-Nubian Shield (Stern, 2018; Abd El Rahman *et al.*, 2019), and the Anti-Atlas Complex (Saquaque *et al.*, 1989; Hodel *et al.*, 2020). In Brazil, the rearrangement of continental masses in the Neoproterozoic led to the development of the 900-550 Ma Brasiliano Orogeny and included accretion of juvenile terranes (Pimentel and Fuck, 1992; Caxito *et al.*, 2014, 2021). The collage of an intra-oceanic arc with ophiolite mélanges and forearc basin is particularly well documented in the southern portion of the Brasiliano Orogen, in the São Gabriel Terrane (Hartmann *et al.*, 2011, 2021; Arena *et al.*, 2016, 2017).

The São Gabriel Terrane is one of the most significant exposures of Neoproterozoic juvenile terranes in South America. The terrane contains ophiolitic, plutonic- and metavolcanosedimentary rocks, metamorphosed under greenschist to amphibolite metamorphic facies (Remus, 1990; Remus *et al.*, 2000; Saalmann *et al.*, 2006). However, pressure-temperature conditions required to fully construct the evolution of the southern Brasiliano Orogeny are yet to be constrained. Furthermore, the pool of metamorphic U-Pb ages available for the region is limited, which leaves the timing of subduction and tectonic accretion of the terrane largely unresolved.

We focus our study on the origin and metamorphic evolution of the Serrinha accretionary basin, in the northern part of the São Gabriel Terrane. We determined the metamorphic P-T evolution of the accreted sedimentary rocks and constrained the temporal setting of tectonic accretion. The adopted methods included pseudosection modeling and LA-ICP-MS U-Pb garnet dating of one selected garnet-staurolite schist. In addition, the novel approach of boron isotopes of tourmaline was used to identify

the forearc depositional environment of the metasedimentary rocks. The integrated information has fundamental implications about terrane accretion in the southern Brasiliano Orogeny, particularly with regard to the thrusting of the São Gabriel Terrane over the Rio de La Plata Craton.

2. Geological setting

Neoproterozoic continental and oceanic environments are recognized in the Brasiliano orogenic cycle during the assembly of West Gondwana (Basei *et al.*, 2010; Santiago *et al.*, 2020). The Dom Feliciano Belt is part of this orogenic system and is exposed in the southernmost portion of Brazil and eastern Uruguay (Fig. 1a), composing the Kaoko-Dom-Feliciano-Gariep orogenic system (De Toni *et al.*, 2020). The evolutionary history of the Dom Feliciano Belt started at 950-930 Ma with the opening of the proto-Adamastor Ocean and associated oceanic crust generation (Arena *et al.*, 2016; Hartmann *et al.*, 2019). The closure of this ocean resulted in the collision of magmatic arcs at 890-680 Ma, followed by the collision between the Rio de La Plata and Kalahari cratons at 600-550 Ma (Hueck *et al.*, 2018). The Sul-Riograndense Shield in the central portion of the Dom Feliciano Belt is composed of several major units (Hartmann *et al.*, 2008), including: (1) Paleoproterozoic basement fragments of the Rio de La Plata Craton; (2) the Tonian, juvenile São Gabriel Terrane associated with ophiolites and oceanic magmatic arcs; (3) the Porongos fold and thrust belt (Pertille *et al.*, 2017), which is composed of metavolcanosedimentary rocks, with magmatic events recorded at ca. 809, 807 and 773 Ma having a crustal magmatic reservoir signature (εHf = -21 to -10), and exposure of gneiss domes of Paleoproterozoic basement; (4) the Pelotas Batholith granitic suites (~630-550 Ma; Hueck *et al.*, 2018); and (5) the foreland Camaquã Basin, which formed at ~630-470 Ma (Borba *et al.*, 2008; Maraschin *et al.*, 2010).

The São Gabriel Terrane is composed of ophiolitic and plutonic-volcanosedimentary rocks. The ophiolites represent the Tonian-Cryogenian oceanic crust and mantle (ca. 923-723 Ma) (Arena *et al.*, 2016, 2017; Hartmann *et al.*, 2019). The main island arcs are the Passinho (ca. 879 Ma; Leite *et al.*, 1998) and the São Gabriel (ca. 794-700 Ma; Saalmann *et al.*, 2006; Hartmann *et al.*, 2011) arcs, formed during 200 Ma of subduction. The São Gabriel Terrane was intruded by Ediacaran granites (ca. 610-540 Ma; Leite *et al.*, 1998; Remus *et al.*, 1999, 2000; Werle *et al.*,

2020). Carbonatite occurrences were described intruding the Vacacaí Complex near to the Caçapava do Sul shear zone (603 Ma; Cerva-Alves *et al.*, 2017). Ophiolitic slivers also occur in the Porongos fold and thrust belt (Arena *et al.*, 2018; Ramos *et al.*, 2020). Magnetoteluric (Bologna *et al.*, 2019) and isotopic studies (Remus *et al.*, 1999; Arena *et al.*, 2017; Werle *et al.*, 2020) indicate the presence of craton underneath the São Gabriel Terrane.

Considering infrastructure-superstructure thermomechanical models (Culshaw *et al.*, 2006; Stern, 2018) and zircon U-Pb-Hf data, the São Gabriel Terrane is composed of two main arc associations: the Cambaí and the Vacacaí Complexes. The Cambaí Complex corresponds to the infrastructure including diorite-tonalite-trondhjemite-granodiorite series from the Vila Nova Suite (Hartmann *et al.*, 2011) and syntectonic granitoids from the Lagoa da Meia Lua and the Sanga do Jobim suites (Leite *et al.*, 1998; Saalmann *et al.*, 2006, 2011; Hartmann *et al.*, 2011).

Crystallization ages of the Vila Nova Suite were constrained by U-Pb zircon geochronology between 794 ± 6 Ma and 701 ± 9.7 Ma (Leite *et al.*, 1998; Hartmann *et al.*, 2011; Saalmann *et al.*, 2011). Values of εHf (+10.1 to +7.4; Cerva-Alves *et al.*, 2020) indicate a depleted mantle derived signature. Ages of emplacement of the Sanga do Jobim Suite range between 704 ± 3 Ma and 673.9 ± 6.8 Ma (Remus, 1990; Hartmann *et al.*, 2011; Cerva-Alves *et al.*, 2020). The εHf values (+2.5 to +9.2; Cerva-Alves *et al.*, 2020) indicate a first phase of continent proximity and influence. The Vacacaí Complex corresponds to the supracrustal portion of the arc and consists of volcanosedimentary successions (Chemale Jr., 2000; Saalmann *et al.*, 2011). This group includes the Campestre, Bela Vista, Pontas do Salso and Serrinha Formations and part of the Passo Feio Complex (Bitencourt, 1983; Remus *et al.*, 1999; Chemale *et al.*, 1995). Zircon ages of volcanic rocks from the Bela Vista and Campestre formations range between 767.2 ± 2.9 and 753 ± 2 Ma (Machado *et al.*, 1990; Remus *et al.*, 1999; Gubert *et al.*, 2016; Arena *et al.*, 2017). Mafic and ultramafic rocks in ophiolites were described from the São Gabriel Terrane (Fig. 1b) as obducted slivers onto both infrastructure and superstructure (Arena *et al.*, 2017, 2020; Hartmann *et al.*, 2021; Massuda *et al.*, 2020).
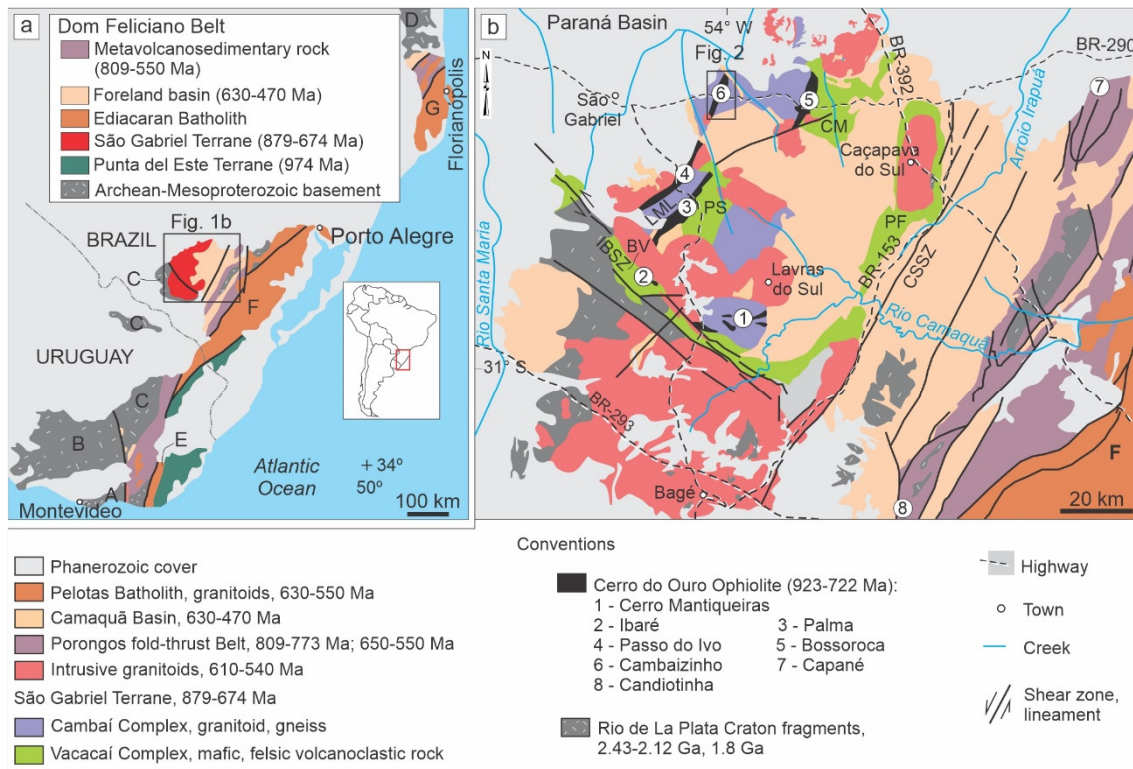
Fig. 1. (a) Tectonostratigraphic terranes of the Uruguayan and southern Brazilian Shields showing the Dom Feliciano Belt and cratonic areas (modified from Hartmann *et al.*, 2019; Will *et al.*, 2019). Cratonic ages are from Hartmann *et al.* (2001), Oyhantçabal *et al.* (2005); Punta del Este Terrane ages obtained from Preciozzi *et al.* (2001); São Gabriel Terrane ages are from Leite *et al.* (1998), Cerva-Alves *et al.* (2020); foreland basin ages are from Borba *et al.* (2008), Maraschin *et al.* (2010); metavolcanosedimentary rocks from Pertille *et al.* (2017). A = Tandilia Terrane; B = Piedra Alta Terrane; C = Nico Pérez Terrane; D = Luís Alves Terrane; E = Aiguá Batholith; F = Pelotas Batholith; G = Florianópolis Batholith. (b) Geological map of the Sul-Riograndense Shield, including São Gabriel Terrane and fragments of Nico Pérez Terrane and Porongos fold-thrust Belt with studied area indicated (modified from Arena *et al.*, 2016; Hartmann *et al.*, 2019; Haag *et al.*, 2020). Ages of the Rio de La Plata Craton are from Girelli *et al.* (2018), ages of the São Gabriel Terrane from Leite *et al.* (1998), Cerva-Alves *et al.* (2020); intrusive granitoid ages from Arena *et al.* (2017), Werle *et al.* (2020); Porongos fold-thrust belt ages from Pertille *et al.* (2017); Camaquã Basin ages from Borba *et al.* (2008), Maraschin *et al.* (2010); Pelotas Batholith ages from Hueck *et al.* (2018). IBSZ = Ibaré shear zone; CSSZ = Caçapava do Sul shear zone; BV = Bela Vista Formation; CM = Campestre Formation; LML = Lagoa da Meia Lua Suite; PF = Passo Feio Complex; PS = Pontas do Salso Formation.

The Serrinha Formation is composed of paragneisses (biotite gneiss, garnet-biotite gneiss), schists (biotite schist, garnet-biotite-plagioclase schist with or without staurolite), and banded amphibolites. These rocks form elongated, continuous tabular bodies about 1 km wide and 11 km long in the Cambaizinho Creek region, dipping to

the northwest (N30ºE/60º to 85º) (Fig. 2). This main orientation of the Serrinha Formation metasedimentary bodies is also observed in the Cambaizinho ophiolite and synorogenic Sanga do Jobim monzogranite units. The sedimentary rocks of the Serrinha Formation formed in a forearc basin related to accretionary environment in the São Gabriel arc (Cerva-Alves *et al.*, 2020), presently located in the western portion of the São Gabriel Terrane. The Serrinha Formation sedimentary environment is indicated by the detrital zircon age distribution (Cawood *et al.*, 2012). A maximum depositional age of ~650 Ma was established for this basin (Lena *et al.*, 2014; Cerva-Alves *et al.*, 2020).

Previous petrographic investigations of metasedimentary sequences in the São Gabriel Terrane identified three ductile structures and one brittle-ductile structure (Remus, 1990; Saalmann *et al.*, 2006). A first deformational event (D1) was locally recognized in the metapelitic rocks as quartz segregations and quartz veins, which developed parallel to the first foliation and formed from a pressure solution of quartz (Saalmann *et al.*, 2006). Two main metamorphic flat-lying fabrics (Sn banding transposed into Sn+1) were described (Remus, 1990) in the Serrinha Formation associated with two main regional metamorphic events and respective mineral assemblages: D2, M2 (amphibolite facies): biotite + garnet + staurolite + muscovite + quartz + plagioclase; and D3, M3 (greenschist facies): chlorite + muscovite + epidote + carbonate. Late semi-brittle thrusting formed locally ductile shear zones (Saalmann *et al.*, 2006).
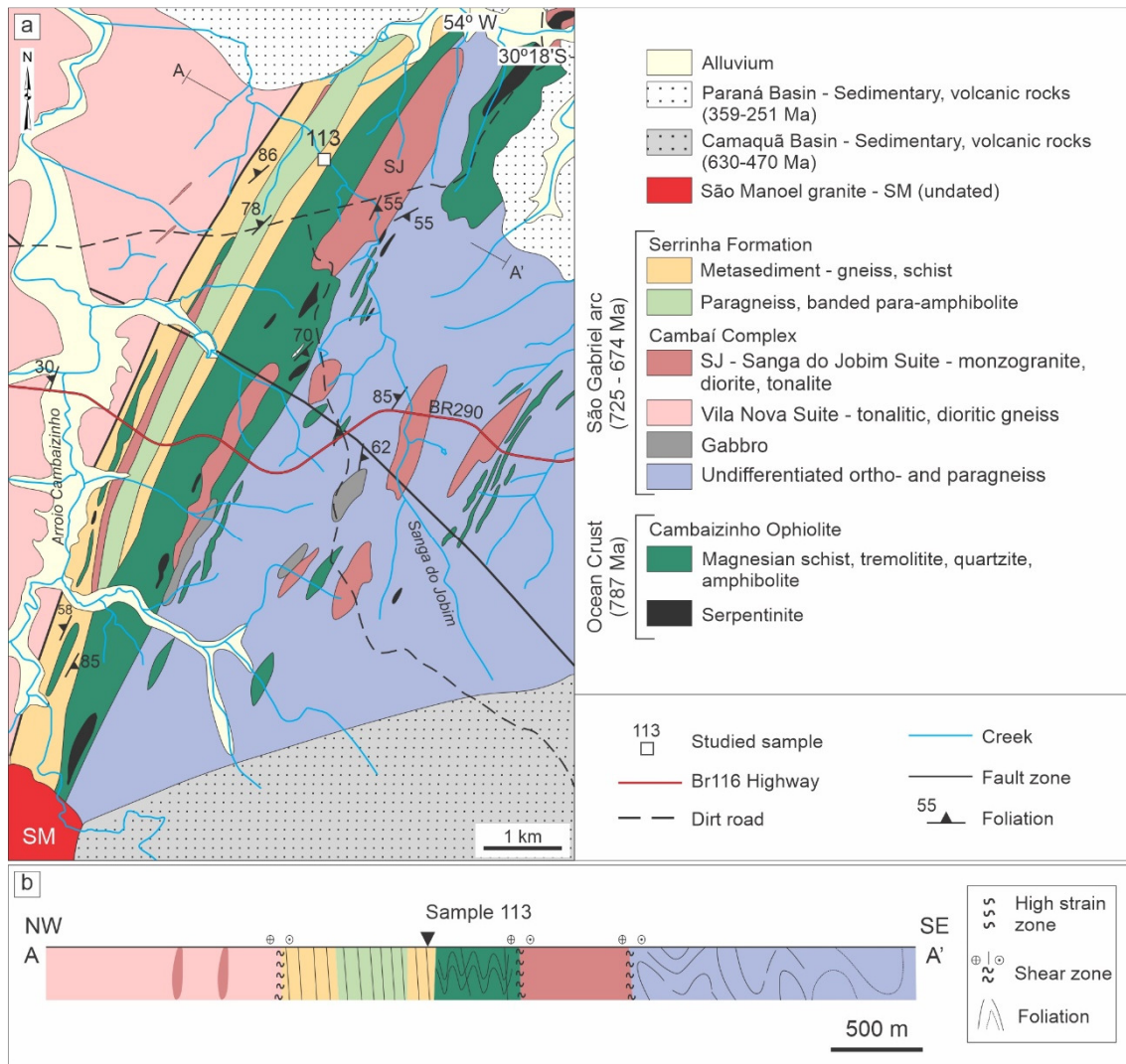
Fig. 2. (a) Geological map of Cambaizinho region, indicating the location of studied sample. Cambaizinho ages obtained from Cerva-Alves *et al.* (2020); Camaquã Basin age interval from Borba *et al.* (2008), Maraschin *et al.* (2010); Paraná Basin age interval from Rocha-Campos *et al.* (2019). (b) Schematic A-A' geological cross-section of the Serrinha Formation and Cambaizinho ophiolite indicated (modified from Remus, 1990; Saalmann *et al.*, 2006; Cerva-Alves *et al.*, 2020).

3. Analytical methods

Petrographic analysis and backscattered electron images (BSE) were made on one selected garnet-staurolite schist sample (sample 113, located at 30°18'44.07" S and 54°01'20.15" W) from the Serrinha Formation. A detailed study was conducted on this sample, including pseudosection modeling, due to the diagnostic assemblage; U-Pb dating of low-U garnet and determination of boron isotopes in dravites were obtained both through laser ablation – inductively coupled plasma – mass spectrometer (LA-ICP-MS).

3.1. Petrography and mineral chemistry

Petrography was carried out at the Instituto de Geociências (IGeo), Universidade Federal do Rio Grande do Sul (UFRGS), using a LEICA optical microscope, where photomicrographic data were obtained (Fig. 3). Mineral chemistry was acquired with an electron microprobe JEOL JXA-8230 at the Microscopy and Microanalysis Laboratory (LMIc), Universidade Federal de Ouro Preto (UFOP). The mineral chemistry analyses were performed under conditions of 15 kV accelerating voltage, 20 nA sample current and 2-5 µm spot size; ZAF matrix corrections were applied. Counting times on the peaks and background were 10/5 s for all elements (Na, Si, Al, Mg, Fe, Cr, Ti, Ca, Ni, K, Mn), except for Ba (30/15 s). Analytical errors are from 0.21 to 1.43%. Standards used are listed in Supplementary Table 1. Because the studied samples contain ilmenite and lack hematite or magnetite, the total iron content from the microprobe was considered as FeO. Chemical maps of garnet were performed to illustrate the mineral zonation and show the quantitative distribution of Ca, Mg, Mn and Fe (Fig. 4). Operating conditions for the maps were the same as the mineral compositions, using 20-ms dwell time per spot (stage mode). The selected elements (Si, Al, Na, Ca, Fe, Mg, Mn) were analyzed by wavelength dispersion spectroscopy (WDS).
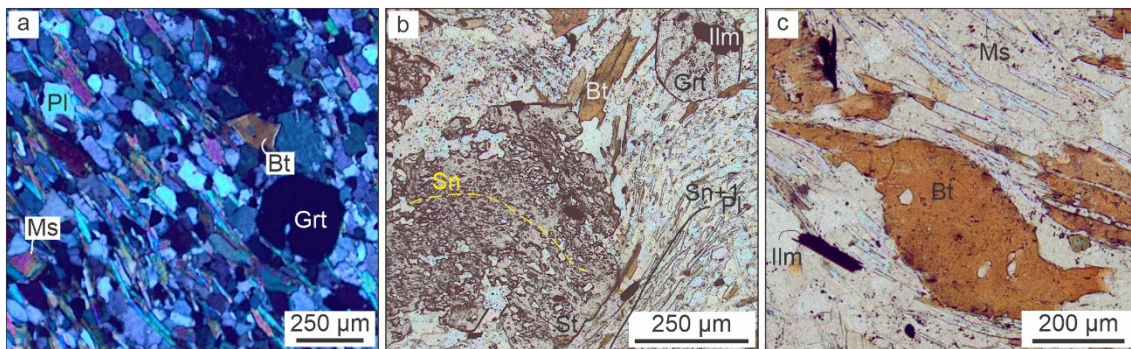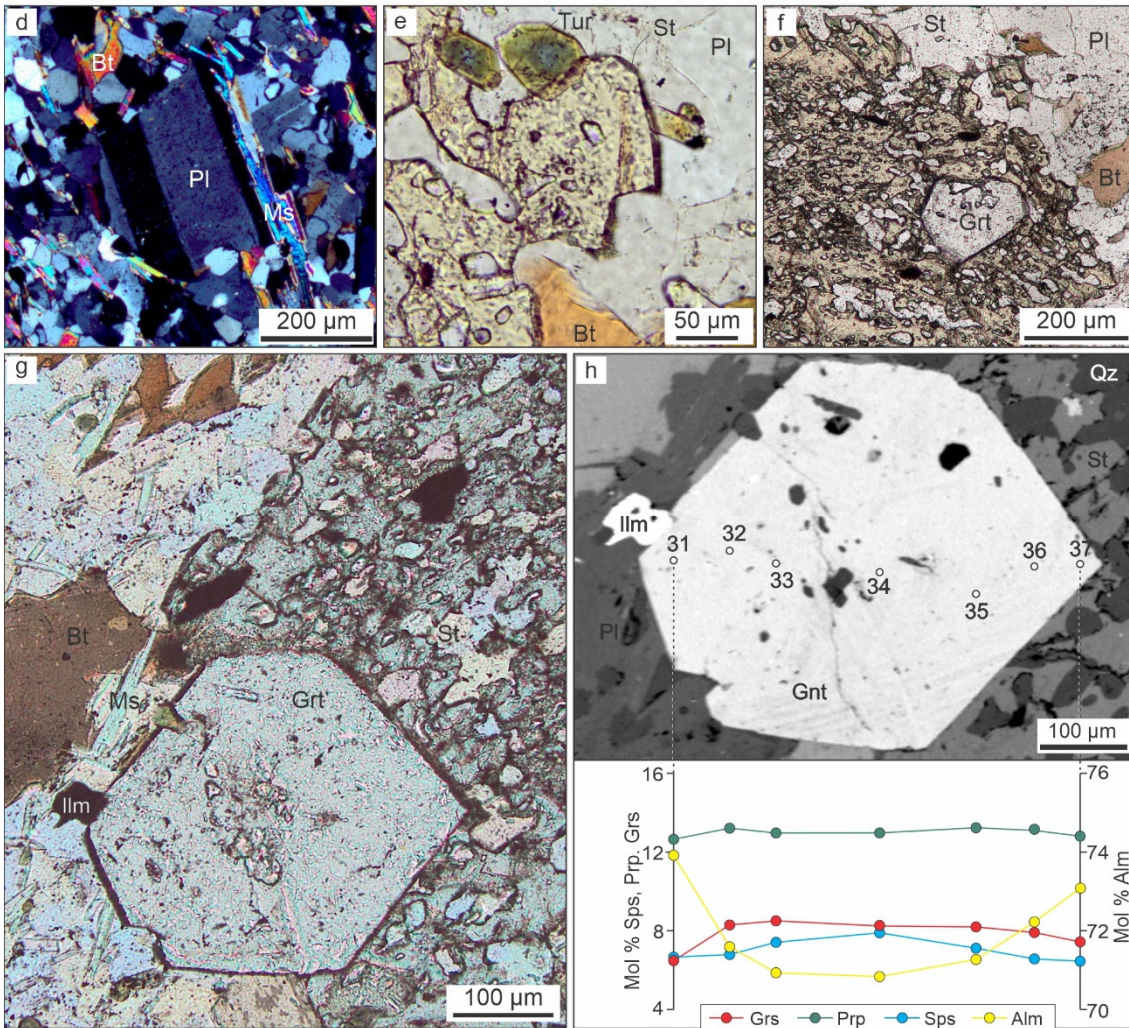
Fig. 3. Selected photomicrographs and BSE image of garnet-staurolite schist. (a) Alignment of micaceous minerals (CP). (b) Regional foliation (Sn+1) of micaceous minerals and relicts of Sn evidenced by alignment of quartz inclusions in staurolite (PP). (c) Biotite fish indicating sinistral movement (PP). (d) Plagioclase porphyroblast in granular matrix with aligned biotite and muscovite (CP). (e) Zoned tourmaline and biotite in matrix and as inclusions in staurolite (PP). (f) Garnet included in staurolite (PP). (g) Garnet partially included in staurolite (PP). (h) BSE image of the same garnet shown in Fig. g with analyzed points indicated and molar contents of grossular (Grs = XCa), pyrope (Prp = XMg), spessartite (Sps = XMn) and almandine (Alm = XFe). Bt = biotite, Grt = garnet, Ms = muscovite, Pl = plagioclase, Tur = tourmaline. CP = crossed polarizers, PP = plane parallel polarizers. Mineral abbreviations follow Whitney and Evans (2010).

3.2. Thermodynamic modeling approach

Metamorphic conditions were constrained by calculating P-T-X pseudosections with the Perple_X software (Connolly, 2005; version 6.9.0) using consistent thermodynamic data (Holland and Powell, 2011; hp633ver.dat). The presented pseudosection was computed for the P-T range of 3.5-7.5 kbar and 400-750 ºC, and

modeled using the MnNCKFMASHT (MnO-Na$_2$O-CaO-K$_2$O-FeO-MgO-Al$_2$O$_3$-SiO$_2$ – H$_2$O-TiO$_2$) chemical system with H$_2$O in excess based on the mineral assemblage and the bulk-rock composition of sample 113. The mineral solution models include: Gt(W) for Grt (White *et al.*, 2014), Mica(W) for Ms (White *et al.*, 2014), MaPa for pg (Bucher *et al.*, 1983; Frank, 1983), Bi(W) for Bt (White *et al.*, 2014), St(W) for St (White *et al.*, 2014), Chl(W) for Chl (White *et al.*, 2014), feldspar for Pl (Fuhrman and Lindsley, 1988), and IlGkPy for Ilm (Andersen and Lindsley, 1988). Mineral abbreviations follow Whitney and Evans (2010). The bulk-rock major elements for pseudosection modeling were determined at Bureau Veritas Minerals (Canada) through inductively coupled plasma emission spectrometry (ICP-ES). The bulk-rock composition was reduced following procedures suggested by Massonne (2012), Li and Massonne (2017), and Li *et al.* (2021); the sum of oxide contents was normalized to 100% (Table 1). CaO was subtracted based on the phosphorus content present in apatite. O$_2$ content was ignored due to the absence of magnetite and the low volume of ferric iron minerals. To constrain the metamorphic stability field of the observed peak mineral assemblage, the P-T pseudosection was contoured by isopleths for molar fraction components and the volume of garnet. Negligible fractionation during porphyroblast growth was presumed because of the weak chemical zoning in the biggest garnet and homogeneity of smaller grains. The used bulk rock composition is therefore considered representative of the modeled equilibrium during the P-T history.

Table 1. Chemical analysis (wt%) of studied sample 113, garnet-staurolite schist, Serrinha Formation, Cambaizinho region. Modified composition for Perple_X (wt%).

	Chemical analysis	Modified composition		Chemical analysis	Modified composition
SiO$_2$	59.90	60.68	CaO	3.32	3.15
TiO$_2$	0.85	0.86	Na$_2$O	3.39	3.43
Al$_2$O$_3$	18.17	18.41	K$_2$O	2.01	2.04
Fe$_2$O$_3$	7.58	-	P$_2$O$_5$	0.16	-
FeO	-	6.91	H$_2$O	-	1.42
MnO	0.14	0.14	LOI	1.40	-
MgO	2.85	2.89	Total	99.85	100.00

3.3. LA-ICP-MS

Garnet and tourmaline were separated using conventional procedures and mounted at IGeo/UFRGS. The analytical method included the isotopic U-Pb

determinations on garnet and boron isotopes on tourmaline through laser ablation. The LA-ICP-MS analyses were performed at the Laboratório de Geoquímica Isotópica (IGL/UFOP) with a ThermoScientific Neptune Plus multi-collector ICP-MS coupled to a Photon Machine 193 nm Excimer laser ablation system equipped with a Hellex two volume ablation cell.

3.3.1. U-Pb dating of garnet

For the U-Pb garnet geochronology, the operating conditions were 6 Hz frequency at 6 J/cm^2. The sample was ablated in a He atmosphere (0.2 L/min) and mixed in the gas line with 0.99 L/min argon and 0.03 L/min nitrogen using an 80 μm beam diameter. Signal strength of the ICP-MS was tuned for maximum sensitivity while keeping oxide formation (monitored as ^{248}ThO/^{232}Th) below 0.2% and no fractionation of the Th/U ratio. Data were acquired overnight in fully automated mode in a sequence of 158 spot analyses, corresponding to 103 in standards and 55 in garnet crystals from sample 113. Seven analyses of garnet were discarded because they had U contents below the detection limit. Each analysis consisted of 20 s background acquisition followed by 35 s of sample ablation and 15 s washout. During data acquisition, the signals of ^{202}Hg, ^{204}Pb, ^{206}Pb, ^{207}Pb, ^{208}Pb, ^{232}Th, and ^{238}U were collected simultaneously in a collector block equipped with nine faradays and five ion counters (Lana *et al.*, 2017). Before analysis, each spot was pre-ablated for 3 s to remove surface contamination. Willsboro garnet (Seman *et al.*, 2017) was used as a reference together with internal standards Ida Dome (Longridge *et al.*, 2011), Mali (Seman *et al.*, 2017), Bushveld (Buick *et al.*, 2001) and MXE (internal reference, unpublished). Raw data were corrected online using in-house Saturn software. Following background correction, outliers (± 2σ) were rejected based on the time-resolved ^{207}Pb/^{206}Pb and ^{206}Pb/^{238}U ratios. The mean ^{207}Pb/^{206}Pb ratio of each analysis was corrected for mass bias (0.3%) and the ^{206}Pb/^{238}U ratio for interelement fractionation (~5%), including drift over the sequence time, using NIST SRM-614 and the 1022 ± 15.2 Ma Willsboro garnet (Seman *et al.*, 2017). Effects for mass bias and drift correction on the Pb/Pb ratios were monitored using USGS BCR and BHVO glasses. Internal standards analyzed include skarn andradite garnet from the Ida Dome in the Central Zone of the Damara Belt, Namibia (Longridge *et al.*, 2011). The 1022 Ma Willsboro garnet of Seman *et al.* (2017) produced an age of 1022 ± 15.2 Ma (n = 7, MSWD = 0.95). The age of skarn formation at the Ida Dome is constrained indirectly by an inferred genetic link to

leucogranitic intrusions and leucocratic dykes that were dated at ~520 Ma and 511-508 Ma, respectively (Longridge *et al.*, 2011). LA-ICP-MS analyses of skarn garnet from the Ida Dome at UFOP resulted in a lower intercept age of 517 ± 7 Ma (n = 16, MSWD = 0.49). This age agrees with the crystallization age of leucogranitic dykes and suggests that the skarn formed at that time. LA-ICP-MS analyses of skarn garnet from the Bushveld Complex yielded a lower intercept age of 2049 ± 28 Ma (n = 16, MSWD = 1.6). This age is in agreement with the published age of 2059 ± 3.5 Ma of Buick *et al.* (2001) for the same skarn deposit. The Yellow Mali grandite dated at UFOP yielded an age of 198.5 ± 1.7 Ma (n = 24, MSWD = 2.3). Our MXE internal garnet reference material yielded an intercept age of 459.8 ± 6.7 Ma (n = 16, MSWD = 1.4). Calculated age and concordia diagrams were built using IsoplotEx 4 (Ludwig, 2003), errors reported at the 2σ level. Details about the analytical parameters are given in Supplementary Table 2 (cf. Horstwood *et al.*, 2016).

3.3.2. Boron isotopes in dravite

Boron isotopes were determined operating with 15 Hz frequency at 7 J/cm^2, with samples ablated in a He atmosphere using a 20 µm beam diameter, with measurements of 98 cycles and 0.5 s of integration time. During the analysis, intensities of Boron isotopes (^{10}B and ^{11}B) were collected simultaneously with the L2 and H2 detectors. Data processing was performed following Devulder *et al.* (2015). The instrumental mass fractionation was corrected using the reference material IAEA B4 schorl, δ^{11}B = -8.62‰ as a primary standard (Tonarini *et al.*, 2003). The primary standard was regularly measured to build a calibration line that allowed correction of the drift.

4. Results

4.1. Petrography and mineral compositions

The sampled garnet-staurolite schist is exposed in the western portion of the Cambaizinho ophiolite (Fig. 2). The investigated rock, which outcrops in a creek is mesocratic greenish-gray, fine- to medium-grained with a well-marked schistosity (Fig. 3a). The sample consists of plagioclase, staurolite, quartz, biotite, muscovite and garnet, with tourmaline, chlorite, ilmenite, monazite and zircon as accessories (<1%), and secondary sericite, chlorite and Fe-oxides. The content of log(Na_2O/K_2O) = 0.52,

and log(SiO_2/Al_2O_3) = 1.19 indicating a litharenite composition for the protolith of the studied rock (Pettijohn *et al.*, 1972).

Two deformation stages were identified in the studied schist. Relicts of a fabric S_n are shown by quartz and opaque mineral inclusion trails in staurolite (Fig. 3b). The foliation S_{n+1} is evidenced by the alignment of biotite and muscovite minerals in a crystallographic preferred direction and granoblastic bands with a homogeneous distribution of plagioclase and quartz (Fig. 3a, b, c).

Representative mineral chemistry analyses are shown in Table 2, and the complete mineral chemistry results are presented in the Supplementary Table 3. The dominant feldspar in the matrix is plagioclase, occurring with granoblastic texture and also forming porphyroblasts (Fig. 3a-d). Plagioclase crystals are andesine to oligoclase in composition ($An_{27.3-37.4}$) showing polygonal contacts and containing quartz and muscovite inclusions.

Table 2. Electron microprobe analyses (in wt%) of selected minerals from the studied garnet-staurolite schist.

Mineral spot	Feldspar 19-1	Biotite 46-1	Muscovite 50-1	Staurolite 8-1	Garnet 1-1	Chlorite 127-1
SiO_2	59.17	36.32	45.96	28.02	37.58	25.52
TiO_2	0.06	1.83	0.49	0.61	0.01	0.12
Al2O3	25.21	19.04	33.75	52.73	21.72	21.90
FeO	0.09	17.24	1.63	13.20	33.14	22.06
MnO		0.04		0.16	2.95	0.04
MgO		12.04	0.92	1.38	3.08	16.38
CaO	7.55	0.04	0.11	0.01	2.21	0.02
Na_2O	7.13	0.23	1.07	0.03		0.03
K_2O	0.08	8.89	9.15	0.01		0.04
BaO			0.07			
Total	99.30	95.79	93.23	96.17	100.75	86.16
No. Oxygen	8	22	22	23	24	28
Si	2.659	5.424	6.240	3.943	5.984	5.361
Ti		0.214	0.050	0.064	0.001	0.019
Al	1.336	3.375	5.399	8.745	4.076	2.639

Mineral spot	Feldspar 19-1	Biotite 46-1	Muscovite 50-1	Staurolite 8-1	Garnet 1-1	Chlorite 127-1
Fe^{2+}	0.003	2.201	0.185	1.553	4.413	3.769
Mn		0.006		0.020	0.397	0.008
Mg		2.615	0.186	0.288	0.730	5.130
Ca	0.363	0.007	0.016	0.002	0.377	0.005
Na	0.621	0.067	0.282	0.008		0.026
K	0.004	1.592	1.584	0.002		0.023
OH						15.973
X_{An} Ca/(Ca+Na+K)	0.37					
X_{Mg} Mg/(Mg+Fe)		0.54				
X_{Fe} Fe/(Mg+Fe+Mn)						0.43
X_{Na} Na/(Ca+Na+K)			0.15			
X_{Pyp}					0.12	
X_{Alm}					0.75	
X_{Grs}					0.06	
X_{Sps}					0.07	

Biotite and muscovite form subhedral crystals, defining the foliation, when occurring in the matrix of metasedimentary rock (Fig. 3a-f), and as inclusions in staurolite (Fig. 3e). Biotite composition is homogeneous for each texture, with X_{Mg} = Mg/(Fe+Mg) from 0.51 to 0.56 and Ti = 0.141-0.226 atom per formula unit (a.p.f.u.). Muscovite is homogeneous, with Si content ranging between 6.079 and 6.240 a.p.f.u. in the matrix. Chlorite is elongate in the matrix, replacing biotite grains; Si content varies between 5.21 and 5.40 a.p.f.u.

Poikiloblastic staurolite occurs as subhedral- to anhedral crystals ranging from 0.5 to 2.0 mm in size with inclusions mainly of quartz and subordinate garnet, tourmaline, biotite, muscovite and ilmenite in different proportions. Quartz is present in the matrix with polygonal contacts and as inclusion trails in staurolite and garnet. Tourmaline occurs included in staurolite and in the matrix (Fig. 3e). The tourmaline composition indicates the dravite end-member – Mg content from 1.72 to 1.97 a.p.f.u., Fe^{2+} content from 0.67 to 1.01 a.p.f.u. and Al + Li values from 0.06 to 0.55.

The total content of garnet is about 3-4 volume% with grains that are variable in size and form. Garnet crystals are commonly euhedral porphyroblasts ranging in size from 0.1 to 10 mm; porphyroblasts are usually in the matrix (Fig. 3a, b) and partly to totally included in staurolite (Fig. 3f, g). One garnet crystal included in staurolite displays higher almandine in the rim (in contact with staurolite) compared to the core (Fig. 3h). Large, rounded garnet in the matrix shows soft core-rim chemical zonation (Fig. 4), with a minor decrease of Ca and Mn and an increase in Fe content from core ($Alm_{0.71}$ $Grs_{0.08}$ $Prp_{0.13}$ $Sps_{0.08}$) to rim ($Alm_{0.73}$ $Grs_{0.07}$ $Prp_{0.13}$ $Sps_{0.07}$). Secondary sericite occurs in plagioclase, and secondary chlorite in biotite.

We recognized two equilibrium assemblages: (A1) Garnet (core) + biotite + muscovite + chlorite + andesine-oligoclase + ilmenite + quartz + tourmaline; (A2) Garnet (rim) + staurolite + biotite + muscovite + chlorite + andesine-oligoclase + ilmenite + tourmaline. Sericite is secondary mineral.
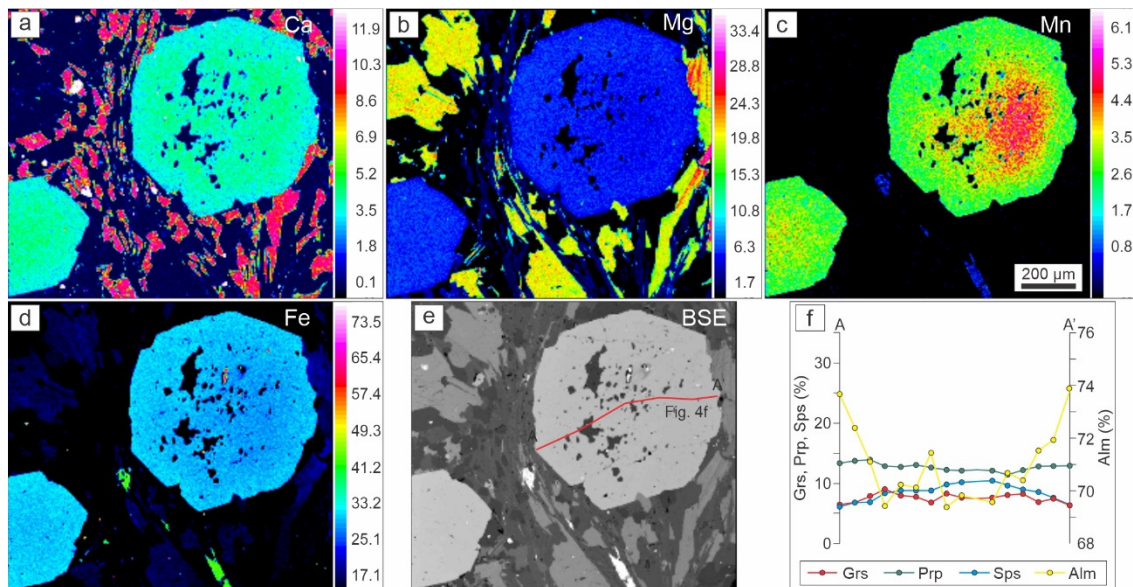
Fig. 4. (a, b, c, d) Element concentration maps of garnet. (e) Garnet BSE image. (f) EMP spot analyses of garnet along a profile (red line in c) plotted in molar fractions. Grs = grossular, Prp = pyrope, Sps = spessartite, Alm = almandine.

4.2. P-T pseudosection results

The bulk-rock composition and described prograde mineral assemblage were used to model the metamorphic conditions at which the garnet-staurolite schist (sample 113) formed and garnet grew. White to dark grey and intermediate grey tones in the pseudosection fields represent the variance of the mineral assemblages (Fig. 5). The metamorphic assemblage of A2 was grt + st + bt + ms + chl + pl + ilm + tur + qz

and is represented by the field chl + grt + ms + st + ilm + pl + qz + H_2O at 3.5-7.5 kbar and 520-583 ºC (Fig. 5a). The pseudosection was contoured with isopleths representing molar contents of grossular (X_{Ca} = Ca/(Ca+Fe+Mg+Mn)), spessartine (X_{Mn} = Mn/(Ca+Fe+Mg+Mn)) and the garnet volume% (Fig. 5a, b). Due to the possibility Fe-Mg exchange between biotite and garnet, we did not use pyrope (PRP) and almandine (ALM) compositional isopleths. The garnet core composition displays X_{Ca} = 0.07-0.09 and X_{Mn} = 0.06-0.11; the intercept of modeled X_{Ca} and X_{Mn} isopleths shown in the pseudosection (Fig. 5b) constrain the growth condition of the garnet core to be 4.6 < P < 5.1 kbar and 537 < T < 546 ºC. The garnet rim composition is X_{Ca} = 0.06-0.08 and X_{Mn} = 0.06-0.09 and the corresponding modeled X_{Ca} and X_{Mn} isopleths (Fig. 5b) suggest growth of the garnet rim at 4.5 < P < 5.0 kbar and 546 < T < 554 ºC in a thermal gradient of 97 ºC/kbar. The garnet core and rim compositions are stable in the field chl + grt + ms + st + ilm + pl + qz + H_2O, as indicated by the isopleths. With increasing temperature, chlorite becomes unstable until disappearing at the onset of biotite stability.
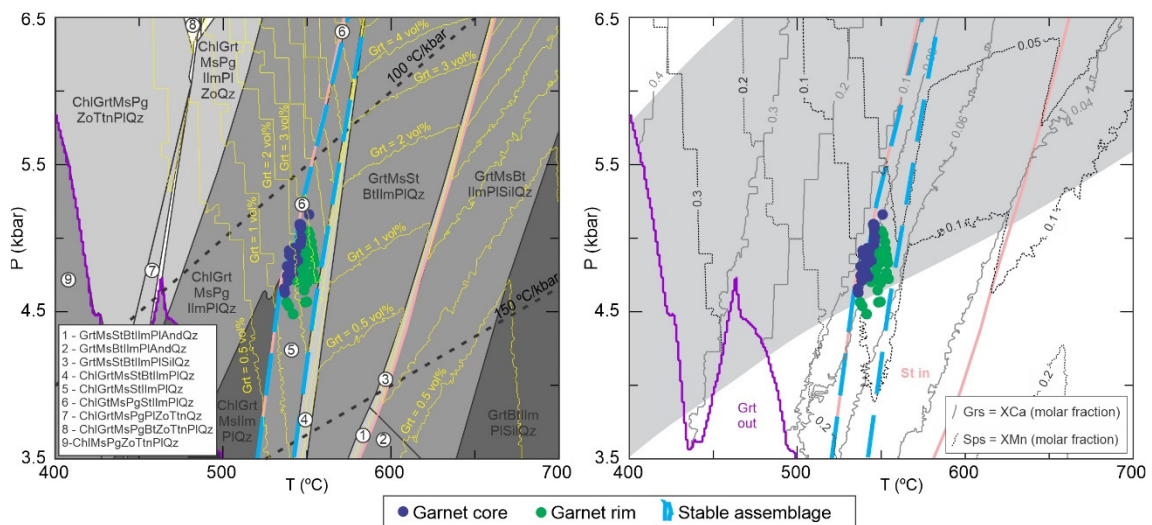
Fig. 5. (a) P-T pseudosection calculated for reduced bulk-rock composition (Table 1) and estimate of P-T conditions for garnet formation. Yellow lines are isopleths for garnet volume, with the software package Perple_X in the MnNCKFMASHT system. Pseudosection was computed by taking H2O in excess. (b) Isopleths for grossular and spessartite contents in garnet. Shaded grey area corresponds to the stability field of Barrovian assemblages (Ryan and Dewey, 2019). Projection of garnet composition is shown as small circles, corresponding to those in Supplementary Table 3.

4.3. U-Pb dating of garnet

LA-ICP-MS U-Pb isotopic analyses were conducted on 31 garnet grains, for a total of 48 spots (Supplementary Table 4). BSE imaging of selected garnet crystals (Fig. 6) shows rounded grains (200-600 μm in diameter), having homogeneous internal structures with inclusions of quartz (5-40 μm long), ilmenite (1-10 μm diameter) and muscovite (1-15 μm long) (Figs. 3c, 4, 6). Due to the low amount of U present in the described mineral inclusions, we consider all U as the pristine garnet U signal. Analyzed spots yielded a regression line with a lower intercept at 721 ± 14 Ma (MSWD = 1.3; Fig. 6), and U concentration of 0.07-0.75 ppm. In most cases, garnet crystal core and rim limits are gradational. The influence of U-rich mineral inclusions on garnet U-Pb analyses (e.g, Millonig *et al.*, 2020; Schannor *et al.*, 2021) was not observed in our study.
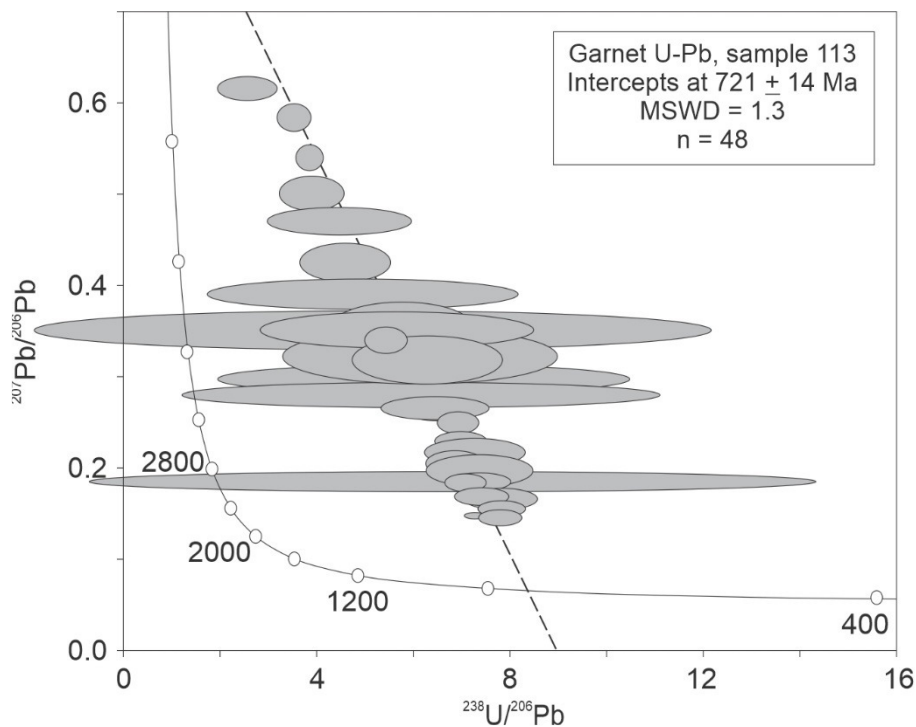
Fig. 6. LA-ICP-MS U-Pb dating of garnet from garnet-staurolite schist (sample 113), displayed in Tera-Wasserburg diagram (Tera and Wasserburg, 1972).

4.4. Boron isotopes in dravite

Boron contents in dravite are homogeneous in the studied sample. Available data include 15 analyzed spots on tourmaline from sample 113 (Fig. 7, Table 3). The boron isotopic composition ranges from $\delta^{11}B$ = +0.51 to +3.39‰.
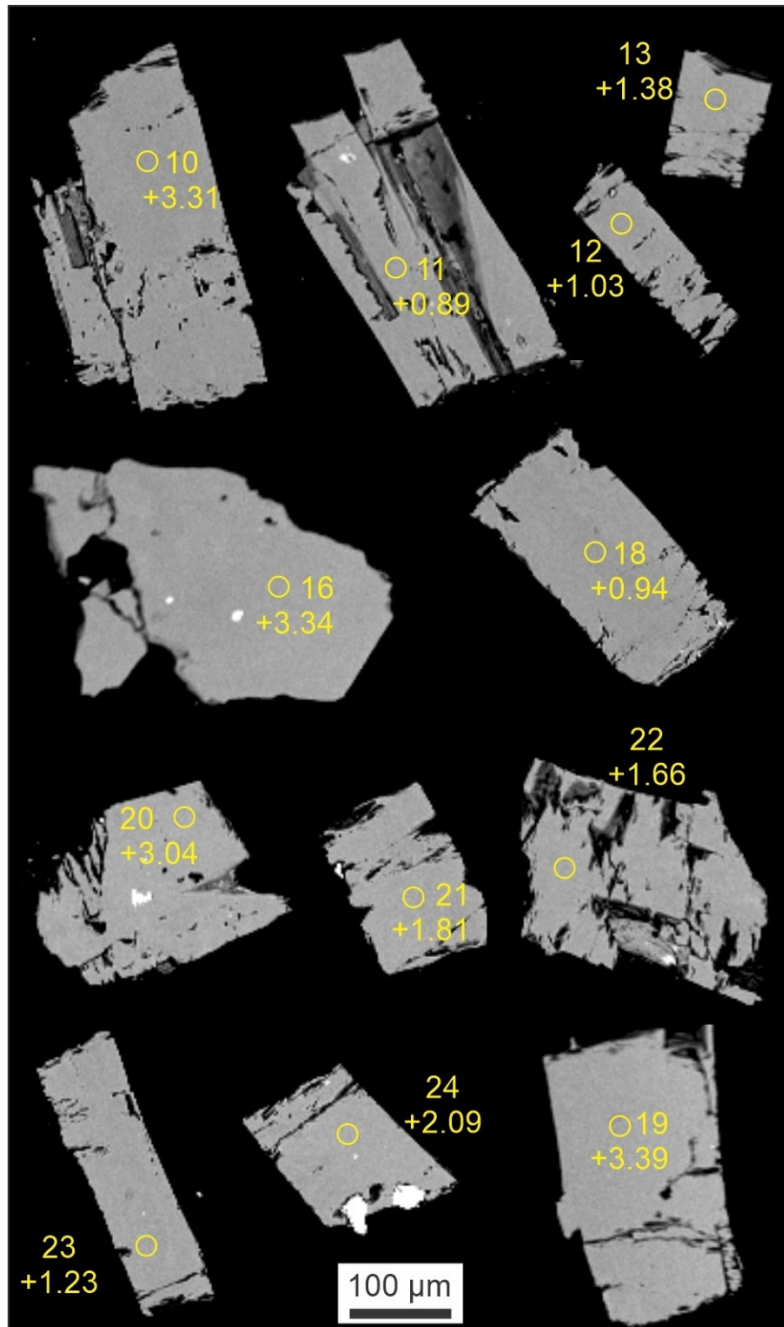
Fig. 7. Selected BSE images of dravite showing analyzed spot number and $\delta^{11}B$ (‰) values.

Table 3. Values of $\delta^{11}B$ for tourmaline from sample 113, garnet-staurolite schist, Serrinha Formation. (*) = grain corresponding to analysis by electron microprobe as shown in Supplementary Table 3.

Spot (*)	$\delta^{11}B$ (‰)	Spot (*)	$\delta^{11}B$ (‰)
10 (5-2*)	+3.31 ± 0.11	20 (21-10*)	+3.04 ± 0.11
11 (9-4*)	+0.89 ± 0.11	21 (43-21*)	+1.81 ± 0.12
12	+1.03 ± 0.12	22 (20*)	+1.66 ± 0.12

Spot (*)	$\delta^{11}B$ (‰)	Spot (*)	$\delta^{11}B$ (‰)
13	+1.38 ± 0.11	23 (28-13*)	+1.23 ± 0.11
15	+2.95 ± 0.11	24 (35-17*)	+2.09 ± 0.11
16 (8-3*)	+3.34 ± 0.11	25	+0.71 ± 0.11
18 (13-6*)	+0.94 ± 0.11	26	+0.51 ± 0.11
19 (19-9*)	+3.39 ± 0.11		

5. Discussion

5.1. Metamorphic P-T conditions in Serrinha Formation

In the Cambaizinho region, metamorphism caused by deformation is registered in the Serrinha Formation. We identified two continuous stages of metamorphism (A1 and A2) based on petrographic observations; two stable mineral assemblages related to the same event were modeled through mineral compositions, thermodynamic calculations and garnet compositional isopleths. The assemblage chl + grt + ms + st + ilm + pl + qz + H_2O was stable at 3.5-6.5 kbar and 520-583 ºC. The intercept of X_{Ca} and X_{Mn} isopleths constrain the garnet growth condition at 4.5-5.1 kbar and 536-555 ºC. The consumption of muscovite and chlorite to form staurolite and biotite was described by Lal *et al.* (1981) and Mohan *et al.* (1989) for Barrovian metamorphism through the reaction: chl + ms = st + grt + bt + H_2O. The observation that muscovite is preserved in sample 113 suggests that the metamorphic peak had a short duration or late muscovite growth is associated with fluid assisted retrogression metamorphism. The complete consumption of chlorite interrupted the growth of garnet. The subtle progressive chemical change from the garnet core to the garnet rim indicates that the process was isobaric and continuous for stage A1 to stage A2, with a small 19 ºC increase in temperature. The steep garnet composition isopleths in the stable field suggest that garnet might present pronounced zonation with increase in temperature (e.g., Zeh and Holness, 2003). However, only subtle zoning is observed in the Serrinha garnet crystals. The poor zoning is explained by growth under nearly constant P-T-X conditions following nucleation or as consequence of an overstepping of the garnet-in reaction. Overstepping nucleation is a common condition in subduction environments where a rapid burial yields isothermal and isobaric conditions for garnet growth (e.g., Spear *et al.*, 2014); this can also occur in regional and contact metamorphism (Spear *et al.*, 2014).

The diagnostic assemblage in metapelites (staurolite zone) and the recorded P-T conditions indicate that metamorphism reached amphibolite facies, as also noted by Remus (1990) and Saalmann *et al.* (2006). The partial replacement textures with sericitized plagioclase and chloritized biotite observed in thin section may be attributed to a late retrograde metamorphic stage, in agreement with the M2 event described by Remus (1990) and the M3 event described by Saalmann *et al.* (2006).

5.2. Garnet age supporting P-T conditions

P-T calculations and temporal determinations of a key mineral such as garnet provide a robust understanding of the metamorphic evolution (Millonig *et al.*, 2020). Isotopic data (e.g., U-Pb) from garnet can be directly used for petrological constraints (Vance, 1995). Garnet crystals from the Serrinha Formation garnet-staurolite schist yielded an age of 721 ± 14 Ma. Because of uncertainty between garnet core and rim, this age is interpreted as the timing of bulk garnet growth during metamorphism. The application of U-Pb geochronology in low-U garnet is a technique used to constrain regional metamorphic events (Millonig *et al.*, 2020), and has been previously applied to rocks from the Brasiliano Orogen to gain insight into the orogenic setting of the Araçuaí Belt (590-565 Ma; Schannor *et al.*, 2021). The present study is among the first to obtain U-Pb ages from low-U garnet and the first to apply this method to a metasedimentary rock related to the Tonian island arc-continent collision and thrusting during the Brasiliano Orogeny.

In typical metapelites, garnet appears at temperatures around 450ºC, depending on pressure, preferably incorporating manganese at low temperatures (Bucher and Grapes, 2011). For garnet core and rim from the Serrinha Formation, the pressure and temperature of growth were established at 5.90-6.15 kbar and 560-590 ºC. In collisional orogens, the increase of 200-300 ºC occurs over ~13-60 Ma (Christensen *et al.*, 1989; Vance, 1995). On the other hand, short-duration (~7-8 Ma) metamorphic thermal peaks can be generated over the decompression by heat pulses during magmatic heat input (Vance, 1995).

Based on our results, a chronological improvement is made regarding the metamorphic evolution of the Serrinha Formation and São Gabriel Terrane. The youngest zircon cluster at 2σ was used previously to estimate the 650 Ma maximum depositional age (MDA) of this formation (Cerva-Alves *et al.*, 2020), considering garnet

schist, garnet-staurolite schist and para-amphibolite samples. This 650 Ma age agrees with the MDA interpreted by Lena *et al.* (2014). When the youngest single zircon grain age from the studied garnet-staurolite schist sample 113 is considered with 2σ uncertainty (Cerva-Alves *et al.*, 2020), an alternative of 710.2 Ma is suggested for the MDA. However, the previously defined MDA is younger than the metamorphic age reported here through garnet U-Pb isotopes and needs to be revised. We applied the 'Maximum Likelihood Age' (MLA) algorithm (Vermeesch, 2021) to recalculate the MDA in the Serrinha Formation, resulting in 739.04 ± 4.47 Ma (Fig. 8a). Zircon U-Pb data from garnet schist samples 30B, 48, and garnet-staurolite schist sample 113 (Cerva-Alves *et al.*, 2020) were used for this calculation through the software IsoplotR (Vermeesch, 2018).

Two age modes are observed in a histogram (Fig. 8b) of the Serrinha Formation U-Pb zircon ages (Cerva-Alves *et al.*, 2020). The oldest age of 769.1 ± 4.6 Ma is coincident (within the error) with U-Pb ages in zircons from the superstructure of the São Gabriel arc in the Campestre Formation = 765 ± 10 Ma (Gubert *et al.*, 2016), and the Bela Vista Formation = 758 ± 4 Ma (Arena *et al.*, 2017). In addition, the deformation in the Ibaré shear zone, which delimits the São Gabriel Terrane from the Rio de La Plata Craton (Ribeiro, 1978), was dated with K-Ar in white mica at 757.7 ± 11.4 Ma, 747.1 ± 9.2 Ma and 743.5 ± 10.2 Ma (Hueck *et al.*, 2020). The younger mode of 731.6 ± 2.2 Ma is close to the zircon U-Pb age of 724.6 ± 3.2 Ma from a metatonalite sample from the Cambaí Complex (Cerva-Alves *et al.*, 2020), which is part of the infrastructure of the São Gabriel arc. Our results also overlap with the U-Pb ages obtained in zircons from Palma (722 ± 3 Ma) and Ibaré (726 ± 2 Ma) metasomatites, interpreted as the emplacement age of ophiolites onto the São Gabriel arc (Arena *et al.*, 2017), and the presently-determined metamorphic age (bulk garnet age) of 721 ± 14 Ma.
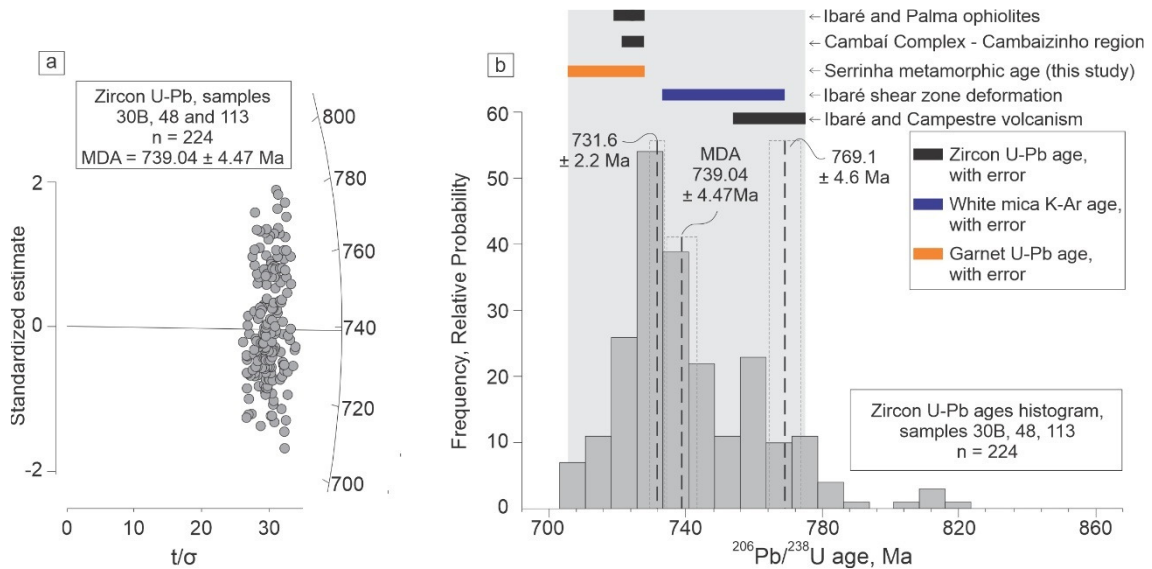
Fig. 8. (a) Radial plot and MDA estimates for garnet schist samples 30B, 48 and garnet-staurolite schist sample 113 (Cerva-Alves *et al.*, 2020). (b) Histogram of U-Pb ages plotted for zircons from the Serrinha Formation (Cerva-Alves *et al.*, 2020). Age peaks and uncertainties obtained by 'Unmix ages' function of Isoplot/Ex (Ludwig, 2003); distribution of U-Pb and K-Ar ages for different rocks from the São Gabriel Terrane (Gubert *et al.*, 2016; Arena *et al.*, 2017; Cerva-Alves *et al.*, 2020; Hueck *et al.*, 2020; this study). BIN = 8 Ma.

5.3. Boron isotope interpretation

Tourmaline is a borosilicate and an important host for boron. Tourmaline occurs in many types of rocks, is chemically and mechanically resistant in clastic sedimentary rocks and is stable under virtually all grades of metamorphism (Henry and Guidotti, 1985). The mineral formula is expressed as $XY_3Z_6(T_6O_{18})(BO_3)_3V_3W$, where X = Ca, Na, K, vacancy; Y = Li, Mg, Fe^{2+}, Mn^{2+}, Al, Cr^{3+}, V^{3+}, Fe^{3+}, (Ti^{4+}); Z = Mg, Al, Fe^{3+}, Cr^{3+}, V^{3+}; T = Si, Al, (B); B = B, vacancy; V = OH, O and W = OH, F, O, with about 3 wt.% B in the crystal structure (Marschall and Jiang, 2011). Boron has the two stable isotopes [11]B and [10]B, with a mass difference of about 10% (Barth, 1993). Boron concentration and $\delta^{11}B$ composition in tourmaline are relevant to distinguish geological environments and determine fluid processes related to crustal metamorphism, magma genesis and evolution, hydrothermal ore formation and fluid-rock interactions (Kowalski *et al.*, 2013; Palmer, 2017).

The occurrence of dravite in metasedimentary rocks from the Serrinha Formation implies that the sedimentary protolith was rich in boron. Enrichment of boron in marine sediments occurs by adsorption in clay minerals (Williams *et al.*, 2001; Palmer, 2017). Mineral chemistry considering Al, Fe and Mg contents in dravites from garnet-staurolite

schist (sample 113) plot in the fields of Al-saturated or unsaturated, Ca-poor metapelites and metapsammitic rocks (Fig. 9). This composition shows a subtle difference with the Ibaré metasomatic dravites (Arena *et al.*, 2020). The Ibaré dravite is interpreted as having formed from seawater-derived fluids in oceanic crust, including tourmalinization in fumaroles (Arena *et al.*, 2020).
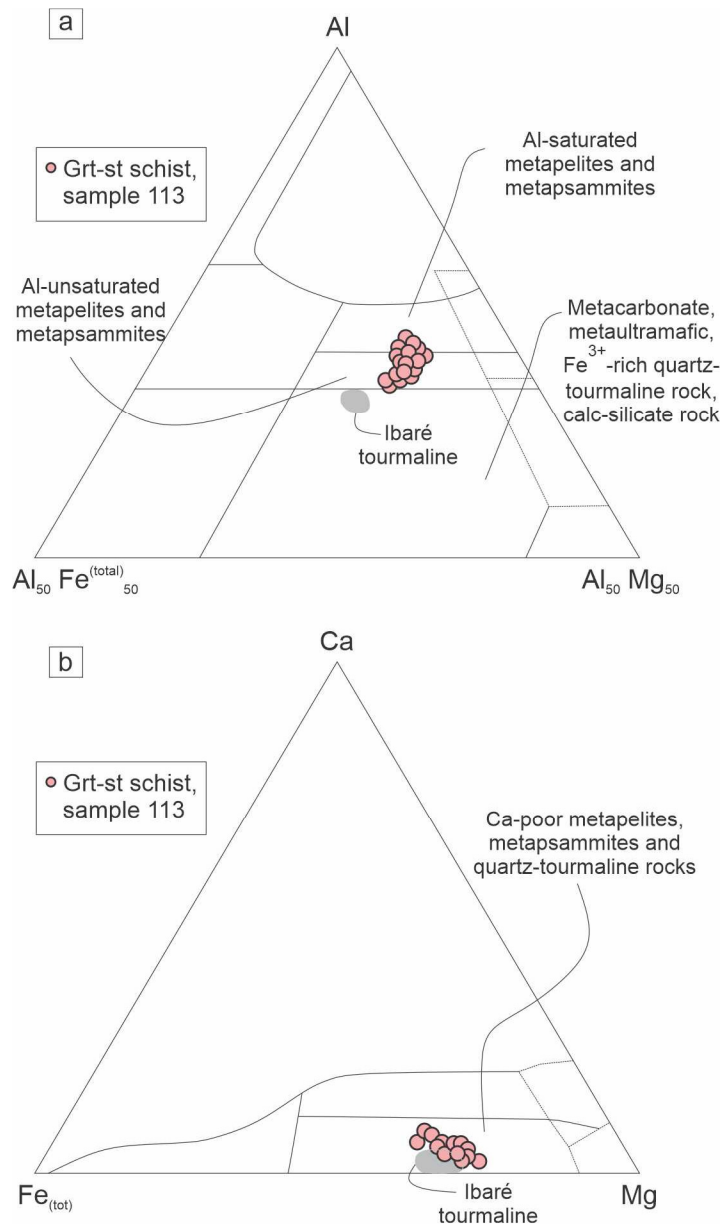
Fig. 9 (a) (b). Ternary diagrams showing the chemical composition of tourmaline from the Serrinha Formation (sample 113); Ibaré tourmaline from Arena *et al.* (2020). (a) Al-Fe-Mg diagram and (b) Ca-Fe-Mg after Henry and Guidotti (1985).

Rocks with marine affinity are submitted to fractionation of seawater boron isotopes and consequently enriched in [11]B when compared to mantle and continental crust contents (Leeman and Sisson, 1996; Palmer, 2017) (Fig. 10). The isotopic characteristics of dravite from the Serrinha Formation garnet-staurolite schist ($\delta^{11}B$ = +0.51 to +3.39‰) overlap with three possible sources (Fig. 10), including (a)

terrigenous marine sediments, (b) oceanic crust and (c) island arc. The terrigenous marine sediments source is discarded because oceanic sediments acquire $\delta^{11}B$ values of -12 to -6‰ after diagenesis (Ishikawa and Nakamura, 1994), which is different from the values found in the Serrinha metasediments. On the other hand, the studied garnet-staurolite schist has a sedimentary protolith and was not part of the oceanic crust. In subduction environments, the formation of an accretionary wedge and tectonic erosion between subduction and oceanic plates are common (Palmer, 2017; Raymond *et al.*, 2019). Fluids rich in boron can originate from subducted altered oceanic crust and are expelled through fractures and faults (Palmer, 2017). However, in this case the $\delta^{11}B$ content varies and decreases continuously with increasing depth and distance from the subducted slab. Such variations have been observed across the Japanese Izu arc complex, for example, with $\delta^{11}B$ values about +7‰ close to the slab and +1‰ further back from the forearc (Ishikawa and Nakamura, 1994). In summary, considering the geological context and $\delta^{11}B$, the sampled tourmaline formed in a forearc basin, across the accretionary wedge with oceanic influence, indicating an island arc source for the garnet-staurolite schist. Although as data were obtained from one sample in this study, further work is needed to determine whether $\delta^{11}B$ values decrease away from the arc.
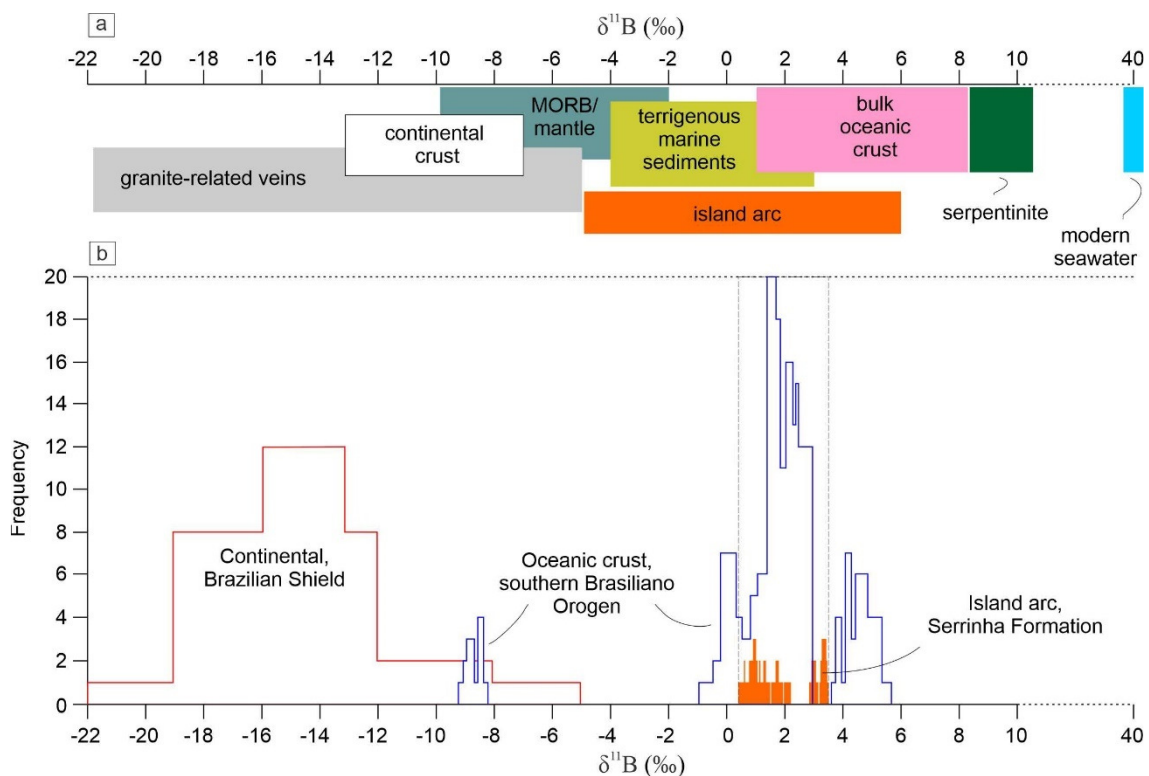
Fig. 10. Histogram of $\delta^{11}B$ (‰) ratios. (a) Different geological environments of $\delta^{11}B$ (‰) concentrations (Palmer and Slack, 1989; Farber *et al.*, 2015; Marschall and Foster,

2018). (b) Histogram of tourmaline from the São Gabriel Terrane (Hartmann *et al.*, 2019; Arena *et al.*, 2020; Werle *et al.*, 2020; this work) and continental Brazilian Shield (Garda *et al.*, 2009; Trumbull *et al.*, 2013; Albert *et al.*, 2018).

5.4. Tectonic implications

The metamorphic conditions defined in this work for the Serrinha Formation are interpreted as one phase of island arc-continent collision, akin to other foreland basins preserved during island arc-continent collisions, e.g., the South Mayo Trough of western Ireland (Ryan, 2008) and Anti-Atlas of Morroco (Thomas *et al.*, 2002; Hodel *et al.*, 2020). The duration of collisional arc-continent orogenies associated with Barrovian conditions varies, and heat pulses of short duration can occur in long lasting collisional orogens (Ryan and Dewey, 2019). Temperatures of 700 ºC in the middle crust can be achieved in hot orogens 20-25 Ma after the onset of collision in the absence of igneous heat advecton (Ryan and Dewey, 2019). In short orogens, the metamorphic peak can occur 10 Ma after the onset of collision (Ryan and Dewey, 2019). Examples include the 478-468 Ma Taconic Orogeny in the Quebec Appalachians (Zagorevski and Van Staal, 2011) and the equivalent 475-467 Ma Grampian Orogeny in the Ireland and the Scotland Caledonian Belt (Dewey, 2005). In our interpretation, the São Gabriel arc was an active island arc with volcanism registered at 767.2-757 Ma (Gubert *et al.*, 2016; Arena *et al.*, 2017) and plutonism at 794-701 Ma (Saalmann *et al.*, 2006, 2011; Hartmann *et al.*, 2011; Philipp *et al.*, 2018) (Fig. 11a). The deformation ages between 757.7 ± 11.4 Ma and 743.5 ± 10.2 Ma from the Ibaré shear zone (Hueck *et al.*, 2020) is in agreement with the age of activity of the São Gabriel arc. In our interpretation, these ages reflect deformation within the arc. A recalculated MDA of 739.04 ± 4.47 Ma for the Serrinha Formation was estimated by the MLA method, indicating sedimentary input until this period. The collision between the São Gabriel island arc and the Rio de La Plata Craton (Saalmann *et al.*, 2006, 2011; Hartmann *et al.*, 2011; Philipp *et al.*, 2018) to form one part of the São Gabriel Terrane started at about 731.6 ± 2.2 Ma (Fig. 9b). This age corresponds to the younger U-Pb age mode of detrital zircons (Cerva-Alves *et al.*, 2020), interpretated as the age of metamorphism. The metamorphic peak was achieved at 721 ± 14 Ma (bulk garnet age), indicating about ~18 Ma between the Serrinha basin sedimentation and deformation due to thrusting of the São Gabriel arc over the Rio de La Plata Craton. The coeval Cambaí tonalite (e.g., 724.6 ± 3.2 Ma; Cerva-Alves *et al.*, 2020) is modeled as contributing to the increase in heat flux.

The Serrinha Formation was deposited in a forearc basin with marine influence, as indicated by the $\delta^{11}B$ ratio. The geological association, including obducted ophiolite and island arc source of the sediments (Cerva-Alves *et al.*, 2020) is comparable with another successor basin, the Hammamat Group in the Tonian Arabian Nubian Shield (Abd El-Raman *et al.*, 2019). Our model exposes some limitations of recent studies (e.g., Konopásek *et al.*, 2020) where oceanic crust and oceanic island arcs are not considered in the Brasiliano Orogen evolution. However, our data support a shift from São Gabriel island arc subduction to a collisional tectonic regime involving the Rio de La Plata Craton (Saalmann *et al.*, 2006, 2011; Hartmann *et al.*, 2011; Cerva-Alves *et al.*, 2020).
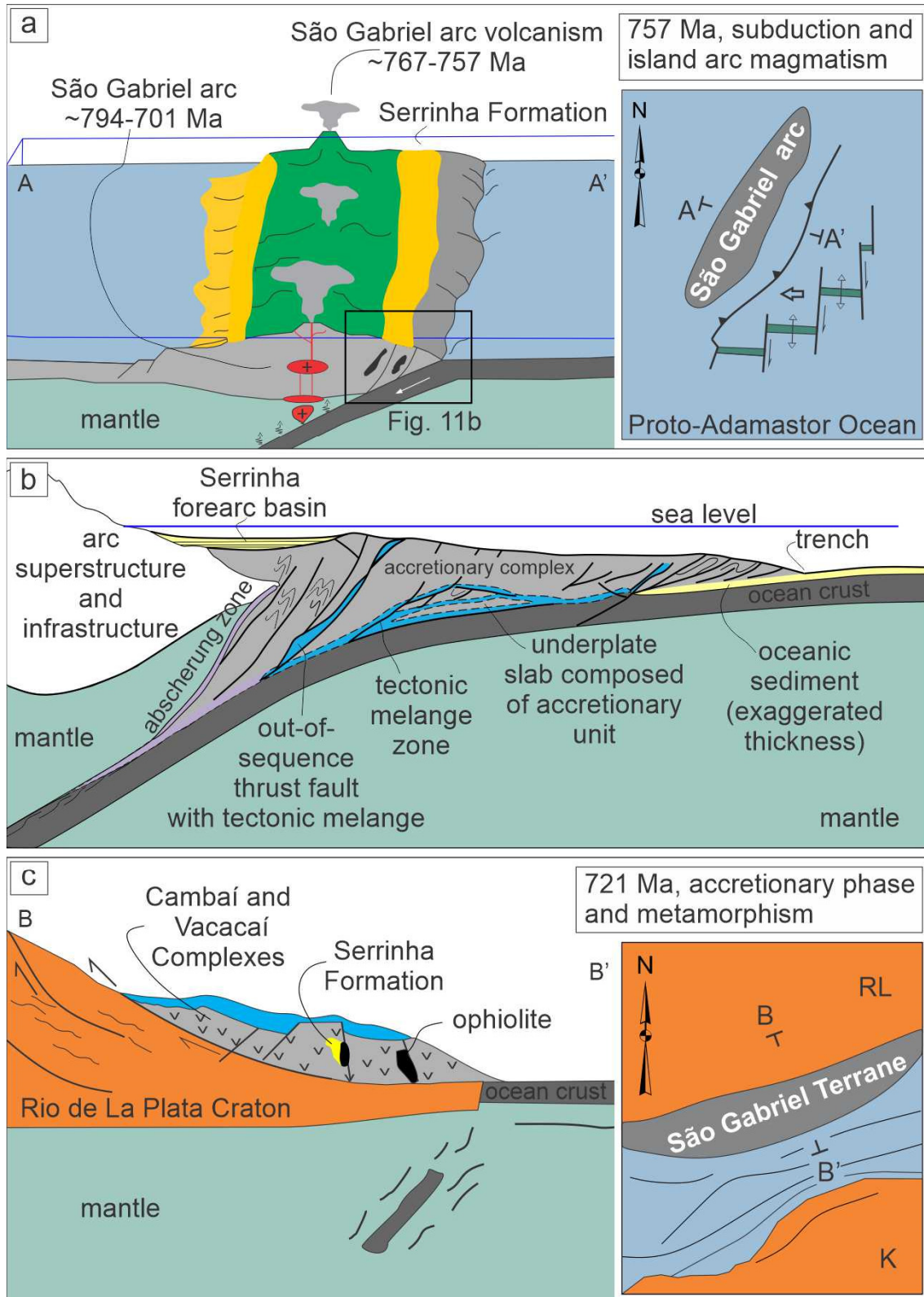
Fig. 11. Model diagram illustrating the reconstruction of the Neoproterozoic Brasiliano Orogeny and the depositional setting of the Serrinha Formation and continental crust contribution. (a) Juvenile crust production with terrane accretion, volcanism (Gubert *et al.*, 2016; Arena *et al.*, 2017) and oceanic crust subduction. (b) Detailed structural model of an accretionary margin showing a simplified subduction accretionary complex (Raymond, 2019; Raymond *et al.*, 2019) and forearc basin position. (c) Arc-continent

collision displaying the São Gabriel Terrane thrusted over the Rio de La Plata Craton (Saalmann *et al.*, 2011; Cerva-Alves *et al.*, 2020).

Voluminous juvenile magmatic activity is registered along the Brasiliano Orogen (Caxito *et al.*, 2021), including occurrences in the Brasília belt (863-630 Ma, Goiás arc; Pimentel *et al.*, 2000), Ribeira Belt (859-838 Ma, Serra da Prata arc; 790-620 Ma, Rio Negro arc; Peixoto *et al.*, 2017; Santiago *et al.*, 2020) and Dom Feliciano Belt (879 Ma, Passinho arc; 794-725 Ma, São Gabriel arc; Babinski *et al.*, 1996; Leite *et al.*, 1998). Ophiolites are preserved in the Brasiliano Orogen, with metasomatism of the oceanic crust and mantle occurring between 923-722 Ma (Dom Feliciano Belt; Arena *et al.*, 2016, 2017; Hartmann *et al.*, 2019, 2021). The Tonian juvenile setting evolved into an Ediacaran environment where magmas formed as a result of mixing of melts of both juvenile Tonian-Cryogenian and continental Archean-Paleoproterozoic basement (Caxito *et al.*, 2021). These processes indicate complete oceanic crust consumption, continental collision and subsequent reworking (Peixoto *et al.*, 2017; De Toni *et al.*, 2020). Coeval intra-oceanic activity and evolution is also observed in the Arabian-Nubian Shield, where multistage processes produced juvenile crust (870-630 Ma) that later collided and coalesced to form larger composite terranes (Kröner and Stern, 2004). The collision and accretion of island arcs to a continent by subduction is an evolutionary consequence of the complete consumption of the oceanic structure (Chekhovich, 2006). This environment is consistent with a setting where greenschist to amphibolite metamorphic facies were achieved, and the preservation of the geological record was favored (Chekhovich, 2006). We interpret that part of the São Gabriel island arc was displaced to the edge of the overriding plate, and then broken and thrusted over the Rio de La Plata continental block before widespread collision during the Brasiliano Orogeny to form West Gondwana.

The rock archive in the Tonian juvenile magmatic arc and oceanic crust displays evidence of the Proto-Adamastor ocean (Hartmann *et al.*, 2019) and an extensive subduction zone occurring around Western Gondwana (Fig. 12) that was active since ca. 879 Ma (Leite *et al.*, 1998; Peixoto *et al.*, 2017). The P-T-t estimate and source determination for the Serrinha Formation allows for the interpretation of the tectono-metamorphic conditions in one key point in space and time of the Gondwana supercontinent evolution.
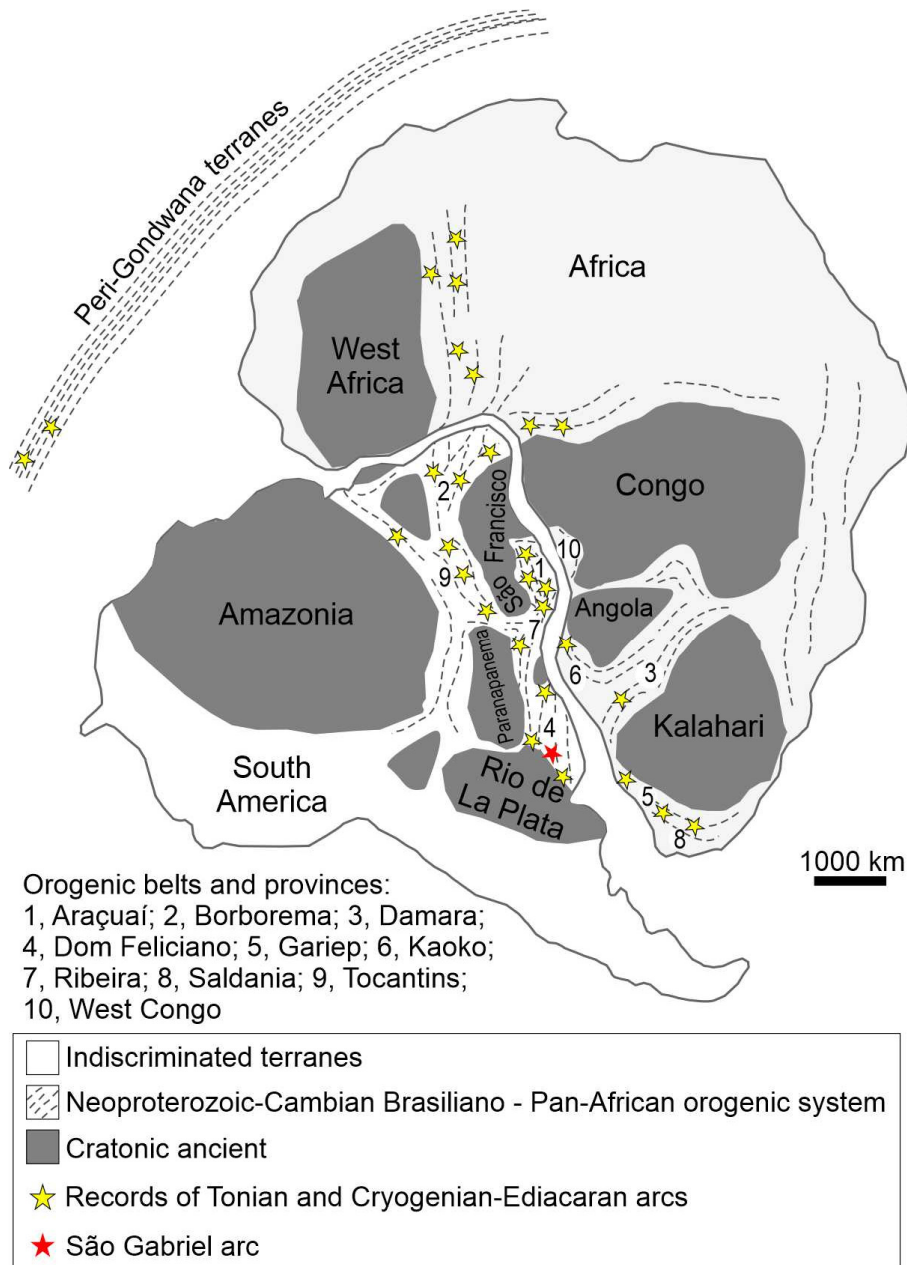
Fig. 12. Western Gondwana map with location of the Tonian arcs (juvenile) and Cryogenian-Ediacaran arcs (both juvenile and crustal-derived) (modified from Meet and Liebermam, 2008; Peixoto *et al.*, 2017; Caxito *et al.*, 2021).

6. Conclusions

The collage of an intra-oceanic arc with an ophiolite and a sedimentary basin contributed to the Gondwana assemblage during the Neoproterozoic Brasiliano Orogeny. The Tonian Serrinha forearc basin is part of the Brasiliano Orogen and was preserved in the Cambaizinho region, recording one step in the accretion-collisional phase of the São Gabriel Terrane. The lower-amphibolite facies was evidenced by a single event, with metamorphic conditions of 4.5-5.1 kbar and 536-555 ºC indicated by

the garnet growth. U-Pb dating of low-U (<1 ppm) garnet yielded 721 ± 14 Ma for bulk garnet growth, about 18 Ma after the MDA. Both Al-saturated and unsaturated Ca-poor sedimentary sources are indicated by the major element composition of dravite, while an island arc source is proposed based on $\delta^{11}B$ ratios (from +0.51 to +3.39‰). The sedimentary rocks from the Serrinha Formation were deposited in an intra-arc environment and evolved to a collisional context, recording part of the history of the Brasiliano Orogen during Gondwana amalgamation.

Acknowledgments

Supplementary Data

Supplementary Table S1. Analytical setup for electron microprobe analyses.

Elements	Energetic Line	Spectrometer	Crystal	Standard
Na	Kα	1	TAPH	Anorthoclase
Si	Kα	2	TAP	Quartz
Al	Kα	2	TAP	Corundum
Mg	Kα	2	TAP	Olivine
Ba	Lα	3	PETH	Barite
Fe	Kα	3	LIFH	Almandine
Cu	Kα	3	LIFH	G-Augite

Elements	Energetic Line	Spectrometer	Crystal	Standard
Ti	Kα	3	LIFH	Ilmenite
Ca	Kα	4	PETJ	Cu-Augite
Ni	Kα	4	LIF	Glass-Rhyolitic IR-X
K	Kα	5	PETL	Microcline
Mn	Kα	5	LIFL	Ilmenite

TAP = Thallium acid phthalate crystal; PET = Pentaerythritol crystal; LIF = Lithium fluoride crystal.

Supplementary Table 2. Analytical setup for U-Pb analyzes.

Laboratory & Sample preparation	
Laboratory name	Instituto de Geociências (IGeo), Universidade Federal do Rio Grande do Sul (UFRGS)
Sample type/mineral	Garnet
Sample preparation	The selected hand sample was crushed; garnet grains were concentrated using conventional magnetic and density separation methods, including jaw and disc crusher, Frantz separator, panning, and heavy liquids. Final selection was carried out by hand picking using a binocular microscope and tweezers. Crystals were mounted in 25 mm-diameter circular epoxy resin and polished using diamond paste to expose their interiors.
Imaging	BSE and optical microscopy
Laboratory & Analyses	
Laboratory name	Isotopic Geochemistry Laboratory, Universidade Federal de Ouro Preto (UFOP)
Laser ablation system	
Make, Model & type	Photon Machines G2 excimer laser ablation
Ablation cell and volume	Low volume HelEx/Hellen two volume ablation cell
Laser wavelenght	193 nm
Pulse width	4 ns
Fluence	6 J/cm^{-2}
Repetition rate	6 Hz
Ablation duration	40 s
Spot size	80 μm
Sampling mode/pattern	Static spot ablation/Single spot
Carrier gas	100 % He in the cell, Ar and N_2 make-up gas, combined using two Y-piece 50% along the sample transport line to the torch
Cell carrier gas flow (He)	0.7 l/min
ICP-MS Instrument	
Make, Model & type	TermoFisher Scientific, Neptune Plus, MC-ICP-MS
Sample introduction	Ablation aerosol
RF power (W)	1100 W
Extraction lenses	X type
Make-up gas flow	0.5 l/min Ar
Detection system	SEM/compact discrete dynode ion counters/Faraday cups

Masses measured	Faraday ^{232}Th and ^{238}U and IC ^{202}Hg, ^{204}Pb, ^{206}Pb, ^{207}Pb, ^{208}Pb
Integration time per peak/dwell times	# Not analyzed
Total integration time per output datapoint	0.131 s
IC Dead time	IC1-2: 20 ns; IC3-4-5: 70 ns and IC6-7-8: 5 ns

Data Processing

Calibration strategy	NIST 614
Reference Material information	WILLSBORO (1022 ± 16 Ma; Seman *et al.*, 2017)
	IDA DOME (520 Ma and 511-508 Ma; Longridge *et al.*, 2011)
	MALI (202 ± 1.2 Ma; Seman *et al.*, 2017)
	BUSHVELD (2059.2 ± 3.5 Ma; Buick *et al.*, 2011)
	MXE (463 ± 1.7 Ma, internal garnet reference)
Data processing package used	SATURN package (Ouro Preto software, beta version). The mean ^{207}Pb/^{206}Pb ratio of each analysis was corrected for mass bias 0.3% and the ^{206}Pb/^{238}U ratio for interelement fractionation (~5%), including drift over the sequence time, using NIST SRM-614 and the 202 Ma Mali Garnet.
Mass discrimination	Using standard sample bracketing with SRM NIST-614 and MALI as primary reference material
Common-Pb correction, composition and uncertainty	No common-Pb correction applied to the data
Uncertainty level and propagation	Ages are quote at 2s absolute, propagation is by quadratic addition. Reproducibility and age uncertainty of reference material and common-Pb composition uncertainty are propagated where appropriate.
Quality control/Validation	WILLSBORO: 1022 ± 15.2 Ma (MSWD = 0.95, N = 7)
	IDA DOME: 517 ± 7 Ma (MSWD = 0.49, N = 16)
	BUSHVELD: 2049 ± 28 Ma (MSWD = 1.6, N = 16)
	MALI: 198.5 ± 1.7 Ma (MSWD = 2.3; N = 24)
	MXE: 459.8 ± 6.7 Ma (MSWD = 1.4, N = 16)

Supplementary Table 3. Major element composition of studied minerals.

FELDSPAR (PARTE 1) – (wt%)

Spot-grain	SiO2	TiO2	Al2O3	FeO	CaO	Na2O	K2O	Total
19-1	59.17	0.06	25.21	0.09	7.55	7.13	0.08	99.30
20-1	59.81	0.00	25.22	0.09	7.46	7.28	0.05	99.94
21-2	59.45	0.01	25.12	0.02	7.62	7.18	0.07	99.51
22-2	59.30	0.02	25.83	0.01	7.28	7.28	0.08	99.85
23-2	59.53	0.00	25.31	0.18	7.53	7.12	0.11	99.80
24-3	59.92	0.00	24.92	0.16	7.62	7.19	0.07	99.90
25-3	59.88	0.00	25.44	0.05	7.01	7.26	0.07	99.77
26-3	59.34	0.00	25.98	0.00	7.53	6.91	0.06	99.85
85-4	59.69	0.01	24.98	0.01	7.33	7.55	0.08	99.70

Spot-grain	SiO2	TiO2	Al2O3	FeO	CaO	Na2O	K2O	Total
86-4	60.85	0.02	23.98	0.00	6.21	8.18	0.09	99.36
87-4	60.95	0.01	24.28	0.01	6.52	7.89	0.09	99.78
88-4	60.90	0.00	24.03	0.00	6.03	8.09	0.09	99.16
90-4	60.96	0.01	23.76	0.06	5.60	8.19	0.09	98.68

FELDSPAR (PARTE 2)

Spot-grain	Cations per 8 oxygens						End-members			Mineral Classification
	Si	Al	Fe	Ca	Na	K	An.	Ab.	Or.	
19-1	2.659	1.336	0.003	0.363	0.621	0.004	0.37	0.63	0.00	Andesine
20-1	2.668	1.326	0.003	0.356	0.629	0.003	0.36	0.64	0.00	Andesine
21-2	2.664	1.327	0.001	0.366	0.624	0.004	0.37	0.63	0.00	Andesine
22-2	2.647	1.360	0.000	0.348	0.630	0.004	0.35	0.64	0.00	Andesine
23-2	2.661	1.333	0.007	0.361	0.617	0.006	0.37	0.63	0.01	Andesine
24-3	2.675	1.311	0.006	0.364	0.622	0.004	0.37	0.63	0.00	Andesine
25-3	2.671	1.338	0.002	0.335	0.628	0.004	0.35	0.65	0.00	Andesine
26-3	2.646	1.365	0.000	0.360	0.597	0.003	0.37	0.62	0.00	Andesine
85-4	2.671	1.318	0.000	0.352	0.655	0.005	0.35	0.65	0.00	Andesine
86-4	2.723	1.265	0.000	0.298	0.709	0.005	0.29	0.70	0.01	Oligoclase
87-4	2.716	1.275	0.000	0.311	0.682	0.005	0.31	0.68	0.00	Andesine
88-4	2.727	1.268	0.000	0.289	0.703	0.005	0.29	0.70	0.01	Oligoclase
90-4	2.740	1.259	0.002	0.270	0.714	0.005	0.27	0.72	0.01	Oligoclase

BIOTITE (PARTE 1) – Wt.%

Spot-grain	SiO2	TiO2	Al2O3	FeO	MnO	MgO	CaO	Na2O	K2O	Cl	F	Total
46-1	36.27	1.90	19.15	17.59	0.04	11.73	0.04	0.23	8.34	0.02	0.01	95.40
47-1	36.32	1.83	19.04	17.24	0.00	12.04	0.04	0.23	8.89	0.01	0.23	95.79
48-1	36.25	1.65	19.66	17.30	0.05	11.17	0.01	0.21	8.72	0.00	0.04	95.05
49-1	36.62	1.64	19.81	17.28	0.07	11.09	0.07	0.22	8.92	0.00	0.19	95.87
68-2	36.42	1.82	19.93	17.05	0.04	10.93	0.03	0.23	8.68	0.01	0.09	95.23
69-2	36.71	1.76	20.00	17.27	0.07	11.14	0.00	0.23	8.79	0.00	0.15	96.11
70-2	36.84	1.57	19.99	16.95	0.04	11.03	0.02	0.21	8.83	0.00	0.11	95.60
71-2	36.64	1.66	19.02	17.13	0.06	11.07	0.00	0.18	8.73	0.00	0.19	94.63
72-2	36.68	1.90	19.42	16.85	0.01	11.75	0.06	0.20	8.85	0.00	0.12	95.85
95-3	36.42	1.44	19.34	18.48	0.02	11.71	0.03	0.11	7.93	0.00	0.16	95.62
96-3	36.48	1.25	19.30	18.82	0.06	11.75	0.06	0.16	7.54	0.00	0.19	95.58
97-3	36.99	1.50	19.47	17.64	0.05	11.22	0.01	0.16	8.37	0.00	0.14	95.56
117-4	36.14	1.77	19.70	17.58	0.08	11.05	0.04	0.17	8.52	0.00	0.21	95.23
118-4	36.03	1.73	19.47	18.08	0.07	10.98	0.04	0.21	8.77	0.00	0.14	95.53
119-4	36.87	1.66	19.45	18.11	0.04	11.31	0.02	0.18	8.25	0.01	0.13	96.05
120-4	36.16	1.77	19.08	17.46	0.05	11.56	0.01	0.19	8.56	0.01	0.22	95.04
121-5	36.07	1.52	19.47	19.28	0.05	11.86	0.05	0.13	6.71	0.01	0.10	94.22
122-5	35.43	1.55	19.35	20.23	0.05	12.15	0.10	0.14	6.29	0.01	0.17	95.42
123-5	35.64	1.66	18.80	20.47	0.09	12.26	0.04	0.12	5.91	0.00	0.08	95.05

Spot-grain	SiO2	TiO2	Al2O3	FeO	MnO	MgO	CaO	Na2O	K2O	Cl	F	Total
124-5	36.60	1.82	18.83	18.05	0.06	10.38	0.06	0.24	8.44	0.01	0.20	94.65
125-5	36.56	1.83	18.05	18.12	0.09	11.54	0.04	0.25	8.45	0.01	0.19	95.05
126-5	36.01	1.99	18.72	18.74	0.01	10.98	0.07	0.20	8.33	0.01	0.15	95.19
137-6	36.90	1.72	19.68	16.66	0.05	10.87	0.02	0.24	8.29	0.00	0.12	94.52
138-6	36.37	1.71	19.71	16.81	0.03	11.08	0.03	0.29	8.59	0.01	0.03	94.67
139-6	36.82	1.71	19.45	16.62	0.06	10.59	0.07	0.27	8.37	0.01	0.12	94.10
140-6	36.36	1.82	19.85	17.04	0.06	10.82	0.00	0.27	8.69	0.01	0.15	95.07
141-6	36.14	1.73	19.57	16.84	0.03	11.11	0.03	0.24	8.48	0.01	0.11	94.30
142-6	36.26	1.73	19.75	17.86	0.06	10.78	0.03	0.26	8.59	0.01	0.08	95.43
153-7	36.46	1.55	19.07	16.95	0.00	11.76	0.04	0.19	8.84	0.01	0.20	95.02
154-7	36.54	1.55	19.74	17.48	0.04	11.08	0.03	0.16	8.75	0.01	0.19	95.55
155-7	36.14	1.58	19.66	18.19	0.06	11.28	0.20	0.25	7.19	0.01	0.21	94.70
157-7	36.71	1.43	19.34	17.29	0.07	10.86	0.06	0.19	8.27	0.01	0.20	94.41
14-8	35.27	1.85	19.96	17.83	0.08	11.50	0.03	0.20	9.03	0.01	0.10	95.85
15-8	36.23	1.71	19.81	17.06	0.05	12.08	0.00	0.17	8.57	0.01	0.20	95.84
16-8	36.12	1.62	19.44	17.18	0.07	11.97	0.04	0.20	8.53	0.00	0.17	95.37
17-8	36.08	1.65	19.55	17.99	0.07	11.06	0.00	0.19	8.59	0.01	0.12	95.29
18-8	36.21	1.69	19.41	17.02	0.02	11.00	0.04	0.20	8.76	0.00	0.22	94.51

BIOTITE (PARTE 2)

Spot-grain	Si	Al iv	Ti	Al vi	Fe	Mn	Mg	Ca	Na	K	XMg = Mg/Mg+Fe
46-1	5.424	2.576	0.214	0.800	2.201	0.006	2.615	0.007	0.067	1.592	0.54
47-1	5.423	2.577	0.205	0.773	2.153	0.000	2.681	0.006	0.066	1.692	0.55
48-1	5.437	2.563	0.186	0.913	2.171	0.006	2.497	0.002	0.060	1.668	0.54
49-1	5.453	2.547	0.183	0.930	2.151	0.009	2.462	0.011	0.063	1.694	0.53
68-2	5.443	2.557	0.204	0.955	2.131	0.005	2.435	0.004	0.066	1.655	0.53
69-2	5.444	2.556	0.197	0.939	2.142	0.008	2.462	0.000	0.065	1.663	0.53
70-2	5.480	2.520	0.176	0.985	2.109	0.005	2.446	0.003	0.061	1.675	0.54
71-2	5.521	2.479	0.188	0.897	2.158	0.007	2.486	0.000	0.053	1.678	0.54
72-2	5.451	2.549	0.212	0.850	2.093	0.002	2.602	0.010	0.059	1.678	0.55
95-3	5.439	2.561	0.162	0.842	2.308	0.003	2.607	0.005	0.033	1.510	0.53
96-3	5.449	2.551	0.141	0.846	2.350	0.008	2.616	0.010	0.046	1.436	0.53
97-3	5.510	2.490	0.168	0.929	2.198	0.007	2.491	0.002	0.046	1.591	0.53
117-4	5.421	2.579	0.200	0.904	2.205	0.010	2.471	0.007	0.049	1.630	0.53
118-4	5.412	2.588	0.196	0.858	2.271	0.009	2.459	0.007	0.060	1.680	0.52
119-4	5.476	2.524	0.185	0.881	2.250	0.006	2.503	0.004	0.052	1.562	0.53
120-4	5.439	2.561	0.200	0.822	2.196	0.007	2.592	0.002	0.056	1.643	0.54
121-5	5.392	2.608	0.171	0.823	2.410	0.006	2.644	0.009	0.038	1.279	0.52
122-5	5.312	2.688	0.175	0.732	2.536	0.007	2.716	0.015	0.041	1.203	0.52
123-5	5.356	2.644	0.187	0.686	2.572	0.012	2.746	0.006	0.034	1.132	0.52
124-5	5.534	2.466	0.206	0.888	2.281	0.008	2.340	0.009	0.072	1.627	0.51
125-5	5.514	2.486	0.208	0.720	2.284	0.012	2.594	0.006	0.074	1.625	0.53
126-5	5.436	2.564	0.226	0.766	2.365	0.001	2.471	0.012	0.059	1.603	0.51
137-6	5.527	2.473	0.194	1.000	2.086	0.007	2.426	0.003	0.070	1.583	0.54
138-6	5.461	2.539	0.193	0.947	2.110	0.004	2.480	0.005	0.083	1.645	0.54

Spot-grain	Si	Al iv	Ti	Al vi	Fe	Mn	Mg	Ca	Na	K	XMg = Mg/Mg+Fe
139-6	5.548	2.452	0.193	1.002	2.095	0.007	2.378	0.012	0.079	1.608	0.53
140-6	5.450	2.550	0.205	0.956	2.136	0.007	2.417	0.000	0.078	1.661	0.53
141-6	5.452	2.548	0.196	0.932	2.124	0.004	2.498	0.005	0.070	1.632	0.54
142-6	5.432	2.568	0.195	0.919	2.237	0.007	2.407	0.005	0.076	1.642	0.52
153-7	5.473	2.527	0.175	0.847	2.127	0.000	2.633	0.007	0.056	1.693	0.55
154-7	5.459	2.541	0.174	0.935	2.184	0.005	2.468	0.004	0.047	1.668	0.53
155-7	5.426	2.574	0.178	0.906	2.283	0.007	2.524	0.032	0.072	1.377	0.53
157-7	5.532	2.468	0.163	0.966	2.179	0.009	2.439	0.010	0.056	1.589	0.53
14-8	5.289	2.711	0.208	0.816	2.235	0.010	2.572	0.004	0.059	1.726	0.53
15-8	5.385	2.615	0.191	0.855	2.120	0.006	2.677	0.000	0.050	1.625	0.56
16-8	5.407	2.593	0.182	0.835	2.150	0.009	2.671	0.006	0.058	1.629	0.55
17-8	5.419	2.581	0.186	0.881	2.260	0.009	2.476	0.000	0.055	1.647	0.52
18-8	5.465	2.535	0.192	0.919	2.149	0.002	2.476	0.007	0.057	1.687	0.54

MUSCOVITE (PARTE 1) – Wt.%

Spot-grain	SiO2	TiO2	Al2O3	FeO	MnO	MgO	CaO	Na2O	K2O	BaO	Total
50-1	45.96	0.49	33.75	1.63	0.00	0.92	0.11	1.07	9.15	0.07	93.23
51-1	45.74	0.55	33.64	2.21	0.00	1.53	0.04	0.92	9.10	0.10	93.82
52-1	45.56	0.49	34.00	1.11	0.00	0.82	0.04	1.09	9.35	0.18	92.73
53-1	45.28	0.54	34.40	0.94	0.00	0.72	0.03	1.20	9.26	0.14	92.55
54-1	45.59	0.62	34.43	1.05	0.02	0.67	0.02	1.16	9.10	0.15	92.88
91-2	45.36	0.63	35.37	0.96	0.00	0.68	0.04	1.16	9.15	0.09	93.56
92-2	45.25	0.57	35.82	0.89	0.00	0.69	0.02	1.17	9.14	0.16	93.77
93-2	44.68	0.42	35.49	1.13	0.00	0.69	0.06	1.16	9.09	0.25	93.03
94-2	44.83	0.56	34.46	1.10	0.00	0.76	0.03	1.14	9.11	0.10	92.17
161-3	45.14	0.56	34.53	1.11	0.00	0.71	0.03	1.15	9.25	0.09	92.58
166-4	45.27	0.44	35.16	0.90	0.00	0.58	0.02	1.20	9.07	0.05	92.74

MUSCOVITE (PARTE 2)

| Spot-grain | Cations per 22 oxygens | | | | | | | | | | End-members | |
	Si	Al iv	Ti	Al vi	Fe	Mn	Mg	Ca	Na	K	XNa	XK
50-1	6.240	1.760	0.050	3.639	0.185	0.000	0.186	0.016	0.282	1.584	0.15	0.84
51-1	6.188	1.812	0.056	3.551	0.250	0.000	0.308	0.006	0.242	1.570	0.13	0.86
52-1	6.219	1.781	0.050	3.690	0.126	0.000	0.166	0.006	0.288	1.628	0.15	0.85
53-1	6.182	1.818	0.055	3.718	0.107	0.000	0.146	0.004	0.316	1.614	0.16	0.83
54-1	6.199	1.801	0.064	3.715	0.120	0.002	0.135	0.002	0.305	1.578	0.16	0.84
91-2	6.121	1.879	0.064	3.747	0.109	0.000	0.137	0.006	0.303	1.575	0.16	0.84
92-2	6.091	1.909	0.057	3.773	0.101	0.000	0.139	0.003	0.306	1.569	0.16	0.84

93-2	6.079	1.921	0.042	3.770	0.128	0.000	0.140	0.009	0.306	1.578	0.16	0.83
94-2	6.148	1.852	0.058	3.717	0.126	0.000	0.156	0.004	0.303	1.594	0.16	0.84
161-3	6.161	1.839	0.057	3.715	0.127	0.000	0.145	0.004	0.304	1.610	0.16	0.84
166-4	6.151	1.849	0.044	3.780	0.102	0.000	0.117	0.003	0.316	1.572	0.17	0.83

STAUROLITE (PARTE 1) – Wt.%

Spot-grain	SiO2	TiO2	Al2O3	FeO	MnO	MgO	CaO	Na2O	K2O	Total
8-1	28.02	0.61	52.73	13.20	0.16	1.38	0.01	0.03	0.01	96.17
9-1	27.59	0.53	52.63	13.20	0.18	1.99	0.00	0.01	0.00	96.17
10-1	28.40	0.48	52.16	14.32	0.17	2.14	0.03	0.03	0.00	97.75
11-1	28.24	0.54	52.89	13.19	0.13	2.12	0.03	0.05	0.00	97.19
12-1	28.39	0.56	52.17	14.29	0.14	2.12	0.04	0.01	0.01	97.75
13-1	28.48	0.64	52.79	13.47	0.14	2.02	0.01	0.02	0.01	97.58
38-2	28.24	0.64	53.36	13.35	0.18	1.83	0.00	0.04	0.00	97.72
39-2	28.58	0.47	53.29	13.19	0.17	1.71	0.00	0.04	0.01	97.49
40-2	27.47	0.49	53.14	13.41	0.14	1.61	0.00	0.00	0.00	96.28
41-2	27.73	0.53	52.72	13.69	0.16	1.59	0.00	0.03	0.01	96.51
42-3	28.60	0.61	53.07	12.82	0.13	2.10	0.09	0.04	0.01	97.52
43-3	28.54	0.56	53.01	12.88	0.15	2.07	0.04	0.01	0.00	97.28
44-3	28.30	0.53	52.93	13.25	0.19	2.00	0.00	0.00	0.01	97.26
45-3	28.68	0.59	53.15	13.03	0.14	1.95	0.02	0.03	0.02	97.62
62-4	28.23	0.63	53.60	13.12	0.16	2.09	0.01	0.00	0.00	97.85
63-4	28.13	0.60	52.00	13.55	0.12	2.14	0.00	0.02	0.01	96.59
64-4	28.42	0.53	52.05	13.07	0.11	2.13	0.01	0.02	0.01	96.36
65-4	28.24	0.56	53.06	13.35	0.18	2.07	0.00	0.02	0.01	97.50
66-4	28.45	0.65	52.78	13.53	0.17	2.00	0.01	0.02	0.00	97.65
67-4	28.25	0.61	53.19	13.54	0.13	1.92	0.00	0.00	0.00	97.68
146-5	27.79	0.63	52.51	13.79	0.14	1.83	0.00	0.02	0.01	96.84
147-5	28.29	0.57	53.24	13.27	0.17	1.95	0.01	0.02	0.00	97.58
148-5	28.42	0.55	52.99	13.44	0.16	2.08	0.02	0.00	0.00	97.75
149-5	28.48	0.57	52.89	13.48	0.18	2.04	0.00	0.05	0.00	97.69
150-5	28.58	0.57	52.65	13.51	0.16	2.03	0.01	0.00	0.00	97.51
151-5	28.38	0.60	52.77	13.52	0.15	2.13	0.04	0.01	0.00	97.65
152-5	28.98	0.61	52.40	13.28	0.11	1.75	0.09	0.01	0.02	97.25

STAUROLITE (PARTE 2)

Spot-grain	Si	Ti	Al	Fe(ii)	Mn	Mg	Ca	Na	K
8-1	3.943	0.064	8.745	1.553	0.020	0.288	0.002	0.008	0.002
9-1	3.889	0.056	8.741	1.555	0.022	0.419	0.000	0.004	0.001
10-1	3.956	0.050	8.563	1.669	0.020	0.444	0.005	0.007	0.000
11-1	3.933	0.056	8.680	1.535	0.016	0.440	0.004	0.014	0.000
12-1	3.954	0.059	8.564	1.664	0.017	0.440	0.006	0.002	0.002
13-1	3.954	0.067	8.637	1.563	0.016	0.418	0.002	0.006	0.002
38-2	3.916	0.067	8.721	1.548	0.021	0.378	0.000	0.011	0.001
39-2	3.964	0.049	8.710	1.530	0.020	0.353	0.000	0.011	0.002
40-2	3.868	0.051	8.818	1.579	0.016	0.338	0.000	0.000	0.000
41-2	3.902	0.056	8.743	1.611	0.019	0.334	0.000	0.008	0.002
42-3	3.961	0.064	8.663	1.484	0.016	0.434	0.014	0.012	0.002

43-3	3.962	0.058	8.674	1.495	0.018	0.429	0.006	0.003	0.000
44-3	3.940	0.055	8.686	1.543	0.022	0.416	0.000	0.001	0.001
45-3	3.969	0.061	8.669	1.508	0.017	0.402	0.003	0.008	0.003
62-4	3.902	0.066	8.731	1.517	0.018	0.430	0.002	0.001	0.000
63-4	3.951	0.063	8.609	1.591	0.015	0.449	0.000	0.005	0.002
64-4	3.989	0.056	8.608	1.534	0.013	0.445	0.002	0.006	0.001
65-4	3.923	0.058	8.688	1.551	0.021	0.430	0.000	0.004	0.001
66-4	3.950	0.067	8.637	1.571	0.020	0.413	0.002	0.006	0.000
67-4	3.921	0.063	8.699	1.571	0.015	0.398	0.000	0.000	0.000
146-5	3.904	0.066	8.692	1.620	0.016	0.383	0.000	0.004	0.002
147-5	3.926	0.060	8.707	1.540	0.020	0.404	0.001	0.006	0.000
148-5	3.941	0.057	8.661	1.559	0.019	0.430	0.003	0.000	0.001
149-5	3.950	0.059	8.646	1.563	0.021	0.422	0.000	0.012	0.000
150-5	3.971	0.059	8.620	1.570	0.019	0.420	0.001	0.000	0.000
151-5	3.942	0.062	8.638	1.570	0.018	0.441	0.006	0.002	0.000
152-5	4.029	0.064	8.586	1.544	0.013	0.362	0.013	0.004	0.004

GARNET (PARTE 1) – Wt.%

Spot-grain	SiO2	TiO2	Al2O3	FeO	MnO	MgO	CaO	Total
1-1	37.58	0.01	21.72	33.14	2.95	3.08	2.21	100.75
2-1	37.20	0.00	21.49	32.63	2.74	3.27	2.47	99.82
3-1	37.63	0.01	21.27	32.09	2.71	3.34	2.51	99.67
4-1	37.75	0.01	21.47	30.97	2.72	3.34	2.56	99.03
5-1	37.44	0.03	21.51	30.99	2.87	3.40	2.76	99.26
6-1	37.81	0.01	21.40	31.09	2.91	3.32	2.97	99.63
7-1	37.35	0.01	21.35	31.13	2.93	3.43	2.75	98.98
8-1	37.56	0.03	21.19	31.36	3.07	3.38	2.91	99.54
9-1	37.08	0.02	21.80	30.72	2.90	3.40	2.90	99.08
10-1	37.23	0.04	21.19	30.79	2.91	3.38	2.85	98.51
11-1	37.54	0.03	21.57	31.31	2.83	3.43	2.87	99.66
12-1	37.41	0.00	21.38	31.60	2.78	3.45	2.58	99.30
13-1	37.33	0.00	21.10	31.71	2.59	3.31	2.54	98.63
14-1	37.20	0.02	21.38	31.91	2.85	3.35	2.32	99.06
21-2	37.87	0.01	21.39	32.63	2.66	2.98	2.26	99.88
22-2	37.96	0.01	21.56	32.78	2.69	3.29	2.35	100.73
23-2	37.99	0.00	21.27	31.96	2.79	3.43	2.38	99.91
24-2	37.73	0.02	21.27	31.89	3.02	3.39	2.59	100.05
25-2	37.01	0.03	21.37	31.11	3.52	3.26	2.67	99.02
26-2	37.73	0.02	21.36	31.25	3.52	3.25	2.84	100.07
27-2	37.90	0.08	21.24	31.54	3.48	3.33	2.75	100.32
28-2	37.65	0.02	21.04	31.53	3.38	3.22	2.78	99.74
29-2	37.65	0.03	21.23	30.72	3.24	3.27	3.01	99.25
30-2	37.71	0.14	21.29	31.08	3.12	3.28	2.80	99.45
31-2	37.94	0.03	21.26	31.62	2.93	3.35	2.73	99.89
32-2	37.83	0.04	21.23	31.37	3.20	3.38	2.58	99.66
33-2	37.94	0.00	21.25	31.41	3.02	3.29	2.46	99.49
34-2	37.70	0.00	21.02	31.82	2.85	3.30	2.16	99.00
35-2	37.74	0.01	21.41	32.25	2.83	3.23	2.40	99.93
36-2	37.89	0.03	21.19	32.05	2.64	3.18	2.41	99.49

Spot-grain	SiO2	TiO2	Al2O3	FeO	MnO	MgO	CaO	Total
37-2	37.63	0.01	21.17	31.66	2.66	3.13	2.40	98.81
38-3	37.97	0.03	21.14	32.14	2.67	3.29	2.23	99.57
39-3	37.80	0.00	21.34	31.73	3.01	3.41	2.35	99.76
40-3	37.85	0.04	21.26	30.93	2.98	3.42	2.72	99.23
41-3	37.92	0.06	21.20	30.22	3.67	3.16	3.10	99.37
42-3	37.73	0.05	21.15	30.26	3.79	3.10	2.71	98.87
43-3	37.92	0.07	21.24	30.67	3.83	3.22	2.69	99.85
44-3	37.77	0.03	21.20	31.88	3.94	3.18	2.40	100.48
45-3	37.99	0.07	20.94	30.65	4.34	3.06	2.91	100.10
46-3	37.88	0.06	21.14	30.93	4.50	3.02	2.67	100.38
47-3	37.72	0.05	21.28	31.29	4.57	3.11	2.63	100.73
48-3	37.50	0.05	20.83	31.65	4.73	3.12	2.74	100.72
49-3	37.56	0.04	21.45	30.73	4.18	2.80	2.77	99.64
50-3	37.65	0.06	21.21	31.18	3.95	3.06	2.87	100.05
51-3	37.58	0.02	21.95	31.78	3.79	3.22	2.41	100.74
52-3	37.66	0.02	21.01	31.93	3.33	3.21	2.61	99.89
53-3	37.35	0.00	21.01	32.50	2.82	3.22	2.27	99.35
1-4	37.38	0.00	20.71	33.53	3.05	3.13	2.45	100.29
2-4	37.09	0.02	20.55	32.36	3.15	3.43	2.83	99.50
3-4	37.27	0.01	20.43	31.79	3.23	3.43	3.01	99.27
4-4	37.51	0.00	20.71	31.72	3.21	3.35	3.07	99.61
5-4	37.65	0.33	20.36	31.27	3.09	3.38	2.92	99.06
6-4	37.32	0.03	20.63	32.25	2.80	3.43	2.83	99.39
7-4	37.44	0.00	20.82	32.89	2.75	3.38	2.44	99.79
31-5	36.58	0.11	20.34	32.83	2.93	3.16	2.33	98.29
32-5	37.36	0.04	20.52	32.37	3.05	3.36	2.97	99.72
33-5	37.33	0.05	20.40	32.24	3.33	3.31	3.07	99.81
34-5	37.95	0.02	20.27	31.50	3.49	3.24	2.86	99.40
35-5	37.96	0.02	20.56	31.86	3.17	3.33	2.90	99.85
36-5	37.17	0.04	20.41	32.35	2.92	3.31	2.81	99.04
37-5	37.17	0.00	20.23	32.90	2.89	3.24	2.67	99.19
105-6	37.20	0.00	20.65	32.86	2.92	3.14	2.54	99.38
106-6	37.25	0.00	20.60	32.39	2.99	3.28	2.66	99.23
107-6	37.25	0.03	20.63	31.58	3.65	3.32	2.90	99.42
108-6	36.94	0.01	20.69	31.66	3.49	3.39	2.92	99.14
109-6	37.15	0.01	20.54	32.11	3.20	3.31	2.87	99.28
110-6	37.38	0.00	20.53	32.46	2.81	3.39	2.71	99.33
111-7	37.28	0.02	20.62	32.22	3.09	3.32	2.70	99.32
112-7	37.11	0.02	20.39	31.80	3.67	3.12	3.02	99.13
113-7	37.37	0.08	20.52	31.03	4.27	3.09	3.13	99.55
114-7	36.79	0.06	20.48	30.89	4.91	2.93	2.92	99.03
115-7	37.56	0.02	20.67	31.09	4.50	3.09	2.98	100.05
116-7	37.15	0.00	20.54	32.18	3.36	3.25	2.55	99.13

GARNET (PARTE 2) – Py = pyrope, Alm = almandine, Gro = grossular, Spe = spessartine.

Spot-grain	Si	Ti	Al	Fe	Mn	Mg	Ca	Py	Alm	Gro	Spe
								End-members, fractions			molar
	Cation per 24 oxygens										
1-1	5.98	0.00	4.08	4.41	0.40	0.73	0.38	0.12	0.75	0.064	0.067
2-1	5.97	0.00	4.06	4.38	0.37	0.78	0.42	0.13	0.74	0.071	0.063
3-1	6.03	0.00	4.02	4.30	0.37	0.80	0.43	0.14	0.73	0.073	0.062
4-1	6.06	0.00	4.07	4.16	0.37	0.80	0.44	0.14	0.72	0.076	0.064
5-1	6.02	0.00	4.08	4.17	0.39	0.81	0.47	0.14	0.71	0.081	0.067
6-1	6.05	0.00	4.03	4.16	0.39	0.79	0.51	0.14	0.71	0.087	0.067
7-1	6.02	0.00	4.05	4.19	0.40	0.82	0.47	0.14	0.71	0.080	0.068
8-1	6.03	0.00	4.01	4.21	0.42	0.81	0.50	0.14	0.71	0.084	0.070
9-1	5.97	0.00	4.14	4.14	0.39	0.82	0.50	0.14	0.71	0.085	0.068
10-1	6.03	0.00	4.04	4.17	0.40	0.82	0.49	0.14	0.71	0.084	0.068
11-1	6.01	0.00	4.07	4.19	0.38	0.82	0.49	0.14	0.71	0.084	0.065
12-1	6.01	0.00	4.05	4.25	0.38	0.83	0.44	0.14	0.72	0.075	0.064
13-1	6.04	0.00	4.02	4.29	0.35	0.80	0.44	0.14	0.73	0.075	0.060
14-1	6.00	0.00	4.06	4.30	0.39	0.81	0.40	0.14	0.73	0.068	0.066
						Core average		0.14	0.72	0.080	0.066
						Rim average		0.13	0.74	0.068	0.065
21-2	6.06	0.00	4.03	4.37	0.36	0.71	0.39	0.12	0.75	0.066	0.062
22-2	6.03	0.00	4.03	4.35	0.36	0.78	0.40	0.13	0.74	0.068	0.061
23-2	6.07	0.00	4.00	4.27	0.38	0.82	0.41	0.14	0.73	0.069	0.064
24-2	6.03	0.00	4.01	4.26	0.41	0.81	0.44	0.14	0.72	0.075	0.069
25-2	5.98	0.00	4.07	4.20	0.48	0.79	0.46	0.13	0.71	0.078	0.081
26-2	6.03	0.00	4.02	4.17	0.48	0.77	0.49	0.13	0.71	0.082	0.080
27-2	6.04	0.01	3.99	4.20	0.47	0.79	0.47	0.13	0.71	0.079	0.079
28-2	6.04	0.00	3.98	4.23	0.46	0.77	0.48	0.13	0.71	0.080	0.077
29-2	6.05	0.00	4.02	4.13	0.44	0.78	0.52	0.13	0.70	0.088	0.075
30-2	6.04	0.02	4.02	4.16	0.42	0.78	0.48	0.13	0.71	0.082	0.072
31-2	6.06	0.00	4.00	4.22	0.40	0.80	0.47	0.14	0.72	0.079	0.067
32-2	6.05	0.00	4.00	4.20	0.43	0.81	0.44	0.14	0.71	0.075	0.074
33-2	6.08	0.00	4.01	4.21	0.41	0.79	0.42	0.13	0.72	0.072	0.070
34-2	6.08	0.00	4.00	4.29	0.39	0.79	0.37	0.14	0.73	0.064	0.066
35-2	6.04	0.00	4.03	4.31	0.38	0.77	0.41	0.13	0.73	0.070	0.065
36-2	6.08	0.00	4.01	4.30	0.36	0.76	0.41	0.13	0.74	0.071	0.061
37-2	6.08	0.00	4.03	4.27	0.36	0.75	0.41	0.13	0.74	0.071	0.063
						Core average		0.13	0.71	0.080	0.075
						Rim average		0.13	0.73	0.070	0.065
38-3	6.08	0.00	3.99	4.31	0.36	0.79	0.38	0.13	0.74	0.066	0.062
39-3	6.05	0.00	4.02	4.24	0.41	0.81	0.40	0.14	0.72	0.069	0.070
40-3	6.07	0.00	4.02	4.15	0.40	0.82	0.47	0.14	0.71	0.080	0.069
41-3	6.07	0.01	4.00	4.05	0.50	0.75	0.53	0.13	0.69	0.091	0.085
42-3	6.08	0.01	4.02	4.08	0.52	0.75	0.47	0.13	0.70	0.080	0.089
43-3	6.07	0.01	4.00	4.10	0.52	0.77	0.46	0.13	0.70	0.079	0.089
44-3	6.03	0.00	3.99	4.26	0.53	0.76	0.41	0.13	0.71	0.069	0.089
45-3	6.07	0.01	3.95	4.10	0.59	0.73	0.50	0.12	0.69	0.084	0.099
46-3	6.05	0.01	3.98	4.13	0.61	0.72	0.46	0.12	0.70	0.077	0.103
47-3	6.01	0.01	3.99	4.17	0.62	0.74	0.45	0.12	0.70	0.075	0.103
48-3	6.00	0.01	3.93	4.24	0.64	0.74	0.47	0.12	0.70	0.077	0.105
49-3	6.03	0.01	4.06	4.13	0.57	0.67	0.48	0.11	0.71	0.082	0.097
50-3	6.03	0.01	4.00	4.17	0.54	0.73	0.49	0.12	0.70	0.083	0.090

Spot-grain	Si	Ti	Al	Fe	Mn	Mg	Ca	Py	Alm	Gro	Spe
51-3	5.97	0.00	4.11	4.22	0.51	0.76	0.41	0.13	0.72	0.069	0.086
52-3	6.04	0.00	3.97	4.28	0.45	0.77	0.45	0.13	0.72	0.075	0.076
53-3	6.03	0.00	4.00	4.39	0.39	0.78	0.39	0.13	0.74	0.066	0.065
						Core average		0.13	0.70	0.080	0.093
						Rim average		0.13	0.73	0.069	0.072
1-4	6.01	0.00	3.92	4.51	0.42	0.75	0.42	0.12	0.74	0.069	0.068
2-4	6.00	0.00	3.92	4.38	0.43	0.83	0.49	0.14	0.71	0.080	0.070
3-4	6.03	0.00	3.90	4.30	0.44	0.83	0.52	0.14	0.71	0.086	0.073
4-4	6.04	0.00	3.93	4.27	0.44	0.80	0.53	0.13	0.71	0.088	0.072
5-4	6.08	0.04	3.87	4.22	0.42	0.81	0.50	0.14	0.71	0.085	0.071
6-4	6.03	0.00	3.93	4.35	0.38	0.83	0.49	0.14	0.72	0.081	0.063
7-4	6.02	0.00	3.95	4.42	0.37	0.81	0.42	0.13	0.73	0.070	0.062
						Core average		0.14	0.71	0.084	0.070
						Rim average		0.13	0.74	0.070	0.065
31-5	6.00	0.01	3.93	4.50	0.41	0.77	0.41	0.13	0.74	0.067	0.067
32-5	6.02	0.00	3.90	4.36	0.42	0.81	0.51	0.13	0.72	0.084	0.068
33-5	6.02	0.01	3.88	4.35	0.46	0.80	0.53	0.13	0.71	0.087	0.074
34-5	6.11	0.00	3.85	4.24	0.48	0.78	0.49	0.13	0.71	0.082	0.079
35-5	6.09	0.00	3.89	4.27	0.43	0.80	0.50	0.13	0.71	0.083	0.072
36-5	6.03	0.01	3.90	4.39	0.40	0.80	0.49	0.13	0.72	0.080	0.066
37-5	6.04	0.00	3.87	4.47	0.40	0.78	0.46	0.13	0.73	0.076	0.065
						Core average		0.13	0.71	0.08	0.07
						Rim average		0.13	0.73	0.07	0.07
105-6	6.02	0.00	3.94	4.45	0.40	0.76	0.44	0.13	0.74	0.073	0.066
106-6	6.03	0.00	3.93	4.38	0.41	0.79	0.46	0.13	0.73	0.076	0.068
107-6	6.02	0.00	3.93	4.27	0.50	0.80	0.50	0.13	0.70	0.083	0.082
108-6	5.99	0.00	3.95	4.29	0.48	0.82	0.51	0.13	0.70	0.083	0.079
109-6	6.02	0.00	3.92	4.35	0.44	0.80	0.50	0.13	0.71	0.082	0.072
110-6	6.04	0.00	3.91	4.39	0.38	0.82	0.47	0.13	0.72	0.078	0.063
						Core average		0.13	0.71	0.08	0.08
						Rim average		0.13	0.73	0.08	0.07
111-7	6.03	0.00	3.93	4.36	0.42	0.80	0.47	0.13	0.72	0.077	0.070
112-7	6.02	0.00	3.90	4.32	0.50	0.75	0.52	0.12	0.71	0.086	0.083
113-7	6.03	0.01	3.90	4.19	0.58	0.74	0.54	0.12	0.69	0.089	0.096
114-7	5.99	0.01	3.93	4.21	0.68	0.71	0.51	0.12	0.69	0.083	0.111
115-7	6.04	0.00	3.92	4.18	0.61	0.74	0.51	0.12	0.69	0.085	0.101
116-7	6.03	0.00	3.93	4.37	0.46	0.79	0.44	0.13	0.72	0.073	0.076
						Core average		0.12	0.69	0.09	0.10
						Rim average		0.13	0.72	0.08	0.07

TOURMALINE (PARTE 1) – Wt.%

Spot-grain	SiO2	TiO2	Al2O3	FeO	MnO	MgO	CaO	Na2O
3-1	37.25	0.21	33.07	5.67	0.02	8.01	0.43	2.37
4-1	36.63	0.34	32.37	6.52	0.01	7.83	0.68	2.43
5-2	36.43	0.35	33.76	5.54	0.04	7.91	0.80	2.36
6-2	36.16	0.39	33.48	5.27	0.01	7.83	0.83	2.29
7-3	36.20	0.85	30.99	6.76	0.03	8.31	1.39	2.16

Spot-grain	SiO2	TiO2	Al2O3	FeO	MnO	MgO	CaO	Na2O
8-3	36.26	0.73	32.06	6.05	0.04	8.17	1.03	2.30
9-4	36.66	0.19	33.56	5.95	0.03	7.43	0.57	2.37
10-4	36.38	0.46	33.45	6.14	0.02	7.44	0.66	2.23
11-5	36.41	0.42	34.67	5.33	0.05	7.58	0.69	2.35
12-5	36.73	1.02	32.57	5.70	0.04	7.99	0.73	2.40
13-6	36.72	0.24	34.37	5.35	0.00	7.36	0.50	2.33
14-6	36.94	0.24	34.51	5.18	0.05	7.24	0.50	2.26
15-7	36.14	0.51	32.46	6.46	0.04	7.97	1.11	2.16
16-7	36.60	0.70	32.11	6.70	0.02	7.92	1.24	2.16
17-8	36.67	0.61	32.21	5.96	0.01	8.19	0.88	2.40
18-8	36.71	0.23	33.09	5.92	0.03	8.07	0.57	2.39
19-9	36.21	0.58	32.77	5.68	0.06	7.95	1.00	2.30
20-9	36.25	0.46	33.85	5.42	0.04	7.82	0.83	2.34
21-10	36.37	0.88	32.57	6.07	0.03	7.92	0.73	2.37
22-10	36.42	1.20	31.95	6.13	0.04	7.60	0.74	2.39
23-11	36.37	0.42	32.64	5.76	0.02	7.85	0.84	2.37
24-11	36.36	0.70	31.62	5.96	0.03	8.28	0.99	2.27
25-12	36.85	0.17	33.75	5.35	0.03	7.92	0.52	2.33
26-12	36.40	0.37	33.49	5.53	0.03	7.97	0.91	2.30
27-13	36.72	0.39	33.61	5.64	0.01	7.50	0.57	2.31
28-13	36.72	0.26	33.09	6.08	0.05	7.50	0.54	2.29
29-14	36.49	0.58	33.22	5.79	0.00	7.66	0.74	2.35
30-14	36.28	1.30	31.67	6.19	0.02	8.00	0.87	2.33
31-15	36.21	0.74	31.36	6.89	0.01	8.10	1.45	2.06
32-15	35.95	0.72	30.86	6.99	0.05	8.15	1.49	2.02
33-16	35.94	0.37	34.01	5.83	0.05	7.25	0.76	2.28
34-16	36.80	0.39	32.61	5.89	0.01	7.90	0.73	2.37
35-17	36.65	0.61	32.36	6.44	0.03	7.98	0.73	2.49
36-17	36.68	0.61	32.79	6.00	0.06	7.87	0.74	2.39
37-18	37.02	0.10	34.32	5.05	0.05	8.00	0.38	2.27
38-18	36.58	0.33	33.78	5.16	0.01	7.73	0.72	2.31
39-19	36.08	0.70	30.90	6.84	0.00	8.20	1.19	2.32
40-19	36.29	0.90	30.57	7.43	0.00	8.28	1.07	2.32
41-20	36.71	0.38	34.06	5.83	0.03	7.24	0.72	2.32
42-20	36.40	0.61	33.88	6.31	0.04	7.28	0.84	2.11
43-21	36.53	0.29	33.15	5.73	0.02	7.92	0.68	2.44
44-21	36.54	0.36	33.28	5.91	0.02	7.68	0.71	2.30
45-22	36.49	0.34	33.84	5.50	0.00	7.77	0.64	2.32
46-22	36.69	0.28	33.83	5.52	0.01	7.62	0.57	2.33

TOURMALINE (PARTE 2)

Spot-grain	K2O	BaO	Cr2O3	F	Cl	Total	H2O*	B2O3*	Li2O*
3-1	0.00	0.01	0.07	0.03	0.01	87.26	3.74	10.86	0.15
4-1	0.01	0.04	0.00	0.00	0.00	86.99	3.71	10.75	0.15
5-2	0.01	0.04	0.07	0.07	0.00	87.44	3.71	10.87	0.19
6-2	0.00	0.03	0.04	0.00	0.01	86.39	3.71	10.77	0.23
7-3	0.01	0.04	0.04	0.00	0.00	86.91	3.68	10.68	0.17

Spot-grain	K2O	BaO	Cr2O3	F	Cl	Total	H2O*	B2O3*	Li2O*
8-3	0.01	0.04	0.00	0.09	0.01	86.87	3.66	10.73	0.19
9-4	0.02	0.03	0.00	0.02	0.00	86.89	3.72	10.81	0.21
10-4	0.03	0.02	0.07	0.06	0.01	87.07	3.69	10.79	0.18
11-5	0.02	0.03	0.05	0.07	0.01	87.67	3.74	10.93	0.23
12-5	0.02	0.05	0.00	0.08	0.00	87.29	3.71	10.85	0.26
13-6	0.02	0.03	0.03	0.00	0.00	87.08	3.75	10.88	0.26
14-6	0.02	0.04	0.07	0.02	0.00	87.05	3.76	10.91	0.29
15-7	0.00	0.02	0.00	0.09	0.00	87.18	3.66	10.73	0.14
16-7	0.01	0.03	0.04	0.07	0.00	87.73	3.70	10.81	0.21
17-8	0.01	0.06	0.07	0.00	0.00	87.36	3.72	10.80	0.21
18-8	0.01	0.02	0.06	0.00	0.00	87.09	3.73	10.82	0.11
19-9	0.02	0.06	0.00	0.00	0.00	86.77	3.71	10.76	0.24
20-9	0.01	0.03	0.05	0.00	0.00	87.11	3.74	10.85	0.22
21-10	0.02	0.01	0.08	0.00	0.00	87.18	3.72	10.79	0.18
22-10	0.02	0.04	0.00	0.00	0.00	86.55	3.70	10.74	0.30
23-11	0.01	0.04	0.02	0.00	0.00	86.42	3.70	10.73	0.23
24-11	0.00	0.03	0.12	0.00	0.00	86.52	3.69	10.70	0.18
25-12	0.01	0.02	0.00	0.01	0.01	87.00	3.74	10.86	0.17
26-12	0.02	0.05	0.06	0.06	0.00	87.27	3.71	10.84	0.21
27-13	0.01	0.05	0.06	0.00	0.00	86.97	3.74	10.84	0.24
28-13	0.02	0.04	0.00	0.04	0.01	86.62	3.70	10.77	0.18
29-14	0.01	0.07	0.05	0.04	0.00	87.07	3.71	10.82	0.24
30-14	0.02	0.07	0.00	0.07	0.00	86.87	3.67	10.73	0.24
31-15	0.01	0.04	0.10	0.01	0.00	87.16	3.69	10.70	0.18
32-15	0.02	0.05	0.06	0.00	0.00	86.46	3.66	10.61	0.15
33-16	0.02	0.03	0.08	0.00	0.00	86.72	3.72	10.77	0.22
34-16	0.01	0.04	0.01	0.08	0.01	86.86	3.68	10.79	0.22
35-17	0.02	0.03	0.00	0.01	0.00	87.47	3.72	10.80	0.17
36-17	0.01	0.04	0.07	0.04	0.01	87.38	3.72	10.83	0.21
37-18	0.02	0.03	0.00	0.00	0.00	87.23	3.77	10.92	0.13
38-18	0.01	0.05	0.02	0.04	0.00	86.82	3.72	10.84	0.26
39-19	0.01	0.06	0.03	0.03	0.01	86.46	3.65	10.62	0.16
40-19	0.01	0.01	0.00	0.12	0.00	87.08	3.62	10.65	0.09
41-20	0.02	0.03	0.06	0.10	0.00	87.51	3.71	10.90	0.29
42-20	0.02	0.05	0.05	0.00	0.00	87.65	3.75	10.87	0.20
43-21	0.02	0.03	0.11	0.03	0.00	86.99	3.72	10.81	0.18
44-21	0.00	0.00	0.04	0.00	0.00	86.97	3.73	10.80	0.19
45-22	0.02	0.05	0.07	0.03	0.00	87.08	3.73	10.85	0.19
46-22	0.01	0.05	0.01	0.00	0.00	86.97	3.74	10.85	0.21

TOURMALINE (PARTE 3)

Spot-grain	O=F*	Total*	Sum T	Si	Al	Sum Z	Al	Mg
				Cations per 31 oxygens				
3-1	0.01	101.90	6.00	5.959	0.041	6.00	6.000	0.000
4-1	0.00	101.48	6.00	5.921	0.079	6.00	6.000	0.000

Spot-grain	O=F*	Total*	Sum T	Si	Al	Sum Z	Al	Mg
5-2	0.03	102.12	6.00	5.828	0.172	6.00	6.000	0.000
6-2	0.00	101.04	6.00	5.836	0.164	6.00	6.000	0.000
7-3	0.00	101.32	6.00	5.892	0.108	6.00	5.837	0.163
8-3	0.04	101.32	6.00	5.871	0.129	6.00	5.990	0.010
9-4	0.01	101.57	6.00	5.894	0.106	6.00	6.000	0.000
10-4	0.03	101.60	6.00	5.858	0.142	6.00	6.000	0.000
11-5	0.03	102.52	6.00	5.789	0.211	6.00	6.000	0.000
12-5	0.03	102.10	6.00	5.884	0.116	6.00	6.000	0.000
13-6	0.00	101.85	6.00	5.865	0.135	6.00	6.000	0.000
14-6	0.01	101.99	6.00	5.884	0.116	6.00	6.000	0.000
15-7	0.04	101.44	6.00	5.852	0.148	6.00	6.000	0.000
16-7	0.03	102.29	6.00	5.885	0.115	6.00	5.970	0.030
17-8	0.00	101.79	6.00	5.904	0.096	6.00	6.000	0.000
18-8	0.00	101.74	6.00	5.898	0.102	6.00	6.000	0.000
19-9	0.00	101.34	6.00	5.848	0.152	6.00	6.000	0.000
20-9	0.00	101.92	6.00	5.807	0.193	6.00	6.000	0.000
21-10	0.00	101.75	6.00	5.857	0.143	6.00	6.000	0.000
22-10	0.00	101.25	6.00	5.896	0.104	6.00	5.991	0.009
23-11	0.00	101.01	6.00	5.889	0.111	6.00	6.000	0.000
24-11	0.00	100.92	6.00	5.907	0.093	6.00	5.962	0.038
25-12	0.00	101.75	6.00	5.897	0.103	6.00	6.000	0.000
26-12	0.02	101.93	6.00	5.835	0.165	6.00	6.000	0.000
27-13	0.00	101.69	6.00	5.889	0.111	6.00	6.000	0.000
28-13	0.02	101.27	6.00	5.926	0.074	6.00	6.000	0.000
29-14	0.02	101.72	6.00	5.863	0.137	6.00	6.000	0.000
30-14	0.03	101.43	6.00	5.874	0.126	6.00	5.917	0.083
31-15	0.00	101.55	6.00	5.880	0.120	6.00	5.882	0.118
32-15	0.00	100.75	6.00	5.890	0.110	6.00	5.850	0.150
33-16	0.00	101.33	6.00	5.798	0.202	6.00	6.000	0.000
34-16	0.03	101.49	6.00	5.928	0.072	6.00	6.000	0.000
35-17	0.00	102.02	6.00	5.897	0.103	6.00	6.000	0.000
36-17	0.02	102.05	6.00	5.885	0.115	6.00	6.000	0.000
37-18	0.00	102.05	6.00	5.891	0.109	6.00	6.000	0.000
38-18	0.02	101.53	6.00	5.865	0.135	6.00	6.000	0.000
39-19	0.01	100.77	6.00	5.905	0.095	6.00	5.866	0.134
40-19	0.05	101.29	6.00	5.923	0.077	6.00	5.804	0.196
41-20	0.04	102.35	6.00	5.855	0.145	6.00	6.000	0.000
42-20	0.00	102.40	6.00	5.821	0.179	6.00	6.000	0.000
43-21	0.01	101.63	6.00	5.876	0.124	6.00	6.000	0.000
44-21	0.00	101.55	6.00	5.879	0.121	6.00	6.000	0.000
45-22	0.01	101.81	6.00	5.846	0.154	6.00	6.000	0.000
46-22	0.00	101.74	6.00	5.878	0.122	6.00	6.000	0.000

TOURMALINE (PARTE 4)

Spot-grain	Cr	Sum Y	Al	Ti	Cr	Mg	Mn	Fe2+
3-1	0.000	3.00	0.195	0.026	0.009	1.911	0.003	0.759
4-1	0.000	3.00	0.089	0.042	0.000	1.886	0.002	0.882

Spot-grain	Cr	Sum Y	Al	Ti	Cr	Mg	Mn	Fe2+
5-2	0.000	3.00	0.193	0.041	0.008	1.885	0.006	0.741
6-2	0.000	3.00	0.204	0.047	0.005	1.884	0.002	0.711
7-3	0.000	3.00	0.000	0.104	0.006	1.852	0.004	0.920
8-3	0.000	3.00	0.000	0.089	0.000	1.962	0.005	0.820
9-4	0.000	3.00	0.254	0.023	0.000	1.780	0.004	0.800
10-4	0.000	3.00	0.205	0.056	0.009	1.786	0.003	0.827
11-5	0.000	3.00	0.286	0.050	0.006	1.797	0.006	0.708
12-5	0.000	3.00	0.033	0.123	0.000	1.909	0.005	0.763
13-6	0.000	3.00	0.335	0.029	0.004	1.753	0.000	0.714
14-6	0.000	3.00	0.362	0.029	0.009	1.719	0.007	0.689
15-7	0.000	3.00	0.047	0.062	0.000	1.923	0.006	0.874
16-7	0.000	3.00	0.000	0.085	0.005	1.868	0.003	0.901
17-8	0.000	3.00	0.014	0.074	0.009	1.965	0.002	0.802
18-8	0.000	3.00	0.163	0.028	0.007	1.932	0.004	0.796
19-9	0.000	3.00	0.087	0.070	0.000	1.914	0.008	0.768
20-9	0.000	3.00	0.198	0.056	0.006	1.866	0.005	0.726
21-10	0.000	3.00	0.040	0.106	0.010	1.901	0.005	0.818
22-10	0.000	3.00	0.000	0.146	0.000	1.825	0.006	0.830
23-11	0.000	3.00	0.117	0.051	0.003	1.894	0.003	0.780
24-11	0.000	3.00	0.000	0.086	0.015	1.966	0.004	0.810
25-12	0.000	3.00	0.262	0.021	0.000	1.889	0.005	0.716
26-12	0.000	3.00	0.164	0.044	0.007	1.904	0.004	0.742
27-13	0.000	3.00	0.242	0.047	0.008	1.793	0.001	0.756
28-13	0.000	3.00	0.218	0.032	0.000	1.804	0.007	0.820
29-14	0.000	3.00	0.155	0.070	0.006	1.836	0.000	0.777
30-14	0.000	3.00	0.000	0.159	0.000	1.847	0.003	0.838
31-15	0.000	3.00	0.000	0.090	0.012	1.844	0.002	0.936
32-15	0.000	3.00	0.000	0.089	0.007	1.840	0.007	0.957
33-16	0.000	3.00	0.264	0.045	0.010	1.744	0.007	0.786
34-16	0.000	3.00	0.119	0.047	0.002	1.897	0.001	0.793
35-17	0.000	3.00	0.032	0.073	0.000	1.914	0.004	0.867
36-17	0.000	3.00	0.087	0.074	0.009	1.883	0.008	0.805
37-18	0.000	3.00	0.330	0.012	0.000	1.899	0.007	0.672
38-18	0.000	3.00	0.249	0.039	0.003	1.849	0.001	0.692
39-19	0.000	3.00	0.000	0.086	0.003	1.867	0.000	0.937
40-19	0.000	3.00	0.000	0.110	0.000	1.818	0.000	1.014
41-20	0.000	3.00	0.259	0.046	0.008	1.722	0.004	0.777
42-20	0.000	3.00	0.205	0.073	0.006	1.735	0.005	0.844
43-21	0.000	3.00	0.159	0.035	0.013	1.900	0.003	0.770
44-21	0.000	3.00	0.190	0.043	0.005	1.841	0.003	0.795
45-22	0.000	3.00	0.237	0.040	0.009	1.855	0.001	0.737
46-22	0.000	3.00	0.264	0.034	0.002	1.820	0.001	0.740

TOURMALINE (PARTE 5)

Spot-grain	Li*	Sum X	Ca	Ba	Na	K	Vacancy		Al+Li	k+Na
3-1	0.10	1.00	0.07	0.00	0.73	0.000	0.191	Dravite	0.29	0.73
4-1	0.10	1.00	0.12	0.00	0.76	0.002	0.115	Dravite	0.19	0.76

Spot-grain	Li*	Sum X	Ca	Ba	Na	K	Vacancy		Al+Li	k+Na
5-2	0.12	1.00	0.14	0.00	0.73	0.002	0.127	Dravite	0.32	0.73
6-2	0.15	1.00	0.14	0.00	0.72	0.000	0.137	Dravite	0.35	0.72
7-3	0.11	1.00	0.24	0.00	0.68	0.001	0.073	Dravite	0.11	0.68
8-3	0.12	1.00	0.18	0.00	0.72	0.003	0.096	Dravite	0.12	0.72
9-4	0.14	1.00	0.10	0.00	0.74	0.004	0.157	Dravite	0.39	0.74
10-4	0.11	1.00	0.11	0.00	0.70	0.005	0.185	Dravite	0.32	0.70
11-5	0.15	1.00	0.12	0.00	0.72	0.003	0.154	Dravite	0.43	0.73
12-5	0.17	1.00	0.12	0.00	0.74	0.003	0.125	Dravite	0.20	0.75
13-6	0.16	1.00	0.09	0.00	0.72	0.005	0.186	Dravite	0.50	0.73
14-6	0.19	1.00	0.08	0.00	0.70	0.003	0.213	Dravite	0.55	0.70
15-7	0.09	1.00	0.19	0.00	0.68	0.001	0.128	Dravite	0.14	0.68
16-7	0.14	1.00	0.21	0.00	0.67	0.003	0.108	Dravite	0.14	0.68
17-8	0.14	1.00	0.15	0.00	0.75	0.003	0.094	Dravite	0.15	0.75
18-8	0.07	1.00	0.10	0.00	0.75	0.002	0.153	Dravite	0.23	0.75
19-9	0.15	1.00	0.17	0.00	0.72	0.005	0.099	Dravite	0.24	0.72
20-9	0.14	1.00	0.14	0.00	0.73	0.003	0.126	Dravite	0.34	0.73
21-10	0.12	1.00	0.13	0.00	0.74	0.004	0.128	Dravite	0.16	0.75
22-10	0.19	1.00	0.13	0.00	0.75	0.003	0.117	Dravite	0.19	0.75
23-11	0.15	1.00	0.15	0.00	0.74	0.002	0.106	Dravite	0.27	0.75
24-11	0.12	1.00	0.17	0.00	0.71	0.001	0.111	Dravite	0.12	0.72
25-12	0.11	1.00	0.09	0.00	0.72	0.002	0.184	Dravite	0.37	0.73
26-12	0.13	1.00	0.16	0.00	0.72	0.003	0.121	Dravite	0.30	0.72
27-13	0.15	1.00	0.10	0.00	0.72	0.002	0.180	Dravite	0.39	0.72
28-13	0.12	1.00	0.09	0.00	0.72	0.005	0.184	Dravite	0.34	0.72
29-14	0.16	1.00	0.13	0.00	0.73	0.001	0.137	Dravite	0.31	0.73
30-14	0.15	1.00	0.15	0.00	0.73	0.003	0.109	Dravite	0.15	0.74
31-15	0.12	1.00	0.25	0.00	0.65	0.002	0.095	Dravite	0.12	0.65
32-15	0.10	1.00	0.26	0.00	0.64	0.003	0.090	Dravite	0.10	0.65
33-16	0.14	1.00	0.13	0.00	0.71	0.003	0.152	Dravite	0.41	0.71
34-16	0.14	1.00	0.13	0.00	0.74	0.002	0.131	Dravite	0.26	0.74
35-17	0.11	1.00	0.12	0.00	0.78	0.004	0.092	Dravite	0.14	0.78
36-17	0.13	1.00	0.13	0.00	0.74	0.003	0.124	Dravite	0.22	0.75
37-18	0.08	1.00	0.07	0.00	0.70	0.003	0.231	Dravite	0.41	0.70
38-18	0.17	1.00	0.12	0.00	0.72	0.002	0.154	Dravite	0.42	0.72
39-19	0.11	1.00	0.21	0.00	0.73	0.002	0.052	Dravite	0.11	0.74
40-19	0.06	1.00	0.19	0.00	0.73	0.002	0.077	Dravite	0.06	0.74
41-20	0.18	1.00	0.12	0.00	0.72	0.004	0.154	Dravite	0.44	0.72
42-20	0.13	1.00	0.14	0.00	0.65	0.005	0.195	Dravite	0.34	0.66
43-21	0.12	1.00	0.12	0.00	0.76	0.003	0.118	Dravite	0.28	0.76
44-21	0.12	1.00	0.12	0.00	0.72	0.000	0.160	Dravite	0.31	0.72
45-22	0.12	1.00	0.11	0.00	0.72	0.004	0.163	Dravite	0.36	0.72
46-22	0.14	1.00	0.10	0.00	0.72	0.003	0.173	Dravite	0.40	0.73

CHLORITE (PARTE 1) – Wt.%

Spot	SiO2	TiO2	Al2O3	FeO	MnO	MgO	CaO	Na2O	K2O	Total
127-1	25.52	0.12	21.90	22.06	0.04	16.38	0.02	0.03	0.04	86.16
128-1	25.58	0.12	21.90	20.95	0.14	16.36	0.02	0.04	0.04	85.18

129-1	25.18	0.08	21.71	21.21	0.11	17.06	0.02	0.05	0.03	85.50
130-2	25.26	0.11	22.09	21.82	0.04	17.04	0.02	0.06	0.09	86.59
131-2	24.94	0.09	22.88	21.95	0.11	16.61	0.05	0.06	0.04	86.75
132-2	25.50	0.10	22.16	21.83	0.10	16.30	0.03	0.00	0.03	86.10

CHLORITE (PARTE 2)

Spot	Si	Al(iv)	Al(vi)	Ti	Fe3+	Fe2+	Mn	Mg	Ca	Na	K	OH*
	Cations per 28 oxygens											
127-1	5.36	2.64	2.80	0.02	0.11	3.77	0.01	5.13	0.01	0.03	0.02	15.97
128-1	5.40	2.60	2.87	0.02	0.16	3.54	0.03	5.15	0.00	0.03	0.02	16.00
129-1	5.32	2.68	2.73	0.01	0.05	3.70	0.02	5.37	0.00	0.04	0.02	15.94
130-2	5.29	2.71	2.74	0.02	0.02	3.80	0.01	5.32	0.01	0.05	0.05	15.99
131-2	5.21	2.79	2.85	0.01	0.04	3.80	0.02	5.17	0.01	0.05	0.02	15.99
132-2	5.35	2.65	2.84	0.02	0.14	3.69	0.02	5.10	0.01	0.00	0.02	15.95

CHLORITE (PARTE 3)

Spot	XFe = Fe/(Fe+Mn+Mg)	XMg = Mg/(Mg+Fe+Mn)	XMn = Mn/(Mg+Fe+Mn)	= Classification
127-1	0.43	0.57	0.00	ripidolite
128-1	0.42	0.58	0.00	ripidolite
129-1	0.41	0.59	0.00	ripidolite
130-2	0.42	0.58	0.00	ripidolite
131-2	0.42	0.57	0.00	ripidolite
132-2	0.43	0.57	0.00	ripidolite

Supplementary Table 4. Analytical results garnet U-Pb isotopes including standards and sample 113, staurolite schist, Serrinha Formation.

PARTE 1

SPOT	U(ppm)	Th/U	^{202}Hg(cps)	^{204}Pb(cps)	^{207}Pb(cps)	^{206}Pb(cps)
MALI						
003std.exp	1.13	1.69	30251	1726	1883	6561
004std.exp	0.98	1.81	30453	1783	932	5318
005std.exp	0.95	1.77	30349	1845	1110	4827
006std.exp	1.01	1.77	30261	2035	605	4457
007std.exp	1.07	1.76	30255	1788	1005	5615
008std.exp	1.18	1.72	30312	1923	690	5588
009std.exp	1.22	1.83	30280	1809	911	5170
010std.exp	1.31	1.77	30302	1634	881	4837
013std.exp	1.14	1.87	33161	1941	828	4833
014std.exp	1.01	1.55	33265	1973	919	5919
015std.exp	1.27	1.73	33393	1892	1197	6102
016std.exp	1.18	1.90	33339	1954	1342	6083
017std.exp	1.18	1.92	33553	1915	1502	5203

SPOT	U(ppm)	Th/U	^{202}Hg(cps)	^{204}Pb(cps)	^{207}Pb(cps)	^{206}Pb(cps)
018std.exp	1.36	1.65	33375	1901	1537	6717
019std.exp	1.27	1.63	33512	1876	1348	6206
020std.exp	1.16	1.58	33418	1864	1661	6151
103std.exp	1.10	1.91	30382	1884	802	5321
104std.exp	1.21	1.85	30485	1723	601	5287
105std.exp	1.23	1.61	30308	1704	574	5197
106std.exp	0.97	1.52	30294	1693	591	5726
107std.exp	1.13	1.86	30246	1685	659	5296
108std.exp	1.30	1.69	30224	1702	626	4402
109std.exp	1.18	1.91	30247	1710	682	5526
110std.exp	1.22	1.81	30263	1707	828	5064
NIST 614						
001std.exp	0.82	1.02	31477	6175	64239	74112
022std.exp	0.83	1.09	33065	5933	64930	73739
022std.exp	0.77	0.99	21393	5780	64447	73698
051std.exp	0.74	1.06	33680	5912	65543	74818
052std.exp	0.80	1.02	33464	6808	64813	68694
061std.exp	0.79	1.01	33699	6528	59591	74377
062std.exp	0.80	1.02	33093	6715	63865	75632
081std.exp	0.81	0.99	33412	6254	63950	74935
082std.exp	0.79	1.01	22239	5953	70401	74404
101std.exp	0.78	1.00	22600	5943	64355	81441
102std.exp	0.81	0.97	30297	6021	64195	74418
121std.exp	0.82	0.98	30587	5941	70085	81117
141std.exp	0.81	1.00	20676	6541	66210	76334
142std.exp	0.83	1.01	21092	6723	66795	77115
001std.exp	0.81	1.05	38712	7370	62913	72568
002std.exp	0.82	1.05	39435	7384	64756	74753
021std.exp	0.84	1.08	39420	7510	64875	74811
022std.exp	0.82	1.08	39119	7457	64011	73856
041std.exp	0.81	1.06	35628	7242	66033	76290
042std.exp	0.77	1.08	35691	6992	64333	74706
061std.exp	0.80	1.06	31140	7103	63518	71677
062std.exp	0.81	1.05	31029	7054	62009	73669
081std.exp	0.79	1.05	31593	6869	63596	74325
082std.exp	0.81	1.05	30365	7029	64389	73440
IDA DOME						
003std.exp	56.89	0.11	30690	1849	37519	610841
004std.exp	50.02	0.10	30685	1797	32832	539812
005std.exp	52.87	0.10	30564	1751	35236	572346
006std.exp	52.26	0.10	30513	1698	36045	569455
007std.exp	58.36	0.10	30678	1732	38559	631506
008std.exp	59.36	0.11	30440	813	39170	642244
009std.exp	59.19	0.11	30639	1699	39066	642264
010std.exp	56.37	0.10	30545	1667	37555	613351
093std.exp	50.74	0.12	30742	1492	33932	549609
094std.exp	46.50	0.11	30376	1558	31031	503582
095std.exp	48.78	0.11	30091	1500	32734	532703
096std.exp	58.60	0.11	30863	1508	39196	639895
097std.exp	44.42	0.11	30804	1550	29369	483361

SPOT	U(ppm)	Th/U	^{202}Hg(cps)	^{204}Pb(cps)	^{207}Pb(cps)	^{206}Pb(cps)
098std.exp	49.05	0.11	30789	1283	33668	538374
099std.exp	54.98	0.11	30728	1486	36895	602742
100std.exp	61.17	0.11	30570	1217	40729	669752
BUSHVELD						
023std.exp	9.35	0.56	30133	2072	58438	444453
024std.exp	6.01	1.00	30645	1988	41210	295705
025std.exp	9.74	0.49	30196	1917	61433	465849
026std.exp	7.88	0.70	30087	1918	48320	376226
027std.exp	9.25	0.68	30048	1877	59418	447888
028std.exp	4.94	1.53	30063	1976	32752	241872
029std.exp	5.00	1.50	32883	1888	32878	245595
030std.exp	4.40	1.53	32815	1877	29473	214722
113std.exp	5.78	0.90	30388	1892	38012	279988
114std.exp	4.74	1.50	30551	1861	33746	232268
115std.exp	4.48	1.58	30645	1669	30566	221424
116std.exp	4.47	1.57	30493	1707	30059	220109
117std.exp	4.91	1.52	30595	1671	32948	241164
118std.exp	4.41	1.61	30390	1657	29634	217488
119std.exp	4.33	1.52	30312	1611	29338	212926
120std.exp	5.02	1.95	30385	1678	34166	249006
WILLSBORO						
151std.exp	1.85	0.29	30985	17832	2384	24621
152std.exp	1.87	0.29	30139	146865	2183	24597
153std.exp	1.71	0.30	30456	181583	2857	23504
154std.exp	1.65	0.29	30415	156215	2029	22110
155std.exp	1.76	0.30	30045	163275	2198	23413
156std.exp	1.81	0.30	30092	12643	2119	23756
157std.exp	1.75	0.29	30069	180604	2334	23406
MXE						
033std.exp	7.77	0.00	30405	1916	4475	74761
034std.exp	7.83	0.00	30479	1919	4490	75360
035std.exp	7.87	0.00	30649	1560	4672	76184
036std.exp	7.66	0.00	30664	1733	4402	74145
037std.exp	7.53	0.00	30584	1802	4248	72465
038std.exp	7.97	0.00	30710	1737	4742	77388
039std.exp	7.98	0.00	30794	1727	4449	76946
040std.exp	8.25	0.00	31947	2174	4673	78671
123std.exp	7.60	0.00	30074	1714	4423	72515
124std.exp	7.67	0.00	30475	1594	4515	73919
125std.exp	7.76	0.00	30548	1606	4474	74614
126std.exp	7.65	0.00	30580	1542	4561	74476
127std.exp	7.73	0.00	30772	1508	4675	74942
128std.exp	7.56	0.00	30643	1501	4501	73469
129std.exp	7.60	0.00	30734	1562	4778	73103
130std.exp	7.82	0.00	30759	1514	4425	74637
Staurolite schist, sample 113						
RUN 1						
053std.exp	0.17	-0.11	32065	1893	240	2676
055std.exp	0.07	-0.33	33163	1853	116	1315

SPOT	U(ppm)	Th/U	^{202}Hg(cps)	^{204}Pb(cps)	^{207}Pb(cps)	^{206}Pb(cps)
057std.exp	0.23	-0.05	33811	1830	321	3608
058std.exp	0.25	0.08	33873	1819	638	4333
059std.exp	0.09	-0.24	33958	1836	369	1798
060std.exp	0.37	0.80	34192	1745	505	5632
064std.exp	0.56	0.34	34130	1890	631	8607
065std.exp	0.26	0.04	34076	1879	329	4062
067std.exp	0.18	0.10	33831	1810	290	3153
070std.exp	0.63	0.13	33747	1883	633	9144
073std.exp	0.18	1.20	32302	1743	338	3021
074std.exp	0.28	0.02	32607	1708	432	4330
075std.exp	0.33	0.40	32823	2096	5315	10610
076std.exp	0.33	0.13	33347	1672	525	5346
077std.exp	0.12	-0.07	33593	1635	147	2167
080std.exp	0.13	-0.14	33253	1748	398	2454
082std.exp	0.59	0.00	33248	1687	578	8599
083std.exp	0.18	-0.14	33267	1766	368	3098
085std.exp	0.07	-0.29	33277	1663	49	1323
088std.exp	0.10	-0.30	33184	1623	191	1905
144std.exp	0.20	0.71	30859	1537	300	3265
146std.exp	0.13	-0.08	31255	1667	2498	4566
150std.exp	0.25	4.60	31521	1479	462	4065
RUN 2						
034std.exp	0.09	-0.14	30117	1662	132	1760
035std.exp	0.21	0.40	33914	1997	1019	4376
036std.exp	0.09	-0.04	33099	1682	198	1838
038std.exp	0.21	0.17	31294	1477	14	3324
040std.exp	0.11	-0.26	28054	1690	158	2032
041std.exp	0.19	0.03	28568	1552	350	3116
042std.exp	0.16	-0.05	28952	1731	1053	3873
043std.exp	0.08	-0.26	29179	1781	335	1717
044std.exp	0.22	-0.04	29486	1917	646	3767
048std.exp	0.24	0.09	30340	1754	507	4186
049std.exp	0.46	0.15	30312	2054	2607	9567
050std.exp	0.35	0.10	30442	1564	1218	6139
056std.exp	0.25	0.47	30212	1753	462	4216
057std.exp	0.07	-0.05	30779	-381	42	387
058std.exp	0.15	0.03	30407	1619	406	3169
059std.exp	0.19	0.25	30527	1489	750	3941
060std.exp	0.75	0.83	30604	1561	1040	11924
064std.exp	0.20	0.06	31211	1515	100	4232
065std.exp	0.09	-0.17	31193	1782	964	4456
066std.exp	0.11	0.65	31101	530	-748	1887
068std.exp	0.38	0.19	31715	1069	636	6675
069std.exp	0.12	-0.07	31922	1709	679	3205
070std.exp	0.16	-0.13	32321	1462	357	3404
073std.exp	0.39	3.40	30545	1815	1154	7378
075std.exp	0.10	-0.37	31372	1735	424	3000

PARTE 2

SPOT	207Pb/206Pb	2σ (%)	207Pb/235U	2σ (%)	206Pb/238U	2σ (%)
	Isotopic ratios					
MALI						
003std.exp	0.2885	4.6	1.832	38.3	0.046	38.0
004std.exp	0.1938	4.6	1.034	8.5	0.039	7.2
005std.exp	0.2311	4.1	1.281	8.7	0.040	7.7
006std.exp	0.1364	6.7	0.656	8.9	0.035	5.8
007std.exp	0.1943	4.1	1.030	13.9	0.038	13.3
008std.exp	0.1342	2.9	0.638	6.3	0.034	5.6
009std.exp	0.1639	2.2	0.816	8.6	0.036	8.3
010std.exp	0.1578	2.1	0.773	5.8	0.036	5.5
013std.exp	0.1567	2.5	0.794	7.0	0.037	6.6
014std.exp	0.1912	1.8	0.999	2.6	0.038	1.9
015std.exp	0.1973	3.0	1.028	3.6	0.038	2.0
016std.exp	0.2282	1.8	1.245	2.4	0.040	1.7
017std.exp	0.2484	2.4	1.394	3.2	0.041	2.2
018std.exp	0.2303	2.0	1.240	2.6	0.039	1.7
019std.exp	0.2186	3.4	1.158	4.0	0.038	2.2
020std.exp	0.2718	1.4	1.567	2.2	0.042	1.7
103std.exp	0.1556	4.4	0.801	4.8	0.037	1.9
104std.exp	0.1146	1.9	0.532	2.6	0.034	1.8
105std.exp	0.1092	2.1	0.512	2.8	0.034	1.8
106std.exp	0.1354	2.2	0.669	2.8	0.036	1.7
107std.exp	0.1313	4.0	0.639	4.4	0.035	1.9
108std.exp	0.1103	2.4	0.515	3.0	0.034	1.8
109std.exp	0.1294	5.2	0.618	5.7	0.035	2.4
110std.exp	0.1511	4.8	0.745	5.2	0.036	1.9
NIST 614						
001std.exp	0.8681	0.6			0.802	1.7
022std.exp	0.8630	0.6			0.823	1.7
022std.exp	0.8649	0.6			0.816	1.7
051std.exp	0.8860	0.6			0.800	1.7
052std.exp	0.8714	0.7			0.807	1.0
061std.exp	0.8727	0.6			0.804	1.9
062std.exp	0.8713	0.6			0.811	1.9
081std.exp	0.8729	0.6			0.802	1.9
082std.exp	0.8696	0.6			0.831	1.9
101std.exp	0.8699	0.6			0.805	1.9
102std.exp	0.8713	0.6			0.800	1.9
121std.exp	0.8692	0.6			0.803	1.9
141std.exp	0.8725	0.6			0.802	1.7
142std.exp	0.8713	0.6			0.792	1.7
001std.exp	0.8678	0.6			0.792	1.9
002std.exp	0.8680	0.6			0.798	1.9
021std.exp	0.8698	0.6			0.806	1.9
022std.exp	0.8702	0.6			0.808	1.9
041std.exp	0.8699	0.6			0.809	1.9
042std.exp	0.8708	0.6			0.816	1.9
061std.exp	0.8710	0.6			0.811	1.9
062std.exp	0.8720	0.6			0.811	1.9

SPOT	207Pb/206Pb	2σ (%)	207Pb/235U	2σ (%)	206Pb/238U	2σ (%)
081std.exp	0.8710	0.7			0.814	2.3
082std.exp	0.8705	0.6			0.819	1.9
IDA DOME						
003std.exp	0.0621	0.4	0.711	1.6	0.083	1.5
004std.exp	0.0620	0.4	0.714	1.8	0.083	1.7
005std.exp	0.0624	0.5	0.720	1.9	0.084	1.8
006std.exp	0.0639	0.4	0.742	1.8	0.084	1.8
007std.exp	0.0619	0.4	0.714	1.8	0.084	1.7
008std.exp	0.0621	0.4	0.717	1.6	0.084	1.5
009std.exp	0.0612	0.3	0.708	1.6	0.084	1.5
010std.exp	0.0615	0.4	0.714	1.6	0.084	1.5
093std.exp	0.0615	0.4	0.708	1.6	0.084	1.5
094std.exp	0.0615	0.4	0.708	1.6	0.084	1.5
095std.exp	0.0613	0.4	0.711	1.6	0.084	1.5
096std.exp	0.0610	0.6	0.708	1.7	0.084	1.6
097std.exp	0.0606	0.3	0.701	1.6	0.084	1.6
098std.exp	0.0625	0.7	0.730	2.0	0.085	1.9
099std.exp	0.0611	0.3	0.712	1.8	0.085	1.7
100std.exp	0.0606	0.4	0.706	2.0	0.085	1.9
BUSHVELD						
023std.exp	0.1366	0.7	6.975	1.9	0.370	1.7
024std.exp	0.1417	0.9	7.480	1.9	0.383	1.6
025std.exp	0.1351	0.6	6.937	1.6	0.372	1.5
026std.exp	0.1357	0.7	6.960	1.6	0.372	1.5
027std.exp	0.1353	0.9	7.032	1.9	0.377	1.7
028std.exp	0.1384	0.7	7.277	1.8	0.381	1.6
029std.exp	0.1372	0.7	7.238	1.8	0.383	1.6
030std.exp	0.1389	0.9	7.293	1.8	0.381	1.5
113std.exp	0.1347	0.7	6.907	1.6	0.372	1.5
114std.exp	0.1441	1.8	7.472	2.5	0.376	1.8
115std.exp	0.1372	1.3	7.181	2.2	0.380	1.7
116std.exp	0.1358	0.7	7.081	1.7	0.378	1.5
117std.exp	0.1363	0.9	7.091	1.9	0.377	1.7
118std.exp	0.1357	0.7	7.085	1.7	0.379	1.5
119std.exp	0.1369	0.9	7.129	1.9	0.378	1.6
120std.exp	0.1366	0.7	7.169	1.8	0.381	1.6
WILLSBORO						
151std.exp	0.0952	3.5	2.312	3.8	0.176	1.4
152std.exp	0.0875	2.7	2.098	3.0	0.174	1.4
153std.exp	0.1188	4.2	2.972	4.4	0.181	1.4
154std.exp	0.0906	2.2	2.213	2.6	0.177	1.4
155std.exp	0.0927	2.8	2.240	3.1	0.175	1.4
156std.exp	0.0879	2.8	2.098	3.1	0.173	1.4
157std.exp	0.0978	5.8	2.367	6.0	0.176	1.4
MXE						
033std.exp	0.0696	0.9	0.720	1.8	0.075	1.6
034std.exp	0.0657	2.7	0.680	3.2	0.075	1.6
035std.exp	0.0658	0.6	0.687	1.6	0.076	1.5
036std.exp	0.0665	0.8	0.693	1.7	0.076	1.5
037std.exp	0.0666	0.6	0.689	1.7	0.075	1.6

SPOT	207Pb/206Pb	2σ (%)	207Pb/235U	2σ (%)	206Pb/238U	2σ (%)
038std.exp	0.0664	0.5	0.694	1.6	0.076	1.5
039std.exp	0.0641	0.5	0.665	1.6	0.075	1.5
040std.exp	0.0651	0.6	0.668	1.7	0.074	1.6
123std.exp	0.0628	0.6	0.635	1.7	0.073	1.6
124std.exp	0.0640	0.6	0.654	1.7	0.074	1.6
125std.exp	0.0634	0.6	0.646	1.6	0.074	1.5
126std.exp	0.0635	2.0	0.655	2.6	0.075	1.6
127std.exp	0.0645	4.1	0.662	4.4	0.075	1.5
128std.exp	0.0627	1.2	0.647	2.0	0.075	1.6
129std.exp	0.0668	1.5	0.682	2.2	0.074	1.6
130std.exp	0.0624	0.6	0.632	1.7	0.073	1.6

Staurolite schist, sample 113

RUN 1

SPOT	207Pb/206Pb	2σ (%)	207Pb/235U	2σ (%)	206Pb/238U	2σ (%)
053std.exp	0.1883	4.3	3.398	10.0	0.131	9.1
055std.exp	0.2799	4.1	6.218	66.0	0.161	65.8
057std.exp	0.1666	6.2	2.910	10.2	0.127	8.1
058std.exp	0.1951	2.6	3.747	3.9	0.139	2.9
059std.exp	0.3222	7.5	7.150	38.8	0.161	38.1
060std.exp	0.1443	4.8	2.512	6.1	0.126	3.8
064std.exp	0.1059	3.2	1.810	4.4	0.124	3.0
065std.exp	0.1551	4.6	2.705	6.9	0.127	5.2
067std.exp	0.1859	5.2	3.591	87.3	0.140	87.2
070std.exp	0.1073	5.9	1.729	11.2	0.117	9.5
073std.exp	0.1982	7.2	3.668	14.3	0.134	12.3
074std.exp	0.1463	4.8	2.565	6.8	0.127	4.8
075std.exp	0.5408	2.3	19.141	6.3	0.257	5.9
076std.exp	0.1715	3.3	3.107	4.5	0.131	3.0
077std.exp	0.2191	2.9	4.421	6.0	0.146	5.3
080std.exp	0.3198	6.7	6.938	21.5	0.157	20.5
082std.exp	0.0940	3.3	1.531	4.4	0.118	3.0
083std.exp	0.1845	4.0	3.570	6.2	0.140	4.7
085std.exp	0.2980	4.5	6.545	56.6	0.159	56.5
088std.exp	0.2613	2.6	5.502	8.0	0.153	7.5
144std.exp	0.1477	2.1	2.768	3.3	0.136	2.6
146std.exp	0.5847	2.2	22.575	8.7	0.280	8.4
150std.exp	0.1853	4.2	3.429	8.4	0.134	7.3

RUN 2

SPOT	207Pb/206Pb	2σ (%)	207Pb/235U	2σ (%)	206Pb/238U	2σ (%)
034std.exp	0.2743	3.7	5.934	7.3	0.157	6.3
035std.exp	0.3086	2.7	7.053	7.2	0.166	6.7
036std.exp	0.3141	2.8	7.253	12.7	0.168	12.4
038std.exp	0.1693	5.8	3.057	9.6	0.131	7.6
040std.exp	0.2690	4.9	5.705	15.4	0.154	14.6
041std.exp	0.1972	5.7	3.673	8.9	0.135	6.9
042std.exp	0.3436	2.4	9.174	14.2	0.194	14.0
043std.exp	0.3508	4.8	8.854	106.4	0.183	106.3
044std.exp	0.2296	4.2	4.479	7.7	0.141	6.5
048std.exp	0.2191	4.3	4.355	8.3	0.144	7.1
049std.exp	0.3105	7.2	7.236	10.2	0.169	7.2
050std.exp	0.2497	3.8	4.914	6.3	0.143	5.1

SPOT	207Pb/206Pb	2σ (%)	207Pb/235U	2σ (%)	206Pb/238U	2σ (%)
056std.exp	0.2179	6.1	4.081	13.2	0.136	11.7
057std.exp	0.3911	3.5	10.756	53.0	0.199	52.9
058std.exp	0.3515	4.7	8.455	41.0	0.174	40.8
059std.exp	0.3557	6.1	8.412	21.5	0.172	20.7
060std.exp	0.1694	5.1	3.022	7.0	0.129	4.7
064std.exp	0.3153	2.4	7.379	6.8	0.170	6.4
065std.exp	0.6163	1.8	32.569	19.2	0.383	19.1
066std.exp	0.4716	2.7	14.397	27.5	0.221	27.3
068std.exp	0.2048	6.2	4.095	9.1	0.145	6.8
069std.exp	0.4256	4.0	12.640	17.1	0.215	16.6
070std.exp	0.3403	3.1	8.475	9.9	0.181	9.4
073std.exp	0.2859	5.5	6.121	16.4	0.155	15.5
075std.exp	0.5020	3.1	17.553	14.6	0.254	14.3

PARTE 3

SPOT	Rho	206Pb/238U	2σ (%)	207Pb/235U	2σ (%)	207Pb/206Pb	2σ (%)
		Ages					
MALI							
003std.exp	1.0	290	110	1057	290	3409	72
004std.exp	0.8	245	17	721	45	2774	75
005std.exp	0.9	254	19	837	51	3059	66
006std.exp	0.7	221	13	512	36	2182	116
007std.exp	1.0	243	32	719	75	2779	68
008std.exp	0.9	219	12	501	26	2154	51
009std.exp	1.0	229	19	606	40	2496	37
010std.exp	0.9	225	12	582	26	2432	35
013std.exp	0.9	233	15	593	32	2420	43
014std.exp	0.7	240	4	703	13	2752	30
015std.exp	0.6	239	5	718	19	2804	49
016std.exp	0.7	250	4	821	14	3040	28
017std.exp	0.7	257	5	887	19	3175	38
018std.exp	0.7	247	4	819	15	3054	32
019std.exp	0.5	243	5	781	22	2971	55
020std.exp	0.8	264	5	957	14	3317	22
103std.exp	0.4	236	4	598	22	2408	75
104std.exp	0.7	213	4	433	9	1874	35
105std.exp	0.7	215	4	420	9	1787	38
106std.exp	0.6	227	4	520	11	2169	38
107std.exp	0.4	224	4	502	17	2115	70
108std.exp	0.6	214	4	421	11	1805	44
109std.exp	0.4	219	5	488	22	2089	91
110std.exp	0.4	226	4	565	23	2358	83
IDA DOME							
003std.exp	1.0	514	8	545	7	678	8
004std.exp	1.0	517	9	547	8	675	8
005std.exp	1.0	518	9	551	8	689	11
006std.exp	1.0	522	9	564	8	738	9

SPOT	Rho	$^{206}Pb/^{238}U$	2σ (%)	$^{207}Pb/^{235}U$	2σ (%)	$^{207}Pb/^{206}Pb$	2σ (%)
007std.exp	1.0	518	9	547	8	671	8
008std.exp	1.0	518	8	549	7	678	9
009std.exp	1.0	520	8	544	7	646	7
010std.exp	1.0	521	8	547	7	658	8
093std.exp	1.0	517	8	543	7	656	8
094std.exp	1.0	517	8	544	7	656	8
095std.exp	1.0	521	8	545	7	648	9
096std.exp	0.9	521	8	543	7	638	13
097std.exp	1.0	520	8	539	7	624	8
098std.exp	0.9	524	9	557	9	692	16
099std.exp	1.0	523	9	546	8	641	7
100std.exp	1.0	523	10	543	8	626	8
BUSHVELD							
023std.exp	0.9	2031	30	2108	17	2185	12
024std.exp	0.9	2090	29	2171	17	2248	15
025std.exp	0.9	2041	26	2103	14	2165	11
026std.exp	0.9	2039	26	2106	15	2173	11
027std.exp	0.9	2063	30	2116	17	2167	15
028std.exp	0.9	2083	29	2146	16	2207	13
029std.exp	0.9	2089	29	2141	16	2192	13
030std.exp	0.9	2080	27	2148	16	2214	16
113std.exp	0.9	2038	26	2100	15	2160	12
114std.exp	0.7	2057	32	2170	23	2278	30
115std.exp	0.8	2075	30	2134	19	2192	23
116std.exp	0.9	2068	27	2122	15	2174	12
117std.exp	0.9	2063	31	2123	17	2181	15
118std.exp	0.9	2071	27	2122	15	2173	13
119std.exp	0.9	2065	29	2128	17	2189	16
120std.exp	0.9	2080	29	2133	16	2184	13
WILLSBORO							
151std.exp	0.4	1046	13	1216	27	1532	67
152std.exp	0.5	1033	13	1148	21	1373	51
153std.exp	0.3	1075	14	1400	34	1938	75
154std.exp	0.5	1052	13	1185	18	1438	41
155std.exp	0.4	1041	13	1194	22	1482	53
156std.exp	0.4	1029	13	1148	22	1380	54
157std.exp	0.2	1043	13	1233	44	1582	109
MXE							
033std.exp	0.9	466	7	551	8	916	18
034std.exp	0.5	466	7	527	13	798	58
035std.exp	0.9	471	7	531	7	801	12
036std.exp	0.9	470	7	535	7	823	16
037std.exp	0.9	467	7	532	7	824	13
038std.exp	0.9	471	7	535	7	819	11
039std.exp	0.9	468	7	518	7	744	11
040std.exp	0.9	463	7	520	7	777	12
123std.exp	0.9	456	7	499	7	701	13
124std.exp	0.9	461	7	511	7	741	12
125std.exp	0.9	459	7	506	6	723	12
126std.exp	0.6	465	7	512	10	725	42

SPOT	Rho	$^{206}Pb/^{238}U$	2σ (%)	$^{207}Pb/^{235}U$	2σ (%)	$^{207}Pb/^{206}Pb$	2σ (%)
127std.exp	0.4	463	7	516	18	757	87
128std.exp	0.8	465	7	506	8	699	25
129std.exp	0.7	460	7	528	9	832	32
130std.exp	0.9	457	7	498	7	689	12

Staurolite schist, sample 113

RUN 1

SPOT	Rho	$^{206}Pb/^{238}U$	2σ (%)	$^{207}Pb/^{235}U$	2σ (%)	$^{207}Pb/^{206}Pb$	2σ (%)
053std.exp	0.9	793	68	1504	82	2727	70
055std.exp	1.0	963	622	2007	854	3362	64
057std.exp	0.8	769	59	1385	80	2524	105
058std.exp	0.7	841	23	1582	32	2786	43
059std.exp	1.0	962	352	2130	423	3580	116
060std.exp	0.6	766	27	1275	45	2279	82
064std.exp	0.7	753	21	1049	29	1730	58
065std.exp	0.7	768	38	1330	53	2402	78
067std.exp	1.0	845	735	1548	1170	2706	85
070std.exp	0.8	712	65	1019	75	1754	109
073std.exp	0.9	812	95	1564	121	2811	118
074std.exp	0.7	771	35	1291	51	2303	83
075std.exp	0.9	1473	78	3049	63	4356	33
076std.exp	0.7	796	23	1434	35	2573	56
077std.exp	0.9	880	44	1716	51	2974	47
080std.exp	1.0	942	183	2104	212	3569	103
082std.exp	0.7	720	21	943	28	1508	62
083std.exp	0.8	847	38	1543	50	2693	66
085std.exp	1.0	953	524	2052	687	3460	69
088std.exp	0.9	916	65	1901	71	3254	41
144std.exp	0.8	821	20	1347	25	2319	36
146std.exp	1.0	1591	121	3209	88	4471	31
150std.exp	0.9	812	56	1511	68	2701	69

RUN 2

SPOT	Rho	$^{206}Pb/^{238}U$	2σ (%)	$^{207}Pb/^{235}U$	2σ (%)	$^{207}Pb/^{206}Pb$	2σ (%)
034std.exp	0.9	940	55	1966	65	3331	57
035std.exp	0.9	989	62	2118	66	3514	42
036std.exp	1.0	998	116	2143	120	3541	44
038std.exp	0.8	793	57	1422	76	2551	98
040std.exp	0.9	922	127	1932	143	3300	77
041std.exp	0.8	817	53	1566	74	2804	93
042std.exp	1.0	1141	149	2356	139	3679	36
043std.exp	1.0	1084	1166	2323	3183	3710	73
044std.exp	0.8	853	52	1727	66	3049	66
048std.exp	0.9	868	59	1704	71	2974	69
049std.exp	0.7	1006	68	2141	95	3524	111
050std.exp	0.8	860	41	1805	55	3183	60
056std.exp	0.9	821	92	1651	114	2965	98
057std.exp	1.0	1172	597	2502	674	3875	53
058std.exp	1.0	1037	405	2281	464	3713	71
059std.exp	1.0	1021	199	2276	217	3731	93
060std.exp	0.7	784	35	1413	55	2552	85
064std.exp	0.9	1011	61	2158	63	3547	37
065std.exp	1.0	2092	353	3568	209	4547	26
066std.exp	1.0	1289	330	2776	302	4155	40

SPOT	Rho	$^{206}Pb/^{238}U$	2σ (%)	$^{207}Pb/^{235}U$	2σ (%)	$^{207}Pb/^{206}Pb$	2σ (%)
068std.exp	0.7	873	56	1653	78	2865	100
069std.exp	1.0	1258	194	2653	175	4002	60
070std.exp	0.9	1070	94	2283	94	3664	48
073std.exp	0.9	930	136	1993	155	3396	86
075std.exp	1.0	1457	190	2966	151	4247	46

References

Abd El-Rahman, Y., Anbar, M.A., Li, X, Li, J., Ling, X., Wu, L., Masoud, A.E., 2019. The evolution of the Arabian-Nubian Shield and survival of its zircon U-Pb-Hf-O isotopic signature: A tale from the Um Had conglomerate, central Eastern Desert, Egypt. Precambrian Research 320, 46-62.

Albert, C., Lana, C., Gerdes, A., Schannor, M., Narduzzia, F., Queiroga, G., 2018. Archean magmatic-hydrothermal fluid evolution in the Quadrilátero Ferrífero (SE Brazil) documented by B isotopes (LA MC-ICPMS) in tourmaline. Chemical Geology 481, 95-109.

Andersen, D.J., Lindsley, D.H., 1988. Internal consistent solution models for Fe-Mg-Mn-Ti oxides: Fe-Ti oxides. American Mineralogist 73, 714-726.

Arena, K.R., Hartmann, L.A., Lana, C., 2016. Evolution of Neoproterozoic ophiolites from the southern Brasiliano Orogen revealed by zircon U-Pb-Hf isotopes and geochemistry. Precambrian Research 285, 299-314.

Arena, K.R., Hartmann, L.A., Lana, C., 2017. Tonian emplacement of ophiolites in the southern Brasiliano Orogen delimited by U-Pb-Hf isotopes of zircon from metasomatites. Gondwana Research 49, 296-332.

Arena, K.R., Hartmann, L.A., Lana, C., 2018. U-Pb-Hf isotopes and trace elements of metasomatic zircon delimit the evolution of the Capané ophiolite in the southern Brasiliano Orogen. International Geology Review 60 (7), 911-928.

Arena, K.R., Hartmann, L.A., Lana, C., Queiroga, G.N., Castro, M.P., 2020. Geochemistry and δ11B evolution of tourmaline from tourmalinite as a record of oceanic crust in the Tonian Ibaré ophiolite, southern Brasiliano Orogen. Annals of the Brazilian Academy of Sciences 92 (1), e20180193.

Babinski, M., Chemale Jr., F., Hartmann, L.A., Van Schmus, W.R., Silva, L.C., 1996. Juvenile accretion at 750-700 Ma in southern Brazil. Geology, 24 (5), 439-442.

Barth, S., 1993. Boron isotope variations in nature: a synthesis. Geologische Rundschau 82, 640-651.

Basei, M.A.S., Brito Neves, B.B., Siga Júnior, O., Babinski, M., Pimentel, M.M., Tassinari, C.C.G., Hollanda, M.H.B., Nutman, A., Cordani, U.G., 2010. Contribution of SHRIMP U–Pb zircon geochronology to unravelling the evolution of Brazilian Neoproterozoic fold belts. Precambrian Research 183, 112-144.

Bitencourt, M.F.A.S., 1983. Geologia, Petrologia e Estrutura dos Metamorfitos da Região de Caçapava do Sul, RS. MSc Thesis, Universidade Federal do Rio Grande do Sul.

Bologna, M.S., Dragone, G.N., Muzio, R., Peel, E., Nuñez-Demarco, P., Ussami, N., 2019. Electrical structure of the lithosphere from Rio de la Plata Craton to Paraná Basin: Amalgamation of cratonic and refertilized lithospheres in SW Gondwanaland. Tectonics 38 (1). Doi 10.1029/2018TC005148

Borba, A.W., Mizusaki, A.M.P., Santos, J.O.S., McNaughton, N.J., Onoe, A.T., Hartmann, L.A., 2008. U-Pb zircon and 40Ar-39Ar K-feldspar dating of syn-sedimentary volcanism of the Neoproterozoic Maricá Formation: constraining the age of foreland basin inception and inversion in the Camaquã Basin of southern Brazil. Basin Research 20, 359-375.

Bucher, K., Frank, E., Frey, M., 1983. A model for the progressive regional metamorphism of margarite-bearing rocks in the Central Alps. American Journal of Science 283-A, 370-395.

Bucher, K., Grapes, R., 2011. Petrogenesis of Metamorphic Rocks. 8th Edition. Springer. 441p. DOI 10.1007/978-3-540-74169-5

Buick, I.S., Maas, R., Gibson, R., 2001. Precise U-Pb titanite age constraints on the emplacement of the Bushveld Complex, South Africa. Journal of the Geological Society 158, 3-6.

Cawood, P.A., Hawkesworth, C.J., Dhuime, B., 2012. Detrital zircon record and tectonic setting. Geology 40 (10), 875-878.

Cawood, P.A., Kröner, A., Collins, W.J., Kusky, T.M., Mooney, W.D., Windley, B.F., 2009. Accretionary orogens through Earth history. In: Cawood, P.A., Kröner, A. (Eds.). Earth accretionary systems in space and time. The Geological Society, London, Special Publications 318, 1-36.

Caxito, F.A., Heilbron, M., Valeriano, C.M., Bruno, H., Pedrosa-Soares, A., Alkmim, F.F., Chemale, F., Hartmann, L.A., Dantas, E., Basei, M.A.S., 2021. Integration of elemental and isotope data supports a Neoproterozoic Adamastor Ocean realm. Geochemical Perspectives Letters 17, 6-10.

Caxito, F.A., Uhlein, A., Stevenson, R., Uhlein, G.J., 2014. Neoproterozoic oceanic crust remnants in northeast Brazil. Geology 42 (5), 387-390.

Cerva-Alves, T., Hartmann, L.A., Remus, M.V.D., Lana, C., 2020. Integrated ophiolite and arc evolution, southern Brasiliano Orogen. Precambrian Research 341, e105648.

Cerva-Alves, T., Remus, M.V.D., Dani, N., Basei, M.A.S., 2017. Integrated field, mineralogical and geochemical characteristics of Caçapava do Sul alvikite and beforsite intrusions: a new Ediacaran carbonatite complex in southernmost Brazil. Ore Geology Reviews 88, 352-369.

Chekhovich, V.D., 2006. Different levels of ensimatic island-arc accretion. Geotectonics 40 (2), 101-110.

Chemale Jr., F., 2000. Evolução geológica do Escudo Sul-rio-grandense. In: Holz, M., De Ros, L.F. (Eds.), Geologia do Rio Grande do Sul. Centro de Investigação do Gondwana, Universidade Federal do Rio Grande do Sul, 13-55.

Chemale Jr., F., Hartmann, L.A., Silva, L.C., 1995. Stratigraphy and tectonism of the Brasiliano Cycle in southern Brazil. Communications of the Geological Survey of Namibia 10, 151-166.

Christensen, J., Rosenfeld, J.L., DePaolo, D.J., 1989. Rates of tectonoetamorphic processes from rubidium and strontium isotopes in garnet. Science 244 (4911), 1465-1469. doi:10.1126/science.244.4911.1465.

Condie, K.C., 2007. Accretionary orogens in space and time. The Geological Society of America Memoir 200, 145-158.

Connolly, J.A.D., 2005. Computation of phase equilibria by linear programming: a tool for geodynamic modeling and its application to subduction zone decarbonation. Earth and Planetary Science Letters 236, 524-541.

Christensen, J., Rosenfeld, J.L., DePaolo, D.J., 1989. Rates of tectonoetamorphic processes from rubidium and strontium isotopes in garnet. Science 244 (4911), 1465 - 1469. DOI: 10.1126/science.244.4911.1465

Culshaw, N.G., Beaumont, C., Jamieson, R.A., 2006. The orogenic superstructure-infrastructure concept: Revisited, quantified, and revived. Geology 34 (9), 733-736.

De Toni, G.B., Bitencourt, M.F., Nardi, L.V.S., Florisbal, L.M., Almeida, B.S., Geraldes, M., 2020. Dom Feliciano Belt orogenic cycle tracked by its pre-collisional magmatism: The Tonian (ca. 800 Ma) Porto Belo Complex and its correlations in southern Brazil and Uruguay. Precambrian Research 342, 105702.

Devulder, V., Gerder, A., Vanhaecke, F., Degryse, P., 2015. Validation of the determination of the B isotopic composition in Roman glasses with laser ablation multi-collector inductively coupled plasma-mass spectrometry. Spectrochimica Acta Part B: Atomic Spectroscopy 105, 116-120.

Dewey, J.F., 2005. Orogeny can be very short. Proceedings of the National Academy of Sciences 102 (43), 15286-15293.

Dirks, P.H.G.M., Offler, R., Collins, W.J., 1993. Timing of emplacement and deformation of the Tia Granodiorite, southern New England Fold Belt, NSW: Implications for the metamorphic history. Australian Journal of Earth Sciences 40 (2), 103-108.

Farber, K., Dziggel, A., Trumbull, R.B., Meyer, F.M., Wiedenbeck, M., 2015. Tourmaline B-isotopes as tracers of fluid sources in silicified Palaeoarchaean oceanic crust of the Mendon Formation, Barberton greenstone belt, South Africa. Chemical Geology 417, 134-147.

Frank, E., 1983. Alpine metamorphism of calcareous rocks along a cross-section in the Central Alps: occurrence and breakdown of muscovite, margarite and paragonite. Schweizerische Mineralogische und Petrographische Mitteilungen 63, 37-93.

Fuhrman, M.L., Lindsley, D.H., 1988. Ternary-feldspar modeling and thermometry. American Mineralogist 73, 201-215.

Garda, G.M., Trumbull, R.B., Beljavskis, P., Wiedenbeck, M., 2009. Boron isotope composition of tourmalinite and vein tourmalines associated with gold mineralization, Serra do Itaberaba Group, central Ribeira Belt, SE Brazil. Chemical Geology 264, 207-220.

Girelli, T.J., Chemale Jr., F., Lavina, E.L.C., Laux, J.H., Bongiolo, E.M., Lana, C. 2018. Granulite accretion to Rio de la Plata Craton, based on zircon U-Pb-Hf isotopes: tectonic implications for Columbia Supercontinent reconstruction. Gondwana Research 56, 105-118.

Gubert, M.L., Philipp, R.P., Basei, M.A.S., 2016. The Bossoroca Complex, São Gabriel Terrane, Dom Feliciano Belt, southernmost Brazil: U-Pb geochronology and tectonic implications for the Neoproterozoic São Gabriel Arc. Journal of South American Earth Sciences 70, 1-17.

Haag, M.B., Freitas, R.B., Sommer, C.A., Savian, J.F., Lima, E.F., Gambeta, J.H., Lyra, D.S., Trindade, R.I.F., 2020. Multi-proxy case study of a Neoproterozoic rhyolite flow in southernmost Brazil: emplacement mechanisms and implications for ancient felsic lavas. Journal of South American Earth Sciences 12, 102982.

Hartmann, L.A., Liu, D., Wang, Y., Massonne, H.J., Santos, J.O.S., 2008. Protolith age of Santa Maria Chico granulites dated on zircons from an associated amphibolite-facies granodiorite in southernmost Brazil. Anais da Academia Brasileira de Ciências 80, 543-551.

Hartmann, L.A., Massuda, A.J., Cerva-Alves, T., Lana, C., Leandro, C.G., Savian, J., 2021. Aeromagnetometry and aerogammaspectrometry integrated with U-Pb zircon geochronology of northern Bossoroca ophiolite, Brasiliano Orogen. Annals of the Brazilian Academy of Sciences 93 (1), e20190791.

Hartmann, L.A., Philipp, R.P., Santos, J.O.S., McNaughton, N.J., 2011. Time frame of the 753-680 Ma juvenile accretion during the São Gabriel Orogeny, southern Brazilian Shield. Gondwana Research 19, 84-99.

Hartmann, L.A., Werle, M., Michelin, C.R.L., Lana, C., Queiroga, G.N., Castro, M.P., Arena, K.R., 2019. Proto-Adamastor ocean crust (920 Ma) described in Brasiliano Orogen from coetaneous zircon and tourmaline. Geoscience Frontiers 10 (4), 1623-1633.

Henry, D.J., Guidotti, C.V., 1985. Tourmaline as a petrogenetic indicator mineral: an example from the staurolite-grade metapelites of NW Maine. American Mineralogist 70 (1-2), 1-15.

Hodel, F., Triantafyllou, A., Berger, J., Macouin, M., Baele, J.-M., Mattielli, N., Monnier, C., Trindade, R.I.F., Ducea, M.N., Chatir, A., Ennih, N., Langlade, J., Poujol, M., 2020. The Moroccan Anti-Atlas ophiolites: Timing and melting processes in an intra-oceanic arc-back-arc environment. Gondwana Research 86, 182-202.

Holland, T., Powell, R., 2011. An improved and extended internally consistent thermodynamic dataset for phases of petrological interest, involving a new equation of state for solids. Journal of Metamorphic Geology 29, 333-383.

Horstwood, M.S.A., Kosler, J., Gehrels, G., Jackson, S.E., McLean, N.M., Paton, C., Pearson, N.J., Sircombe, K., Sylvester, P., Vermeesch, P., Bowring, J.F., Condon, D.J., Schoene, B., 2016. Community-Derived Standards for LA-ICP-MS U-(Th-)Pb Geochronology – Uncertainty propagation, age interpretation and data reporting. Geostandards and Geoanalytical Research 40 (3), 311-332.

Hueck, M., Oyhantçabal, P., Philipp, R.P., Basei, M.A.S., Siegesmund, S., 2018. The Dom Feliciano belt in Southern Brazil and Uruguay. In: Siegesmund, S., Basei, M.A.S., Oyhantcabal, P., Oriolo, S. (Eds.), Geology of Southwest Gondwana. Regional Geology Reviews, Springer Nature 243-265.

Hueck, M., Wemmer, K., Basei, M.A.S., Philipp, R.P., Oriolo, S., Heidelbach, F., Oyhantçabal, P., Siegesmund, S., 2020. Dating recurrent shear zone activity and the transition from ductile to brittle deformation: White mica geochronology applied to the Neoproterozoic Dom Feliciano Belt in south Brazil. Journal of Structural Geology 141, 104199.

Ishikawa, T., Nakamura, E., 1994. Origin of the slab component in arc lavas from across-arc variation of B and Pb isotopes. Nature 370, 205-208.

Isozaki, Y., Maruyama, S., Furuoka, F., 1990. Accreted oceanic materials in Japan. Tectonophysics 181, 179-205.

Kimura, G., Ludden, J., 1995. Peeling oceanic crust in subduction zones. Geology 23, 217-220.

Konopásek, J., Cavalcante, C., Fossen, H., Janousek, V., 2020. Adamastor – an ocean that never existed? Earth-Science Reviews 205, 103201.

Kowalski, P.M., Wunder, B., Jahn, S., 2013. Ab initio prediction of equilibrium boron isotope fractionation between minerals and aqueous fluids at high P and T. Geochemica et Cosmochimica Acta 101, 285-301.

Kröner, A., Stern, R.J., 2004. Africa/Pan-African Orogeny. In: Selley, R.C., Cocks, L.R., Plimer, I.R. (Eds). Encyclopedia of Geology V.1, Elsevier, Amsterdam, 1-12.

Kusky, T.M., Windley, B.F., Safonova, I., Wakita, K., Wakabayashi, J., Polat, A., Santosh, M., 2013. Recognition of ocean plate stratigraphy in accretionary orogens through Earth history: a record of 3.8 billion years of sea floor spreading, subduction, and accretion. Gondwana Research 24, 501-547.

Lal, R.K., Mukerjee, S., Ackermand, D., 1981. Deformation and Barrovian metamorphism at Takdah, Darjeeling Eastern Himalaya. In: P. S. Saklani Ed., Metamorphic Tectonites of the Himalaya Today and Tomorrow publication, Delhi, 231-278.

Lana, C., Farina, F., Gerdes, A., Alkmim, A., Gonçalves, G.O., Jardim, A.C., 2017. Characterization of zircon reference materials via high precision U-Pb LA-MC-ICPMS. Journal of Analytical Atomic Spectrometry 32 (10), 2011-2023.

Leeman, W.P., Sisson, V.B., 1996. Geochemistry of boron and its implications for crustal and mantle processes. In: Grew, E.S., Anovitz, L.M. (eds) Boron: Mineralogy, Petrology and Geochemistry. Reviews in Mineralogy 33, 645-708.

Leite, J.A.D., Hartmann, L.A., McNaughton, N.J., Chemale Jr., F., 1998. SHRIMP U/Pb zircon geochronology of Neoproterozoic juvenile and crustal-reworked terranes in southernmost Brazil. International Geology Review 40, 688-705.

Lena, L.O.F., Pimentel, M.M., Philipp, R.P., Armstrong, R., Sato, K., 2014. The evolution of the Neoproterozoic São Gabriel juvenile terrane, southern Brazil based on high spatial resolution U-Pb ages and δ18O data from detrital zircons. Precambrian Research 247, 126-138.

Li, B., Massonne, H.-J., 2017. Contrasting metamorphic evolution of metapelites from the Malpica-Tuy unit and the underlying so-called parautochthon at the coast of NW Spain. Lithos 286, 92-108.

Li, B., Massonne, H.-J., Hartmann, L.A., Zhang, J., Luo, T., 2021. Kyanite-garnet granulite from the Andrelândia nappe system, Brasília belt, registers two late Neoproterozoic metamorphic cycles. Precambrian Research 355, 106086.

Longridge, L., Gibson, R. L., Kinnaird, J. A., Armstrong, R.A., 2011. Constraining the timing of deformation in the southwestern Central Zone of the Damara Belt, Namibia. Geological Society, London, Special Publications 357, 107-135.

Ludwig, K.R., 2003. Isoplot/Ex Version 3.00: A Geochronological Tool kit for Microsoft Excel. Berkeley Geochronology Center, Berkely, CA (Special Publication 4, 71 http://bgc.org/isoplot_etc/isoplot.html).

Machado, N., Koppe, J.C., Hartmann, L.A., 1990. A late Proterozoic U-Pb age for the Bossoroca Belt, Rio Grande do Sul, Brasil. Journal of South American Earth Sciences 3 (2-3), 87-90.

Maraschin, A.J., Mizusaki, A.M., Zwingmann, H., Borba, A.W., Sbrissa, G.F., 2010. Illite authigenesis in sandstones of the Guaritas Allogroup (Early Paleozoic): Implications for the depositional age, stratigraphy and evolution of the Camaquã Basin (Southern Brazil). Journal of South American Earth Sciences 29, 400-411.

Marschall, H.R., Foster, G.L., 2018. Boron Isotopes in the Earth and Planetary Sciences – A Short History and Introduction. In: Marschall, H.R., Foster, G.L. (Eds.) Boron Isotopes, Advances in Isotope Geochemistry. Springer International Publishing AG 2018. https://doi.org/10.1007/978-3-319-64666-4_1.

Marschall, H.R., Jiang, S-Y., 2011. Tourmaline isotopes: No element left behind. Elements 7, 313-319.

Massonne, H.-J., 2012. Formation of amphibole and clinozoisite–epidote in eclogite owing to fluid infiltration during exhumation in a subduction channel. Journal of Petrology 53, 1969-1998.

Massuda, A.J., Hartmann, L.A., Queiroga, G.N., Castro, M.P., Leandro, C.G., Savian, J.F., 2020. Mineralogical evolution of the northern Bossoroca ophiolite, São Gabriel Terrane. Brazilian Journal of Geology 50 (4), e20190120.

Meet, J.G., Liebermam, B.S., 2008. The Neoproterozoic assembly of Gondwana and its relationship to the Ediacaran-Cambrian radiation. Gondwana Research 14, 5-21.

Millonig, L.J., Albert, R., Gerdes, A., Avigad, D., Dietsch, C., 2020. Exploring laser ablation U–Pb dating of regional metamorphic garnet – The Straits Schist, Connecticut, USA. Earth and Planetary Science Letters 552, 116589.

Mohan, A., Windley, B.P., Searle, M.P., 1989. Geothermometry and development of inverted metamorphism in the Darjeeling- Sikkim region of the eastern Himalaya. Journal of Metamorphic Geology 7, 95-110.

Oyhantçabal, P., Sánchez Bettucci, L., Pecoits, E., Aubet, N., Peel, E., Preciozzi, F., Basei, M.A.S., 2005. Nueva propuesta estratigráfica para las supracorticales del Cinturón Dom Feliciano (Proterozoico Uruguay). In: 12 Congreso Latinoamericano de Geología, Quito.

Palmer, M.R., 2017. Boron cycling in subduction zones. Elements 13, 237-242.

Palmer, M.R., Slack, J.F., 1989. Boron isotopic composition of tourmaline from massive sulfide deposits and tourmalinites. Contributions to Mineralogy and Petrology 103, 434-451.

Peixoto, C.A., Heilbron, M., Ragatky, D., Armstrong, R., Dantas, E., Valeriano, C.M., Simonetti, A., 2017. Tectonic evolution of the juvenile Tonian Serra da Prata magmatic arc in the Ribeira Belt, SE Brazil: implications for early West Gondwana amalgamation. Precambrian Research 302, 221-254.

Pertille, J., Hartmann, L.A., Santos, J.O.S., McNaughton, N.J., Armstrong, R., 2017. Reconstructing the Cryogenian-Ediacaran evolution of the Porongos fold and thrust Belt, southern Brasiliano Orogen, based on zircon U-Pb-Hf-O isotopes. International Geology Review 1532–1560. doi:https://doi.org/10.1080/00206814.2017.1285257.

Pettijohn, F.J., Potter, P.E., Siever, R., 1972. Sand and Sandstones: New York, Springer-Verlag.

Philipp, R.P., Pimentel, M.M., Basei, M.A.S., 2018. The tectonic evolution of the São Gabriel Terrane, Dom Feliciano Belt, southern Brazil: The closure of the Charrua Ocean. In: Siegesmund, S., Basei, M.A.S., Oyhantcabal, P., Oriolo, S. (Eds.), Geology of Southwest Gondwana. Regional Geology Reviews. Springer Nature, 243-265.

Pimentel, M.M., Fuck, R.A., 1992. Neoproterozoic crustal accretion in central Brazil. Geology 20 (4), 375-379.

Pimentel, M.M., Fuck, R.A., Gioia, S.M.C.L., 2000. The Neoproterozoic Goiás magmatic arc, central Brasil: a review and new Sm-Nd isotopic data. Revista Brasileira de Geociências 30 (1), 35-39.

Preciozzi, F., Muzio, R., Guerequiz, R., 2001. Dom Feliciano belt and Punta del Este Terrane: geochronological features. In: 3. South American symposium on isotope geology. Extended abstracts, Pucon, p. 217-230.

Ramos, R.C., Koester, E., Vieira, D.T., 2020. Sm–Nd systematics of metaultramafic-mafic rocks from the Arroio Grande Ophiolite (Brazil): Insights on the evolution of the South Adamastor paleo-ocean. Geoscience Frontiers 11 (6), 2287-2296.

Raymond, L.A., 2019. Perspectives on the roles of mélanges in subduction accretionary complexes: A review. Gondwana Research 74, 68-89.

Raymond, L.A., Ogawa, Y., Maddock, M.E., 2019. Accretionary unit formats in subduction complexes: examples from the Franciscan and Miura-Boso and complexes. International Geology Review 62 (12), 1-29.

Remus, M.V.D., 1990. Geologia e Geoquímica do Complexo Cambaizinho, São Gabriel, RS. MSc. Thesis, Instituto de Geociências, Universidade Federal do Rio Grande do Sul.

Remus, M.V.D., Hartmann, L.A., McNaughton, N.J., Groves, D.I., Fletcher, I.R., 2000. The link between hydrothermal epigenetic copper mineralization and the Caçapava Granite of the Brasiliano Cycle in southern Brazil. Journal of South American Earth Science 13, 191-216.

Remus, M.V.D., McNaughton, N.J., Hartmann, L.A., Koppe, J.C., Fletcher, I.R., Groves, D.I., Pinto, V.M., 1999. Gold in the Neoproterozoic juvenile Bossoroca Volcanic Arc of southernmost Brazil: isotopic constraints on timing and sources. Journal of South American Earth Sciences 12, 349-366.

Ribeiro M.J. 1978. Mapa previsional do cobre no Escudo Sul-Rio-Grandense, escala 1:500.000. Porto Alegre: DNPM, Seção Geologia Econômica, 104 p.

Rocha-Campos, A.C., Basei, M.A.S., Nutman, A.P., Santos, P.R., Passarelli, C.R., Canile, F.M., Rosa, O.C.R., Fernandes, M.T., Santa Ana, H., Veroslavsky, G., 2019. U-Pb zircon dating of ash fall deposits from the Paleozoic Paraná Basin of Brazil and Uruguay: A reevaluation of the stratigraphic correlations. The Journal of Geology 127 (2). DOI 10.1086/701254.

Ryan, P.D., 2008. Preservation of forearc basin during island arc-continent collision: Some insights from the Ordovician of western Ireland. Special Paper of the Geological Society of America 436, 1-9.

Ryan, P.D., Dewey, J.F., 2019. The source of metamorphic heat during collisional orogeny: The Barrovian enigma. Canadian Journal of Earth Sciences 56 (12), 1309-1317.

Saalmann K., Gerdes A., Lahaye Y., Hartmann L.A., Remus M.V.D., Laufer A., 2011. Multiple accretion at the eastern margin of the Rio de la Plata craton: the prolonged Brasiliano Orogeny in southernmost Brazil. International Journal of Earth Sciences 100 (2-3), 355-378.

Saalmann, K., Remus, M.V.D., Hartmann, L.A., 2006. Tectonic evolution of the Neoproterozoic São Gabriel block, southern Brazil: Constraints on Brasiliano orogenic evolution of the Rio de La Plata cratonic margin. Journal of South American Earth Sciences 21, 204-227.

Safonova, I., 2017. Juvenile versus recycled crust in the Central Asian Orogenic Belt: Implications from ocean plate stratigraphy, blueschist belts and intra-oceanic arcs. Gondwana Research 47, 6-27.

Santiago, R., Caxito, F.A., Pedrosa-Soares, A., Neves, M.A., Dantas, E.L., 2020. Tonian island arc remnants in the northern Ribeira Orogen of Western Gondwana: The Caxixe batholith (Espírito Santo, SE Brazil). Precambrian Research 351, 105944.

Saquaque, A., Admou, H., Karson, J., Hefferan, K., Reuber, I., 1989. Precambrian accretionary tectonics in the Bou Azzer-El Graara region, Anti-Atlas, Morroco. Geology 17, 1107-1110.

Schannor, M., Lana, C., Nicoli, G., Cutts, K., Buick, I., Gerdes, A., Hecht, L., 2021. Reconstructing the metamorphic evolution of the Araçuaí orogen (SE Brazil) using in situ U-Pb garnet dating and P-T modelling. Journal of Metamorphic Geology. Doi:

10.1111/JMG.12605.

Seman, S., Stockli, D.F., McLean, N.M., 2017. U-Pb geochronology of grossular-andradite garnet. Chemical Geology 460 (5) 106-116.

Spear, F.S., Thomas, J.B., Hallett, B.W., 2014. Overstepping the garnet isograd: a comparison of QuiG barometry and thermodynamic modeling. Contributions to Mineralogy and Petrology 168, 1059.

Stern, R.J., 2018. Neoproterozoic formation and evolution of Eastern Desert continental crust - The importance of the infrastructure-superstructure transition. Journal of African Earth Sciences 146, 15-27.

Tera, F., Wasserburg, G.J., 1972. U-Th-Pb systematics in three Apollo 14 basalts and the problem of initial Pb in lunar rocks. Earth and Planetary Science Letters 14, 281-304.

Thomas, R.J., Chevallier, L.P., Gresse, P.G., Harmer, R.E., Eglington, B.M., Armstrong, R.A., de Beer, C.H., Martini, J.E.J., de Kock, G.S., Macey, P.H., Ingram,

B.A., 2002. Precambrian evolution of the Sirwa Window, Anti-Atlas Orogen, Morocco. Precambrian Research 118, 1-57.

Tonarini, S., Pennisi, M., Adorni-Braccesi, A., Dini, A., Ferrara, G., Gonfiantini, R., Wiedenbeck, M., Gröning, M., 2003. Intercomparison of boron isotope and concentration measurements. Part I: selection, preparation and homogeneity tests of the intercomparison materials. Geostandards and Geoanalytical Research 27(1), 21-39.

Trumbull, R.B., Beurlen, H., Wiedenbeck, M., Soares, D.R., 2013. The diversity of B-isotope variations in tourmaline from rare-element pegmatites in the Borborema Province of Brazil. Chemical Geology 352, 47-62.

Underwood, M.B., Laughland, M.M., 2001. Paleothermal structure of the Point San Luis slab of central California: Effects of Late Cretaceous underplating, out-of-sequence thrusting, and late Cenozoic dextral offset. Tectonics 20, 97-111.

Vence, D., 1995. Rate and time controls on metamorphic processes. Geological Journal 30, 241-259.

Vermeesch, P., 2018. IsoplotR: a free and open toolbox for geochronology. Geoscience Frontiers 9, 1479-1493.

Vermeesch, P., 2021. Maximum depositional age estimation revisited. Geoscience Frontiers 12, 843-850.

Wakita, K., 2015. OPS mélange: A new term for mélanges of convergent margins of the world. International Geology Review 57 (5-8), 529-539.

Wakita, L., Metcalfe, O., 2005. Ocean plate stratigraphy in east and southeast Asia. Journal of Asian Earth Sciences 24 (6), 679-702.

Werle, M., Hartmann, L.A., Queiroga, G.N., Lana, C., Pertille, J., Michelin, C.R.L., Remus, M.V.D., Roberts, M.P., Castro, M.P., Leandro, C.G., Savian, J.F., 2020. Oceanic crust and mantle evidence for the evolution of Tonian-Cryogenian ophiolites, southern Brasiliano Orogen. Precambrian Research 351, 105979.

White, R.W., Powell, R., Holland, T.J.B., Johnson, T.E., Green, E.C.R., 2014. New mineral activity–composition relations for thermodynamic calculations in metapelitic systems. Journal of Metamorphic Geology 31, 261286.

Whitney, D.L., Evans, B.W., 2010. Abbreviations for names of rock-forming minerals. American Mineralogist 95, 185-187.

Will, T.M., Gaucher, C., Ling, X.-X., Li, X.-H., Frimmel, H.E., 2019. Neoproterozoic magmatic and metamorphic events in the Cuchilla Dionisio Terrane, Uruguay, and possible correlations across the South Atlantic. Precambrian Research 320, 303-322.

Williams, L.B., Hervig, R.L., Holloway, J.R., Hutcheon, I., 2001. Boron isotope geochemistry during diagenesis. Part I. Experimental determination of fractionation during illitization of smectite. Geochimica et Cosmochimica Acta 65 (11), 1769-1782.

Zagorevski, A., Van Staal, C.R., 2011. The record of Ordovician arc-arc and arc-continent collision in the Canadian Appalachians during the closure of Iapetus. In: Brown, D., Ryan, P.D. (Eds.). Arc-continent collision. Springer, 341-371.

Zeh, A., Holness, M.B., 2003. The effect of reaction overstep on garnet microtextures in metapelitic rocks of the Ilesha Schist Belt, SW Nigeria. Journal of Petrology 44 (6), 967-994.

Artigo 3 – Tiara CERVA-ALVES, Léo Afraneo HARTMANN, Cristiano LANA, Gláucia Nascimento QUEIROGA, Luis Antonio Cruz MACIEL, Carolina Gonçalves LEANDRO, Jairo Francisco SAVIAN. 2021. *Rutile and zircon age and geochemistry in the evolution of the juvenile São Gabriel Terrane early in the Brasiliano Orogeny. Journal of South American Earth Sciences*, v.112, 103505.

https://doi.org/10.1016/j.jsames.2021.103505

Rutile and zircon age and geochemistry in the evolution of the juvenile São Gabriel Terrane early in the Brasiliano Orogeny

T. Cerva-Alves [a] ✉, L.A. Hartmann [a] ✉, C. Lana [b] ✉, G.N. Queiroga [b] ✉, L.A.C. Maciel [c] ✉, C.G. Leandro [a] ✉, J.F. Savian [a] ✉

[a] Instituto de Geociências, Universidade Federal do Rio Grande do Sul, Avenida Bento Gonçalves, 9500, 91501-970, Porto Alegre, Rio Grande do Sul, Brazil

[b] Departamento de Geologia, Escola de Minas, Universidade Federal de Ouro Preto, Morro do Cruzeiro, 35400-000, Ouro Preto, Minas Gerais, Brazil

[c] Agência Nacional de Mineração, Rua Washington Luiz, 815, 90010-460, Porto Alegre, Rio Grande do Sul, Brazil

ABSTRACT

Major issues in the tectonic evolution of continents include oceanic crust generation, the subduction of oceanic island arcs and their accretion to a craton. The understanding of geological events in the Neoproterozoic of South America and Gondwana is a challenge due to tectonic disturbance caused by the Brasiliano Orogeny. We selected key units in the South Atlantic Brasiliano Orogen to solve problems related to dating and environment of metamorphism, magmatism and metasomatism. Multiproxy methodology included aerogammaspectrometry in the Cambaizinho and Palma ophiolites. Rutile and zircon U-Pb geochronology combined with Lu-Hf-trace element analyses were conducted on metagabbro and chloritite. The aerogammaspectrometric survey delimitated the extent of ophiolite bodies. Rutile U-Pb dating in the Cambaizinho metagabbro provided a metamorphic age of 706 ±11 Ma. Zircon U-Pb dating in the São Luís metagabbro yielded an age of 731.6 ±0.5 Ma for the magmatic activity; chloritite yielded an 889.2 ±2.3 Ma age for metasomatism. Zircon Hf analyses display positive εHf$_{(t)}$ values (metagabbro = +7.1 to +11.1; chloritite = +9.9 to +17.5). REE element diagrams show positive Ce anomalies for both metagabbro and chloritite zircons. Positive εHf$_{(t)}$ in zircon from metagabbro and chloritite indicates depleted mantle origin. Trace element contents of zircon (e.g., U, Yb) from the metagabbro are consistent with magma generation by partial melting of older juvenile crust; data from chloritite indicate a N-MORB magma source. We infer that the final phase of collision and thrusting of the São Gabriel arc over the Rio de La Plata Craton occurred at 706 Ma; the São Gabriel island arc had main activity at 731 Ma; mid-ocean ridge metasomatism in the ophiolite occurred at 889 Ma. Our studies provide evidence of geotectonic processes during Rodinia break-up and early Brasiliano orogeny and similar juvenile Tonian terrains within Gondwana.

Keywords: Ophiolite, São Gabriel arc, Aerogeophysics, U-Pb LA-ICP-MS, Brasiliano Orogen, Rutile and zircon.

1. Introduction

The register of diachronous juxtaposition of geological units containing ophiolites, ocean arc-affinity plutons and volcano-sedimentary rocks is indicative of the accretion of intra-oceanic arcs to the continents (Tapster *et al.*, 2014). These geological

processes were responsible for the generation of oceanic crust and orogenic belts along the Neoproterozoic. The spreading of Rodinia fragments led to the generation of oceanic crust and formed the Proto-Adamastor Ocean at 1.2-0.9 Ga, extending to 750 Ma (Hartmann *et al.*, 2019). This ocean was the predecessor of the 750-600 Ma Adamastor Ocean (Hartmann *et al.*, 2019; Caxito *et al.*, 2021). The largest addition of island-arc juvenile crust to the continents is observed in the Arabian-Nubian shield, part of the Pan-African/Brasiliano Orogen (Stern *et al.*, 2004). Another significant addition is in the Anti-Atlas Orogen, Morocco (Hodel *et al.*, 2020).

In the South Atlantic Brasiliano Orogen (Caxito *et al.* 2021), the Dom Feliciano Belt extends for >1100 km, in a NE-SW direction (Fig. 1a) (Hueck *et al.*, 2018; Caxito *et al.*, 2021). In the central part of the belt, the São Gabriel Terrane provides a rare example to study the evolution of the preserved Tonian-Cryogenian oceanic lithosphere. Studies of the São Gabriel Terrane identified plutonic and volcanic assemblages with juvenile signature and mafic-ultramafic rocks with MORB chemistry (Arena *et al.*, 2017). However, the dating of oceanic crust and mantle is a challenge due the low U content aggravated by the absence of datable minerals in mafic-ultramafic rocks. Understanding the processes involved in the route from a mid-Adamastor oceanic ridge to subduction and collision to the Rio de La Plata Craton remains a fundamental challenge in the geotectonics of the Neoproterozoic. Main problems include the timing of formation of igneous (gabbro) and metamorphic (metasomatic chloritite) that mark fundamental steps in the evolution of accreted terranes.

Here, we advance the knowledge about the processes involving the proto-Adamastor oceanic crust, the associated island arc, and the continental tectonic settings. We integrate results from field geology, aerogammaspectrometry, and isotope compositions of rutile (U-Pb) and zircon (U-Pb, Lu-Hf, trace elements). We selected two metagabbros (Cambaizinho and Palma regions) and one metasomatic chloritite (Palma Leste region) to develop the evolutionary model. The juvenile São Gabriel Terrane is shown as a complex collage of Tonian-Cryogenian oceanic island arcs to the Rio de La Plata Craton. Timing of events is better constrained, relevant to Rodinia rifting and primeval Gondwana amalgamation.

2. Geological setting

The Dom Feliciano Belt is part of the South Atlantic Brasiliano Orogen, and records units formed during Rodinia break-up and assembly of western Gondwana (Fig. 1a, b) (Oyhantçabal *et al.*, 2021), with collision between Kalahari, Congo and Rio de La Plata cratons (Fernandes *et al.*, 1995; Hueck *et al.*, 2018). In the central portion of the Dom Feliciano Belt, the Sul-Riograndense Shield is divided into five tectonic units: (1) Archean to Mesoproterozoic basement in the Rio de La Plata Craton, preserving deformational evidences of reworking during the Neoproterozoic (Hueck *et al.*, 2018); (2) São Gabriel Terrane, representing the juvenile section of the Brasiliano Orogen and recording two Tonian-Cryogenian magmatic arcs (Babinski *et al.*, 1996; Leite *et al.*, 1998); (3) Porongos fold and thrust belt containing Tonian and Ediacaran volcano-sedimentary rocks and inliers of Paleoproterozoic basement rocks (Pertille *et al.*, 2017); (4) Ediacaran granitic rocks of the Pelotas Batholith (Hueck *et al.*, 2018); and (5) the foreland, Ediacaran-Ordovician Camaquã Basin (Borba *et al.*, 2008; Maraschin *et al.*, 2010).

In the São Gabriel Terrane (Fig. 1c; Table 1), dated metamorphosed plutonic and volcanosedimentary rocks spread between the ca. 879-875 Ma Passinho arc (Leite *et al.*, 1998; Philipp *et al.*, 2014) and the 794-674 Ma São Gabriel arc (Vedana *et al.*, 2018; Cerva-Alves *et al.*, 2020). The arcs are interlayered with disrupted, folded and faulted ophiolites (e.g., Arena *et al.*, 2016, 2017). Plutonic rocks from the infrastructure of the São Gabriel island arc belong to the Cambaí Complex (e.g., Saalmann *et al.*, 2011). These rocks include diorite, tonalite, trondhjemite and granodiorite from the Vila Nova Suite, and granitoids from the Sanga do Jobim and Lagoa da Meia Lua suites (Hartmann *et al.*, 2011). Metavolcanosedimentary rocks are part of the superstructure of the São Gabriel arc, belonging to the Vacacaí Group. The juvenile terrane was intruded by post-tectonic granites (ca. 610-540 Ma) (Chemale *et al.*, 2000; Werle *et al.*, 2020). Carbonatite occurrences are described near the eastern boundary of the terrane (e.g., ~603 Ma; Cerva-Alves *et al.*, 2017). The Tonian Cerro do Ouro Ophiolite includes all ophiolites in the terrane; it obducted over and wedged into the São Gabriel arc. Main bodies are the Cerro Mantiqueiras, Ibaré, Palma, Passo do Ivo, Bossoroca and Cambaizinho ophiolites (Goñi, 1962; Arena *et al.*, 2016, 2017; Hartmann *et al.*, 2019).
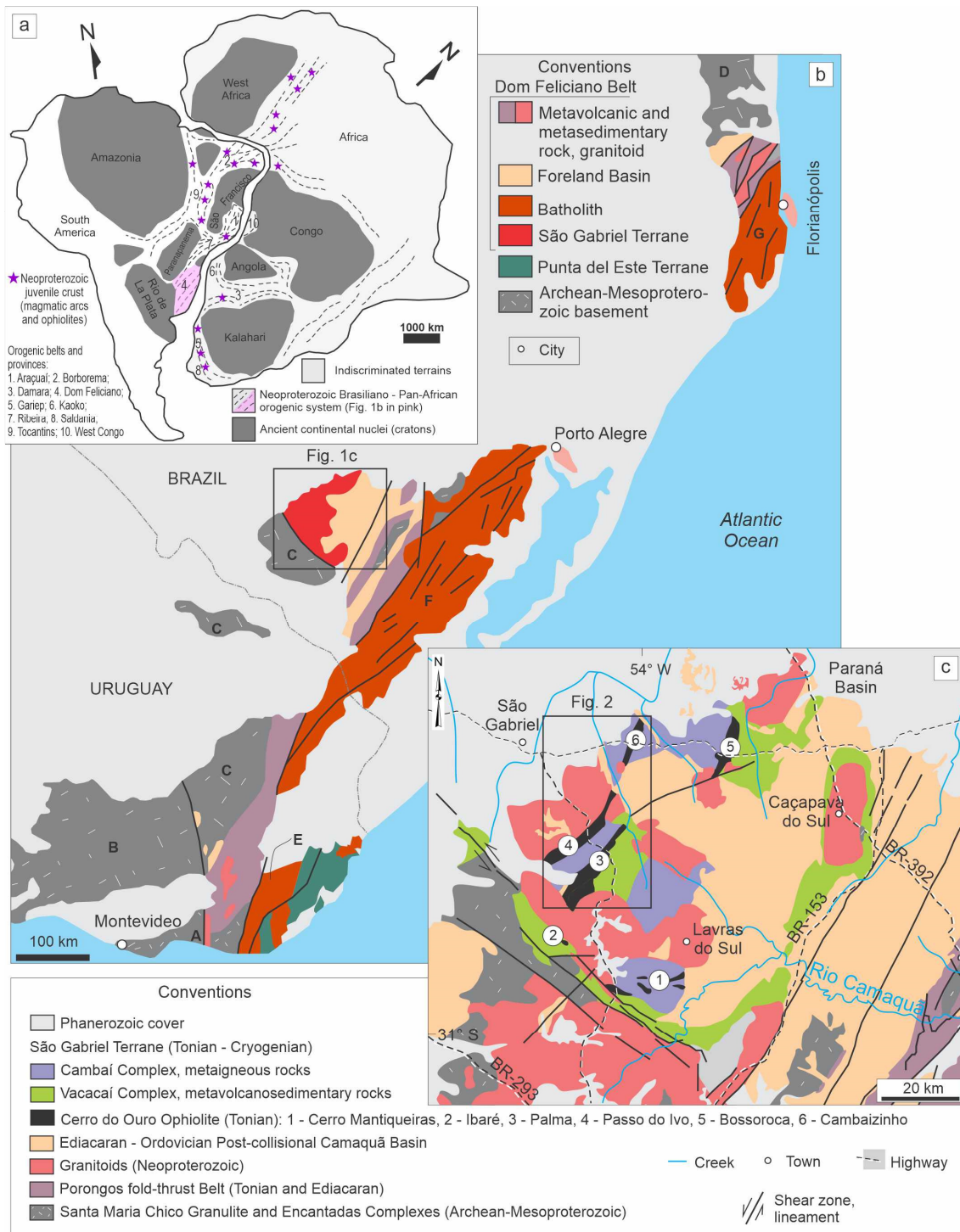
Fig. 1. (a) Simplified Western Gondwana configuration at ~530 Ma indicating location of the Dom Feliciano Belt. Modified from Li *et al.* (2008), Caxito *et al.* (2021). LA = Luís Alves Craton; PP = Paranapanema Craton; RP = Rio de La Plata Craton, SF = São Francisco Craton. (b) Tectonostratigraphic map of the Dom Feliciano Belt. Modified from Hartmann *et al.* (2019), Will *et al.* (2019). A = Tandilia Terrane; B = Piedra Alta Terrane; C = Nico Pérez Terrane; D = Luiz Alves Craton; E = Aiguá Batholith; F = Pelotas Batholith; G = Florianópolis Batholith. (c) Geologic map of the western portion of the Sul-Riograndense Shield with ophiolite fragments indicated in the São Gabriel Terrane (Cerva-Alves *et al.*, 2020; Haag *et al.*, 2021).

Deformational events in the São Gabriel Terrane include three ductile and one ductile-brittle phases (Remus, 1990; Saalmann *et al.*, 2011). The D1 event refers to the first folding event. The D2 deformation generated isoclinal, recumbent, rootless folds, reaching the amphibolite metamorphic facies. Both D1 and D2 are described only in metavolcanosedimentary rocks. D3 deformation formed subvertical foliation planes dipping WNW or ESE along major NE shear zones, as observed in most ophiolite bodies, schist, gneiss and syntectonic plutonic rocks from the Cambaí Complex. The D4 deformation caused local cataclastic rock fragmentation.

The Cambaizinho and Palma regions are the key areas selected for our study in the São Gabriel Terrane (Fig. 2). In the Cambaizinho region (extreme northwest of the Terrane), the Cambaí Complex is formed by undifferentiated ortho- and paragneisses of the Vila Nova Suite. Minor ultramafic bodies (100-500 m) are inserted in the oceanic crust rocks that are 20 km long and 1 km wide. Metagabbro and monzogranite from the Sanga do Jobim Suite are present intruding the Vila Nova Suite and Cambaizinho Ophiolite, forming elliptical bodies with major axis oriented NNE (Remus, 1990). The Cambaizinho Ophiolite extends for 11 km long trending NE-SW and 2 km width, dipping either 80º-85º NW or 60º-85º SE. The ophiolite consists mainly of serpentinite, magnesian schist and quartzite, and was obducted during the Neoproterozoic onto the Cambaí DTTG Complex, Vila Nova Suite (Remus, 1990; Cerva-Alves *et al.*, 2020). The widespread jackstraw texture (talc + olivine) described in serpentinite outcrops is indicative of low amphibolite metamorphic facies (Remus, 1990). The Ordovician to Cretaceous Paraná Basin covers the São Gabriel Terrane in the north and northwest, and the Ediacaran-Early Cambrian Camaquã Basin in the south.
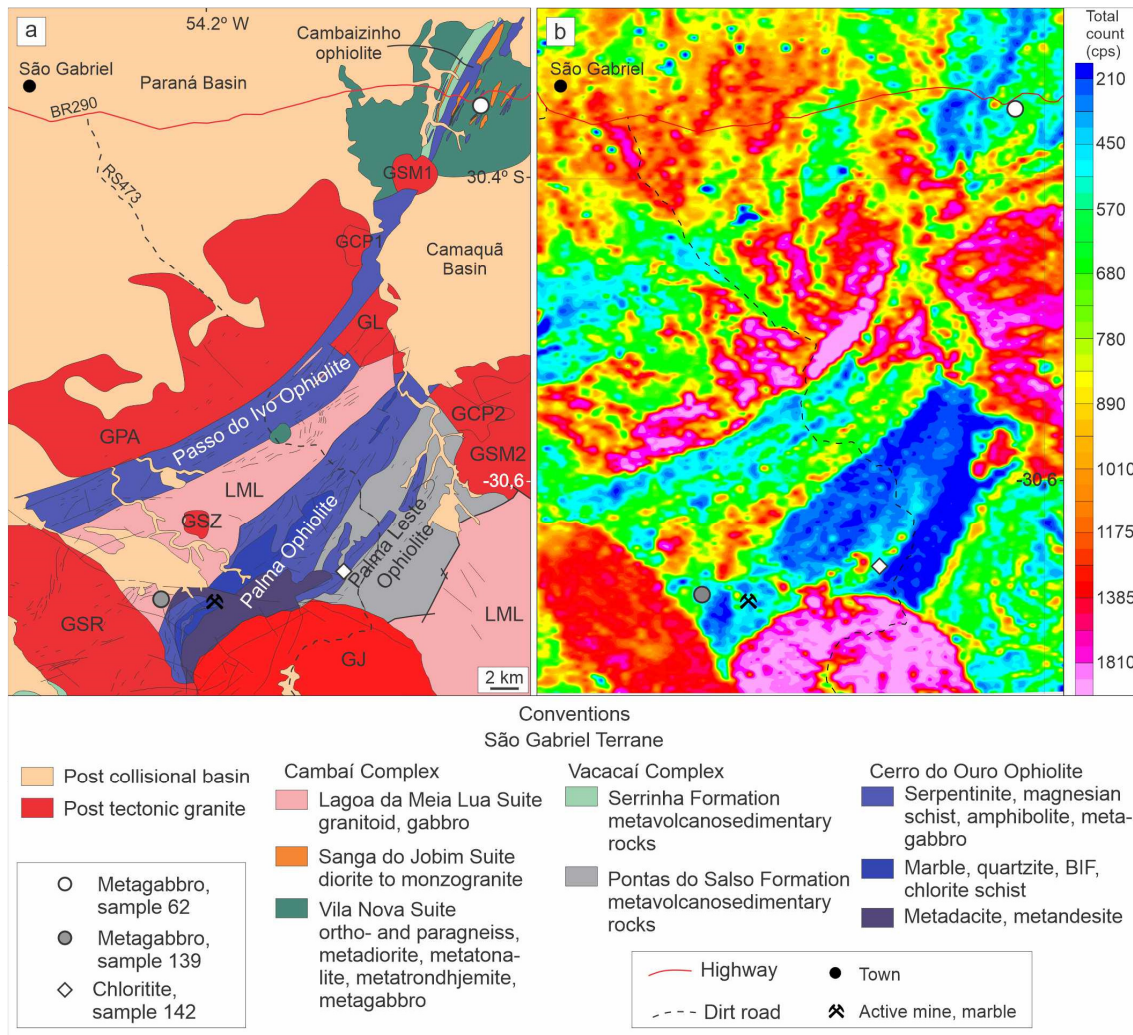
Fig. 2. (a) Simplified geological map of the western portion of the São Gabriel Terrane with location of sampled rock indicated. GCP = Camaquã Pelado Granite; GJ = Jaguari Granite; GL = Lajeado Granite; GPA = Passo da Areia Granite; GSM = São Manoel Granite; GSR = Santa Rita Granite; GSZ = Santa Zélia Granite; LML = Lagoa da Meia Lua Suite. (b) Map of the total count signal. Modified from Laux (2017).

The Palma region is situated to the south-southwest of the Cambaizinho Ophiolite. In this region, the São Gabriel arc infrastructure is represented by the Lagoa da Meia Lua Suite, composed by granitoids and metagabbro (including the São Luís metagabbro). The infrastructure was obducted by the Passo do Ivo and Palma ophiolites. The Palma Ophiolite is 25 km long and 4.4 km wide in the NE-SW direction, formed by amphibolite, serpentinite, magnesian schist, quartzite and pelitic paragneiss (Arena *et al.*, 2017). The Palma Ophiolite is in contact with the São Luís metagabbro in the southwestern portion and granitoids in the western-northern portion, both part of the Lagoa da Meia Lua Suite. The Santa Rita and Jaguari post-tectonic granites are in the south, the Camaquã Basin is in the northeast. To the east, connected with the

Palma Ophiolite, the Palma Leste Ophiolite is a disrupted, dominantly ultramafic body with dimensions 13 km x 1 km, in contact with metavolcanosedimentary rocks from the Vacacaí Group, Pontas do Salso Formation (Vedana *et al.*, 2018).

3. Methodology

We integrated aerogammaspectrometry with field mapping in the selected Cambaizinho and Palma ophiolites and surrounding region. Representative metagabbros from the Cambaizinho (sample 62) and Palma (sample 139) regions were collected for dating and isotopic geology. One chloritite body was described in the Palma Leste ophiolite and sampled for laboratory studies (sample 142). Thin sections of rocks and polished mounts of rutile (one Cambaizinho metagabbro from the São Gabriel arc) and zircon (one metagabbro São Luís from São Gabriel arc and one chloritite from Palma Leste Ophiolite) were studied with optical microscopy at Laboratório de Geologia Isotópica, Universidade Federal do Rio Grande do Sul (UFRGS). Backscattered electron images (BSE), cathodoluminescence images (CL) and energy dispersive spectroscopy (EDS) analyses were performed at the Departamento de Geologia, Universidade Federal de Ouro Preto (UFOP), Minas Gerais. The images allowed selection of best spots for analysis. Analyses were made with a laser for isotopic U-Pb determinations in rutile and isotopic U-Pb-Hf and trace element determinations in zircon. Detailed analytical procedures are presented in Supplementary File 1.

4. Results

4.1. Aerogammaspectrometry and field survey

The total-count gamma-ray-intensity (Fig. 2b) survey permits to measure a spectrum of radioactivity emitted by radioactive materials (K, eU, eTh) exposed at and near (1 m) the surface. Mafic and ultramafic rocks from the Palma and Cambaizinho ophiolites have low contents of radioactive minerals, showing the lowest values (<30 counts per second, cps) of total-count (Fig. 2b). Similarly, parts of the Vacacaí metavolcanosedimentary rocks show low radiometric signature. On the other hand, the Passo do Ivo Ophiolite contains ultramafic rocks and has indistinct contrasts in radiometric signal. Rocks from the Cambaí Complex show higher values when compared with ophiolites, while the highest peak (< 1385 cps) is observed in syn- and

post-tectonic granites and post-collisional basins. The application of separate eTh, eU and K (Fig. 3a-c) showed that the eTh (Fig. 3a) and K (Fig. 3c) have contours analogous to the total-count signature, whereas eU (Fig. 3b) has negligible influence in the identification of ophiolitic bodies. The eTh, eU and K maps show high values where granitic rocks are exposed; high eTh and eU but low K ares observed in the Paraná Basin. The digital terrain elevation (Fig. 3d) indicates that the highest elevation is near 350 m above sea level (a.s.l.); the highest elevation is underlain by the post-tectonic Jaguari Granite. High elevation in the east is associated with volcanic units from the Camaquã Basin.

Digital elevation model (m)

eTh (ppm)
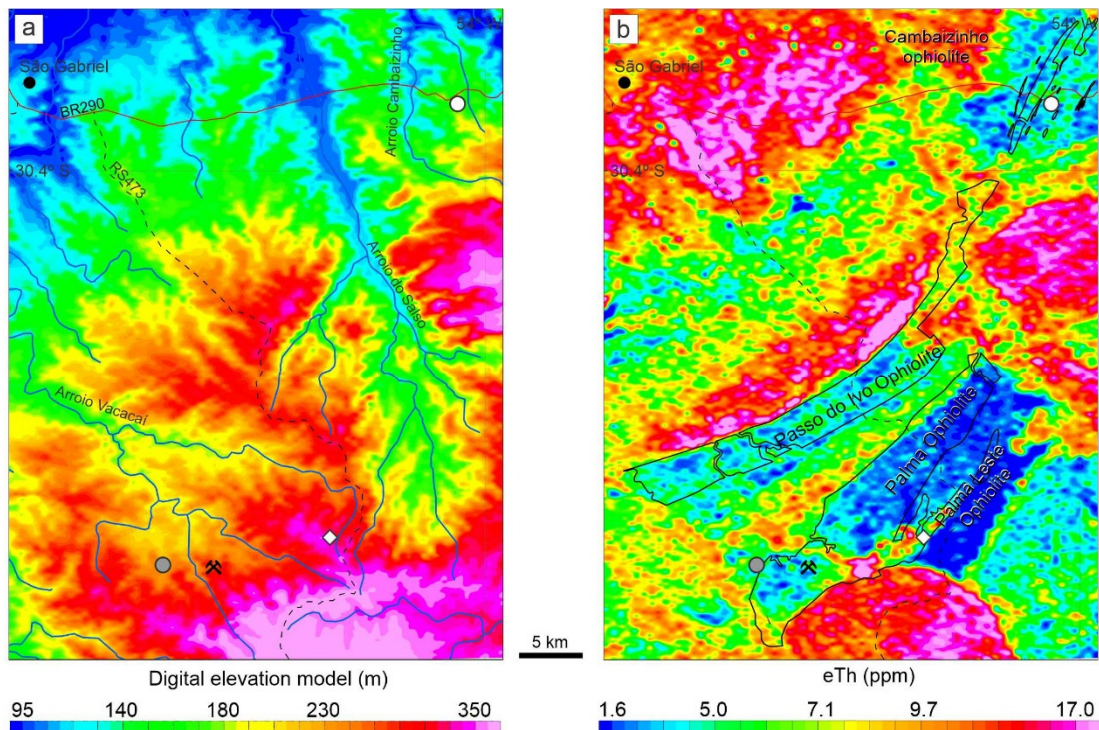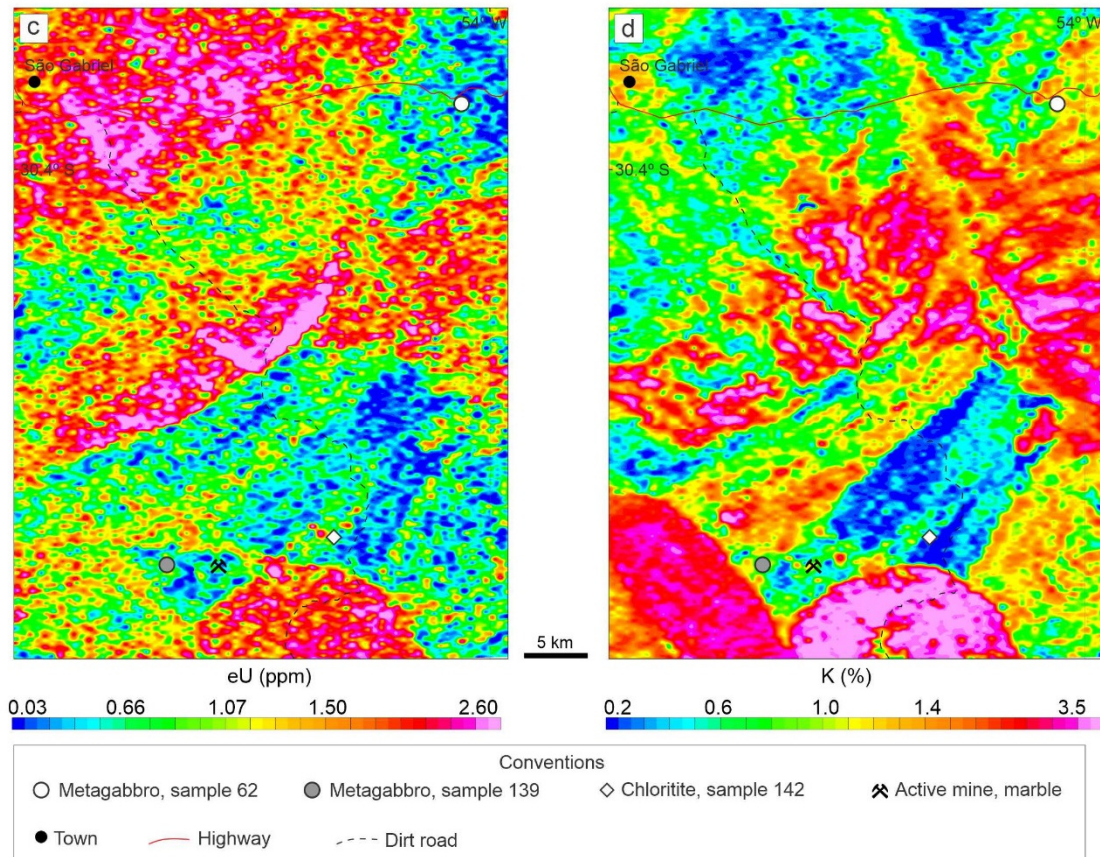
Fig. 3. Aerogammaspectrometric and digital elevation map (a) map of eTh; ophiolite limit indicated in black line; (b) map of eU; (c) map of K; (d) digital terrain elevation of study area; red region corresponds to higher elevations; blue lines are rivers.

Metagabbro outcrops are scattered, restricting their identification with aerogammaspectrometry. Massive metagabbros mapped in the Cambaizinho region are NNE-trending and 1 km-long and, 10 m wide, fine to medium-grained. These bodies are confined to the eastern portion of the ophiolite, intercalated with undifferentiated ortho- and paragneiss. Another significant, massive metagabbro occurrence is in the south-southwestern portion of the Palma Ophiolite and is 3.2 km long and 3.5 km wide, coarse-grained and foliated (Fig. 4a). Centimetric mafic minerals occur in the felsic matrix, some with sinistral kinematic indication (Fig. 4b). This unit is in contact with the intrusive post-tectonic Santa Rita Granite in the west and south, with serpentinites from the Palma Ophiolite in the east and south and covered by sediments from the Paraná Basin in the north. Geological contacts are covered in both metagabbros.

In the eastern portion of the Palma Ophiolite, a 13 km long x 1 km wide (NNE-SSW), dominantly mafic-ultramafic body was mapped and called Palma Leste

Ophiolite. The identified rocks include serpentinite, mafic schist and amphibolite. The set of rocks was obducted onto volcanosedimentary rocks, disrupted internally, with chaotic native serpentinite blocks mixed in a pervasive deformed matrix (Fig. 4c, d). We mention "broken to dismembered rocks" (broken formation, *sensu* Hsü, 1968; dismembered formation, *sensu* Raymond, 1984) for this rock because the serpentinites have mostly serpentinite blocks, representing the intraformational equivalent of mélange. Schistose chloritite occurs as blocks (0.5 x 2.0 m) in the serpentinite broken rocks (Fig. 4e), composed by chlorite and euhedral magnetite (up to 1 cm large).
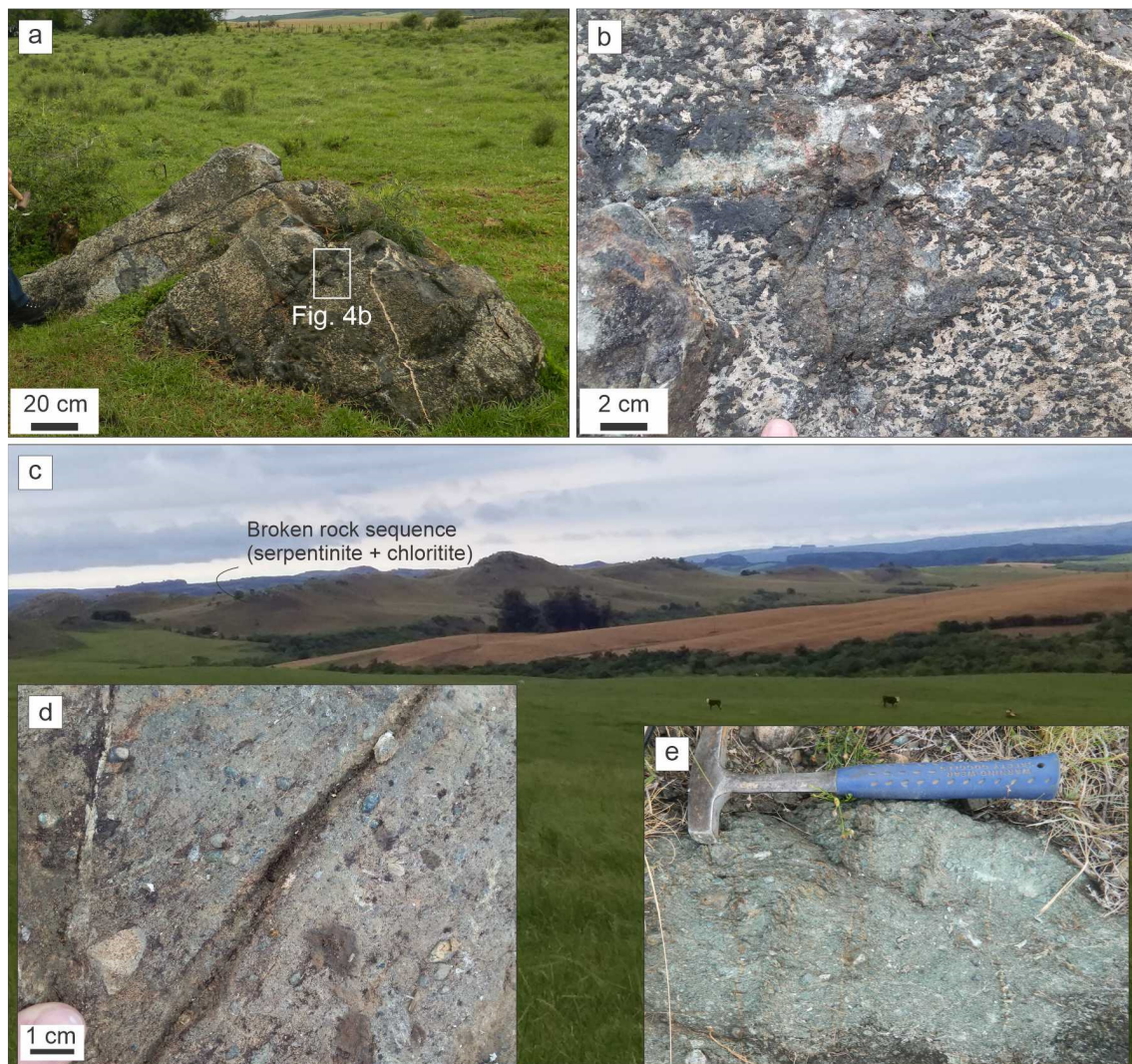
Fig. 4. Selected studied outcrops. (a, b) Palma region, São Luís metagabbro; in (b) mafic aggregates indicating sinistral sense of shear. (c, d, e) Palma Leste region, serpentinite broken in disrupted rock sequence highlighted in topography; (d) detail of broken and disrupted rock; (e) chloritite block in broken to disrupted rock showing schistosity.

4.2. Mineral description

Metagabbro sample 62 from the Cambaizinho region is fine-grained, with granular isotropic texture, containing hornblende (50 vol.%), plagioclase (49%) and rutile (1%), accessory zircon and secondary chlorite and sericite. Two populations of hornblende with different sizes are observed. Hornblende 1 (Hbl1) is clustered in fine crystals in the matrix and has rutile inclusions; some portions are chloritized (Fig. 5a). Poikiloblastic hornblende crystals (Hbl2) range in length between 0.5 and 1.2 cm, with 3:1 to 5:1 aspect ratio, free of inclusions. The borders of plagioclase crystals are irregular, with rutile inclusions; crystals are partly sericitized in cores and along cleavages. Rutile is included in plagioclase and Hbl2, varying in size from 50 to 500 µm (Fig. 5b).

Metagabbro São Luís sample 139 is from the Palma region, medium to coarse grained with granular isotropic texture. The rock comprises hornblende (50 vol.%), plagioclase (45%), magnetite (4%), biotite (1%), accessory zircon and secondary sericite and chlorite. Similar to the Cambaizinho metagabbro, the São Luís metagabbro has two hornblende generations (Fig. 5c, d). Both Hbl1 and Hbl2 are poikiloblastic, varying in size between 0.1 and 1.0 cm. Hbl1 is light brown in parallel nicols, while Hbl2 is medium green. Magnetite occurs included in both hornblende generations and also in plagioclase. Plagioclase is strongly sericitized.

The chloritite shows faint schistosity, dipping to the northeast (N330º/45º to 60º), concordant with the broken to dismembered host rock, grey colored, fine-grained. The sample shows an assemblage of green chlorite and magnetite, with minor talc and zircon. Chlorite occurs as fine-grained crystals in the matrix and as poikiloblastic crystals up to 0.5 cm (Fig. 5e, f).
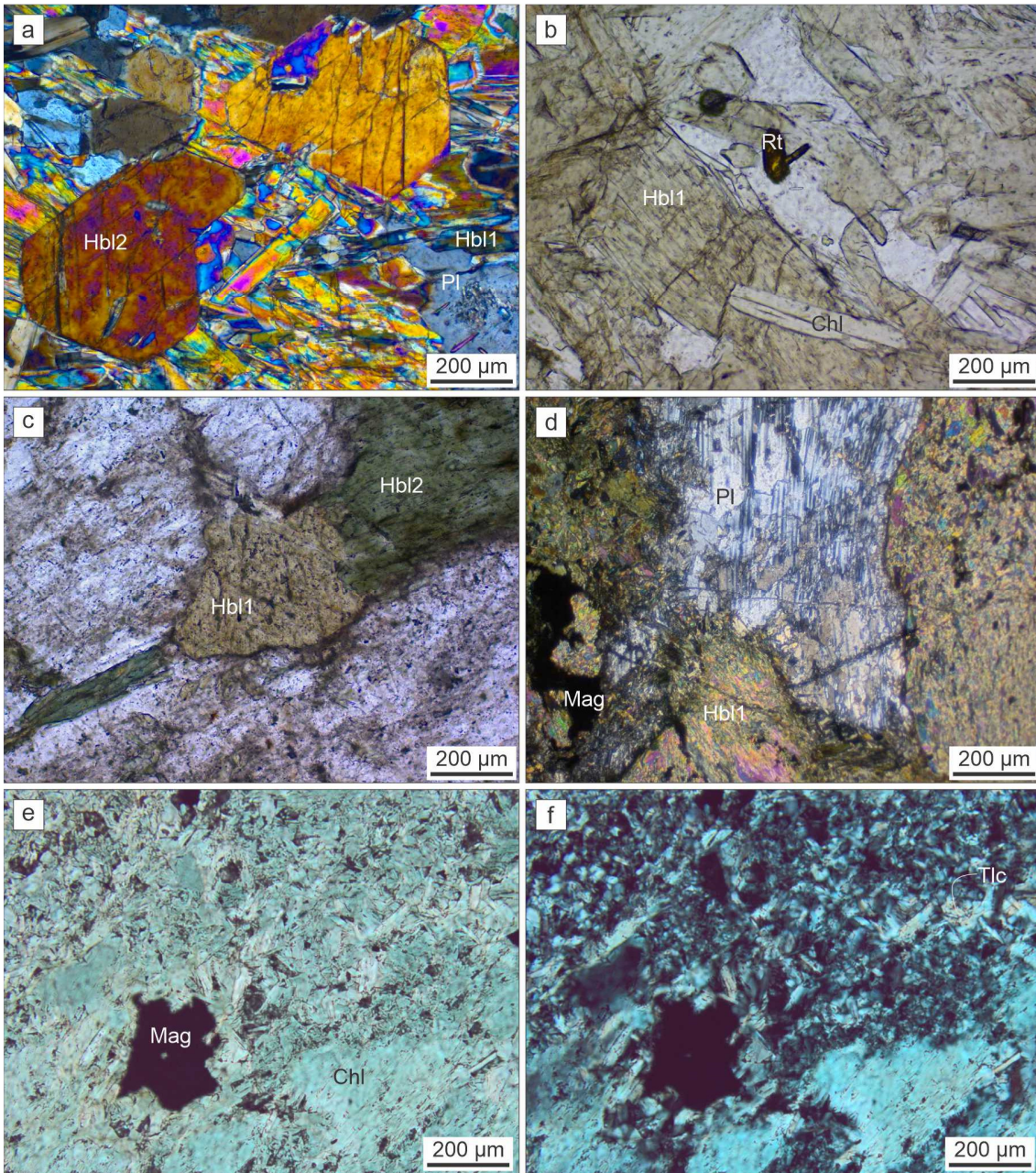
Fig. 5. Photomicrography images. (a, b) Cambaizinho metagabbro; (c, d) São Luís metagabbro; (e, f) Palma Leste chloritite. Mineral abbreviations from Whitney and Evans (2010).

4.3. Rutile U-Pb isotopes

Rutile from the Cambaizinho metagabbro is fine-grained, brown colored in plane polarized light and occurs in the matrix. BSE images of rutile crystals (Fig. 6) display anhedral shape, no internal contrast and ew quartz inclusions. Rutile U-Pb analyses (Supplementary File 2) yielded the intercept age of 706 ±11 Ma (Fig. 7); measured U contents vary from 0.42 to 2.32 ppm.
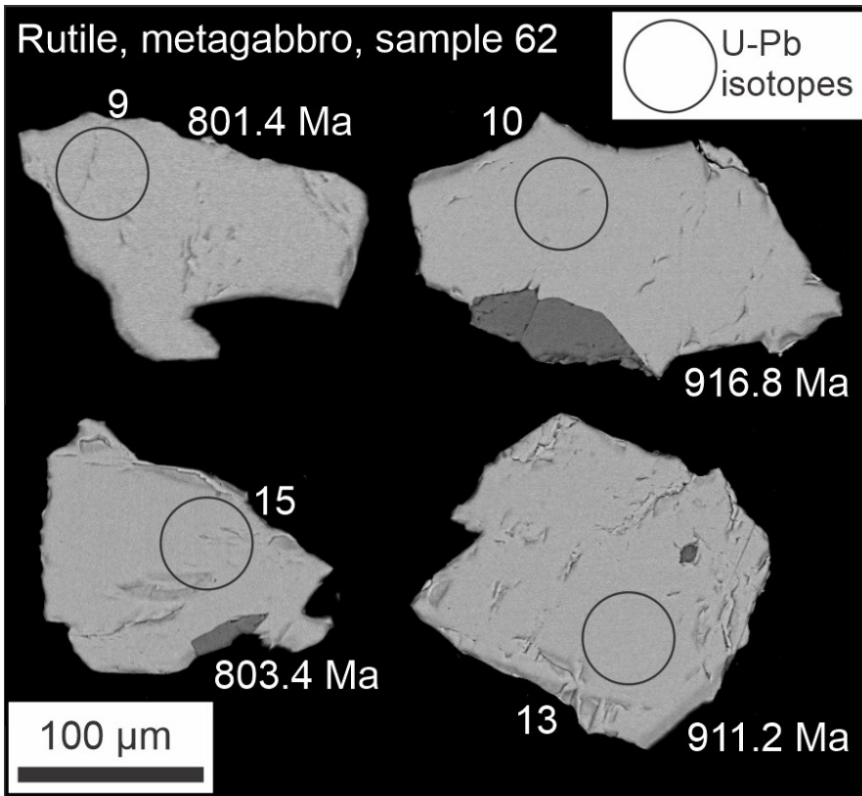
Fig. 6. Selected backscattered electron images of rutile from Cambaizinho metagabbro showing analyzed spots and individual $^{206}Pb/^{238}U$ ages.
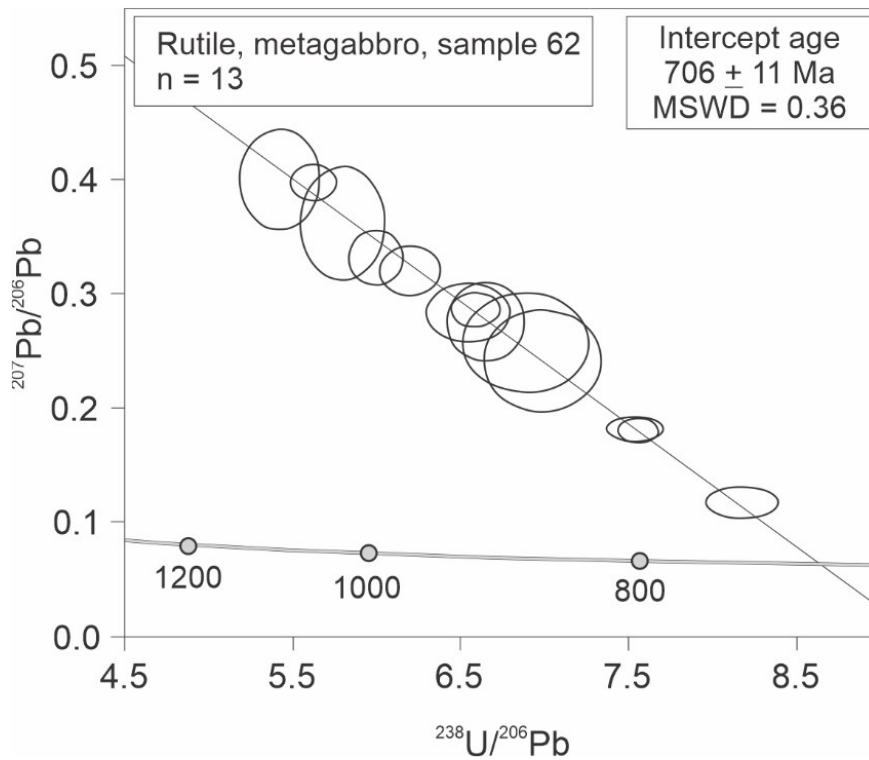
Fig. 7. Tera-Wasserburg inverse Concordia diagram for rutile from the Cambaizinho metagabbro showing intercept age. Data-point error ellipses are 2σ.

4.4. Zircon U-Pb geochronology

Zircon crystals from the Palma metagabbro are prismatic (Fig. 8a) with 50-500 µm in length (aspect ratio 2:1 to 1:1), displaying patchy and oscillatory zoning and mean Th/U of 0.47. Selected isotopic U-Pb data (Supplementary File 2) yielded a Concordia age of 731.6 ±0.5 Ma (Fig. 9a). One younger spot indicates apparent common Pb loss, and six spots are discordant exhibiting a common lead contamination trend (Fig. 9b).
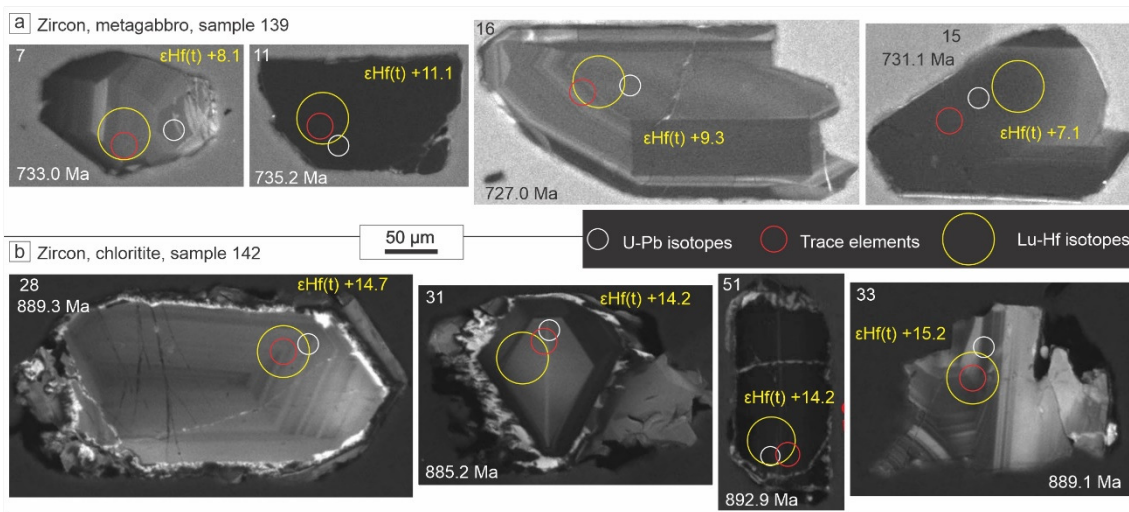
Fig. 8. Selected CL images of zircon from (a) São Luís metagabbro; (b) Palma Leste chloritite showing analyzed spots with concordant U-Pb ages in yellow circles, εHf(t) in red circles and trace elements in white circles.

Palma chloritite has prismatic zircon grains, that range in length between 50 µm and 300 µm, with 2:1 aspect ratio. In CL images (Fig. 8b), zircon shows fractures, euhedrally zoned cores, oscillatory luminescence, sector zoning and light-colored overgrowths. By applying a 10% discordant filter, the accepted concordia age of 889.2 ±4.8 Ma (Th/U = 0.17-0.43) was obtained for 13 out of 56 data points and correspond to zircon crystallization (Fig. 9c; Supplementary File 2). Among the rejected data, 4 analyzed points were obtained in rim portions of zircons and show a trend towards younger ages; 1 zircon crystal yielded an older age and 38 are discordant plotting above a common lead contamination trend (Fig. 9d).
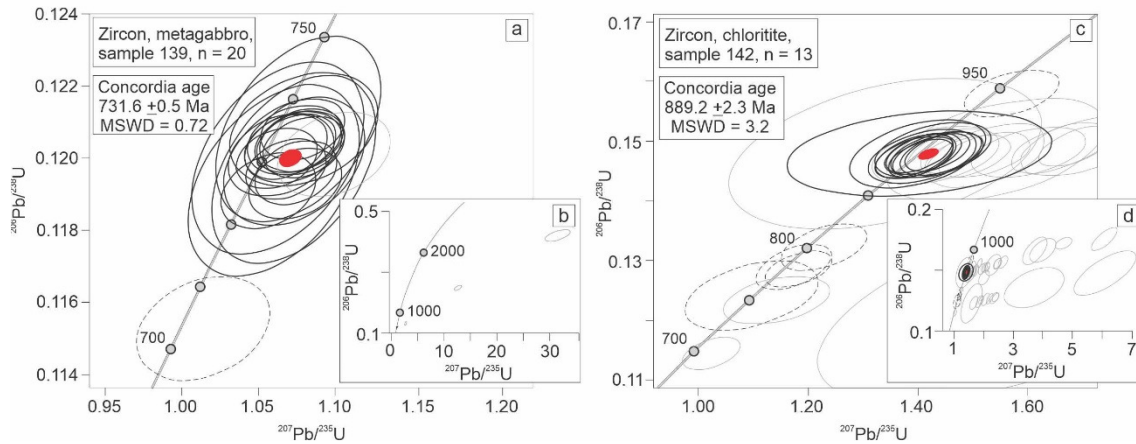
Fig. 9. U-Pb Concordia diagram for zircon from (a) São Luiz metagabbro and (b) Palma Leste chloritite. Data-point error ellipses are 2σ. Dotted and gray line ellipses not included in the average.

4.5. Zircon Lu-Hf isotope composition

Lu-Hf isotopic analyses in selected, concordant U-Pb dated zircons (Fig. 10) are provided in Supplementary File 3. Analyses of Lu-Hf isotopes were carried out in 19 zircons from the São Luís metagabbro (sample 139) and 22 zircons from the Palma chloritite (sample 142). The São Luís metagabbro $^{176}Hf/^{177}Hf$ ratios vary from 0.282524 to 0.282634, and $\varepsilon Hf_{(t)}$ = +7.1 to +11.1. Results from chloritite zircons have a $^{176}Hf/^{177}Hf$ range between 0.282613 and 0.282743, more radiogenic than the São Luís metagabbro; the $\varepsilon Hf_{(t)}$ = +9.9 to +17.5, a higher positive interval than sample 139.
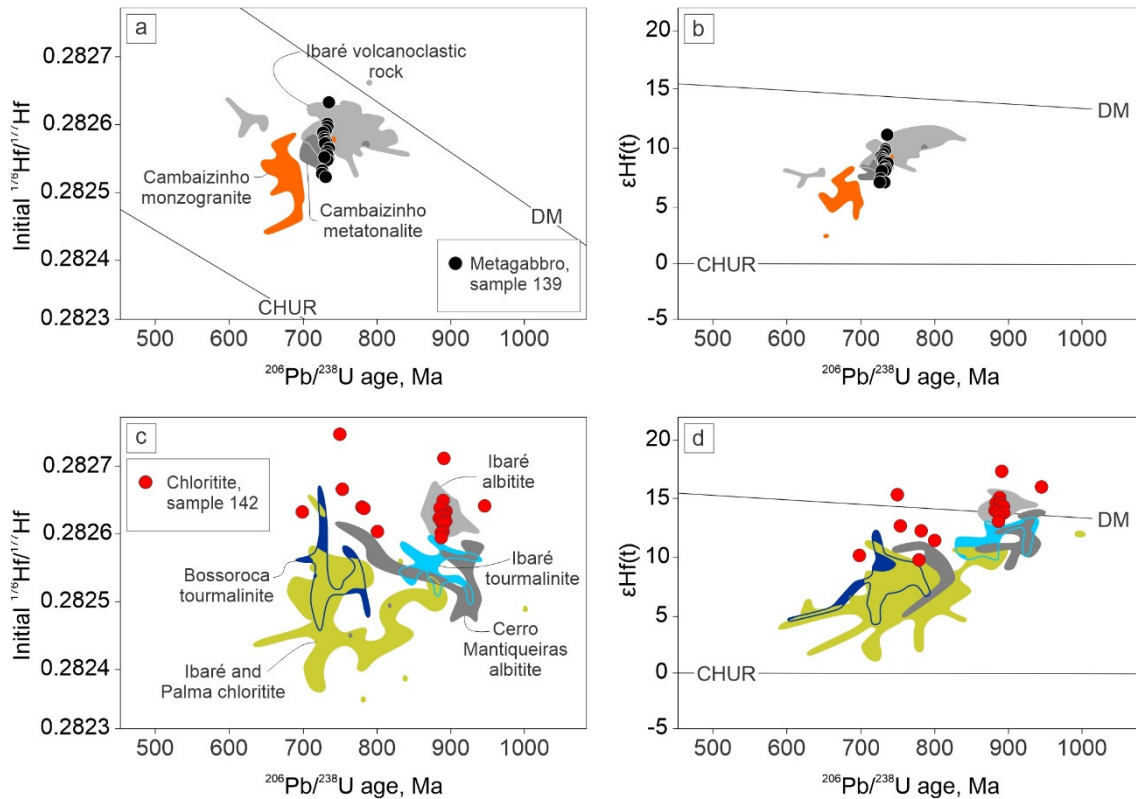
Fig. 10. Initial ^{176}Hf/^{177}Hf and εHf values plotted against U-Pb ages for zircon grains from (a, b) São Luís metagabbro and (c, d) Palma Leste chloritite. Crustal evolution limits were projected to the depleted mantle curve using the Lu/Hf ratio of average crust (0.015; Griffin *et al.*, 2004). CHUR = chondritic uniform reservoir, DM = depleted mantle.

4.6. Trace element composition

The trace element composition of the studied zircon crystals is presented in Supplementary File 4. The chondritic-normalized REE patterns (Sun and McDonough, 1989) are shown in the plots for the São Luís metagabbro and the Palma Leste chloritite samples (Fig. 11). The São Luís metagabbro zircon has moderate to high REE contents (ΣREE = 437.47 to 2762.09 ppm), with enrichment distribution of MREE to HREE compared to the more scattered LREE. Low to moderate negative Eu [(Eu/Eu*)$_N$ = 0.17 - 0.52) and positive Ce anomalies are observed. Zircon crystals from the Palma Leste chloritite have low to moderate REE contents (ΣREE = 140.23 to 1561.77 ppm), with enrichment of MREE to HREE compared to LREE, showing positive Ce anomalies.

We also present trace element data obtained in zircon crystals from metatonalite (sample 114) and monzogranite (sample 115) sampled in the Cambaizinho region. Trace elements were analyzed in the same zircon grainss previously dated by Cerva-

Alves *et al.* (2020). The data display U/Yb values ranging between 0.73 and 4.54 for São Luís metagabbro (sample 139), 0.35-0.95 for Cambaizinho metatonalite, 0.16-1.05 for Cambaizinho monzogranite and 0.03-0.26 for Palma Leste chloritite (sample 142). Positive correlation between U and Yb is observed in samples 139, 115 and 142 (Fig. 12).
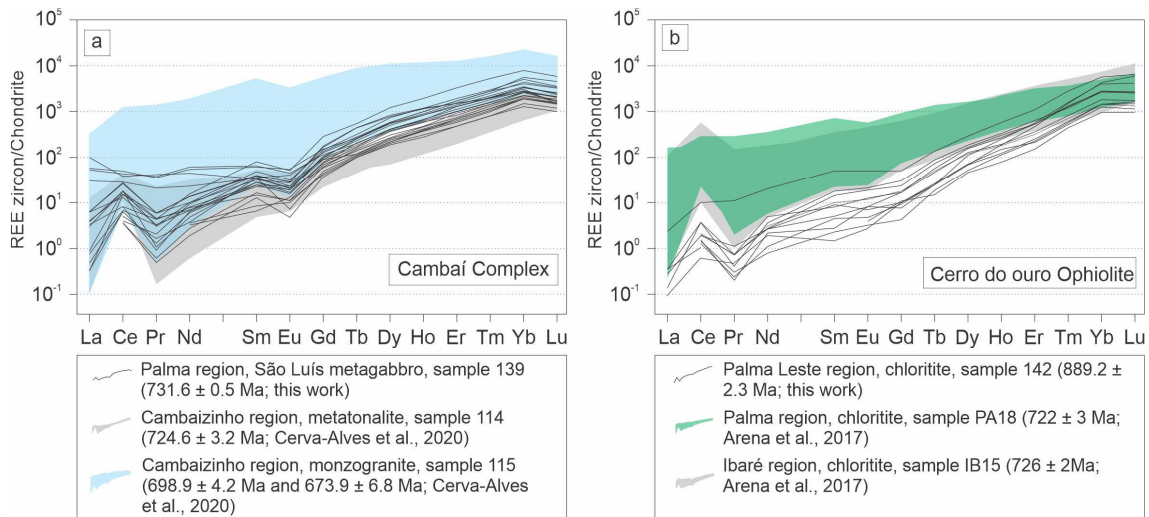
Fig. 11. Chondrite-normalized REE for plutonic and metasomatic zircon (Sun and McDonough, 1989).
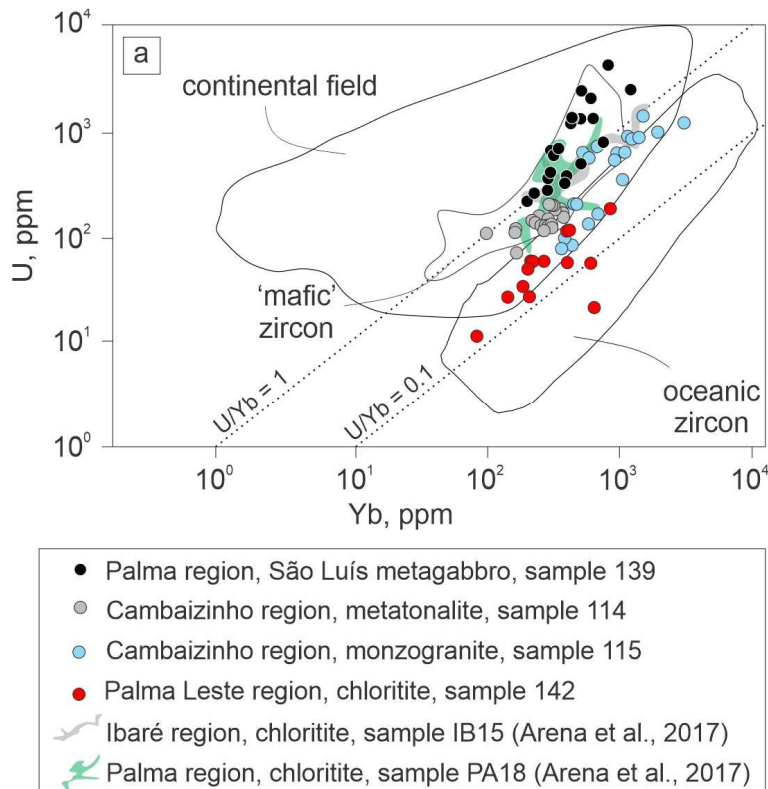
Fig. 12. U-Yb diagram for - modern zircon. Discriminant fields from Grimes *et al.* (2007).

5. Discussion

The application of aerogammaspectrometry and field survey integrated with isotopic determinations of rutile (U-Pb) and zircon (U-Pb, Lu-Hf, also trace elements), provided a robust data set. The results are here interpreted in an integrated discussion of the tectonic evolution of the São Gabriel Terrane and implications for Rodinia break-up and Gondwana assembly.

5.1. Aerogammaspectrometry and field survey interpretation

The geological complexity of Neoproterozoic terranes, including island-arc units and ophiolites, occurs due to processes related to the Brasiliano orogeny (e.g., Hartmann *et al.*, 2015). The application of aerogammaspectrometry to distinguish ophiolitic rocks in these terranes is an efficient tool, considering the lower content of radioactive minerals in mafic and ultramafic rocks when compared with granitoid rocks. However, in some cases, ophiolitic bodies are not detectable in the airborne scale, leading to complementary mapping of the Cambaizinho and Palma regions. In the total gamma-ray-intensity image of the studied regions (Fig. 2b), we interpret the lower values as resulting from an exposition of the Palma, Passo do Ivo and Cambaizinho ophiolites. Similar behavior is observed in eTh, eU and K (Fig. 3b, c, d), and is better discernible in the eTh and K images. The higher-cps domains in the aerogammaspectrometric images correspond to post-tectonic granites. Rocks from the São Gabriel arc show intermediate aerogammaspectrometric values.

The distribution and limits of domains delimited by their radiometric signal are mostly different from the mapped domains (e.g., Hartmann *et al.*, 2015), but some are similar. This is because of the diversity of rocks with different properties and extensions. The inconsistences may be due to erosional transport of radioactive minerals and blurring of contacts.

5.2. Rutile and zircon U-Pb isotopes

The study of U-Pb isotopes in rutile from metagabbro and zircon from metagabbro and chloritite led to dating and characterization of three main geological events: (1) metamorphic, (2) magmatic and (3) metasomatic. The metamorphic age of the bodies in the Cambaizinho region is positioned at ca. 721 Ma from bulk garnet U-Pb isotopes in a metasedimentary rock (staurolite-garnet schist; Cerva-Alves *et al.*, 2021). Thus,

we interpret the rutile age of 706 ±11 Ma from this work, albeit slightly younger. This age overlaps with ~700 Ma metamorphic event recognized in the São Gabriel Terrane (Leite *et al.*, 1998; Remus *et al.*, 1999; Hartmann *et al.*, 2000; Saalmann *et al.*, 2005a, 2005b, 2006). Considering the closure temperature for U-Pb diffusion in rutile (430to ~630 ºC; Mezger *et al.*, 1991; Vry and Baker, 2006) and garnet (~425-500 to >800 ºC; Mezger *et al.*, 1991;), rutile yields usually younger ages than garnet (Mezger *et al.*, 1991), and this is in accordance with our results. The 706 ±11 Ma is interpreted therefore as the cooling age related to the 721 ±14 Ma metamorphism registered by garnet bulk growth. This technique was used in the dating of metamorphic ages in other complexly deformed terranes (Millonig *et al.*, 2020; Schannor *et al.*, 2021). Muscovite and white mica were dated using K-Ar and yielded ages from 757.7 ±11.4 Ma to 743.5 ±10.2 Ma for metamorphism (Hueck *et al.*, 2020). We consider these ages as corresponding to deformation events during arc evolution.

The Concordia age of 731.6 ±0.5 Ma for São Luís metagabbro zircon is interpreted as emplacement and crystallization in the São Gabriel arc. Previous published U-Pb results on zircon and other accessory minerals (e.g., Leite *et al.*, 1998; Cerva-Alves *et al.*, 2020) were integrated with our results to define tectonic activity, lasting 205 Ma. In this period, two island arcs were built named Passinho (879 ±14 Ma; Leite *et al.*, 1998) and São Gabriel (794-674 Ma; Vedana *et al.*, 2018; Cerva-Alves *et al.*, 2020; Siviero *et al.*, 2021). A range of 920-840 Ma (modal maximum peak at 842 ±5 Ma) obtained by zircon from metavolcaniclastic rocks from the Campestre Formation (Hartmann *et al.*, 2021) is the missing link between the Passinho and São Gabriel arcs, corresponding to continuous arc construction. The interpretation of a continuous arc along time is corroborated by detrital zircon U-Pb ages with depleted mantle signature obtained in the Serrinha Formation (710-817 Ma; Cerva-Alves *et al.*, 2020) and Ibaré Complex (703-1033 Ma; Arena *et al.*, 2017) , which indicates a continued activity of the arc, with continuous apport of sediments.

Metasomatic events occur during serpentinization of the mantle peridotite in the mid-ocean ridge and are evidence of transport of significant materials dissolved in fluids, causing rock alteration. The generation of albitite, rodingite and chloritite is an example of metasomatism (Ague, 2003; Penniston-Dorland & Ferry, 2008; Bach *et al.*, 2013; Arena *et al.*, 2016). The metasomatism of ultramafic rocks in ophiolites was described in the São Gabriel arc as starting in the early Tonian (Arena *et al.*, 2016, 2017). For the presently studied chloritite, the Concordia age of 889.2 ±2.3 Ma yields

the age of metasomatism in the oceanic crust. The schistosity observed in the chloritite corroborates with the interpretation that this metassomatite was formed in the oceanic crust and the whole sequence was thrusted into the island arc superstructure. This understanding was similarly achieved for the Ibaré Ophiolite, where coeval ages were obtained by U-Pb in zircon from albitite (890 Ma; Arena *et al.*, 2016) and chloritite (880 Ma; Arena *et al.*, 2017).

5.3. Zircon Hf isotopes and trace elements

The Hf isotopic signature present during the zircon crystallization is preserved even under high grade metamorphic events, due to the high blocking temperature (~1,100 ºC) of Hf loss in zircon, about 200 ºC higher than Pb (Choi *et al.*, 2006; Alves *et al.*, 2019). Positive $\varepsilon Hf_{(t)}$ and $^{176}Hf/^{177}Hf$ ratios for the metagabbro ($\varepsilon Hf_{(t)}$ = +7.1 to +11.1; $^{176}Hf/^{177}Hf$ = 0.282524 to 0.282634) and chloritite ($\varepsilon Hf_{(t)}$ = +9.9 to +17.5; $^{176}Hf/^{177}Hf$ = 0.282613 to 0.282743) in the analyzed zircon are consistent with an exclusively depleted mantle source relative to the chondritic uniform reservoir (CHUR). Similar $^{176}Hf/^{177}Hf$ interval and positive $\varepsilon Hf_{(t)}$ signature is also observed in zircon crystals from rocks belonging to the São Gabriel arc (Fig. 10a, b) and Cerro do Ouro Ophiolite (Fig. 10c, d). The arc units with available Hf data include plutonic rocks from the Cambaizinho region, metatonalite (sample 114; Cerva-Alves *et al.*, 2020) and Sanga do Jobim monzogranite (sample 115; Cerva-Alves *et al.*, 2020), and a volcanic unit from the Ibaré Complex (sample IB1; Arena *et al.*, 2017). The subtle decrease in εHf(t) in the younger Sanga do Jobim Suite is interpreted as a first indicative of environmental change at the beginning of continentalization, in accordance with Saalmann *et al.* (2011), Lena *et al.* (2014) and Cerva-Alves *et al.* (2020). In samples from the Cerro do Ouro Ophiolite, similar intervals of $^{176}Hf/^{177}Hf$ ratios and εHf(t) were observed between Palma Leste chloritite (this study) and Ibaré albitite (Arena *et al.*, 2016).

One striking feature of the REE distribution in both studied samples is the enrichment in heavy REE, indicating crystallization in the absence of a heavy REE-enriched phase. The positive slope from La to Lu, together with negative Eu and positive Ce anomalies is common in zircon crystals from rocks sampled in the São Gabriel arc (Fig. 11a), and common in igneous zircon (Whitehouse, 2003) including magmatic oceanic crust zircon (Grimes *et al.*, 2009). On the other hand, metasomatic zircon from chloritites in the Cerro do Ouro Ophiolite (Fig. 11b) show similar behavior,

but with absence of negative Eu anomaly. This characteristic is due to lack of plagioclase, considered an important collector of Eu in magmatic systems (e.g, Dunn and Sen, 1994), maintaining the melt with high Eu contents during zircon saturation. LREE and MREE concentrations in chloritite zircon crystals are substantially higher in Palma and Ibaré ophiolites (Fig. 11b) when compared to the Palma Leste Ophiolite, leading us to interpret a more primitive depleted mantle source for the crystallization of the Palma Leste chloritite zircon. This interpretation is validated by positive εHf values.

The diagram considering U/Yb ratios in zircon proposed by Grimes *et al.* (2007) is a robust tool to discriminate mid-ocean ridge and continental crustal igneous rocks. We observed that in the studied zircon grains from the São Gabriel arc, the U-Yb signature has a trend towards the lower limit of the continental zircon field; most values from the São Luís metagabbro (Palma) and Cambaizinho metatonalite plot in the 'mafic' field (Fig. 12). This is consistent with magmas generated by partial melting of older juvenile island arc crust (e.g., arc granitoids in the Egyptian Nubian Shield; Dessouky *et al.*, 2021); or in intermediate magmatic settings between mid-ocean ridge and continental settings with U/Yb = 0.1 – 1.0 (Grimes *et al.*, 2015). In subduction-related rocks, U/Yb values plot higher in the diagram (Grimes *et al.*, 2015). This behavior is observed in the São Luís metagabbro zircon, with highest U/Yb values compared with the other results. Thus, the high U/Yb ratio can be explained by contamination either by recycled crustal components or by competition from minerals that fractionated Nb from U (e.g., titanite or ilmenite; Grimes *et al.*, 2015). The Palma Leste chloritite zircon plot in U/Yb diagram in the oceanic zircon field (Fig. 12).

5.4. Tectonic implications

The geological evolution of the São Gabriel Terrane is here constrained by aerogammaspectrometry, geochemical and geochronological studies of the main units of the São Gabriel arc and Cerro do Ouro Ophiolite. Rocks from the São Gabriel Arc, including the plutonic Cambaí Complex, are interpreted as a continental margin arc (Philipp *et al.*, 2018; Hueck *et al.*, 2020) or oceanic island arc (Cerva-Alves *et al.*, 2020; Siviero *et al.*, 2021). One phase of the island arc-continent collision is now constrained by the metamorphic rutile U-Pb age of the Cambaizinho metagabbro from the São Gabriel arc infrastructure. This is 706 ±11 Ma and establishes a continuity for metamorphism in the region, with peak age determined through garnet bulk growth at 721 ±14 Ma (Cerva-Alves *et al.*, 2021). The accretionary event was identified in

metasomatic zircon from Palma and Ibaré at 722-726 Ma (Arena *et al.*, 2017). The 731.6 ±0.5 Ma crystallization age for the São Luís metagabbro is consistent with plutonic activity registered in the São Gabriel arc (ca. 794-674 Ma; Vedana *et al.*, 2018; Cerva-Alves *et al.*, 2020). A hybrid Hf isotope signature is expected for continental magmatic arcs due to interaction between depleted juvenile magmas and enriched components formed by melting of crustal rocks (Pitombeira *et al.*, 2021). The $\varepsilon Hf_{(t)}$ signature of the São Luís metagabbro zircon ranges between +7.1 and +11.1, indicating an island-arc signature. This range led us to discard a continental margin arc environment. The 889.2 ±2.3 Ma age and $\varepsilon Hf_{(t)}$ signature (+9.9 to +17.5) provided by metasomatic zircon from the Palma Leste chloritite (sample 142) are in accordance with the 892-880 Ma metasomatic event, interpreted to represent the age of metasomatism in the mid-ocean ridge (Arena *et al.*, 2016, 2017).

In the early Brasiliano Orogeny, the 706 ±11 Ma age of metamorphism corresponds to a continuous 726-706 Ma (Arena *et al.*, 2017; Cerva-Alves *et al.*, 2020; this work) collision and thrusting of the São Gabriel arc + ophiolite against and over the Rio de La Plata Craton. This thrusting occurred at the beginning of formation of the Dom Feliciano Belt. In the Brasiliano Orogen, ophiolites were emplaced in both oceanic island arcs and continental arcs (e.g., Peixoto *et al.*, 2017; Caxito *et al.*, 2021) and accretionary edges (Amaral *et al.*, 2020). Ophiolites are also emplaced in fold and thrust belts registered in the Dom Feliciano belt (722 Ma; Arena *et al.*, 2018), Araguaia belt (708 Ma; Souza *et al.*, 2019), Brasília belt (760 Ma; Brown *et al.*, 2020), and Riacho do Pontal fold belt, Borborema Province (630 Ma; Caxito *et al.*, 2014). Juvenile magmatism at 731.6 ±0.5 Ma (U-Pb zircon age; this work) was active during the Tonian-Cryogenian in the São Gabriel arc. Juvenile magmatism was also recognized in the Brasília Belt (863-630 Ma, Goiás arc; Pimentel *et al.*, 2000) and in the Ribeira Belt (859-836 Ma, Serra da Prata arc; 790-620 Ma, Rio Negro arc; Peixoto *et al.*, 2017; Santiago *et al.*, 2020). Isotopic (U-Pb-Hf) studies developed in metasedimentary rocks from the Araçuaí Belt (Schannor *et al.*, 2019) indicate a source from a juvenile arc or oceanic crust coeval with the São Gabriel arc. Tonian-Cryogenian geological activity related to ophiolite and arc domains was observed in both NE Brazil and NW Africa (Caxito *et al.*, 2020). Neoproterozoic geological activity and similar evolution is also observed in the Arabian-Nubian Shield, where a prolonged process involved juvenile crust generation (870-630 Ma) and later collision to form composite terranes (Kröner and Stern, 2005). In the Anti-Atlas orogenic belt, Neoproterozoic Sirwa and Bou Azzer

Ophiolites (762-759 Ma; Samson *et al.*, 2004) thrusting over fragments of intra-oceanic arc system (760-740 Ma and 735-725 Ma; Thomas *et al.*, 2002; Triantafyllou *et al.*, 2016; 2020; Hodel *et al.*, 2020). The ~889 Ma metasomatic age registers one point in Rodinia break-up evolution. Island arc activity followed by collision and thrusting events here recognized are spread along the Brasiliano Orogen and related to Gondwana assembly.

6. Conclusions

Tonian-Cryogenian evolution of juvenile terranes in the South Atlantic Brasiliano Orogen included metamorphic, magmatic and metasomatic events in the São Gabriel Terrane. Palma and Cambaizinho ophiolites are units obducted into the Tonian São Gabriel island arc. A protracted metamorphic event occurred until at least 706 Ma as delimited in rutile of a metagabbro. Magmatism related to the island arc was active at 731 Ma, with crystallization of zircon in metagabbro. Ophiolites document metasomatism at mid-ocean ridge at 889 Ma, through zircon crystallization in chloritites. Hf isotopic data in zircon indicate the juvenile character, derivation from a depleted mantle source. The timing and setting of formation of igneous (metagabbro) and metamorphic (metasomatic chloritite) rocks are constrained and characterized. We thus establish an advance in the knowledge of processes involving Rodinia break-up with proto-Adamastor oceanic crust formation, associated to the São Gabriel island arc construction. Collision and thrusting of the juvenile terrane over the Rio de La Plata Craton in better delimited within the South Atlantic Brasiliano Orogen and formation of Gondwana.

Supplementary data

Supplementary data to this article can be found online at https://doi.org/10.1016/j.jsames.2021.103505.

Supplementary File 1. Descriptions of analytical methods.

A.1. Aerogeophysics

The airborne geophysical survey used in this paper was available by Geological Survey of Brazil (CPRM, 2010). The data acquisition methodology is disponible in Hartmann *et al.* (2016) and include aerogammaspectrometry obtained along the Brazilian territory. We selected the proper scale and produced maps of the U, eTh, eU, K-Th-U, total magnetic field and total count analytical signal to interpret the geological evolution adding the perspective of geophysics. Regional and detailed geological maps (e.g., Jost and Hartmann, 1984; Remus, 1990; Laux, 2017) were integrated with aerogammaspectrometry (CPRM, 2010). We used the digital terrain elevation (Fig. 3a), total count gamma-ray-intensity (Fig. 2b), eTh content (Fig. 3b), eU content (Fig. 3c) and K content (Fig. 3d). The study area presents varied relief (Fig. 3a); the highest elevation is near 350 m above sea level (a.s.l.). The high elevation observed in the south is underlain by the post tectonic Jaguari Granite, whereas the elevation in the east is associated with volcanic units from the Camaquã Basin. The northern strip of Figure 3a corresponds to the Paraná Basin, where altitudes are below 140 m a.s.l.

A.2. Rutile U-Pb dating analyses

Rutile grains were separated using crush, jaw and hand-picked, mounted in epoxy resin and polished at the Instituto de Geociências laboratories, Universidade Federal do Rio Grande do Sul (IGeo, UFRGS). Fractures and internal textures were revealed with backscattered electron (BSE) images obtained with a ZEISS EVO MA10 conventional scanning electron microscope fitted with tungsten filament, operating at voltages of 0.2–20 kV at Centro de Estudos em Petrologia e Geoquímica, Instituto de Geociências, UFRGS. Rutile laser-ablation inductively coupled plasma mass spectrometry (LA-ICP-MS) U-Pb dating was determined in 13 rutile grains, with a Thermo-Fisher Element II sector field ICPMS 193 nm Photon Machines Arf Excimer laser at Isotopic Geochemistry Laboratory, Universidade Federal de Ouro Preto (IGL, UFOP). Fixed spot size of 50 μm was adopted with a laser energy density of ca. 2-3 J/cm^2 and repetition rates of 5 Hz. The rutile Antônio Pereira AP (average ID TIMS age

of 499.4 ± 0.5/0.6/0.8 Ma; Santos *et al.*, 2020) and rutile Diamantina DR2 (average ID TIMS age of 527.8 ± 1.1/1.2/1.3 Ma and 531.3 ± 1.8/1.9/2.1 Ma - variation detected by the TIMS technique only; Santos *et al.*, 2020) were used as standards to correct mass fractionations. Calculated $^{206}Pb/^{238}U$ weighted mean average ages for Antonio Pereira AP primary standard are within 1.2% accuracy of the reported ages. The use of ^{208}Pb to correct for Pbcm is discarded because the high Th concentrations and variable common-Pb (Pbcm) compositions. For this reason, screening the dataset with Th/U < 2 filter should also eliminate potential sources of non-rutile bonded Th. Pbcm corrections were applied either using ^{204}Pb- or the ^{208}Pb-based method.

A.3. Zircon U-Pb dating analyses

U-Pb LA-ICP-MS analyses of zircon (n = 84 crystals, one per crystal) from samples 139 (n = 28 analyses), 142 (n = 56 analyses) were undertaken at IGL, UFOP. The separating procedures were done in the UFRGS, and included crush, conventional magnetic and density separation methods. Zircon crystals were carried out, mounted in 25 mm-diameter epoxy resin and polished to half-section for Cathodo-luminescence (CL) images to define internal structures and inclusions. The analytical thecnique used a ThermoScientific Element 2 sector field (SF) ICP-MS coupled to a CETAC LSX-213 G2 + laser system. Calibration was performed employing the BB zircon standard (Santos *et al.*, 2017), with additional GJ-1 (Jackson *et al.* 2004) and Plešovice (Sláma *et al.*, 2008) standards. In sample 139, Concordia age was 598.2 ± 1.7 Ma (2σ in %, n = 10; MSWD = 1.19) for GJ-1 standard and 336.91 ± 0.65 Ma (2σ in %, n = 10; MSWD = 1.5) for Plešovice standard. In sample 142, Concordia age was 562.0 ± 2.0 Ma (2σ in %, n = 10; MSWD = 0.33) for BB standard and 338.9 ± 2.1 Ma (2σ in %, n = 24; MSWD = 0.24) for Plešovice standard. The equipment worked in standard high-sensitivity mode (STDS), with spot size set for 20 μm, laser energy of 15%, laser shot frequency of 10 Hz and shutter delay of 15 s. Methodology is detailed in Gerdes and Zeh (2006, 2009) and Lana *et al.* (2017). Glitter Data Reduction Software for laser ablation microprobe was initially used to on-line reduce data (Van Achterbergh *et al.*, 2001) and common Pb corrections were done with an in-house spreadsheet. Calculated ages and Concordia diagrams were done using IsoplotEx 4 (Ludwig, 2003). Errors are reported at the 2σ level.

A.4. Zircon Lu-Hf isotopic analyses

For the Lu and Hf isotopic measurements, the Thermo-Finnigan Neptune with a multicollector ICP-MS coupled to a Photon-Machines 193 nm laser system was used at IGL, UFOP. The static mode was set for data collect, during 60 s of ablation with a spot laser of 50 μm, fired at 5 Hz repetition rate and 3 J cm^{-2} energy density. Nitrogen (~0.080 l/min) was introduced into the Ar sample-carrier gas. The signal intensity was ca. 10 V for 180Hf. During the analysis step, the isotopes ^{172}Yb, ^{173}Yb and ^{175}Lu were simultaneously monitored to permit corrections of isobaric interferences of Lu and Yb isotopes on mass 176. The ^{176}Yb and ^{176}Lu were calculated using a ^{176}Yb/^{173}Yb of 0.796218 (Chu *et al.* 2002) and ^{176}Lu/^{175}Lu of 0.02658 (in-house value). Corrections for instrumental mass bias used an exponential law and ^{179}Hf/^{177}Hf value of 0.7325 (Patchett and Tatsumoto 1981) for correction of Hf isotopic ratios. Yb and Lu isotopic ratios were corrected using βHf of individual integration steps of each analysis divided by the average offset factor of the complete analytical session. For calibration, were used the standards BB, 560 Ma, 0.2816713±0.0000028 ^{176}Hf/^{177}Hf (Santos *et al.*, 2017); GJ-1, 602 Ma, 0.282000±0.000005 ^{176}Hf/^{177}Hf (Morel *et al.*, 2008) and Temora, 417 Ma, 0.282686 ±0.000007 ^{176}Hf/^{177}Hf (Woodhead *et al.*, 2005). The ^{176}Lu decay constant of 1.867×10^{-11} yr^{-1} was used for initial epsilon hafnium εHf(t) calculations (Söderlund *et al.*, 2004). The average MORB (DM) value of 0.03933 for ^{176}Lu/^{177}Lu, 0.283294 for ^{176}Hf/^{177}Hf (Blichert-Toft and Puchtel, 2010); 0.0113 for the average continental crust (Rudnick and Gao, 2003); the average Chondritic Uniform Reservoir (CHUR) of 0.0336 for ^{176}Lu/^{177}Hf, and 0.282785 for ^{176}Hf/^{177}Hf (Bouvier *et al.* 2008) were used.

A.5. Zircon trace elements

The composition of trace elements in zircon was obtained using the Thermo-Fisher Element II sector field ICP-MS coupled to a Photon Machines 193 nm ArF Excimer laser at IGL, UFOP. The laser produces spot sizes of 25 μm in diameter, during a period of 30 s at 10 Hz frequency, in 0.7 L/min He stream and a laser energy density of 10–12 J cm^{-2}. The procedure for data acquisition consisted of bracketing mode with 3 to 4 analyses of standards (NIST 612 and NIST 610) and 10-15 analyses in our sample. The data reduction followed Van Achterbergh *et al.* (2001) and Jackson *et al.* (2004) using the Glitter software (GEMOC Lase ICP-Ms Total Trace Element Reduction), the NIST 612 glass as primary standard, BCR and BHVO basaltic glasses as secondary standards (Schannor *et al.*, 2019). Error was derived from the averaged

counts for each mass for all the standards. REE concentrations were normalized to C1 chondrite (Sun and McDonough, 1989).

References

Blichert-Toft, J., Puchtel, I.S., 2010. Depleted mantle sources through time: evidence from Lu-Hf and Sm-Nd isotope systematics of Archean komatiites. Earth and Planetary Science Letters, 297 (3-4), 598-606.

Bouvier, A., Vervoort, J.D., Patchett, P.J., 2008. The Lu-Hf and Sm-Nd isotopic composition of CHUR: constraints from unequilibrated chondrites and implications for the bulk composition of terrestrial planets. Earth and Planetary Science Letters, 273 (1-2), 48-57.

CPRM – Serviço Geológico do Brasil., 2010. Projeto Aerogeofísico Escudo do Rio Grande do Sul. LASA PROSPECÇÕES S.A., Relatório Técnico, 260 p.

Gerdes, A., Zeh, A., 2006. Combined U-Pb and Hf isotope LA-(MC)-ICP-MS analyses of detrital zircons: comparison with SHRIMP and new constraints for the provenance and age of an Armorican metasediment in Central Germany. Earth and Planetary Science Letters, 249 (1-2), 47-61.

Gerdes, A., Zeh, A., 2009. Zircon formation versus zircon alteration d new insights from combined U-Pb and Lu-Hf in-situ LA-ICP-MS analyses, and consequences for the interpretation of Archean zircon from the Central Zone of the Limpopo Belt. Chemical Geology, 261 (3-4), 230-243.

Jackson, S.E., Pearson, N.J., Griffin, W.L., Belousova, E.A., 2004. The application of laser ablation inductively coupled plasma mass spectrometry to in situ U-Pb zircon geochronology. Chemical Geology, 211, 47-69.

Hartmann, L.A., Lopes, W.R., Savian, J.F., 2016. Integrated evaluation of the geology, aerogammaspectrometry and aeromagnetometry of the Sul-Riograndense Shield, southernmost Brazil. Annals of the Brazilian Academy of Sciences. Online version ISSN 1678-2690.

Lana, C., Farina, F., Gerdes, A., Alkmim, A., Gonçalves, G.O., Jardim, A.C., 2017. Characterization of zircon reference materials via high precision U-Pb LA-MC-ICPMS. Journal of Analytical Atomic Spectrometry, 32 (10), 2011-2023.

Ludwig, K.R., 2003. Isoplot/Ex Version 3.00: A Geochronological Tool kit for Microsoft Excel. Berkeley Geochronology Center, Berkely, CA. Special Publication 4, 71 (http://bgc.org/isoplot_etc/isoplot.html).

Morel, M.L.A., Nebel, O., Nebel-Jacobsen, Y.J., Miller, J.S., Vroon, P.Z., 2008. Hafnium isotope characterization of the Gj-1 zircon reference material by solution and laser ablation MC-ICPMS. Chemical Geology, 255, 231-235.

Patchett, P.J., Tatsumoto, M., 1981. A routine high-precision method for Lu-Hf isotope geochemistry and chronology. Contributions to Mineralogy and Petrology, 75, 263-267.

Rudnick, R.L., Gao, S., 2003. Composition of the continental crust. In: Rudnick, R.L. (Ed.), Treatise on Geochemistry. Elsevier-Pergamon, Oxford, 1-64.

Sláma, J., Kosler, J., Condon, D.J., Crowely, J.L., Gerdes, A., Hanchar, J.M., Horstwood, M.S.A., Morris, G.A., Nasdala, L., Norberg, N., Schaltegger, U., Schoene, B., Tubrett, M.N., Whitehouse, M.J., 2008. Plesovice zircon - a new natural reference material for U-Pb and Hf isotopic microanalysis. Chemical Geology, 249, 1-35.

Santos, M.M., Lana, C., Scholz, R., Buick, I.S., Kamo, S., Corfu, F., Queiroga, G., 2020. LA-ICP-MS U-Pb dating of rutiles associated with hydrothermal mineralization along the southern Araçuaí Belt, SE Brazil. Journal of South American Earth Sciences, 99, 102502.

Santos, M.M., Lana, C., Scholz, R., Buick, I., Schmitz, M.D., Kamo, S.L., Gerdes, A., Corfu, F., Tapster, S., Lancaster, P., Storey, C.D., Basei, M.A.S., Tohver, E., Alkmim, A., Nalini, H., Krambrock, K., Fantini, C., Wiedenbeck, M., 2017. A new appraisal of Sri Lankan BB zircon as a reference material for LA-ICP-MS U-Pb geochronology and Lu-Hf isotope tracing. Geostandards and Geoanalytical Research, 41 (3), 335-358.

Schannor, M., Lana, C., Fonseca, M.A., 2019. São Francisco-Congo Craton break-up delimited by U-Pb-Hf isotopes and trace-elements of zircon from metasediments of the Araçuaí Belt. Geoscience Frontiers, 10, 611-628.

Söderlund, U., Patchett, P.J., Vervoort, J.D., Isachsen, C.E., 2004. The ^{176}Lu decay constant determined by Lu-Hf and U-Pb isotope systematics of Precambrian mafic intrusions. Earth and Planetary Science Letters, 219 (3-4), 311-324.

Sun, S.S., McDonough, W.F., 1989. Chemical and isotopic systematics of oceanic basalts: implications for mantle composition and processes. In: Saunders, A.D., Norry, M. (Eds.), Magmatism in Ocean Basins, Geological Society of London, Special Publication, 42, 313-345.

Van Achterbergh, E., Ryan, C.G., Jackson, S.E., Griffin, W.L., 2001. Data reduction software for LA-ICP-MS. In: Sylvester, P.J. (Ed.), Laser Ablation-ICP Mass Spectrometry in the Earth Sciences: Principles and Applications. Mineralogical Association of Canada, Short Course, Ottawa, Ontario, 29, 239-243.

Woodhead, J.D., Hergt, J.M., 2005. A preliminary appraisal of seven natural zircon reference materials for in situ Hf isotope determination. Geostandards and Geoanalytical Research, 29, 183-195.

Supplementary File 2. Rutile and zircon U-Pb analyses.

PARTE1

Spot	U (ppm)	Th/U	Ages 207Pb/206Pb	2s	206Pb/238U	2s	207Pb/235U	2s
Cambaizinho region, rutile metagabbro, sample 62								
8	2.3	0.29	1896.30	67.40	743.77	15.08	1103.88	65.69
9	1.5	0.16	2627.01	40.76	801.42	9.60	1473.49	39.61
10	0.4	0.04	3353.33	76.02	916.82	26.72	1970.16	71.17
11	0.6	0.05	3722.65	114.31	1025.99	33.24	2294.17	109.37
12	0.7	0.06	3542.38	58.17	964.70	21.48	2126.98	54.06
13	0.6	0.05	3368.86	44.08	911.24	15.65	1973.23	41.20
14	0.6	0.05	3201.09	133.97	874.05	36.67	1841.76	128.85
15	0.8	0.05	2645.76	40.78	803.41	13.93	1484.45	38.32
16	1.2	0.08	3103.56	141.30	862.51	33.26	1777.18	137.32
17	0.5	0.03	3874.41	97.21	1091.20	35.78	2448.55	90.39
18	1.2	0.06	3307.63	97.00	903.30	23.82	1930.72	94.03
19	0.7	0.03	3865.29	40.86	1054.89	19.39	2409.02	35.97
20	0.6	0.03	3593.70	60.54	994.94	20.53	2186.95	56.95
Palma region, zircon metagabbro, sample 139								
7	150.8	0.36	770.85	44.05	733.04	4.14	742.43	11.44
8	684.2	0.29	766.89	42.16	735.22	4.00	743.10	10.95
9	211.3	0.34	764.48	49.06	732.06	4.67	740.09	12.72
10	9.1	4.21	3791.56	51.86	1428.00	34.67	2654.06	41.82
11	2113.6	0.64	761.03	77.85	735.22	12.12	741.63	21.55
12	27.4	0.41	2347.96	73.50	798.70	29.79	1336.99	44.22
13	1112.4	0.53	765.18	40.98	732.69	3.82	740.75	10.60
14	422.2	0.37	761.24	47.28	733.50	4.57	740.38	12.26
15	284.5	0.38	751.97	53.64	731.08	5.42	736.24	13.91
16	308.0	0.58	754.63	82.65	726.99	12.46	733.80	22.62
17	2860.9	1.22	764.54	40.29	729.01	3.92	737.79	10.43
18	788.7	0.47	746.77	41.45	730.79	3.93	734.73	10.65
19	255.8	0.32	673.20	59.47	726.48	6.11	713.57	14.95
20	266.6	0.45	752.43	48.29	725.50	4.96	732.12	12.49
27	419.6	0.49	733.72	71.36	703.69	6.82	710.89	18.02
28	898.7	0.28	753.81	41.88	732.41	4.26	737.70	10.86
30	3997.0	0.43	775.77	77.47	728.66	12.17	740.33	21.53
31	360.2	0.30	749.97	82.89	730.33	12.50	735.18	22.68
32	2.1	2.35	4366.07	72.36	2257.26	71.89	3533.87	62.94
33	740.1	0.43	771.17	42.09	733.33	4.03	742.73	10.94
34	382.8	0.42	784.55	46.28	726.30	4.61	740.72	12.09
35	573.8	0.66	1130.22	47.38	739.88	7.80	844.43	15.07
36	181.4	0.35	768.56	73.75	735.17	7.37	743.47	19.32
37	193.7	0.53	818.29	54.86	731.14	5.53	752.95	14.58
38	1875.8	0.43	776.81	40.62	732.46	4.03	743.48	10.61
39	570.8	0.57	779.78	40.70	728.15	4.20	740.94	10.65
40	186.3	0.41	771.69	69.46	730.10	8.41	740.41	18.51
Palma leste ophiolite, zircon chloritite, sample 142								
27	47.3	0.13	1024.37	76.54	889.01	16.53	928.77	26.18
28	24.4	0.18	797.38	334.84	889.29	58.54	863.36	106.09
29	14.5	0.19	890.66	280.14	889.41	32.77	889.77	86.70
30	59.4	0.34	1874.31	73.86	930.05	20.01	1258.39	34.33
31	186.0	0.21	904.81	60.58	885.19	14.67	890.82	20.43

Spot	U (ppm)	Th/U	Ages 207Pb/206Pb	2s	206Pb/238U	2s	207Pb/235U	2s
32	39.3	0.17	1928.10	77.83	765.23	24.11	1133.25	37.92
33	87.6	0.38	900.95	73.20	889.12	16.08	892.52	24.13
34	21.9	0.19	887.02	135.51	889.24	26.45	888.60	43.79
35	97.7	0.24	890.27	62.21	889.57	15.12	889.77	20.93
36	118.6	0.06	770.74	78.94	698.42	12.86	715.82	21.76
37	75.2	0.15	830.33	76.59	779.59	14.18	792.85	22.93
38	170.3	0.23	877.25	70.64	885.87	15.75	883.41	23.16
39	168.1	0.11	2036.10	55.42	767.81	19.85	1177.57	29.30
40	80.3	0.26	904.86	55.52	887.55	14.62	892.52	19.17
47	46.7	0.34	904.26	106.25	886.93	20.93	891.91	34.41
48	252.2	0.35	935.37	59.30	890.58	14.44	903.55	20.25
49	21.2	0.31	1770.54	149.89	925.25	39.66	1213.54	68.53
50	387.1	0.51	1992.73	75.41	938.58	22.87	1313.77	37.23
51	55.2	0.17	917.74	113.12	892.89	21.25	900.07	36.58
52	94.7	0.18	807.70	87.53	781.70	17.59	788.48	26.56
53	51.9	0.22	947.87	76.31	889.29	16.76	906.27	25.55
54	54.0	0.31	1272.83	91.31	899.39	23.23	1014.75	35.28
55	169.2	0.46	1227.42	72.52	897.04	19.37	998.14	27.90
56	325.8	0.62	2802.26	71.01	1023.95	21.48	1763.34	41.69
57	91.6	0.18	850.44	95.71	800.52	18.34	813.84	29.37
58	435.4	0.66	1257.62	49.94	898.10	15.57	1008.77	20.27
59	21.8	0.18	2586.28	128.81	990.75	44.13	1626.31	76.19
60	345.0	0.48	957.49	73.27	893.05	17.91	911.81	25.29
67	23.1	0.29	1649.97	120.68	866.34	27.45	1119.27	50.73
68	303.8	0.38	1358.57	57.37	933.17	16.75	1069.31	23.59
69	101.9	0.49	989.73	81.71	945.60	17.95	958.96	28.16
70	286.7	0.36	1614.47	76.57	911.94	18.04	1143.70	32.08
71	19.7	0.40	2473.84	118.36	988.71	50.96	1570.58	73.81
72	85.8	0.16	745.56	174.33	754.29	27.42	752.09	49.15
73	44.0	0.20	2191.62	57.72	774.10	16.14	1246.45	28.92
74	64.4	0.15	1885.31	61.02	932.17	18.81	1264.57	29.37
75	28.0	0.47	1493.45	85.87	905.89	20.08	1095.14	34.71
76	78.4	0.19	1634.57	53.48	917.09	16.01	1155.28	23.85
77	37.5	0.12	1508.45	295.57	745.63	75.94	966.11	124.97
78	52.0	0.48	844.32	133.59	749.64	18.94	773.84	38.09
79	82.2	0.22	887.32	78.73	886.88	16.99	887.00	25.74
80	38.2	0.43	939.96	89.09	888.51	17.66	903.39	29.17
87	326.6	0.28	1818.43	52.34	761.57	16.01	1088.74	24.50
88	54.4	0.24	1561.75	68.32	913.51	17.93	1125.68	28.87
89	108.2	0.23	1781.40	79.08	755.15	23.10	1069.25	36.24
90	171.6	0.41	2162.01	76.69	771.64	21.16	1231.86	38.15
91	27.1	0.22	951.09	124.77	889.35	22.16	907.25	40.44
92	26.3	0.24	2805.65	328.90	820.70	76.38	1570.76	196.21
93	16.1	1.12	3464.03	152.36	887.55	84.14	1987.58	130.60
94	99.3	0.19	1084.16	190.41	894.57	39.73	951.06	67.30
95	271.9	0.77	1068.33	102.97	889.91	24.08	942.76	36.56
96	94.0	0.41	3185.76	60.83	1042.45	43.07	1983.65	52.54
97	57.9	0.26	1578.61	107.85	746.26	25.31	990.11	43.62
98	399.4	0.43	1050.36	79.53	890.19	17.69	937.49	27.63
99	40.5	0.29	1148.22	95.38	892.77	19.67	969.65	33.76
100	256.7	0.38	969.09	55.59	891.37	15.06	914.01	19.77

PARTE2

Spot	Isotopic ratios 207Pb/206Pb	2s	207Pb/235U	2s (%)	206Pb/238U	2s (%)	Rho	% conc	
Cambaizinho region, rutile metagabbro, sample 62									
8	0.1168	7.3080	1.9688	9.6083	0.1223	2.1449	0.22		
9	0.1794	4.2366	3.2737	5.0480	0.1324	1.2739	0.25		
10	0.2835	3.1717	5.9733	8.0476	0.1528	3.1228	0.39		
11	0.3614	5.5932	8.5973	11.7164	0.1725	3.4995	0.30		
12	0.3207	3.1274	7.1390	5.9952	0.1614	2.3949	0.40		
13	0.2863	2.9972	5.9944	4.6913	0.1518	1.8407	0.39		
14	0.2569	4.6635	5.1442	14.6991	0.1452	4.4801	0.30		
15	0.1814	3.1709	3.3202	4.8693	0.1327	1.8431	0.38		
16	0.2414	7.3690	4.7653	15.8356	0.1432	4.1150	0.26		
17	0.4001	3.2366	10.1747	9.5710	0.1844	3.5593	0.37		
18	0.2752	6.6595	5.7073	10.6448	0.1504	2.8232	0.27		
19	0.3976	1.8922	9.7477	3.8746	0.1778	1.9912	0.51		
20	0.3318	3.7868	7.6347	6.2611	0.1669	2.2246	0.36		
Palma region, zircon metagabbro, sample 139									
7	0.0649	2.0856	1.0775	2.1696	0.1204	0.5979	0.28	101.3	
8	0.0648	1.9947	1.0789	2.0762	0.1208	0.5761	0.28	101.1	
9	0.0647	2.3204	1.0728	2.4166	0.1203	0.6750	0.28	101.1	
10	0.3700	3.4199	12.6515	4.3569	0.2480	2.6995	0.62	185.9	not included in the average
11	0.0646	3.6797	1.0759	4.0718	0.1208	1.7433	0.43	100.9	
12	0.1502	4.2918	2.7312	5.8372	0.1319	3.9565	0.68	167.4	not included in the average
13	0.0647	1.9384	1.0741	2.0153	0.1204	0.5515	0.27	101.1	
14	0.0646	2.2350	1.0733	2.3301	0.1205	0.6591	0.28	100.9	
15	0.0643	2.5317	1.0649	2.6501	0.1201	0.7835	0.30	100.7	
16	0.0644	3.9024	1.0600	4.3020	0.1194	1.8107	0.42	100.9	
17	0.0647	1.9054	1.0681	1.9885	0.1197	0.5688	0.29	101.2	
18	0.0642	1.9545	1.0618	2.0356	0.1200	0.5688	0.28	100.5	
19	0.0620	2.7705	1.0193	2.9095	0.1193	0.8886	0.31	98.2	not included in the average
20	0.0643	2.2795	1.0565	2.3911	0.1191	0.7221	0.30	100.9	

Spot	Isotopic ratios 207Pb/206Pb	2s	207Pb/235U	2s (%)	206Pb/238U	2s (%)	Rho	% conc	
27	0.0638	3.3581	1.0140	3.5105	0.1153	1.0231	0.29	101.0	not included in the average
28	0.0644	1.9773	1.0679	2.0709	0.1203	0.6153	0.30	100.7	
30	0.0650	3.6705	1.0732	4.0729	0.1197	1.7652	0.43	101.6	
31	0.0643	3.9110	1.0627	4.3088	0.1200	1.8083	0.42	100.7	
32	0.5444	4.9391	31.4704	6.2037	0.4193	3.7540	0.61	156.6	not included in the average
33	0.0649	1.9926	1.0781	2.0757	0.1205	0.5816	0.28	101.3	
34	0.0653	2.1958	1.0740	2.2959	0.1193	0.6708	0.29	102.0	
35	0.0773	2.3718	1.2971	2.6210	0.1216	1.1154	0.43	114.1	not included in the average
36	0.0648	3.4902	1.0797	3.6475	0.1208	1.0596	0.29	101.1	
37	0.0664	2.6172	1.0992	2.7365	0.1201	0.7993	0.29	103.0	not included in the average
38	0.0651	1.9249	1.0797	2.0110	0.1203	0.5821	0.29	101.5	
39	0.0652	1.9298	1.0745	2.0238	0.1196	0.6095	0.30	101.8	
40	0.0649	3.2887	1.0734	3.5069	0.1199	1.2177	0.35	101.4	

Palma leste ophiolite, zircon chloritite, sample 142

Spot	207Pb/206Pb	2s	207Pb/235U	2s (%)	206Pb/238U	2s (%)	Rho	% conc	
27	0.0734	3.7715	1.4960	4.2635	0.1479	1.9882	0.47	104.5	not included in the average
28	0.0657	15.9205	1.3403	17.3975	0.1479	7.0150	0.40	97.1	not included in the average
29	0.0687	13.5195	1.4020	14.0802	0.1479	3.9340	0.28	100.0	
30	0.1146	4.0877	2.4533	4.6937	0.1552	2.3067	0.49	135.3	not included in the average
31	0.0692	2.9302	1.4045	3.4239	0.1472	1.7711	0.52	100.6	
32	0.1181	4.3354	2.0529	5.4695	0.1260	3.3345	0.61	148.1	not included in the average
33	0.0691	3.5385	1.4085	4.0325	0.1479	1.9339	0.48	100.4	
34	0.0686	6.5361	1.3992	7.2676	0.1479	3.1776	0.44	99.9	
35	0.0687	3.0020	1.4020	3.5096	0.1480	1.8181	0.52	100.0	
36	0.0649	3.7373	1.0238	4.2113	0.1144	1.9411	0.46	102.5	not included in the average
37	0.0668	3.6611	1.1833	4.1383	0.1286	1.9292	0.47	101.7	not included in the average
38	0.0683	3.4019	1.3870	3.8969	0.1473	1.9008	0.49	99.7	
39	0.1255	3.1264	2.1891	4.1562	0.1265	2.7384	0.66	153.4	not included in the average
40	0.0692	2.6853	1.4085	3.2115	0.1476	1.7614	0.55	100.6	
47	0.0692	5.1387	1.4070	5.7242	0.1475	2.5220	0.44	100.6	
48	0.0702	2.8820	1.4348	3.3637	0.1482	1.7346	0.52	101.5	

Spot	Isotopic ratios 207Pb/206Pb	2s	207Pb/235U	2s (%)	206Pb/238U	2s (%)	Rho	% conc	
49	0.1083	8.1903	2.3041	9.3874	0.1543	4.5873	0.49	131.2	not included in the average
50	0.1225	4.2326	2.6469	4.9743	0.1567	2.6132	0.53	140.0	not included in the average
51	0.0696	5.4822	1.4265	6.0439	0.1486	2.5444	0.42	100.8	
52	0.0660	4.1687	1.1739	4.8031	0.1289	2.3857	0.50	100.9	not included in the average
53	0.0707	3.7159	1.4413	4.2269	0.1479	2.0146	0.48	101.9	
54	0.0832	4.6675	1.7166	5.4239	0.1497	2.7628	0.51	112.8	not included in the average
55	0.0812	3.6830	1.6725	4.3471	0.1493	2.3094	0.53	111.3	not included in the average
56	0.1971	4.3353	4.6782	4.8916	0.1722	2.2655	0.46	172.2	not included in the average
57	0.0674	4.5894	1.2289	5.1946	0.1322	2.4332	0.47	101.7	not included in the average
58	0.0825	2.5472	1.7006	3.1511	0.1495	1.8550	0.59	112.3	not included in the average
59	0.1729	7.7047	3.9613	9.0716	0.1661	4.7887	0.53	164.1	not included in the average
60	0.0710	3.5734	1.4547	4.1673	0.1486	2.1441	0.51	102.1	not included in the average
67	0.1014	6.4940	2.0111	7.3204	0.1438	3.3788	0.46	129.2	not included in the average
68	0.0869	2.9683	1.8666	3.5384	0.1558	1.9260	0.54	114.6	not included in the average
69	0.0721	4.0045	1.5713	4.4933	0.1580	2.0381	0.45	101.4	not included in the average
70	0.0995	4.1015	2.0844	4.6166	0.1520	2.1190	0.46	125.4	not included in the average
71	0.1617	7.0013	3.6964	8.9266	0.1658	5.5376	0.62	158.9	not included in the average
72	0.0641	8.2193	1.0974	9.0737	0.1241	3.8439	0.42	99.7	not included in the average
73	0.1372	3.3137	2.4129	3.9832	0.1276	2.2102	0.55	161.0	not included in the average
74	0.1153	3.3815	2.4743	4.0147	0.1556	2.1641	0.54	135.7	not included in the average
75	0.0933	4.5263	1.9404	5.1105	0.1509	2.3727	0.46	120.9	not included in the average
76	0.1006	2.8724	2.1198	3.4278	0.1529	1.8707	0.55	126.0	not included in the average
77	0.0940	15.6110	1.5895	18.9386	0.1226	10.7222	0.57	129.6	not included in the average
78	0.0672	6.3999	1.1428	6.9356	0.1233	2.6728	0.39	103.2	not included in the average
79	0.0686	3.7975	1.3954	4.3143	0.1475	2.0476	0.47	100.0	
80	0.0704	4.3329	1.4344	4.8258	0.1478	2.1248	0.44	101.7	
87	0.1112	2.8768	1.9219	3.6372	0.1254	2.2256	0.61	143.0	not included in the average
88	0.0967	3.6341	2.0302	4.1982	0.1522	2.1019	0.50	123.2	not included in the average
89	0.1089	4.3269	1.8664	5.4034	0.1243	3.2365	0.60	141.6	not included in the average

Spot	Isotopic ratios 207Pb/206Pb	2s	207Pb/235U	2s (%)	206Pb/238U	2s (%)	Rho	% conc	
90	0.1348	4.3888	2.3642	5.2633	0.1272	2.9054	0.55	159.6	not included in the average
91	0.0708	6.0788	1.4437	6.6367	0.1479	2.6634	0.40	102.0	not included in the average
92	0.1975	20.0854	3.6972	22.3718	0.1358	9.8528	0.44	191.4	not included in the average
93	0.2988	9.8206	6.0814	14.0738	0.1476	10.0811	0.72	223.9	not included in the average
94	0.0756	9.4674	1.5514	10.5885	0.1489	4.7418	0.45	106.3	not included in the average
95	0.0750	5.1076	1.5306	5.8694	0.1480	2.8918	0.49	105.9	not included in the average
96	0.2502	3.8376	6.0540	5.8838	0.1755	4.4601	0.76	190.3	not included in the average
97	0.0976	5.7500	1.6515	6.7760	0.1227	3.5850	0.53	132.7	not included in the average
98	0.0743	3.9343	1.5176	4.4712	0.1481	2.1244	0.48	105.3	not included in the average
99	0.0781	4.7878	1.5986	5.3362	0.1485	2.3563	0.44	108.6	not included in the average
100	0.0714	2.7157	1.4600	3.2621	0.1483	1.8073	0.55	102.5	not included in the average

Supplementary File 3. Zircon Lu-Hf analyses.

PARTE1

Spot	^{176}Yb/^{177}Hf[a]	±2σ	^{176}Lu/^{177}Hf[a]	±2σ	^{178}Hf/^{177}Hf	^{180}Hf/^{177}Hf	SigHf (V)[b]
Vila Nova Suite, metagabbro, sample 139							
7	0.0081	11	0.00032	4	1.467175	1.886888	8
8	0.0132	21	0.00055	8	1.467250	1.886860	11
11	0.0486	44	0.00179	13	1.467239	1.886866	8
13	0.0259	27	0.00071	6	1.467246	1.886785	6
14	0.0165	17	0.00064	5	1.467237	1.886894	8
15	0.0132	11	0.00052	3	1.467240	1.886900	7
16	0.0160	13	0.00069	4	1.467219	1.886876	7
17	0.0246	23	0.00094	7	1.467236	1.886820	10
18	0.0131	12	0.00052	4	1.467279	1.886892	9
20	0.0098	9	0.00039	3	1.467244	1.886788	8
28	0.0187	15	0.00073	5	1.467185	1.886889	9
30	0.0251	21	0.00098	6	1.467214	1.886828	9
31	0.0217	18	0.00092	6	1.467234	1.886861	8
33	0.0289	23	0.00116	7	1.467173	1.886803	8
34	0.0113	12	0.00046	4	1.467227	1.886972	8
36	0.0153	14	0.00058	4	1.467262	1.886879	6
38	0.0217	18	0.00092	6	1.467216	1.886782	9
39	0.0235	20	0.00092	6	1.467204	1.886760	8
40	0.0123	11	0.00052	3	1.467202	1.886833	8
Palma leste mélange, chloritite, sample 142							
28	0.0181	15	0.00101	6	1.467258	1.886999	6
29	0.0109	10	0.00058	4	1.467300	1.886916	8
31	0.0165	15	0.00093	7	1.467215	1.886754	7
33	0.0203	22	0.00110	10	1.467259	1.886874	6
34	0.0155	15	0.00089	8	1.467319	1.886910	6

35	0.0198	19	0.00105	8	1.467251	1.886868	8
36	0.0146	14	0.00076	6	1.467249	1.886838	7
37	0.0168	24	0.00090	11	1.467292	1.886851	7
38	0.0168	24	0.00090	11	1.467292	1.886851	7
40	0.0169	14	0.00091	6	1.467248	1.886872	6
47	0.0186	16	0.00099	7	1.467279	1.886960	6
48	0.0344	41	0.00170	18	1.467238	1.886933	12
51	0.0122	16	0.00071	8	1.467231	1.886837	7
52	0.0262	37	0.00142	18	1.467263	1.886830	7
53	0.0125	12	0.00072	5	1.467198	1.886895	8
57	0.0180	15	0.00099	6	1.467236	1.887012	4
60	0.0276	22	0.00146	9	1.467221	1.886941	8
69	0.0211	19	0.00116	8	1.467237	1.886789	8
72	0.0335	30	0.00171	13	1.467314	1.886909	7
78	0.0294	25	0.00147	9	1.467333	1.886873	8
79	0.0104	8	0.00061	4	1.467234	1.886859	8
100	0.0216	18	0.00113	7	1.467265	1.886984	9

Quoted uncertainties (absolute) relate to the last quoted figure. The effect of the inter-element fractionation on the Lu/Hf was estimated to be about 6 % or less based on analyses of the GJ-1 zircon. Accuracy and reproducibilty was checked by repeated analyses of reference zircon GJ-1 (data given as mean with 2 standard deviation uncertainties)

[a] $^{176}Yb/^{177}Hf = (^{176}Yb/^{173}Yb)_{true}$ x $(^{173}Yb/^{177}Hf)_{meas}$ x $(M_{173(Yb)}/M_{177(Hf)})^{b(Hf)}$, $b(Hf) = \ln(^{179}Hf/^{177}Hf_{true}$ / $^{179}Hf/^{177}Hf_{meas})$ / $\ln (M_{179(Hf)}/M_{177(Hf)})$, M=mass of respective isotope. The $^{176}Lu/^{177}Hf$ were calculated in a similar way by using the $^{175}Lu/^{177}Hf$ and b(Yb);

[b] Mean Hf signal in volt;

[c] Uncertainties are quadratic additions of the within-run precision and the daily reproducibility of the zircon standards;

[d] Initial $^{176}Hf/^{177}Hf$ and ε_{Hf} calculated using the apparent U-Pb age determined by LA-ICP-MS dating, and the CHUR parameters: $^{176}Lu/^{177}Hf = 0.0336$, and $^{176}Hf/^{177}Hf = 0.282785$ (Bouvier *et al.*, 2008);

[e] Two stage "maximum" model age in billion years using the measured $^{176}Lu/^{177}Hf$ of each spot (first stage = age of zircon), a value of $^{176}Lu/^{177}Hf = 0.0113$ for the average continental crust (second stage), and an average MORB (DM) $^{176}Lu/^{177}Lu$ and $^{176}Hf/^{177}Hf$ of 0.03933 and 0.283294, respectively (Blichert-Toft and Puchtel, 2010);

PARTE2

Spot	$^{176}Hf/^{177}Hf$	$\pm 2\sigma^c$	$^{176}Hf/^{177}Hf_{(t)}^d$	$\varepsilon_{Hf(t)}^d$	$\pm 2\sigma^c$	TDM (Ga)	$^{206}Pb/^{238}U$ Ma	Age
Vila Nova Suite, metagabbro, sample 139								
7	0.282555	23	0.282550	8.1	1.2	1.130	733.04	
8	0.282574	19	0.282566	8.7	1.0	1.098	735.22	
11	0.282659	18	0.282634	11.1	0.9	0.965	735.22	
13	0.282570	27	0.282561	8.4	1.3	1.110	732.69	
14	0.282562	18	0.282553	8.2	0.9	1.124	733.50	
15	0.282531	25	0.282524	7.1	1.3	1.184	731.08	
16	0.282597	23	0.282588	9.3	1.2	1.060	726.99	
17	0.282592	18	0.282579	9.0	0.9	1.075	729.01	
18	0.282582	20	0.282575	8.9	1.0	1.082	730.79	
20	0.282533	21	0.282528	7.1	1.1	1.178	725.50	
28	0.282560	20	0.282550	8.0	1.0	1.132	732.41	
30	0.282597	26	0.282584	9.2	1.3	1.066	728.66	
31	0.282604	22	0.282592	9.5	1.1	1.050	730.33	
33	0.282617	25	0.282601	9.9	1.3	1.030	733.33	
34	0.282539	23	0.282533	7.3	1.2	1.168	726.30	

Spot	$^{176}Hf/^{177}Hf$	$\pm2\sigma^c$	$^{176}Hf/^{177}Hf_{(t)}{}^d$	$\varepsilon Hf_{(t)}{}^d$	$\pm2\sigma^c$	TDM (Ga)	$^{206}Pb/^{238}U$ Ma	Age
36	0.282574	24	0.282566	8.7	1.2	1.098	735.17	
38	0.282610	24	0.282597	9.7	1.2	1.038	732.46	
39	0.282565	22	0.282552	8.0	1.1	1.129	728.15	
40	0.282580	25	0.282573	8.8	1.3	1.087	730.10	
Palma leste mélange, chloritite, sample 142								
28	0.282655	26	0.282638	14.7	1.3	0.884	889.29	
29	0.282635	22	0.282625	14.3	1.1	0.910	889.41	
31	0.282640	24	0.282625	14.2	1.2	0.912	885.19	
33	0.282670	22	0.282652	15.2	1.1	0.857	889.12	
34	0.282631	25	0.282616	13.9	1.3	0.928	889.24	
35	0.282648	21	0.282630	14.5	1.1	0.899	889.57	
36	0.282645	27	0.282635	10.3	1.3	0.980	698.42	
37	0.282655	23	0.282642	9.9	1.1	1.065	779.59	
38	0.282655	23	0.282640	14.7	1.1	0.882	885.87	
40	0.282635	24	0.282619	14.0	1.2	0.922	887.55	
47	0.282613	33	0.282596	13.2	1.6	0.968	886.93	
48	0.282743	19	0.282714	17.5	1.0	0.733	890.58	
51	0.282634	22	0.282622	14.2	1.1	0.915	892.89	
52	0.282662	26	0.282642	12.4	1.3	0.928	781.70	
53	0.282619	24	0.282607	13.6	1.2	0.946	889.29	
57	0.282622	35	0.282607	11.6	1.8	0.988	800.52	
60	0.282661	23	0.282637	14.8	1.2	0.885	893.05	
69	0.282664	19	0.282644	16.2	1.0	0.846	945.60	
72	0.282694	25	0.282670	12.8	1.2	0.886	754.29	
78	0.282771	25	0.282750	15.5	1.3	0.729	749.64	
79	0.282614	21	0.282603	13.4	1.1	0.954	886.88	
100	0.282614	15	0.282595	13.3	0.7	0.968	891.37	

Supplementary File 4. Major and trace element analyses of zircon, with indication of the $^{206}Pb/^{238}U$ age and $\varepsilon Hf_{(t)}$, when analyzed.

PARTE1

Spot	$^{206}Pb/^{238}U$ age	$\varepsilon Hf(t)$	Th	Zr	Y	La	Ce	Pr	Nd
Palma region, zircon metagabbro, sample 139									
7	733.04	8.09	149.21	506739.25	531.11	<0.060	2.14	0.048	0.88
11	735.22	11.10	2761.13	444412.84	3638.69	0.083	8.92	0.4	7.42
13	732.69	8.45	1191.08	474769.88	1896.64	1.53	16.02	0.57	6.39
14	733.50	8.21	258.35	508806.03	984.63	<0.065	3.01	0.15	1.75
15	731.08	7.10	1280.47	455588.69	1176.44	0.93	8.87	0.54	4.73
16	726.99	9.27	474.72	487179.59	1337.11	<0.098	2.42	0.2	4.43
17	729.01	9.03	1832.45	473906.06	1652.62	0.75	10.26	0.31	3.67
18	730.79	8.92	619.08	638899.50	908.41	0.79	5.11	0.39	3.63
20	725.50	7.11	216.16	471085.38	960.81	0.109	3.65	0.123	2.79
28	732.41	8.05	1061.84	477649.53	1113.37	12.43	27.32	3.67	29.06
30	728.66	9.18	829.26	478540.66	1200.90	<0.066	4.45	0.089	3.06
113	n.d.	n.d.	145.23	497837.06	644.19	<0.032	2.79	<0.052	1.64

Spot	206Pb/238U age	εHf(t)	Th	Zr	Y	La	Ce	Pr	Nd
114	n.d.	n.d.	375.67	538983.19	679.01	7.16	17.12	1.98	10.89
116	n.d.	n.d.	241.59	457537.09	729.52	0.94	10.71	0.43	3.23
119	n.d.	n.d.	203.05	489012.97	554.50	<0.071	2.15	0.056	1.28
125	n.d.	n.d.	764.42	477400.16	1900.79	0.19	4.28	0.3	4.81
133	n.d.	n.d.	2552.60	441478.66	1390.06	0.22	9.71	0.106	2.38
134	n.d.	n.d.	3882.84	448519.69	1652.46	1.48	8.07	0.32	3.14
136	n.d.	n.d.	1276.03	441688.88	1494.26	13.8	29.6	3.58	24.52
138	n.d.	n.d.	209.25	411686.28	699.99	23.44	23.52	3.82	20.99
140	n.d.	n.d.	372.02	498547.44	750.99	0.079	3.39	<0.036	1.54
Palma leste ophiolite, zircon chloritite, sample 142									
28	889.29	14.74	5.47	695065.44	466.69	0.022	0.37	0.044	0.89
29	889.41	14.27	17.20	735485.25	243.95	0.064	1.14	0.107	1.22
31	885.19	14.16	58.24	750569.88	531.34	<0.051	2.06	<0.026	0.89
33	889.12	15.21	3.10	789381.00	80.78	0.1	0.57	<0.0204	1.35
34	889.24	13.94	8.78	721834.88	229.50	<0.054	0.87	0.028	0.36
35	889.57	14.46	35.32	708234.88	320.88	<0.060	1.28	0.07	1.43
36	698.42	10.31	27.26	733479.19	363.52	<0.058	1.51	0.052	1.8
37	779.59	12.38	7.21	695513.81	84.35	<0.053	0.68	<0.00	0.85
38	885.87	14.72	60.09	667734.94	536.41	0.082	2.15	0.07	1.28
40	887.55	14.03	32.99	689100.19	368.60	<0.055	1.23	0.07	2.26
47	886.93	13.20	12.58	694795.56	325.31	<0.062	0.92	0.019	0.96
48	890.58	17.45	159.85	679768.69	1054.52	0.56	6.1	1.04	9.38
51	892.89	14.23	16.56	705045.69	244.55	<0.067	1.18	<0.034	<0.62
52	781.70	12.42	42.90	681951.44	607.72	<0.052	1.76	0.052	1.7
53	889.29	13.61	8.50	624635.44	150.46	0.082	0.63	<0.035	1.45
57	800.52	11.61	18.53	585019.44	244.86	0.053	1.18	0.077	1.43
60	893.05	14.77	156.08	611698.94	807.44	0.106	3.58	0.166	3.03
69	945.60	16.20	85.98	622022.19	585.12	<0.061	2.81	0.166	2.44
72	754.29	12.79	51.16	636539.31	808.47	<0.069	1.97	0.086	1.31
78	749.64	15.53	55.75	581903.19	1329.02	0.27	2.46	0.5	7.53
79	886.88	13.44	23.99	567091.50	260.15	<0.053	0.78	0.022	0.5
80	888.51	n.d.	42.66	581849.88	591.68	0.033	2.23	0.038	1.67
100	891.37	13.3	140.28	519046.09	754.75	<0.125	2.8	<0.062	2.2
Vila Nova Suite, metatonalite, sample 114									
7	723.17	7.77	75.94	525494.63	466.85	0.05	10.49	0.04	0.86
8	723.75	8.24	77.81	481162.38	678.9	0.05	10.71	0.09	1.52
10	719.37	7.95	61.71	524658.38	531.13	0.04	10.25	0.06	0.93
11	719.20	8.33	67.24	533657.44	729.88	0.09	10.98	0.11	1.41
13	717.64	8.10	78.09	492019.84	587.06	<0.0165	12.21	0.04	0.73
14	725.24	n.d.	71.56	468277.56	790.19	0.17	14.45	0.17	2.03
15	717.35	8.81	22.94	560988.06	226.29	1.51	9.13	0.80	8.39
16	702.19	n.d.	140.68	482355.22	635.75	0.04	14.90	0.04	0.92
17	703.46	8.41	23.34	471142.16	312.15	<0.0191	6.61	0.02	0.29
19	716.78	n.d.	127.2	462533.44	664.83	0.03	14.45	0.06	1.18
27	726.51	7.71	124.4	466251.88	757.78	0.10	15.15	0.06	1.20
28	723.75	n.d.	130.61	467098.59	717.24	1.11	19.08	0.98	10.10
30	725.64	8.23	71.85	557617.44	718.67	0.11	11.19	0.15	2.01
31	717.59		69.43	467905.63	638.63	0.46	12.39	0.52	5.16
33	711.65	n.d.	76.01	489422.31	609.78	0.03	9.75	0.08	1.49
32	717.24	n.d.	64.84	498725.03	339.28	0.90	9.85	0.51	5.08
36	709.34	n.d.	94.09	477435.41	554.14	3.02	25.79	2.17	14.92
37	714.99	7.53	138.34	459462.94	709.27	1.52	20.95	0.93	7.87
38	785.42	10.10	71.2	470846.69	480.2	0.85	10.39	0.39	3.41

Spot	206Pb/238U age	εHf(t)	Th	Zr	Y	La	Ce	Pr	Nd
89	780.29	n.d.	66.68	507383.94	347.76	0.29	8.09	0.14	1.82
88	719.26	n.d.	92.03	464742.72	785.04	<0.0179	12.69	0.04	1.07

Sanga do Jobim suite, monzogranite, sample 115

Spot	206Pb/238U age	εHf(t)	Th	Zr	Y	La	Ce	Pr	Nd
7	740.43	n.d.	115.13	465217.56	2407.16	5.29	51.32	9.52	60.28
12	740.89	5.58	259.69	462952.5	3247.59	1.48	30.49	2.88	23.70
19	695.36	6.22	181.24	463677.78	4302.65	7.57	72.93	10.82	64.39
27	694.04	n.d.	864.46	447138.38	7114.08	26.97	252.70	54.09	350.36
29	693.87	n.d.	169.62	533643.88	4823.22	13.68	126.45	36.33	199.61
30	692.55	n.d.	272.82	492338.13	9190.65	41.63	370.51	72.64	497.38
31	687.11	n.d.	409.78	422694.31	17207.55	75.79	759.69	130.91	871.14
36	684.77	n.d.	80.93	470855.47	1661.51	2.06	21.37	3.02	21.34
39	693.64	6.44	116.49	431260.53	2002.56	3.83	32.72	5.58	34.17
47	699.30	5.92	93.17	465977.88	2403.83	1.71	21.42	3.19	23.96
48	705.07	n.d.	232.34	423939.13	6088.92	33.24	217.40	43.11	275.39
50	687.40	n.d.	319.69	438377.81	4337.13	12.96	125.94	26.01	184.30
53	696.21	5.24	256.89	481380	6936.88	17.75	190.67	37.68	256.40
54	689.86	n.d.	78.21	482808.63	1362.22	0.19	12.10	0.17	2.41
55	696.61	n.d.	179.68	456708.91	3932.26	4.19	55.58	8.93	66.13
59	682.99	6.84	24.04	478393.09	991.56	0.03	4.50	0.05	1.39
60	692.55	8.28	37.27	486506	1409.95	0.28	5.13	0.35	3.55
70	691.69	n.d.	117.87	465485.81	1429.62	0.32	6.29	0.34	3.40
71	698.56	n.d.	32.20	481297.88	1203.98	0.77	11.73	1.55	11.40
72	692.55	4.77	53.51	462560.16	1758.06	0.05	6.59	0.18	3.22

PARTE2

Spot	Nd	Sm	Eu	Gd	Tb	Dy	Ho	Er	Tm

Palma region, zircon metagabbro, sample 139

Spot	Nd	Sm	Eu	Gd	Tb	Dy	Ho	Er	Tm
7	0.88	1.98	0.28	8.02	3.69	50.42	16.53	79.5	20.8
11	7.42	12.67	3	58.51	20.81	314.54	112.78	551.81	140.62
13	6.39	5.94	1.64	35.18	16.6	206.87	65.87	262.26	51.08
14	1.75	5.09	1.14	21.04	6.78	98.78	34.63	144.29	36.81
15	4.73	4.75	1.5	19.03	6.63	107.1	38.89	184.17	47.41
16	4.43	5.97	1.33	20.52	8.96	133.51	44.09	221.86	53.94
17	3.67	3.91	1.25	27.46	10.35	146.05	54.57	271.55	66.84
18	3.63	2.25	0.64	12.63	5.8	78.27	27.78	150.92	37.16
20	2.79	3.65	0.84	15.53	5.91	90.6	32.06	161.53	38.64
28	29.06	10.06	2.74	25.02	7.74	108.39	37.45	171.4	42.07
30	3.06	4.22	0.97	15.77	7.87	104.12	38.82	208.89	50.81
113	1.64	1.29	0.56	9.3	4.1	57	21.15	97.78	26.99
114	10.89	5.55	0.43	10.41	4.31	57.79	22.45	105.03	27.97
116	3.23	3.29	1.13	12	4.44	68.19	24.06	118.05	30.2
119	1.28	2.49	0.63	8.7	3.69	52.55	17.58	81.59	21.21
125	4.81	7.3	1.79	30.03	12.32	181.65	67.24	315.44	75.79
133	2.38	4.42	1.07	21.87	8.76	126.83	45.25	215.02	51.31
134	3.14	5.49	2.32	25.78	9.56	149.27	56.8	286.56	71.89
136	24.52	9.38	3.23	31.48	9.84	142.91	49.9	247.07	62.67
138	20.99	4.94	1.14	17.4	4.46	61.37	21.69	115.16	28.8
140	1.54	1.01	0.73	13.92	5.11	65.17	25.23	117.51	32.35

Spot	Nd	Sm	Eu	Gd	Tb	Dy	Ho	Er	Tm
Palma leste ophiolite, zircon chloritite, sample 142									
28	0.89	0.22	0.157	2	0.92	27.89	14.18	91.91	40.78
29	1.22	1.35	0.41	2.01	0.98	18.03	8.64	35.66	13.43
31	0.89	0.77	0.46	3.5	2.12	40.4	15.42	87.29	33.65
33	1.35	<0.49	<0.091	0.3	0.32	4.94	2.3	12.96	6.02
34	0.36	0.35	0.187	0.86	0.68	12.98	6.47	37.93	15
35	1.43	1.53	0.69	3.65	1.88	30.2	10.5	51.45	18.07
36	1.8	1.9	0.69	5.03	1.97	32.43	11.59	56.12	20.1
37	0.85	0.35	<0.083	0.57	0.36	5.73	2.64	13.81	5.32
38	1.28	2.16	1.1	4.88	2.71	41.23	17.44	92.39	31.97
40	2.26	1.23	0.74	3.6	1.71	32.5	11.09	60.22	21.2
47	0.96	0.42	0.44	1.55	0.89	16.66	10.37	79.01	39.59
48	9.38	7.58	3.03	10.44	5.11	76.25	33.2	182.75	71.55
51	<0.62	0.62	0.19	1.8	0.88	16.14	6.69	43.49	15.27
52	1.7	1.85	0.89	4.87	2.33	46.7	16.92	104.33	36.1
53	1.45	<0.40	0.22	2.18	0.55	11.8	4.46	25.15	11.35
57	1.43	1.13	0.34	0.87	0.86	16.87	7.6	45.76	17.04
60	3.03	2.31	1.26	7.64	3.96	64.6	25.78	133.95	46.2
69	2.44	2.2	1.03	5.15	2.3	40.54	16.28	94.94	38.9
72	1.31	1.69	1.1	6.69	3.99	59.48	25.39	139.38	49.91
78	7.53	<1.79	1.62	12.61	4.65	62.32	37.47	274.5	90.42
79	0.5	0.67	0.27	1.93	0.9	17.42	7.03	42.07	15.61
80	1.67	2.7	1.2	6.25	3.28	48.03	19.32	107.68	30.97
100	2.2	2.02	1.01	9.94	4.03	62.26	23.28	132.39	41.45
Vila Nova Suite, metatonalite, sample 114									
7	0.86	1.43	0.55	7.32	2.78	36.80	15.31	75.41	20.78
8	1.52	2.69	1.13	12.36	4.54	57.73	23.20	110.88	29.49
10	0.93	1.87	0.74	9.36	3.52	43.97	17.82	88.10	24.19
11	1.41	2.35	0.98	11.98	4.40	54.96	22.65	113.05	27.77
13	0.73	1.67	0.74	9.16	3.62	48.64	20.05	98.95	27.20
14	2.03	2.56	1.10	12.33	4.67	62.91	26.39	130.55	36.07
15	8.39	5.92	1.71	10.38	2.00	18.07	6.75	33.30	8.90
16	0.92	1.84	0.74	10.23	3.97	51.56	20.94	104.16	28.05
17	0.29	0.72	0.37	4.44	1.72	23.44	9.89	50.83	14.40
19	1.18	1.99	0.90	10.79	4.15	55.03	22.99	106.01	29.22
27	1.20	2.17	1.01	12.39	4.86	62.10	26.14	127.50	33.86
28	10.10	8.25	2.69	20.93	5.95	67.77	24.90	115.53	30.40
30	2.01	3.16	1.13	13.72	4.67	57.13	23.65	116.48	29.42
31	5.16	3.64	1.30	12.41	4.32	53.74	21.91	104.24	28.70
33	1.49	2.84	1.10	12.37	4.20	53.08	20.72	97.82	26.09
32	5.08	4.25	1.25	9.11	2.62	29.49	11.03	52.36	14.58
36	14.92	6.57	1.67	13.83	4.16	47.75	18.69	88.98	23.08
37	7.87	4.64	1.70	15.11	5.03	60.50	24.24	114.86	30.13
38	3.41	3.20	1.21	11.00	3.49	41.23	16.23	76.99	20.95
89	1.82	1.90	0.69	7.08	2.33	27.92	11.40	54.87	15.30
88	1.07	2.23	0.97	12.52	4.93	63.65	26.90	127.81	34.82
Sanga do Jobim suite, monzogranite, sample 115									
7	60.28	57.88	12.34	101.97	33.31	315.13	88.61	335.57	76.77
12	23.70	33.39	7.16	110.62	36.37	382.32	123.22	488.68	105.03
19	64.39	58.68	16.07	122.48	49.41	538.43	156.37	593.38	133.41
27	350.36	336.67	66.32	480.78	138.93	1120.46	257.33	838.50	177.43
29	199.61	182.86	33.37	288.87	78.84	653.04	177.59	655.53	133.62
30	497.38	436.36	98.66	652.10	164.04	1241.09	306.07	1065.32	198.39

Spot	Nd	Sm	Eu	Gd	Tb	Dy	Ho	Er	Tm
31	871.14	765.04	184.77	1133.08	327.48	2632.03	626.88	2023.01	390.60
36	21.34	27.46	5.18	68.47	22.08	215.30	63.36	235.76	51.11
39	34.17	35.82	5.78	72.74	24.32	234.45	69.13	271.98	64.09
47	23.96	28.77	8.03	80.27	26.90	279.18	89.42	347.33	76.90
48	275.39	225.08	44.49	371.75	110.16	906.10	220.09	760.10	153.18
50	184.30	170.27	33.35	275.64	79.02	660.16	163.62	585.22	122.10
53	256.40	258.41	72.47	409.29	121.42	991.58	246.05	839.92	177.65
54	2.41	4.65	1.01	25.24	10.23	128.17	49.06	215.06	51.98
55	66.13	69.46	16.68	167.78	51.19	493.42	148.65	563.03	123.29
59	1.39	3.87	0.83	20.99	7.95	96.95	36.73	159.63	38.68
60	3.55	7.03	1.55	34.65	12.52	143.37	51.46	213.81	48.65
70	3.40	5.25	0.94	26.55	10.94	140.55	52.21	228.45	56.24
71	11.40	14.66	3.18	36.69	12.54	135.10	44.37	182.10	41.64
72	3.22	7.96	1.58	41.48	15.45	184.85	66.83	286.22	65.59

PARTE3

Spot	Yb	Lu	Si	Hf	U	Sc	Sr	Nb	Ba
Palma region, zircon metagabbro, sample 139									
7	227.67	25.51	147710.83	10752.07	215.06	1101.29	0.22	1.26	<0.36
11	1380.06	150.47	147710.83	11324.65	2476.11	1067.12	0.58	1.71	<0.25
13	501.44	41.19	147710.83	8190.74	1327.96	1341.02	76.89	1.88	71.56
14	436.86	47.54	147710.83	11664.47	319.47	1162.49	0.39	1.19	<0.35
15	507.21	57.31	147710.84	10470.50	1311.97	1046.57	0.67	1.13	0.42
16	580.49	64.38	147710.83	10001.80	488.30	1135.25	0.19	1	<0.25
17	692.78	81.55	147710.83	13836.36	2040.29	1118.97	0.83	2.06	<0.43
18	392.85	52.21	147710.83	15944.28	680.07	1518.51	0.69	1.19	<0.42
20	453.72	50	147710.83	11806.75	373.83	1139.21	0.49	1.14	<0.25
28	486.31	54.25	147710.83	13064.66	1174.76	1054.28	3.24	1.27	1.62
30	574.26	65.27	147710.83	13005.70	1312.13	1072.89	0.24	1.07	<0.32
113	325.46	37.45	147710.84	10637.81	274.31	1087.88	0.21	1.24	<0.28
114	343.94	40.76	147710.84	15179.43	655.56	1124.19	0.41	1.11	0.70
116	328.33	38.44	147710.84	10779.22	354.79	978.79	0.81	0.92	1.87
119	258.36	30.19	147710.83	10446.58	257.20	1083.61	0.19	4.29	<0.39
125	855.14	93.53	147710.83	10254.46	783.81	1153.83	0.65	1.43	0.78
133	586.57	64.39	147710.83	13119.69	2418.12	1070.20	0.42	1.44	1.62
134	930.82	115.69	147710.83	11362.47	4222.87	1137.34	15.54	1.9	3.73
136	719.55	84.52	147710.83	12263.82	1329.43	1109.46	3.62	1.26	18.34
138	341.71	37.39	147710.83	10511.25	404.64	1058.26	0.26	0.98	<0.36
140	360.65	43.33	147710.83	14423.67	583.10	1202.12	0.62	1.07	<0.40
Palma leste ophiolite, zircon chloritite, sample 142									
28	700.1	106.31	147710.88	10596.36	56.77	1193.34	0.46	1.75	0.41
29	214.74	29.94	147710.88	7781.60	34.18	1110.32	0.29	0.97	0.49
31	483.06	71.01	147710.86	8072.41	118.83	1245.75	0.38	1.43	<0.22
33	95.64	15.73	147710.88	8615.07	11.56	1140.90	0.184	0.87	<0.21
34	240.01	37.92	147710.88	6677.80	27.97	1210.70	0.158	0.90	<0.26
35	248.13	34.71	147710.88	9043.39	60.60	1182.03	0.22	0.97	<0.23
36	288.7	40.35	147710.88	7770.30	49.12	1287.81	0.19	1.05	<0.25
37	85.02	11.99	147710.88	8114.57	23.46	1083.29	0.228	0.93	<0.32
38	459.99	66.57	147710.88	7925.74	119.27	1184.84	0.5	1.46	<0.33

Spot	Yb	Lu	Si	Hf	U	Sc	Sr	Nb	Ba
40	311.01	44.76	147710.88	7771.71	59.93	1146.29	0.197	0.93	<0.163
47	747.42	156.43	147710.88	8967.52	21.83	1182.02	0.47	0.61	0.31
48	983.69	171.09	147710.88	11728.36	190.48	1665.38	1.53	8.73	1.55
51	235.12	42.73	147710.86	8890.04	50.26	1330.04	0.31	1.16	<0.30
52	520.56	76.72	147710.86	6976.79	72.50	1250.17	0.37	1.15	<0.36
53	164.26	25.41	147710.84	8863.16	27.18	1179.12	0.242	0.91	<0.25
57	280.9	41.27	147710.86	8189.75	64.62	1161.66	0.26	1.42	<0.35
60	656.55	98.96	147710.86	8601.21	227.38	1422.69	0.191	1.63	<0.27
69	523.7	83.58	147710.86	10160.23	151.79	1503.93	0.89	3.55	0.54
72	691.61	99.81	147710.86	8920.77	74.32	1335.51	0.75	1.39	0.38
78	1025.02	269.75	147710.86	15596.90	59.35	1851.98	1.53	5.29	2.76
79	253.99	42.46	147710.86	9580.25	59.83	1241.62	<0.134	1.07	<0.62
80	465.74	65.93	147710.86	6781.60	58.49	1229.40	0.45	1.12	<0.42
100	525.69	89.94	147710.84	10805.12	192.71	1376.57	0.37	1.20	<0.247

Vila Nova Suite, metatonalite, sample 114

Spot	Yb	Lu	Si	Hf	U	Sc	Sr	Nb	Ba
7	247.42	44.22	147570.58	10646.97	140.65	927.03	0.86	2.86	3.18
8	348.36	59.80	147570.56	8574.75	123.23	875.54	1.44	2.68	0.65
10	288.95	50.92	147570.58	11230.65	126.26	946.23	0.83	2.81	0.25
11	306.34	69.87	147570.58	11081.61	112.83	1039.94	1.06	2.57	0.39
13	329.73	56.21	147570.58	9706.40	146.15	885.79	1.79	2.87	3.59
14	429.64	71.51	147570.58	8933.22	152.28	889.72	0.78	3.08	0.43
15	112.04	26.31	147570.58	13592.92	106.86	934.25	1.07	2.68	1.90
16	337.48	56.56	147570.58	9585.78	200.56	859.80	0.78	3.02	0.32
17	189.24	31.35	147570.59	9740.04	69.39	792.63	1.18	2.35	1.51
19	347.58	56.78	147570.59	8617.95	197.73	841.22	1.10	3.01	1.28
27	406.94	67.61	147570.59	9020.06	182.51	845.13	1.07	3.06	0.51
28	369.84	59.45	147570.59	9365.07	180.62	830.28	1.22	2.78	0.90
30	326.68	71.10	147570.59	12743.58	124.96	1005.81	1.10	2.70	1.19
31	345.79	56.54	147570.58	8261.57	129.70	811.86	19.39	2.68	6.16
33	313.07	51.93	147570.59	8958.59	124.88	818.38	0.85	2.56	1.15
32	184.01	30.61	147570.59	9929.53	109.10	821.00	1.90	2.66	1.65
36	279.40	45.86	147570.59	9259.00	156.18	789.50	36.06	2.95	3.27
37	361.42	58.61	147570.59	8789.65	195.60	790.79	1.51	2.87	6.13
38	260.34	43.37	147570.58	8582.73	136.24	805.13	8.59	2.76	99.67
89	186.74	32.19	147570.59	10710.06	117.94	821.28	1.36	2.72	1.85
88	425.27	69.26	147570.59	8527.37	166.47	843.32	0.82	2.92	0.26

Sanga do Jobim suite, monzogranite, sample 115

Spot	Yb	Lu	Si	Hf	U	Sc	Sr	Nb	Ba
7	770.11	99.68	147570.59	10249.69	719.9	777.03	19.62	9.79	7.06
12	1050.73	139.06	147570.59	8522.62	534.87	782.65	6.79	6.90	2.11
19	1316.35	164.52	147570.59	9938.28	896.11	840.38	30.54	19.77	8.81
27	1585.23	182.16	147570.59	9901.33	881.64	1064.99	80.54	18.50	37.86
29	1245.17	172.58	147570.59	10069.31	632.62	997.36	41.18	9.24	19.20
30	2208.78	287.83	147570.59	11211.62	976.76	1267.25	100.19	16.08	47.65
31	3511.75	391.64	147570.61	10194.72	1210.27	1214.36	170.70	33.87	89.59
36	514.87	65.27	147570.61	7844.39	203.93	771.28	3.45	3.88	2.28
39	669.47	85.16	147570.61	9054.22	554.73	704.64	6.99	8.65	1.94
47	786.61	96.00	147570.61	7461.1	163.23	760.09	5.28	4.60	1.39
48	1407.87	173.72	147570.61	9550.12	848.74	809.83	71.76	14.75	14.91
50	1086.47	141.98	147570.61	9476.42	617.53	848.68	49.72	12.06	17.32
53	1711.29	215.27	147570.61	11147.85	1399	880.34	57.52	24.38	21.64
54	538.23	77.96	147570.61	8506.48	200.41	812.35	1.09	6.14	0.54
55	1198.93	150.13	147570.61	7027.41	346.61	799.66	12.61	7.76	4.64
59	413.41	59.40	147570.61	7680.35	76.18	758.24	0.79	3.77	<0.218

Spot	Yb	Lu	Si	Hf	U	Sc	Sr	Nb	Ba
60	499.95	66.47	147570.61	7771.03	81.95	803.10	1.08	3.17	0.58
70	599.15	79.38	147570.61	9973.36	629.93	744.16	1.37	6.86	<0.22
71	437.81	57.92	147570.61	7554.99	95.73	781.79	3.67	3.24	1.31
72	665.05	90.29	147570.61	7489.92	130.86	769.12	0.94	4.20	0.30

PARTE4

Spot	La[139]	Ce[140]	Pr[141]	Nd[146]	Sm[147]	Eu[153]	Gd[157]	Tb[159]	Dy[163]
Palma region, zircon metagabbro, sample 139									
7		3.50	0.51	1.88	12.94	4.83	39.03	98.66	198.50
11	0.35	14.58	4.21	15.89	82.81	51.72	284.72	556.42	1238.35
13	6.46	26.18	6.00	13.68	38.82	28.28	171.19	443.85	814.45
14		4.92	1.58	3.75	33.27	19.66	102.38	181.28	388.90
15	3.92	14.49	5.68	10.13	31.05	25.86	92.60	177.27	421.65
16		3.95	2.11	9.49	39.02	22.93	99.85	239.57	525.63
17	3.16	16.76	3.26	7.86	25.56	21.55	133.63	276.74	575.00
18	3.33	8.35	4.11	7.77	14.71	11.03	61.46	155.08	308.15
20	0.46	5.96	1.29	5.97	23.86	14.48	75.57	158.02	356.69
28	52.45	44.64	38.63	62.23	65.75	47.24	121.75	206.95	426.73
30		7.27	0.94	6.55	27.58	16.72	76.74	210.43	409.92
113		4.56		3.51	8.43	9.66	45.26	109.63	224.41
114	30.21	27.97	20.84	23.32	36.27	7.41	50.66	115.24	227.52
116	3.97	17.50	4.53	6.92	21.50	19.48	58.39	118.72	268.46
119		3.51	0.59	2.74	16.27	10.86	42.34	98.66	206.89
125	0.80	6.99	3.16	10.30	47.71	30.86	146.13	329.41	715.16
133	0.93	15.87	1.12	5.10	28.89	18.45	106.42	234.22	499.33
134	6.24	13.19	3.37	6.72	35.88	40.00	125.45	255.61	587.68
136	58.23	48.37	37.68	52.51	61.31	55.69	153.19	263.10	562.64
138	98.90	38.43	40.21	44.95	32.29	19.66	84.67	119.25	241.61
140	0.33	5.54		3.30	6.60	12.59	67.74	136.63	256.57
Palma leste ophiolite, zircon chloritite, sample 142									
27	1.48	3.38	4.74	10.19	12.09	16.38	18.54	39.57	104.25
28	0.09	0.60	0.46	1.91	1.44	2.71	9.73	24.60	109.80
29	0.27	1.86	1.13	2.61	8.82	7.07	9.78	26.20	70.98
30	1.00	3.25	1.22	3.96	14.05	20.17	19.17	47.86	163.70
31		3.37		1.91	5.03	7.93	17.03	56.68	159.06
32	1.60	4.75	7.16	16.62	23.92	20.86	16.59	16.31	31.14
33	0.42	0.93		2.89			1.46	8.56	19.45
34		1.42	0.29	0.77	2.29	3.22	4.18	18.18	51.10
35		2.09	0.74	3.06	10.00	11.90	17.76	50.27	118.90
36		2.47	0.55	3.85	12.42	11.90	24.48	52.67	127.68
37		1.11		1.82	2.29		2.77	9.63	22.56
38	0.35	3.51	0.74	2.74	14.12	18.97	23.75	72.46	162.32
39		4.43	0.62	3.73	8.95	8.45	21.80	56.68	129.25
40		2.01	0.74	4.84	8.04	12.76	17.52	45.72	127.95
47		1.50	0.20	2.06	2.75	7.59	7.54	23.80	65.59
48	2.36	9.97	10.95	20.09	49.54	52.24	50.80	136.63	300.20
49	0.17	1.32	0.32	2.23	2.68	1.41	3.31	14.17	33.98
50	145.49	360.10	627.79	877.15	1019.35	1045.00	951.68	1236.63	1773.70
51		1.93			4.05	3.28	8.76	23.53	63.54

Spot	La^{139}	Ce^{140}	Pr^{141}	Nd^{146}	Sm^{147}	Eu^{153}	Gd^{157}	Tb^{159}	Dy^{163}
52		2.88	0.55	3.64	12.09	15.34	23.70	62.30	183.86
53	0.35	1.03		3.10		3.79	10.61	14.71	46.46
54		0.85		0.41		2.17	6.67	12.83	34.45
55	1.22	5.46	5.47	9.08	21.31	28.62	32.75	90.91	205.67
56	13.00	26.27	39.79	70.41	134.31	125.34	111.09	193.85	310.00
57	0.22	1.93	0.81	3.06	7.39	5.86	4.23	22.99	66.42
58	10.68	25.47	34.00	48.78	87.45	101.90	96.93	224.60	490.94
59	0.14	1.80		3.28		4.83	7.98	21.12	74.09
60	0.45	5.85	1.75	6.49	15.10	21.72	37.18	105.88	254.33
67	0.14	1.96	0.99	3.02	7.97	9.31	17.23	32.62	96.02
68	4.81	13.43	16.11	29.19	52.48	55.86	72.17	125.67	307.52
69		4.59	1.75	5.22	14.38	17.76	25.06	61.50	159.61
70		6.54	1.15	3.51	16.60	17.07	40.97	116.31	283.94
71		0.98	0.07	2.59	6.60	6.21	14.45	34.49	115.91
72		3.22	0.91	2.81	11.05	18.97	32.55	106.68	234.17
73		1.99	0.25	1.18	5.10	5.34	9.05	28.07	71.73
74	13.92	21.85	27.16	73.43	188.10	213.79	164.91	283.69	636.22
75		1.81		0.96		4.66	14.50	24.06	72.36
76	0.36	2.01	1.15	1.91	15.56	16.90	14.89	39.84	81.30
77	4.09	7.81	13.05	26.17	32.35	43.28	38.00	73.53	184.21
78	1.14	4.02	5.26	16.12		27.93	61.36	124.33	245.35
79		1.27	0.23	1.07	4.38	4.66	9.39	24.06	68.58
80	0.14	3.64	0.40	3.58	17.65	20.69	30.41	87.70	189.09
87	10.68	25.92	42.63	53.66	117.32	128.97	139.51	238.77	467.48
88	2.91	6.44	16.00	38.50	171.37	137.76	329.29	373.80	704.76
89	37.05	77.60	138.74	216.79	378.24	306.03	350.22	525.40	816.93
90	45.44	96.70	212.32	449.21	960.52	1121.21	1242.87	1725.40	2173.27
91	0.30	1.27		1.07		3.62	10.71	11.23	34.92
92	56.29	132.29	277.26	385.12	715.10	903.45	1025.94	1358.82	2046.46
93	67.68	87.24	176.84	210.64	388.76	647.93	745.99	956.42	1691.50
94		1.58	0.37	1.91	3.27	3.79	6.62	23.80	40.51
95	0.54	5.62	1.71	9.76	41.37	53.10	77.23	120.32	261.22
96	0.19	4.28	0.43	4.58	17.52	29.83	39.90	112.03	260.67
97	43.54	100.38	166.95	234.88	308.17	317.41	371.68	315.24	507.44
98	9.45	34.54	63.58	101.01	210.13	207.76	206.96	339.04	502.87
99		1.96	1.45	5.10	13.14	9.83	18.49	47.33	86.26
100		4.58		4.71	13.20	17.41	48.37	107.75	245.12

PARTE5

Spot	Ho^{165}	Er^{166}	Tm^{169}	Yb^{172}	Lu^{175}
Palma region, zircon metagabbro, sample 139					
7	292.05	480.36	815.69	1339.24	1004.33
11	1992.58	3334.20	5514.51	8118.00	5924.02
13	1163.78	1584.65	2003.14	2949.65	1621.65
14	611.84	871.84	1443.53	2569.76	1871.65
15	687.10	1112.81	1859.22	2983.59	2256.30
16	778.98	1340.54	2115.29	3414.65	2534.65
17	964.13	1640.79	2621.18	4075.18	3210.63
18	490.81	911.90	1457.25	2310.88	2055.51
20	566.43	976.01	1515.29	2668.94	1968.50

Spot	Ho^{165}	Er^{166}	Tm^{169}	Yb^{172}	Lu^{175}
28	661.66	1035.65	1649.80	2860.65	2135.83
30	685.87	1262.18	1992.55	3378.00	2569.69
113	373.67	590.82	1058.43	1914.47	1474.41
114	396.64	634.62	1096.86	2023.18	1604.72
116	425.09	713.29	1184.31	1931.35	1513.39
119	310.60	492.99	831.76	1519.76	1188.58
125	1187.99	1905.98	2972.16	5030.24	3682.28
133	799.47	1299.21	2012.16	3450.41	2535.04
134	1003.53	1731.48	2819.22	5475.41	4554.72
136	881.63	1492.87	2457.65	4232.65	3327.56
138	383.22	695.83	1129.41	2010.06	1472.05
140	445.76	710.03	1268.63	2121.47	1705.91

Palma leste ophiolite, zircon chloritite, sample 142

Spot	Ho^{165}	Er^{166}	Tm^{169}	Yb^{172}	Lu^{175}
27	181.45	346.28	851.37	2146.47	2051.18
28	250.53	555.35	1599.22	4118.24	4185.43
29	152.65	215.47	526.67	1263.18	1178.74
30	282.16	567.13	1324.31	2876.88	3085.83
31	272.44	527.43	1319.61	2841.53	2795.67
32	44.52	71.18	187.84	516.24	565.75
33	40.64	78.31	236.08	562.59	619.29
34	114.31	229.18	588.24	1411.82	1492.91
35	185.51	310.88	708.63	1459.59	1366.54
36	204.77	339.09	788.24	1698.24	1588.58
37	46.64	83.44	208.63	500.12	472.05
38	308.13	558.25	1253.73	2705.82	2620.87
39	216.78	388.28	848.63	1816.41	1761.81
40	195.94	363.87	831.37	1829.47	1762.20
47	183.22	477.40	1552.55	4396.59	6158.66
48	586.57	1104.23	2805.88	5786.41	6735.83
49	61.84	118.37	238.04	582.12	633.07
50	2049.65	3128.58	5224.71	8228.59	12565.35
51	118.20	262.78	598.82	1383.06	1682.28
52	298.94	630.39	1415.69	3062.12	3020.47
53	78.80	151.96	445.10	966.24	1000.39
54	56.89	125.86	337.65	732.47	762.20
55	328.45	569.00	1303.14	2604.18	2793.70
56	384.98	680.30	1413.33	3094.24	3200.79
57	134.28	276.50	668.24	1652.35	1624.80
58	944.70	1889.91	4305.49	9287.06	7450.79
59	164.66	334.80	891.76	2174.53	2374.02
60	455.48	809.37	1811.76	3862.06	3896.06
67	159.89	319.94	680.39	1400.53	1500.00
68	513.96	1066.65	2366.27	4850.65	4940.55
69	287.63	573.66	1525.49	3080.59	3290.55
70	469.79	908.94	1878.43	4319.94	4343.70
71	236.04	528.22	1388.63	3396.12	3061.81
72	448.59	842.18	1957.25	4068.29	3929.53
73	140.64	329.06	828.63	1730.35	2113.78
74	1021.02	2334.62	5207.84	8322.06	13243.70
75	115.72	201.39	517.65	1303.88	1314.96
76	133.04	240.91	541.57	1201.59	1293.31
77	488.52	1174.44	3128.63	5435.41	7212.20

Spot	Ho^{165}	Er^{166}	Tm^{169}	Yb^{172}	Lu^{175}
78	662.01	1658.61	3545.88	6029.53	10620.08
79	124.20	254.20	612.16	1494.06	1671.65
80	341.34	650.63	1214.51	2739.65	2595.67
87	799.82	1536.19	3403.53	7688.00	7207.87
88	976.33	2094.14	3931.76	7390.35	11440.94
89	1220.32	2195.77	4008.63	6839.41	10678.35
90	3162.72	6320.30	11697.65	20421.88	30968.50
91	69.08	139.03	343.53	727.76	843.31
92	3179.15	7231.78	15036.86	24543.76	35911.81
93	2005.83	3418.91	7180.78	14282.41	21443.70
94	71.38	161.57	351.76	909.65	1000.00
95	455.12	956.50	2035.29	4529.76	4662.99
96	439.40	770.09	1527.06	3528.47	3353.15
97	636.93	1068.46	1919.22	3005.00	5108.27
98	807.95	2052.93	5005.49	9987.00	10914.17
99	188.16	327.49	677.65	1383.47	1462.99
100	411.31	799.94	1625.49	3092.29	3540.94

References

Ague, J.J. 2003. Fluid infiltration and transport of major, minor and trace elements during regional metamorphism of carbonate rocks, Wepawaug Schist, Connecticut, USA. American Journal of Science, 30, 753-816.

Amaral, L., Caxito, F.A., Pedrosa-Soares, A.C., Queiroga, G., Babinski, M., Trindade, R., Lana, C., Chemale, F., 2020. The Ribeirão da Folha ophiolite-bearing accretionary wedge (Araçuaí orogen, SE Brazil): New data for Cryogenian plagiogranito and metasedimentary rocks. Precambrian Research, 336, 105522.

Arena, K.R., Hartmann, L.A., Lana, C., 2016. Evolution of Neoproterozoic ophiolites from the southern Brasiliano Orogen revealed by zircon U-Pb-Hf isotopes and geochemistry. Precambrian Research, 285, 299-314.

Arena, K.R., Hartmann, L.A., Lana, C., 2017. Tonian emplacement of ophiolites in the southern Brasiliano Orogen delimited by U-Pb-Hf isotopes of zircon from metasomatites. Gondwana Research, 49, 296-332.

Arena, K.R., Hartmann, L.A., Lana. C., 2018. U-Pb-Hf isotopes and trace elements of metasomatic zircon delimit the evolution of Neoproterozoic Capané Ophiolite in the southern Brasiliano Orogen. International Geology Review, 60 (7), 911-928.

Babinski, M., Chemale Jr. F., Hartmann, L.A., Van Schmus, W.R., Silva, L.C., 1996. Juvenile accretion at 750-700 Ma in southern Brazil. Geology, 24 (5), 439-442.

Bach, W., Jons N., Klein, F., 2013. Metasomatism within the ocean crust. In: Metasomatism and the chemical transformation of rock the role of fluids in terrestrial and extraterrestrial processes (Eds.), Harlov, D.E. & Austrheim, 253-288.

Borba, A.W., Mizusaki, A.M.P., Santos, J.O.S., McNaughton, N.J., Onoe, A.T., Hartmann, L.A., 2008. U-Pb zircon and ^{40}Ar-^{39}Ar K-feldspar dating of syn-sedimentary volcanism of the Neoproterozoic Maricá Formation: constraining the age of foreland

basin inception and inversion in the Camaquã Basin of southern Brazil. Basin Research, 20, 359-375.

Caxito, F.A., Heilbron, M., Valeriano, C.M., Bruno, H., Pedrosa-Soares, A., Alkmim, F.F., Chemale, F., Hartmann, L.A., Dantas, E., Basei, M.A.S., 2021. Integration of elemental and isotope data supports a Neoproterozoic Adamastor Ocean realm. Geochemical Perspectives Letters, 17, 6-10.

Caxito, F.A., Santos, L.C.M.L., Ganade, C.E., Bendaoud, A., Fettour, E-H., Bouyo, M.H., 2020. Toward an integrated model of geological evolution for NE Brazil-NW Africa: The Borborema Province and its connections to the Trans-Saharan (Benino-Nigerian and Tuareg shields) and Central African orogens. Brazilian Journal of Geology, 50 (2), e20190122.

Caxito, F.A., Uhlein, A., Stevenson, R., Uhlein, G.J., 2014. Neoproterozoic oceanic crust remnants in northeast Brazil. Geology, 42 (5), 387-390.

Cerva-Alves, T.; Hartmann, L.A., Queiroga, G.N., Lana, C., Castro, M.P., Maciel, L.A.C., Remus, M.V.D., 2021. Metamorphic evolution of juvenile Serrinha forearc basin in the southern Brasiliano Orogen. Precambrian Research, (submitted).

Cerva-Alves, T., Hartmann, L.A., Remus, M.V.D., Lana, C., 2020. Integrated ophiolite and arc evolution, southern Brasiliano Orogen. Precambrian Research, 341, 105648.

Cerva-Alves, T., Remus, M.V.D., Dani, N., Basei, M.A.S., 2017. Integrated field, mineralogical and geochemical characteristics of Caçapava do Sul alvikite and beforsite intrusions: a new Ediacaran carbonatite complex in southernmost Brazil. Ore Geology Reviews, 88, 352-369.

Chemale, F., 2000. Evolução Geológica do Escudo Sul-rio-grandense. In: Holz, M., De Ros, L.F. (Eds.), Geologia do Rio Grande do Sul. Centro de Investigação do Gondwana, Universidade Federal do Rio Grande do Sul, Porto Alegre, Brasil, 13-55.

Choi, S.H., Mukasa, S.B., Andronikov, A.V., Osanai, Y., Harley, S.L., Kelly, N.M., 2006. Lu-Hf systematics of the ultra-high temperature Napier Metamorphic Complex in Antarctica: Evidence for the early Archean differentiation of Earth's mantle. Earth and Planetary Science Letters, 246 (3-4), 305-316.

Chu, N.C., Taylor, R.N., Chavagnac, V., Nesbitt, R.W., Boella, R. M., Milton, J.A., German, C.R., Bayon, G., Burton, K., 2002. Hf isotope ratio analysis using multi-collector inductively coupled plasma mass spectrometry: An evaluation of isobaric interference corrections. Journal of Analytical Atomic Spectrometry, 17, 1567-1574.

CPRM – Serviço Geológico do Brasil., 2010. Projeto Aerogeofísico Escudo do Rio Grande do Sul. LASA PROSPECÇÕES S.A., Relatório Técnico, 260 p.

Dessouky, O.K., Sun, W., Ibrahim, W.S., Ali, H.H., Hassan, M.M., Li, C., Omran, A.A., Dardier, A.M., 2021. New insights into Cryogenian arc granitoids hosting Th-U mineralized Ediacaran syenogranite dikes, Ra's Abdah area in the northern Egyptian Nubian Shield: Constraints from U-Pb ages and zircon geochemistry. Precambrian Research, 352, 105986.

Dunn, T., Sen, C., 1994. Mineral/matrix partition coefficients for orthopyroxene, plagioclase, and olivine in basaltic to andesitic systems: A combined analytical and experimental study. Geochimica at Cosmochimica Acta, 58 (2), 717-733.

Fernandes, L.A.D., Menegat, R., Costa, A.F.U., Porcher, C.C., Tommasi, A., Kraemer, G., Ramgrab, G.E., Camozzato, E., 1995. Evolução tectônica do Cinturão Dom Feliciano no Escudo Sul-Rio-Grandense: Parte I – uma contribuição a partir do registro geológico. Revista Brasileira de Geociências, 25 (4), 351-374.

Goñi, J.C., 1962. Origine des roches ultrabasiques et serpentineuses du précambrien de Rio Grande do Sul (Brésil). Mode de gisement et minéralisations. Escola de Geologia, UFRGS 12, 7-91.

Griffin, W.L., Belousova, E.A., Shee, S.R., Pearson, N.J., O'Reilly, S.Y., 2004. Archean crustal evolution in the northern Yilgarn Craton: U-Pb and Hf-isotope evidence from detrital zircons. Precambrian Research, 131, 231-282.

Grimes, C.B., John, B.E., Cheadle, M.J., Mazdab, F.K., Wooden, J.L., Swapp, S., Schwartz, J.J., 2009. On the occurrence, trace element geochemistry, and crystallization history of zircon from in situ ocean lithosphere. Contribution to Mineralogy and Petrology, 158, 757-783.

Grimes, C.B., John, B.E., Kelemen, P.B., Mazdab, F., Wooden, J.L., Cheadle, M.J., Hanghøj, K., Schwartz, J.J., 2007. The trace element chemistry of zircons from oceanic crust: a method for distinguishing detrital zircon provenance. Geology, 35, 643-646.

Grimes, C.B., Wooden, J.L., Cheadle, M.J., John, B.E., 2015. "Fingerprinting" tectono-magmatic provenance using trace elements in igneous zircon. Contribution to Mineralogy and Petrology, 170, 46.

Gubert, M.L., Philipp, R.P., Basei, M.A.S., 2016. The Bossoroca Complex, São Gabriel Terrane, Dom Feliciano Belt, southernmost Brazil: U-Pb geochronology and tectonic implications for the Neoproterozoic São Gabriel Arc. Journal of South American Earth Sciences, 70, 1-17.

Haag, M.B., Freitas, R.B., Sommer, C.A., Savian, J.F., Lima, E.F., Gambeta, J.H., Lyra, D.S., Trindade, R.I.F., 2021. Multi-proxy case study of a Neoproterozoic rhyolite flow in southernmost Brazil: Emplacement mechanisms and implications for ancient felsic lavas. Journal of South American Earth Sciences, 107, 102982.

Hartmann, L.A., Leite, J.A.D., Silva, L.C., Remus, M.V.D., McNaughton, N.J., Groves, D.I., Fletcher, I.R., Santos, J.O.S., Vasconcellos, M.A.Z., 2000. Advances in SHRIMP geochronology and their impact on understanding the tectonic and metallogenic evolution of southern Brazil. Australian Journal of Earth Sciences, 47 (5), 829-844.

Hartmann, L.A., Massuda, A.J., Cerva-Alves, T., Lana, C., Leandro, C.G., Savian, J.F., 2021. Aeromagnetometry and aerogammaspectrometry integrated with U-Pb zircon geochronology of northern Bossoroca ophiolite, Brasiliano Orogen. Annals of the Brazilian Academy of Sciences, 93 (1): e20190791.

Hartmann, L.A., Lopes, W.R., Savian, J.F., 2016. Integrated evaluation of the geology, aerogammaspectrometry and aeromagnetometry of the Sul-Riograndense Shield, southernmost Brazil. Annals of the Brazilian Academy of Sciences, 188 (1): 75-92.

Hartmann, L.A., Philipp, R.P., Santos, J.O.S., McNaughton, N.J., 2011. Time frame of the 753-680 Ma juvenile accretion during the São Gabriel orogeny, Southern Brazilian shield. Gondwana Research, 19, 84-99.

Hartmann, L.A., Savian, J.F., Lopes, W.R., 2015. Airborne geophysical characterization of geotectonic relationships in the southern Ribeira Belt, Luís Alves Craton, and northern Dom Feliciano Belt, Brazilian Shield. International Geology Review, 58 (4), 471-488.

Hartmann, L.A., Werle, M., Michelin, C.R.L. Lana, C., Queiroga, G.N., Castro, M.P., Arena, K.R., 2019. Proto-Adamastor ocean crust (920 Ma) described in Brasiliano Orogen from coetaneous zircon and tourmaline. Geoscience Frontiers, 10 (4), 1623-1633.

Hsü, K.J., 1968. Principles of mélanges and their bearing on the Franciscan-Knoxville Paradox. Geological Society of America Bulletin, 79, 1063-1074.

Hodel, F., Triantafyllou, A., Berger, J., MAcouin, M., Baele, J.-M, Mattielli, N., Monnier, C., Trindade, R.I.F., Ducea, M.N., Chatir, A., Ennih, N., Langlade, J., Poujol, M., 2020. The Moroccan Anti-Atlas phiolites: Timing and melting processes in an intra-oceanic arc-back-arc environment. Gondwana Research, 86, 182-202.

Hueck, M., Oyhantçabal, P., Philipp, R.P., Basei, M.A.S., Siegesmund, S., 2018. The Dom Feliciano Belt in southern Brazil and Uruguay. In: Siegesmund, S., Basei, M.A.S., Oyhantcabal, P., Oriolo, S. (Eds.), Geology of Southwest Gondwana. Regional Geology Reviews, Springer Nature, 243-265.

Hueck, M., Wemmer, K., Basei, M.A.S., Philipp, R.P., Oriolo, S., Heidelbach, F., Oyhantçabal, P., Siegesmund, S., 2020. Dating recurrent shear zone activity and the transition from ductile to brittle deformation: White mica geochronology applied to the Neoproterozoic Dom Feliciano Belt in south Brazil. Journal of Structural Geology, 141, 104199.

Jost, H., Hartmann, L.A., 1984. Província Mantiqueira - Setor Meridional. In: Almeida, F. F.M., Hasui, Y. (Eds.). O Pré-Cambriano do Brasil. São Paulo, Ed. Edgard Blucher, 345-368.

Kröner, A., Stern, R.J., 2005. Africa: Pan-African Orogeny. Encyclopedia of Geology, Elsevier, Oxford (2005), 1-13.

Laux, J.H., 2017. Geologia e Recursos Minerais da Folha Lagoa da Meia-Lua - SH. 21-Z-B-VI, Escala 1:100.000. Porto Alegre. CPRM, 2017. 255 p.http://rigeo.cprm.gov.br/xmlui/handle/doc/18035,12/20/2020.

Leite, J.A.D., Hartmann, L.A., McNaughton, N.J., Chemale Jr., F., 1998. SHRIMP U/Pb zircon geochronology of Neoproterozoic juvenile and crustal-reworked terranes in southernmost Brazil. International Geology Review, 40, 688-705.

Li, Z.X., Bogdanova, S.V., Collins, A.S., Davidson, A., De Waele, B., Ernst, R.E., Fitzsimons, I.C.W., Fuck, R.A., Gladkochub, D.P., Jacobs, J., Karlstrom, K.E., Lu, S., Natapov, L.M., Pease, V., Pisarevsky, S.A., Thrane, K., Vernikovsky, V., 2008. Assembly, configuration, and break-up history of Rodinia: A synthesis. Precambrian Research, 160, 179-210.

Maraschin, A.J., Mizusaki, A.M., Zwingmann, H., Borba, A.W., Sbrissa, G.F., 2010. Illite authigenesis in sandstones of the Guaritas Allogroup (Early Paleozoic): Implications for the depositional age, stratigraphy and evolution of the Camaquã Basin (southern Brazil). Journal of South American Earth Sciences, 29, 400-411.

Massuda, A.J., Hartmann, L.A., Queiroga, G.N., Castro, M.P., Leandro, C.G., Savian, J.F., 2020. Mineralogical evolution of the northern Bossoroca ophiolite, São Gabriel Terrane. Brazilian Journal of Geology, 50 (4), e20190120.

Mezger, K., Rawnsley, C., Bohlen, S., Hanson, G., 1991. U-Pb garnet, sphene, monazite and rutile ages: Implications for the duration of high-grade metamorphism and cooling histories, Adirondack Mts., New Yourk. The Journal of Geology, 99 (3), 415-428.

Millonig, L.J., Albert, R., Gerdes, A., Avigad, D., Dietsch, C., 2020. Exploring laser ablation U-Pb dating of regional metamorphic garnet – The Straits Schist, Connecticut, USA. Earth and Planetary Science Letters, 552, 116589.

Oyhantçabal, P., Oriolo, S., Wemmer, K., Basei, M.A.S., Frei, D., Siegesmund, S., 2021. Provenance of metasedimentary rocks of the western Dom Feliciano Belt in Uruguay: Insights from U–Pb detrital zircon geochronology, Hf and Nd model ages, and geochemical data. Journal of South American Earth Sciences, 108, 103139.

Peixoto, C.A., Heilbron, M., Ragatky, D., Armstrong, R., Dantas, E., Valeriano, C.M., Simonetti, A., 2017. Tectonic evolution of the juvenile Tonian Serra da Prata magmatic arc in the Ribeira Belt, SE Brazil: implications for early West Gondwana amalgamation. Precambrian Research, 302, 221-254.

Penniston-Dorland S.C., Ferry, J.M., 2008. Element mobility and scale of mass transport in the formation of quartz veins during regional metamorphism of the Waits river formation, east-central Vermont. American Mineralogy, 93, 7-21.

Pertille, J., Hartmann, L.A., Santos, J.O.S., McNaughton, N.J., Armstrong, R., 2017. Reconstructing the Cryogenian-Ediacaran evolution of the Porongos fold and thrust Belt, southern Brasiliano Orogen, based on zircon U-Pb-Hf-O isotopes. International Geology Review, 59, 1532-1560.

Philipp, R.P., Hartmann, L.A., Lusa, M., Basei, M.A.S., Santos, J.O.S., 2014. Oldest age of magmatism in the Passinho Arc in the southwestern portion of Gondwana, Rio Grande do Sul, Brazil. In: 9th South American Symposium on Isotope Geology, Abstracts. São Paulo, p. 186.

Philipp, R.P., Pimentel, M.M., Basei, M.A.S., 2018. The tectonic evolution of the São Gabriel Terrane, Dom Feliciano Belt, Southern Brazil: the closure of the Charrua

Ocean. In: Siegesmund, S., Basei, M.A.S., Oyhantcabal, P., Oriolo, S. (Eds.), Geology of Southwest Gondwana. Regional Geology Reviews. Springer Nature, 243-265.

Pimentel, M.M., Fuck, R.A., Gioia, S.M.C.L., 2000. The Neoproterozoic Goiás magmatic arc, Central Brazil: A review and new Sm-Nd isotopic data. Revista Brasileira de Geociências, 30(1), 35-39.

Pitombeira, J.P.A., Amaral, W.S., Santos, T.J.S., Dantas, E.L., Fuck, R.A., 2021. A new record of continental arc magmatism in the Ceará Central Domain, Borborema Province (NE Brazil): evidence from the Pacatuba-Maranguape Complex. Precambrian Research, 359, 106192.

Raymond, L.A., 1984. Classification of mélanges. In Raymond, L.A. (Ed.). Melanges: Their Nature, Origin, and Significance. Geological Society of America Special Paper 198, 7-20.

Remus, M.V.D., 1990. Geologia e Geoquímica do Complexo Cambaizinho, São Gabriel, RS. MSc thesis. Instituto de Geociências, UFRGS, Porto Alegre, 267 p.

Remus, M.V.D., McNaughton, N.J., Hartmann, L.A., Koppe, J.C., Fletcher, I.R., Groves, D.I., Pinto, V.M., 1999. Gold in the Neoproterozoic juvenile Bossoroca Volcanic Arc of southernmost Brazil: isotopic constraints on timing and sources. Journal of South American Earth Sciences, 12, 349-366.

Saalmann, K., Gerdes, A., Lahaye, Y., Hartmann, L.A., Remus, M.V.D., Läufer, A., 2011. Multiple accretion at the eastern margin of the Rio de la Plata craton: the prolonged Brasiliano orogeny in southernmost Brazil. International Journal of Earth Sciences, 100, 355-378.

Saalmann, K., Hartmann, L.A., Remus, M.V.D., Koester, E., Conceição, R.V., 2005a. Sm-Nd isotope geochemistry of metamorphic volcano-sedimentary successions in the São Gabriel Block, southernmost Brazil: evidence for the existence of juvenile Neoproterozoic ocean crust to the east of the Rio de la Plata craton. Precambrian Research, 136, 159-175.

Saalmann, K., Remus, M.V.D., Hartmann, L.A., 2005b. Geochemistry and crustal evolution of volcano-sedimentary successions and orthogneisses in the São Gabriel Block, southernmost Brazil – Relics of Neoproterozoic magmatic arcs. Gondwana Research, 8 (2), 143-161.

Saalmann, K., Remus, M.V.D., Hartmann, L.A., 2006. Tectonic evolution of the Neoproterozoic São Gabriel block, southern Brazil: constraints on Brasiliano Orogenic evolution of the Rio de La Plata cratonic margin. Journal of South American Earth Sciences, 21, 204-227.

Saalmann K., Gerdes A., Lahaye Y., Hartmann L.A., Remus M.V.D., Laufer A., 2011. Multiple accretion at the eastern margin of the Rio de La Plata craton: the prolonged Brasiliano Orogeny in southernmost Brazil. International Journal of Earth Sciences, 100 (2-3), 355-378.

Samson, S.D., Inglis, J.D., D'Lemos, R.S., Admou, H., Blichert-Toft, J., Hefferan, K., 2004. Geochronological, geochemical, and Nd–Hf isotopic constraints on the origin of Neoproterozoic plagiogranites in the Tasriwine ophiolite, Anti-Atlas orogen, Morocco. Precambrian Research, 135, 133-147.

Santiago, R., Caxito, F.A., Pedrosa-Soares, A., Neves, M. A., Dantas, E. L., 2020. Tonian island arc remnants in the northern Ribeira orogen of Western Gondwana: The Caxixe batholith (Espírito Santo, SE Brazil). Precambrian Research, 351, 105944.

Schannor, M., Lana, C., Fonseca, M.A., 2019. São Francisco-Congo Craton break-up delimited by U-Pb-Hf isotopes and trace-elements of zircon from metasediments of the Araçuaí Belt. Geoscience Frontiers, 10, 611-628.

Schannor, M., Lana, C., Nicoli, G., Cutts, K., Buick, I., Gerdes, A., Hecht, L., 2021. Reconstructing the metamorphic evolution of the Araluaí orogen (SE Brazil) using in situ U-Pb garnet dating and P-T modelling. Journal of Metamorphic Geology. https://doi.org/10.1111/jmg.12605

Siviero, R.S., Bruguier, O., Fernandes, L.A.D., Koester, E., Porcher, C.C., Kraemer, G., 2021. Age and geochemistry of Cambaí Complex, São Gabriel Terrane, Brazil: Arc-related TTG-like rocks. Journal of South American Earth Sciences, 108, 103165.

Souza, C.S.M., Hauser, N., Dantas, E.L., Reimold, W.U., Schmitt, R.T., Chaves, J.G.S., Osorio, L.F.B., 2019. Does the metavolcanic-sedimentary Rio do Coco Group, Araguaia Belt, Brazil, represent a continuity of the Quatipuru ophiolitic complex? - Constraints from U-Pb and Sm-Nd isotope data. Journal of South American Earth Sciences, 94, 102233.

Stern, R.J., Johnson, P.R., Kröner, A., Yibas, B., 2004. Neoproterozoic ophiolites of the Arabian-Nubian shield. In: Kusky, T.M. (Ed.), Precambrian Ophiolites and Related Rocks. Developments in Precambrian Geology, 13, 95-128.

Sun, S.S., McDonough, W.F., 1989. Chemical and isotopic systematics of oceanic basalts: implications for mantle composition and processes. In: Saunders, A.D., Norry, M. (Eds.), Magmatism in Ocean Basins, Geological Society of London, Special Publication, 42, 313-345.

Tapster, S., Roberts, N.M.W., Petterson, M.G., Saunders, A.D., Naden, J., 2014. From continent to intra-oceanic arc: Zircon xenocrysts record the crustal evolution of the Solomon island arc. Geology, 42 (12), 1087-1090.

Thomas, R.J., Chevallier, L.P., Gresse, P.G., Harmer, R.E., Eglington, B.M., Armstrong, R.A., de Beer, C.H., Martini, J.E.J., de Kock, G.S., Macey, P.H., Ingram, B.A., 2002. Precambrian evolution of the Sirwa Window, Anti-Atlas Orogen, Morocco. Precambrian Research, 118, 1-57.

Triantafyllou, A., Berger, J., Baele, J.-M., Diot, H., Ennih, N., Plissart, G., Monnier, C.,Watlet, A., Bruguier, O., Spagna, P., Vandycke, S., 2016. The Tachakoucht–Iriri–Tourtit arc complex (Moroccan Anti-Atlas): Neoproterozoic records of polyphased

subduction accretion dynamics during the Pan-African orogeny. Journal of Geodynamics, 96, 81-103.

Triantafyllou, A., Berger, J., Baele, J.M., Mattielli, N., Ducea, M.N., Sterckx, S., Ennih, N., 2020. Episodic magmatism during the growth of a Neoproterozoic oceanic arc (Anti-Atlas, Morocco). Precambrian Research, 339, 105610.

Vedana, L.A., Philipp, R.P., Basei, M.A.S., 2018. Tonian to early Cryogenian synorogenic basin of the São Gabriel terrane, Dom Feliciano Belt, southernmost Brazil. International Geology Review, 60 (1), 109-133.

Vry, J.K., Baker, J.A., 2006. LA-MC-ICPMS Pb Pb dating of rutile from slowly cooled granulites: Confirmation of the high closure temperature for Pb diffusion in rutile. Geochimica et Cosmochimica Acta, 70 (7), 1807-1820.

Werle, M., Hartmann, L.A., Queiroga, G.N., Lana, C., Pertille, J., Michelin, C.R.L., Remus, M.V.D., Roberts, M.P., Castro, M.P., Leandro, C.G., Savian, J.F., 2020. Oceanic crust and mantle evidence for the evolution of Tonian-Cryogenian ophiolites, southern Brasiliano Orogen. Precambrian Research, 351, 105979.

Whitehouse, M.J., 2003. Rare earth elements in zircon: a review of applications and case studies from the Outer Hebridean Lewisian Complex, NW Scotland. Geological society, London, Special Publications, 220 (1), 49-64.

Whitney, D.L., Evans, B.W., 2010. Abbreviations for names of rock-forming minerals. American Mineralogist, 95, 185-187.

Will, T.M., Gaucher, C., Ling, X.-X., Li, X.-H., Frimmel, H.E., 2019. Neoproterozoic magmatic and metamorphic events in the Cuchilla Dionisio Terrane, Uruguay, and possible correlations across the South Atlantic. Precambrian Research, 320, 303-322.

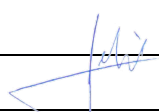| ANEXO I |
|---|
| Título da Dissertação/Tese: |
| **"Evolução geológica integrada do ofiolito Cerro do Ouro e do arco São Gabriel, Escudo Sul-riograndense, Brasil"** |
| Área de Concentração: **Geoquímica** |
| Autor: **TIARA CERVA ALVES** |
| Orientador: **Prof. Dr. Léo Afraneo Hartmann** |
| Examinadora: **Prof. Dr. Felipe Guadagnin** |
| Data: 12 de novembro de 2021 |
| Conceito: **A (EXCELENTE)** |

PARECER:

A Tese apresentada é um documento original que apresenta as hipóteses de uma forma bastante clara e utiliza distintas ferramentas para produzir novos dados que, junto com os dados da literatura, permitem ter uma delimitação muito mais precisa dos eventos responsáveis pelo registro geológico dos ofiolitos e do arco São Gabriel. O capítulo que aborda o problema científico deixa clara a complexidade do Terreno São Gabriel, atestada por uma série de trabalhos publicados, que por sua vez, serviram de base para o estabelecimento das hipóteses investigadas na Tese. O corpo da Tese contém três artigos científicos publicados em revistas internacionais de alto impacto, um dos quais já possui mais de uma dezena de citações. Além dos artigos publicados, o documento da Tese está apresentado conforme as normas do programa, incluindo as evidências que permitem delimitar o problema científico, as hipóteses e os métodos utilizados para produzir resultados que, em conjunto com os dados da literatura, permitem concluir a respeito da evolução geológica do ofiolito Cerro do Ouro e do arco São Gabriel. A abordagem inovadora pelo uso de diferentes ferramentas até então não utilizadas nos estudos prévios, permite estabelecer os eventos que foram responsáveis pelo metassomatismo da crosta oceânica próximo a paleo-cordilheira meso-oceânica, pela subducção da litosfera oceânica, pela construção da infraestrutura e da supraestrutura do arco, incluindo análise de proveniência sedimentar e determinação da idade deposicional máxima, permitem concluir que a

Tese deve receber o conceito A (excelente) e o grau de distinção de louvor a candidata.
Assinatura: Data: 12 de novembro de 2021
Ciente do Orientador:
Ciente do Aluno: